DENSITY FUNCTIONAL THEORY STUDIES OF BIOMASS CONVERSION ON METAL SURFACES: FROM SMALL TO LARGE MOLECULES

Qiang Li

UNIVERSITAT ROVIRA i VIRGILI

Density Functional Theory Studies of Biomass Conversion on Metal Surfaces: From Small to Large Molecules

Qiang Li

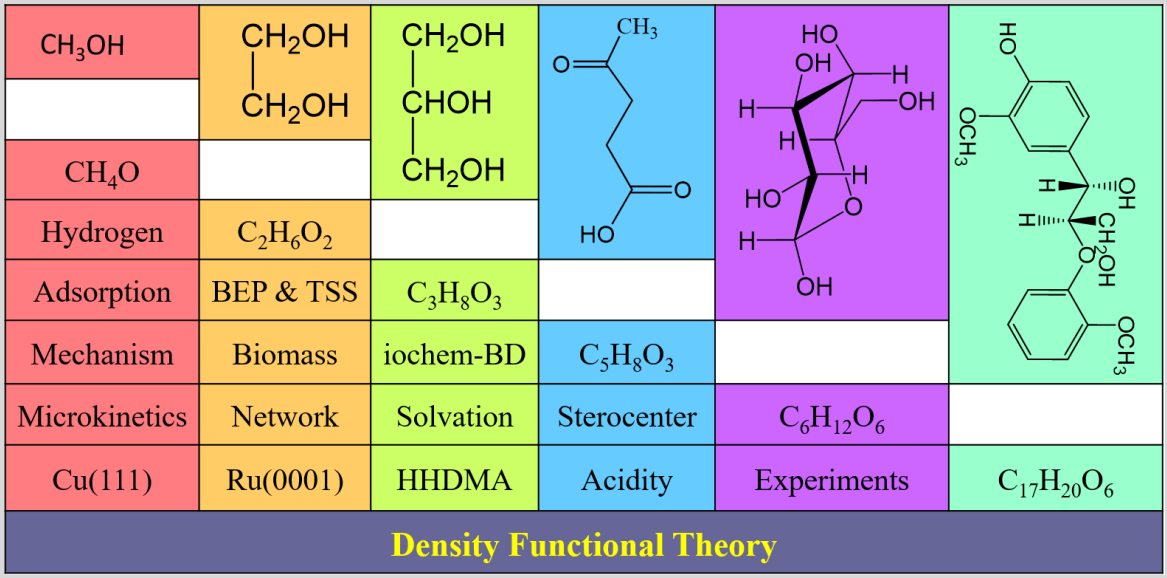

DOCTORAL THESIS
2017

UNIVERSITAT ROVIRA I VIRGILI
DENSITY FUNCTIONAL THEORY STUDIES OF BIOMASS CONVERSION ON METAL SURFACES:
FROM SMALL TO LARGE MOLECULES
Qiang Li

Density functional theory studies of biomass conversion on metal surfaces: from small to large molecules

DOCTORAL THESIS

Qiang Li

Supervised by

Prof. Núria López Alonso

Institute of Chemical Research of Catalonia
(ICIQ)
and Rovira i Virgili University (URV)

Tarragona
2017

UNIVERSITAT ROVIRA I VIRGILI
DENSITY FUNCTIONAL THEORY STUDIES OF BIOMASS CONVERSION ON METAL SURFACES:
FROM SMALL TO LARGE MOLECULES
Qiang Li

ICIQ
Institut
Català
d'Investigació
Química

I STATE that the present study, entitled "*Density functional theory studies of biomass conversion on metal surfaces: from small to large molecules*", presented by Qiang Li, for the award of the degree of Doctor, has been carried out under my supervision at Institut Català d'Investigació Química (ICIQ).

Tarragona, September, 09, 2017

Doctoral Thesis Supervisor

Núria López Alonso

UNIVERSITAT ROVIRA I VIRGILI
DENSITY FUNCTIONAL THEORY STUDIES OF BIOMASS CONVERSION ON METAL SURFACES:
FROM SMALL TO LARGE MOLECULES
Qiang Li

Sponsors

The accomplish of this PhD study was sponsored by European Research Council (ERC) and Ministry of Economy and Competitiveness (MINECO) under the following projects:

ERC-2010-StG-258406 Bio2Chem-d

ERC-2015-PoC-680900 BigData4Cat

MINECO CTQ2015-68770-R

The author appreciates their generous fund. The author would also thank

Barcelona Supercomputing Center (BSC)

Centro de Supercomputación y Visualización de Madrid (CeSViMa)

and the Spanish Supercomputing Network (RES)

for offering generous computaional resources.

UNIVERSITAT ROVIRA I VIRGILI
DENSITY FUNCTIONAL THEORY STUDIES OF BIOMASS CONVERSION ON METAL SURFACES:
FROM SMALL TO LARGE MOLECULES
Qiang Li

Acknowledgements

This work was done under the supervision of Prof. Núria López. In the three and half years study, I have always been holding these impressions on her: she knows everything, she is serious in science and warmhearted in life, above all, she is full of confident which originates from her truly love in science and solid theoretical knowledge. It is such a good fortune for me to continue the PhD career here.

Secondly, I would like to give my sincerely thanks to my family, my parents, brother, and especially to my wife, who scarified her time and job to be here. She is a very generous, caring woman and always gives me pertinent suggestions and encouragements when I feel frustrated.

Thirdly, I would like to thank all the brave and brilliant soldiers as listed from the three kingdoms (Núria López, Carles Bo, and Feliu Maseras). Deep friendships have been built when we fought together in these four years. Here I list names to acknowledge their kind help in my PhD studies and to remember the time we shared together. The former group members are Neyvis Almora-Barrios, Miquel Garcia Ratés, Luca Bellarosa, Guillem Revilla-López, Max Garcíía-Melchor, Sergey Pogodin, and Damien Cornu. And the president group members: Javier Navarro, Marçal Capdevila, Masoud Shahrokhi, Rodrigo García Muelas, Marcos Rellán, Michael Higham, Franziska S. Hegner Nathan Daelman, and Edvin Fako.

Specific thankfulness should be given to Rodrigo García Muelas, Marcos Rellán, and Neyvis Almora-Barrios, during the period we working together, I gained a lot and grown up fast as a baby soon after birth.

Thanks Núria Vendrell, Martin Gumbau, Moisés Àlvarez, and Maria Besora who supply the firmly back-support and advices for me to study and live here far away from troubles.

Great thanks should also be given to people I have collaborated with, Davide Albani, Giacomo M. Lari, Cecilia Mondelli and Prof. Javier Pérez-Ramírez from ETH Zurich, Karoliina Honkala from University of Jyvääskylää, Chunchao Hou and Prof. Yong Chen from TIPC, Chinese Academy of Sciences.

Finally, living and studying abroad in this small and tranquil coastal city are tough and boring, especially for the people who has accustomed to the metropolis. I would like to thank all the people listed below who spent time with me

and offered me generous help.

Zhongling Lang, Xiaoli Pei, Lingjun Hu, Yichen Wu, Chunxiao Wang, Liang Shao, Chuanjun Wang, Hongwei Zhang, Zhongyan Cao, Wusheng Guo, Rui Huang, Shaofei Ni, Shangzheng Sun, Yangyang Shen, Xiang Yin, Jincheng Wu, Xueqiang Wang, Xinyuan Fan, Zhongting Rong, Haijie Liu and Yachong Guo.

All my best wishes to all of your success in the future.

Above all, thanks all of you above and its a great treasure for me to have interactions between you and me in the short life and the big world.

List of Publications

Publications related with this thesis

1. Rodrigo García-Muelas, Qiang Li, and Núria López,
Density Functional Theory Comparison of Methanol Decomposition and Reverse Reactions on Metal Surfaces,
ACS Catal., 2015, **5**,1027–1036.

   DOI: 10.1021/cs501698w

2. Qiang Li, Rodrigo García-Muelas, and Núria López,
Microkinetics of alcohol reforming for H_2 production from a FAIR density functional theory database,

   In Review Process

3. Giacomo M. Lari, Olivier G. Gröninger, Qiang Li, Cecilia Mondelli, Núria López, and Javier Pérez-Ramírez,
Catalyst and Process Design for the Continuous Manufacture of Rare Sugar Alcohols by Epimerization Hydrogenation of Aldoses,
ChemSusChem, 2016, **9**, 3407–3418.

   DOI: 10.1002/cssc.201600755

4. Davide Albani, Qiang Li, Gianvito Vilé, Sharon Mitchell, Neyvis Almora-Barrios, Peter T. Witte, Núria López and Javier Pérez-Ramírez,
Interfacial acidity in ligand-modified ruthenium nanoparticles boosts the hydrogenation of levulinic acid to gamma-valerolactone,
Green Chem., 2017, **19**, 2361-2370.

   DOI: 10.1039/c6gc02586b

5. Qiang Li, Núria López,
Lignin decomposition on pure and Ru doped Ni(111) surfaces: density functional theory study on stereo and synergistic effects.

   In Preparation

Author contributions

Following the order above, the author contributions to the work in this thesis are listed as below:

1. Performed all calculations on Cu(111) and Ru(0001) surfaces, data analysis and discussions, wrote the first draft of this publication.
2. Performed calculations on Cu(111) and Ru(0001) surfaces, data analysis and discussions, and wrote the adsorption, reaction network, and TSS analysis parts in this publication.
3. Performed all DFT calculations in this paper and mechanism explanations, and wrote the theoretical part of this publication.
4. Performed all DFT calculations in this paper and mechanism explanations, and wrote the theoretical part of this publication.
5. Hold the idea, performed calculations, data analysis and discussions, wrote the advanced draft paper.

Publications out of the scope of this thesis

1. Qiang Li, Marcos Rellán-Piñeiro, Neyvis Almora-Barrios, Miquel Garcia-Ratés, Ioannis N. Remediakis,and Núria López,
Shape Control in Concave Metal Nanoparticles by Etching,

   Nanoscale, 2017, **9**, 13089-13094 .
   DOI: 10.1039/C7NR03889E

2. Chun-Chao Hou, Qiang Li, Chuan-Jun Wang, Cheng-Yun Peng, Qian-Qian Chen, Hui-Fang Ye, Wen-Fu Fu, Chi-Ming Che, Núria López and Yong Chen,
Ternary Ni-Co-P Nanoparticles and Their Hybrids with Graphene as Noble-metal-free Catalysts to Boost the Hydrolytic Dehydrogenation of Ammonia-Borane
Energy Environ. Sci., 2017, **10**, 1770-1776.

   DOI: 10.1039/C7EE01553D

3. Rodrigo García-Muelas, Qiang Li, and Núria López,
Initial Stages in the Formation of Nickel Phosphides.

   J. Phys. Chem. B, 2017.

   DOI: 10.1021/acs.jpcb.7b06020

Author contributions

1. Performed calculations on slab surfaces, data analysis and discussions.
2. Performed all DFT calculations in this paper and mechanism explanations, and wrote the theoretical part of this publication.
3. Performed reactions on Ni(100) surface, bader and magnetization calculations.

UNIVERSITAT ROVIRA I VIRGILI
DENSITY FUNCTIONAL THEORY STUDIES OF BIOMASS CONVERSION ON METAL SURFACES:
FROM SMALL TO LARGE MOLECULES
Qiang Li

世之奇伟、瑰怪、非常之观，常在于险远，
而人之所罕至焉，故非有志者不能至也。
《游褒禅山记》
——北宋 · 王安石

UNIVERSITAT ROVIRA I VIRGILI
DENSITY FUNCTIONAL THEORY STUDIES OF BIOMASS CONVERSION ON METAL SURFACES:
FROM SMALL TO LARGE MOLECULES
Qiang Li

Abstract

In this thesis, Density Functional Theory was used to understand the surfaces reactions related to various biomass molecules' transformations starting from small ones (methanol, ethylene glycol) to middle one, glycerol, and to large ones α/β-mannose and glucose, γ-valerolactone and lignin conversions.

In the first objective, methanol decomposition and synthesis have been studied on Cu(111) and Ru(0001) surfaces. Elementary reactions in the full decomposition network have been calculated by considering the van der Waals interactions. Reaction profiles, Brønsted and Evans-Polanyi relationship (BEP) and Transition State Scalings (TSS) for C–O, C–H and O–H bond scissions have been discussed. Furthermore, inter-molecular interactions which account for altering the initial decomposition steps (C–H or O–H breakings) has been clarified.

In the second objective, ethanol, and ethylene glycol decomposition mechanisms on Cu(111) and Ru(0001) surfaces have been systematically investigated and their results provides a rich database for linear scaling relationship (LSR) methods such as BEP and TSS relationships. Then, all adsorption species correlated with glycerol decompositions were optimized on Ru(0001) surface and the related transitions states' energies were obtained via the TSS method. Finally, from results of these elementary steps, *ab initio* microkinetic study about ethanol, EG, glycerol decomposition, aqueous phase reforming, auto-thermal reforming and steam reforming were performed.

In the third objective, levulinc acid conversion to γ-valerolactone on Ru-HHDMA was systematically studied, an in-depth molecular analysis by Density Functional Theory demonstrates that the intrinsic acidic properties at the ligand-metal interface under reaction conditions altered reactions starting from surface levulate form to less energy demanding path started from the surface levulinic form. The reaction does not obey the expected cascade mechanism and intercalates hydrogenation steps, hydroxyl/water eliminations, and ring closings to ensure high selectivity. Moreover, the interfacial acidity increases the robustness of the material against ruthenium oxide formation. These results provide valuable improvements for the sustainable production of GLV and insights for the rationalization of the exceptional selectivity of Ru-based catalysts.

In the fourth objective, mechanisms of glucose, mannose hydrogenation to their corresponding polyalcohols on Ru(0001) were investigated. The concentrations of different reactant isomers in the liquid phase, their adsorption nature on

the surface, as well as the different rate limiting steps (hydrogenation and ring opening reactions for glucose and mannose) determine the overall reaction rates. Langmuir-Hinshelwood adsorption model and transition state theory were employed to describe the kinetic differences between glucose and mannose hydrogenations, our predicted reaction rate ratio are close to the experiment observations. Given the simple approximations, the agreement between DFT derived value and experiment result is remarkable. This opens a prospective route to the efficient valorization of renewable to added-value chemicals.

In the fifth objective, β-O_4 bond breaking mechanisms of lignin dimer model were investigated on Ni(111) surface, more complex molecular surrogates presenting stereocenters and based on coniferyl alcohol (G) dimers were selected in this work. By performing DFT calculations, the most stable two geometries were identified and the decomposition pathways have been mapped and computed. Furthermore, the Ru doping effects on reactions were investigated via replacing one surface Ni by Ru atom. Our results firstly demonstrate the effects of the stereocenters in decomposition process and the synergistic of Ru and Ni, detailed reaction mechanisms can also provide atomic guidelines for the catalysts design and improvements.

Abbreviations

IUPAC	International Union of Pure and Applied Chemistry
DFT	Density Functional Theory
GGA	Generalized Gradient expansion Approximation
LDA	Local Density Approximation
PW91	Perdew-Wang functional
PBE	Perdew-Burke-Ernzerhof
MGCM	Multigrid Continuum Model
GPE	Generalized Poisson Equation
PAW	Projector Augmented Wave
FCC	Face-Centered Cubic
BCC	Body-Centered Cubic
vdW	van der Waals
VASP	Vienna *Ab-initio* Simulation Package
EG	Ethylene Glycol
MK	Microkinetic
BEP	Bronsted and Evans-Polanyi relationship
TSS	Transition State Scaling
TST	Transition State Theory
IS	Initial State
TS	Transition State
FS	Final State
NEB	Nudged Elastic Band
CINEB	Climbing Image Nudged Elastic Band
IDM	Improved Dimer Method
ZPE	Zero Point Energy
LA	Levulinc Acid
HMF	HydroxyMethylFurfural
GVL	Gamma-valerolactone
HHDMA	Hexadecyl(2-Hydroxyethyl)DiMethylAmmonium dihydrogen phosphate ligand
WGS	Water Gas Shift reactions
DD	Direct Decomposition
ATR	Auto Thermal Reforming
APR	Aqueous Phase Reforming
SR	Steam Reforming
FAIR	Findability, Accessibility, Interoperability and Reusability
BTX	Benzene, Toluene, and Xylenes

Contents

Chapter 1

Introduction

Energy crisis

While people are enjoying the benefits resulted from the increasing developments of our society and technology, numerous detrimental effects and problems come along, such as energy crisis, global warming and the deteriorating environment. From the Organization of the Petroleum Exploring Countries (OPEC) annual statistical bulletin,[1] the total world proven crude oil reserves are 1,492,164.0 million barrels and daily production is 75.4767 million barrels in the year of 2016. Based on this production speed, crude oil will be approximately dried up in the next 54 years. The depletion of fossil resources, especially crude oil and the improvements of environmental protection awareness force us to continue seeking for alternative, renewable, cheap and safer energies to solve energy crisis. And this is one of the most important issue in embracing the future of our society.

Two crucial points exist in crude oil substitution, energy and materials replacement. So far, hydrogen, solar energy, biomass, nuclear, tide, wind, geothermal resources, as well as other kind of energies have been studied since last century. Among them, hydrogen, solar energy holding the advantages such as clean, high energy density, zero-carbon release, are well recognized as the ideal candidates

[1] www.opec.org

for future energy vectors. In the meanwhile, biomass can both supply the energy and materials. Nevertheless, there are still many obstacles for their large industry or widely applications and the way of substitution of crude oil resources are doomed to be a long way. For example, because of low boiling point and volumetric density of hydrogen, its production, storage and release are main limiting factors for widely usage. For solar energy, the efficient of solar panels, pollution from solar energy systems, and its weather dependence. For biomass, the main difficult parts come from the collection, degradation or reforming process, and the low energy density.

Hydrogen production according to its resources can be separated into two main methods: carbon-based and water-based.[1–3] For carbon based method, it mainly relies on fossil fuel (natural gas, coal, naphtha), and biomass and biomass derived feed stocks (ethanol, glycerol and the others) through reforming, cracking, partial oxidation and gasifications, in the meanwhile, water-gas shift reaction, one important water-based method, would also takes apart in some of these processes. For other water-based methods, hydrogen can be generated via water electrolysis, photocatalysis, and thermochemical cycles.

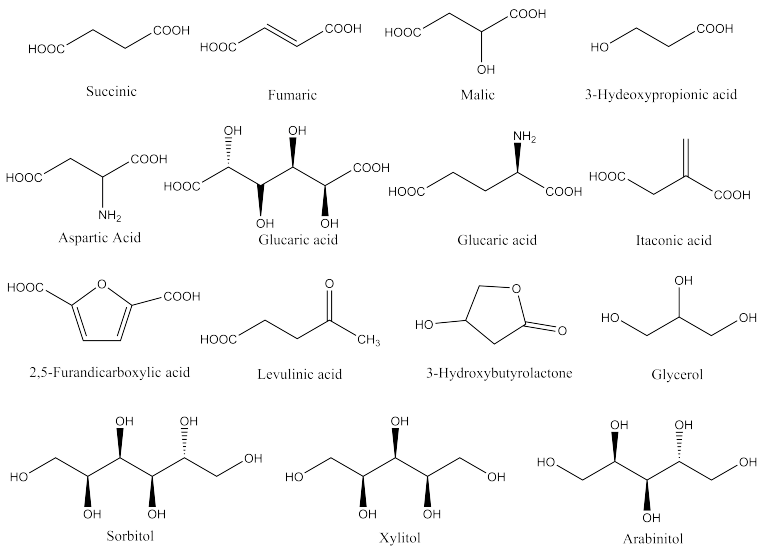

Figure 1.1: Top value added chemicals from biomass conversions, reported by US Department of Energy in 2004.

Biomass, which contains materials produced by microorganisms, plants and animals, is a renewable and sustainable resources from nature. They provide us both energies and materials.[4,5] In 2004, the US Department of Energy reported a seriers of top value added chemicals (See Figure 1.1) in biomass conversion.[6,7] These building block chemicals are obtained from starch, hemicellolose, cellulose, and oil conversions, and can be subsequently converted into fuel additives and a series high-value added derivatives. Besides, the other important part of the biomass, lignin, have the potential to supply us the aromatic materials such as BTX (benzene, toluene, and the three xylene isomers).[8,9] And this is the only nature and available way to obtain the aromatic compounds in large industry scale without using fossil resources.

Catalysis

By the definition of International Union of Pure and Applied Chemistry (IUPAC), catalyst is a substance that increases the rate of a reaction without modifying the overall standard Gibbs energy change in the reaction, in the meanwhile, catalyst itself is not being consumed. Catalysts play the central role in modern chemical industry and are the workhorse of chemical transformations, such as ammonia synthesis, crude oil catalytic cracking, methane steam reforming, water-gas shift reactions and others. Approximately 85-90% of the chemicals are produced with the help of catalysts[10] and developing catalysts with high activity, selectivity is always the goal in chemists' investigations, which also lies in the heart of solving the fossil resources replacement problems.[11] For a good catalyst, its interaction with surface intermediates should neither be too strong nor too weak. Too strong interaction would lead to the surface poisoning and reactions would not happen if the interactions are too weak.[12] This qualitative principle is the so called Sabatier principle, proposed by the French chemist Paul Sabatier in 1902.[13]

In the catalytic process, the reactants are activated and the reaction barriers have been dramatically decreased via the interaction between catalyst and the reactants. Classified by the reaction phase, catalysis can be divided into three subdisciplines: homogeneous, heterogeneous and bio catalysis. Among them, heterogeneous catalysis holds the 80% global market share[14] and this percentage is estimated to increase in the next few years. In heterogeneous catalysis,

reactions are accelerated via the solid catalysts and proceed on the interface of solid-gas or solid-liquid. Several elementary steps are involved in one catalytic cycle and most widely accepted is the Langmuir-Hinshelwood mechanism.[15] Taken the reaction of A + B → AB in a solid-gas system as an example, the reaction follows as

$$\begin{aligned} A_{gas} + * &\underset{k_1^-}{\overset{k_1^+}{\rightleftharpoons}} A^* \\ B_{gas} + * &\underset{k_2^-}{\overset{k_2^+}{\rightleftharpoons}} B^* \\ A^* + B^* &\underset{k_3^-}{\overset{k_3^+}{\rightleftharpoons}} AB^* + * \\ AB^* &\underset{k_4^-}{\overset{k_4^+}{\rightleftharpoons}} AB_{gas} + * \end{aligned} \tag{1.1}$$

firstly, reactants A and B adsorb on the surface, followed by the surface reaction to produce the surface product AB*, and the products leave the surface in the end. In the surface reaction step, the reaction rates can be calculated via the transition state theory which was formalized by Eyring and Evans and Polanyi in 1935,[16,17]

$$k = \left(\frac{k_B T}{h}\right) \frac{q_{AB}^{\#}}{q_A * q_B} e^{-\frac{E_a}{RT}} \tag{1.2}$$

where $q_{AB}^{\#}$, q_A, and q_B are partition function of transition states and reactants A and B, E_a is the activation energy.

Besides, Brøsted-Evans-Polanyi relationship (BEP) which connects the thermodynamics and kinetics exists.[18–20]

$$E_a = \alpha \Delta E + \beta \tag{1.3}$$

where ΔE is reaction energy in one elementary reaction, α and β are fitted linear parameters.

For a simple system having a series elementary reactions, the overall rate is a function of the adsorption, desorption and elementary transition states. However, the real catalytic process is far simple than the steps above. It is a combination of numerous factors such as reaction conditions (pressure, temperature),

catalysts' morphologies and various active sites, promoters, supports, deactivation, and time et al. Those mentioned factors work together and affect the reaction rates and selectivity. Moreover, based on the catalysts and reaction conditions, reactor design is also a crucial part for its widely industry application. Therefore, catalyst design is a systematic and multi-corroborated work, as the hierarchical scheme classified by Ertl[21] in the time and length scale.

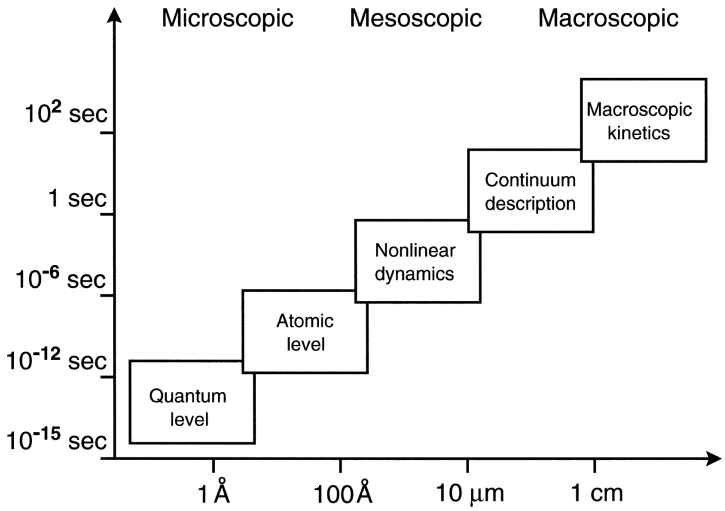

Figure 1.2: Schematic classification of the dynamics of surface reactions in multiscale aspects. Adapted from Ref. [21]

As shown in Figure 1.2, quantum level understanding of the reaction related properties forms the foundation base of the multiscale study. With the great development of supercomputers in the last few decades, and improvement of their calculation speed and ability, together with the development of the theoretical methods and related software packages, efficient and convenient density functional theoretical study on the surface reactions becomes practicable and less time consuming. This expands our visual sight in understanding the surface reaction mechanisms in atomic level, enables us to explain phenomena that are difficult to be interpreted by the limited experiment equipments, and supplies the theoretical guidelines for catalysts design.

In practice, the Vienna *Ab-initio* Simulation Package (VASP),[22,23] based on

plane waves and periodic conditions can serve as the workhorse in materials modeling from first principles. Catalysts electronic and structure properties, surface reactions can be computed to compare with the experiment results. To model the reactions on typical metal and metal oxide catalysts, we can optimize the adsorption structures and searching the transition states via slab models under the theoretical instruction of Langmuir adsorption, transition state theory. Calculated data can then be expanded into the larger scale by using the linear methods, such as BEP and TSS relationship, microkinetic simulations as well as other techniques.[24]

DFT calculations in this thesis

In this thesis, the purposes are mainly consisted of two parts: energy and material substitutions. The author focused on the conversion of a series of biomass derived molecules with H_2 is produced from the alcohols and the rest large molecules to represente the material substitutions. All molecules studies in this thesis are list as below:

- C_1, C_2 and C_3 alcohols: methanol, ethanol, ethylene glycol, and glycerol;
- Cellulose derived products: levulinic acid (LA), γ-valerolatone (GVL), glucose, and mannose.
- Lignin: representative lignin dimer.

Hydrogen production from small alcohols

For the first purpose, H_2 was selected as the ideal energy vector and H_2 releasing from C_{1-3} alcohols was investigated on Cu(111) and Ru(0001) surfaces. Those calculations are divided into four parts as following:

- Gas phase of the related close-shell molecules.
- Complete C_1 and C_2 alcohols decomposition intermediates' optimization on the Cu(111) and Ru(0001) surfaces.
- Complete glycerol decomposition species optimization on Ru(0001) surface.

- Complete transition states searching in the C_1 and C_2 alcohols decomposition network.

The objectives of these calculations are as listed below:

- Create a FAIR (findability, accessibility, interoperability and reusability) database from the complete decomposition networks.
- Investigate the adsorption properties of the intermediates in the complex reaction network
- Define the reaction profile via transition state theory.
- Study the linear scaling method such as BEP and TSS.
- Combine the database with the linear scaling method and *ab initio* microkinetic study to expand the DFT calculations into a larger scale, both time and molecule size.
- Interpret some experiment observations both in surface studies and reforming techniques.
- Above all, deepen our understanding on surface reactions and promotes the catalysts' design process.

Biomass molecules' conversions

The second purpose consists of the conversions of several large biomass molecules as they provide us rich materials compounds. According to the investigated molecules, biomass conversions are split into three parts,

- LA conversion to GVL on Ru(0001) and HHDMA decorated Ru(0001) surfaces.
- Glucose and mannose hydrogenation to sorbitol and mannitol on Ru(0001) surface
- Lignin dimer decomposition and hydrogenation on Ni(111) and Ru decorated Ni(111) surfaces.

All these three objectives are tightly related with available experiment observations. By performing DFT calculations, the main goals are to explain and interpret the phenomenon that can not be easily understood by the limited

experiment techniques and formalize the reaction mechanisms. The detailed purposes are listed as below:

- Study the mechanism of LA conversion to GVL and elucidate the reason why HHDMA decorated Ru catalysts have higher activity and stability than the commercialized Ru catalyst.
- Study the mechanisms of glucose and mannose hydrogenation to their sugar alcohols and interpret the experiment results that mannose has the faster hydrogenation rates than glucose.
- Study the mechanism of lignin de-polymerization mechanisms and explain the stereocenter's role in lignin conversion and Ru doping effects in promoting the catalysts behaviors.

Outlook

In order to fulfill the rational catalysts designment, surface reaction studies at the atomic level are one of the crucial points to understand the elementary processes. And these are also the starting and footing points of those studies in this thesis. In spite that the systems studied in this thesis are limited, the author believes that these calculations would expand our view sights in heterogeneous catalyzed biomass conversions and provide rich atomic information about adsorption and elementary reaction steps in the complex reaction network. This would strengthen our understanding about how catalytic surface reaction proceed and also offer useful guidelines for the catalysts design.

Chapter 2

Computational Methods

Brief DFT introduction

Schrödinger equation

The Schrödinger equation, is named after Erwin Schrödinger who derived it in 1925 and published in 1926,[25] is the fundamental equation in quantum physics. This equation describes how a physical system in which quantum effects evolves over time. For the time-independent and non-relativistic systems, it can be written generally as

$$\hat{H}\Psi = E\Psi \tag{2.1}$$

where $\hat{H}$ is the Hamiltonian operator, Ψ is the wave function, and E is the energy of the system. Further reading are refered to a few density functional theory (DFT) related textbooks.[26–30]

Born-Oppenheimer approximation

The Born-Oppenheimer Approximation is the assumption that the motion of atomic nuclei and electrons in a molecule can be separated. The physical basis for this assumption is the fact that the mass of an atomic nucleus in a molecule is much larger than the mass of an electron (1800 times for the lightest of all

nuclei, ^{1}H, proton).[26] Because of huge mass difference, the nuclei move much more slowly than the electrons. As a result, the electrons are moving and responding to forces or displacement of the nuclei very quickly, and the nuclei are not. Therefore, instead of solving the Schrödinger equation for all the particles simultaneously, separating a molecular wave function into terms of electron positions and nuclear positions significantly helps in dealing with the Schrödinger Equation.

$$\Psi_{tot} = \psi_{electronic} \times \psi_{nuclei} \tag{2.2}$$

hence, equation 2.1 can be regarded as solving the ground state energy of the electronic system in external potential set by the nuclei. And the Hamiltonian for the system is[1]:

$$\begin{aligned}\hat{H} &= \hat{H}_e + \hat{H}_n \\ &= \left(\hat{K}_e + V_{ee}(r) + V_{en}(r,R)\right) + \left(\hat{K}_n + V_{nn}(R)\right) \\ &= \left(-\sum_i \frac{1}{2}\nabla^2 + \sum_{i>j}\frac{1}{r_{ij}} - \sum_{i,A}\frac{Z_A}{r_{iA}}\right) + \left(-\sum_A \frac{1}{2M_A}\nabla_A^2 + \sum_{B>A}\frac{Z_A Z_B}{R_{AB}}\right)\end{aligned} \tag{2.3}$$

where $\hat{K}_e$, $\hat{K}_n$, are kinetic energies of electrons and nucleus, V_{ee}, V_{en}, V_{en}, are columbic interaction energies of electron-electron, electron-nuclei, and nuclei-nuclei.

The many-body problem

For a N electrons system within the chosen Hamiltonian, ψ is the electronic wave function, which containing all of the spatial coordinations of N electrons, so

$$\psi = \psi(\mathbf{r_1}, ..., \mathbf{r_n}) = \psi_\mathbf{1}(\mathbf{r})\psi_\mathbf{2}(\mathbf{r}), ..., \psi_\mathbf{N}(\mathbf{r}) \tag{2.4}$$

With increasing the size of the system, dimensions of wave function increase significantly. For example, when spin is not considered, 66 and more than 23,000 dimensions (xyz directions) are needed for CO_2 and a Pt nanocluster containing 100 atoms.[27] Furthermore, this situation become more difficult to tackle with when taking the Hamiltonian, $\hat{H}$, in consideration. As the individual electron

[1] Atomic units are used: $e = a_0 = m_e = \hbar = 1$

wave function $\psi_i(\mathbf{r})$ associates with all other electrons, it can only be found when considering all electrons simultaneously and this task turns out to be far beyond reach. In other words, the Schrödinger equation is a many-body problem. Fortunately, this task can be handled by using the density of electrons at a particular position in space, $n\mathbf{r}$, a summation goes over all individual electron wave functions that are occupied by electrons. Besides, electron density also has the physical obserable properties and can be mesured and compared from experiment techniques and theory prospects.[31–34] This can be written in terms of the individual electron wave functions as

$$n(\mathbf{r}) = 2\sum_{i}^{N} \psi_i^*(\mathbf{r})\psi_i(\mathbf{r}) \tag{2.5}$$

where the factor of 2 is the occupation of orbital i (with spin-degeneracy included) because of the Pauli exclusion priciple for electrons with spins. By doing so, the N-body problem has been turned into solving a N single-body problem with only three dimensions, which dramatically simplifies the solution of Schrödinger equation.

The Hohenberg-Kohn theorems

The Hohenberg-Kohn theorems proved by Hohenberg and Kohn in 1964[35] relate to any system consisting of electrons moving under the influence of an external potential, $v(\mathbf{r})$, is the simplest way to obtain approximations to the Schrödinger equation.

- Theorem 1: The external potential is a unique functional of the electron density only. Thus the Hamiltonian, and hence all ground state properties, are determined solely by the electron density.

It is provided that there exists a universal functional of the density, $F_{HK}[n(\mathbf{r})]$, which is independent of the external potential $v(\mathbf{r})$. So, the total energy of system can be written as

$$\begin{aligned} E_{tot} &= F_{HK}[n(\mathbf{r})] + V_{ext}[n(\mathbf{r})] \\ &= T[n] + U[n] + V_{ext}[n(\mathbf{r})] \\ &= T[n] + U[n] + \int v(\mathbf{r})n(\mathbf{r})d\mathbf{r} \end{aligned} \tag{2.6}$$

where $T[n]$ and $U[n]$ are classical kinetic and coulombic energies, respectively, $V_{ext}[n(\mathbf{r})]$ is the external potential energy.

- Theorem 2: The ground state energy may be obtained variationally: the density that minimizes the total energy is the exact ground state density.

For N electrons in the external potential $V(\mathbf{r})$ with the ground-state energy of E_0, for all v-representable densities $n(\mathbf{r})$, there exists

$$E_V[n] \geq E_0 \tag{2.7}$$

Thus the problem of solving the Schrödinger equation for non-degenerate ground-states can be turned into a variational problem of minimizing the functional $E_V[n]$ with respect to v-representable densities.

The Kohn-Sham equations

Based on The Hohenberg-Kohn theorems, approximated methods for treating inhomogeneous system of interaction electrons were developed by Kohn and Sham in 1965.[36] The Kohn-Sham system is a fictitious system of non-interaction particles (typically electrons) that generate the same density as any given system of interaction particles. The system is described by Hamiltonian

$$\begin{aligned} \hat{H}_s &= \hat{T}_s + \hat{V}_s \\ &= \hat{T}_s + \hat{V}_{ext} + \hat{V}_H + \hat{V}_{xc} \end{aligned} \tag{2.8}$$

where V_s is the Kohn-Sham potential, a local effective external potential in which the non-interacting particles move. Hence, the total energy can be written as

$$E_{tot} = T_s[n] + E_{ext}[n] + E_H[n] + E_{xc}[n] \tag{2.9}$$

where $T_s[n]$ is the Kohn-Sham kinetic energy, $E_{ext}[n]$ is the energy of external potential action on the system. E_H is the classical Coulomb interaction energy, and E_{xc} is the exchange-correlation energy.

Generally, the KS equation is represented by the eigenvalue equation

$$\left(-\frac{\hbar^2}{2m}\nabla^2 + v_s(\mathbf{r})\right)\phi_i(\mathbf{r}) = \varepsilon_i\phi_i(\mathbf{r}) \tag{2.10}$$

where ε_i is the energy of the corresponding Kohn-Sham orbital and the related density $n(\mathbf{r})$ for an N-particle system considering electron spin is expressed in Equation 2.5.

Exchange-Correlation functional

The work from Hohenberg, Kohn and Sham paves the way for solving the Schrödinger equation by minimizing the energy functional. However, for the exchange-correction term in KS equation, which comes from the quantum effects, its functional are unknown. Therefore, exchange-correction term determines the solution accuracy of the KS equation. Figure 2.1, proposed by Perdew[37,38] as the Jacob's ladder of DFT, illustrates the the hierarchy of exchange-correlation functionals.

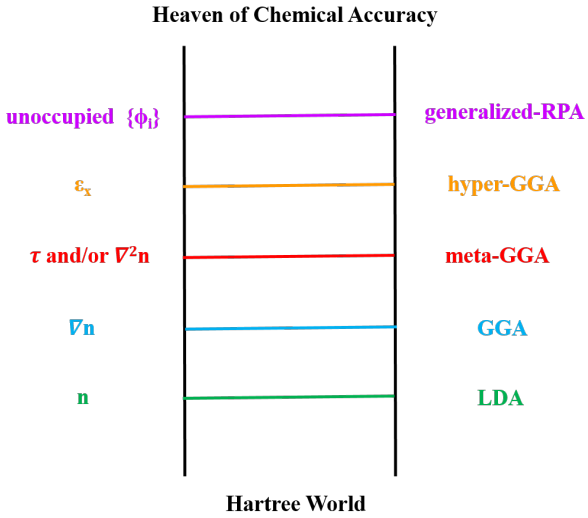

Figure 2.1: Jacob's ladder of the exchange-correlation term in DFT approximations. Adapted from Ref.[38]

Approximately, exchange-correction can be derived from the uniform electron gas with accurately describing the physical properties. Figure 2.2 shows the Local Density Approximation (LDA),[26,36] which lies in the ladder's bottom. In this method, the functional depends only on the density at the coordinate where it can be evaluated as:

$$E_{XC}^{LDA}[\rho] = \int \rho(\vec{r})\varepsilon_{xc}(\rho(\vec{r}))d\vec{r} \tag{2.11}$$

with $\rho(\vec{r})$ is the electron density at position $\vec{r}$.

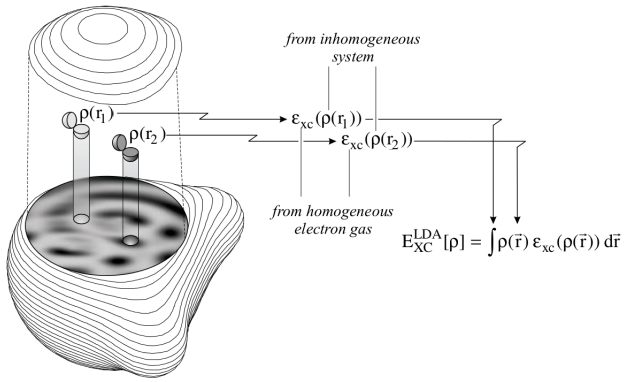

Figure 2.2: The local density approximation. Adapted from Ref. [26]

Because LDA assumes that the density is the same (homogeneous electron gas) in the volume $d\vec{r}$, it has a tendency to over-estimate the exchange-correlation energy. To correct this over-estimation, the density has been expanded in terms of the gradient in order to account for the non-homogeneity of the true electron density. This approach defines a Generalized Gradient Approximation (GGA).

$$E_{XC}^{GGA}[\rho] = \int [\rho(\vec{r}), \nabla\rho(\vec{r})]\varepsilon_{xc}(\rho(\vec{r}))d\vec{r} \tag{2.12}$$

Among the large number of GGA functionals, two of the most widely used functionals in periodic solids systems are Perdew-Wang functional (PW91) [39] and the Perdew-Burke-Ernzerhof functional (PBE). [40]

DFT in periodic systems

Blöch theorem

Blöch Theorem states that the wave function of a particle, $\psi(\mathbf{r})$, in periodically-repeating system has the form

$$\psi(\mathbf{r} + \mathbf{R_n}) = e^{i\mathbf{k}\cdot\mathbf{R_n}}\psi(\mathbf{r}) \tag{2.13}$$

where k is a vector with real numbers and $\mathbf{R_n}$ is the crystal vector. Therefore, the state of the system is determined by the $\psi(\mathbf{r})$, instead of k or $\mathbf{R_n}$. The wave function can be rewritten as

$$\psi(\mathbf{r}) = e^{i\mathbf{k}\cdot\mathbf{r}}u(\mathbf{r}) \tag{2.14}$$

where $u(\mathbf{r})$ is a function having the same periodicity with the crystal potential. Express the function $u(\mathbf{r})$ as a Fourier series

$$u(\mathbf{r}) = \sum_{\mathbf{G}} \widetilde{u}_{\mathbf{G}} e^{i\mathbf{G}\cdot\mathbf{r}} \tag{2.15}$$

where the $\mathbf{G}$ is the reciprocal lattice vectors. The eigenstates of the Hamiltonian, $|\psi_{\mathbf{j},\mathbf{k}}\rangle$, can be expanded as

$$\psi_{\mathbf{j},\mathbf{k}}(\mathbf{r}) = \sum_{\mathbf{G}} c_{\mathbf{j},\mathbf{k}+\mathbf{G}} e^{i(\mathbf{k}+\mathbf{G})\cdot\mathbf{r}} \tag{2.16}$$

where $\mathbf{j}$ is the quantum number labeling different eigenstates with the same vector $\mathbf{k}$. Therefore, the problem has been changed from an infinite number of electrons in solid into the finite number electrons in the unit cell by applying Bloch's theorem. The k-points numbers can be finite, because when the numbers are sufficient enough, the wave function at Δk can be regarded as identical.

Pseudopotential plane wave method

Pseudopotential approximation was first introduced by Hans Hellmann in 1934, [41] which simplifies the core nucleus and electrons in an atom by an effective potential and therefore reduces the basis set size the number of electrons for solving Schrödinger equations (Figure 2.3). It is based on the concept in chemistry that only the valence electrons are chemically active and the core electrons remain inactive and can be separated by a frozen core approximation. [42] In practice, by combining plane wave basis sets with pseudopotential, the valence properties of a system can be described by solving the Schrödinger equation.

Augmented plane wave method

In 1937, Slater proposed the Augmented plane wave method [43] in which the muffin-tin approximation is used for the potential field in an atomistic environment. The potentials supposed to be spherically symmetrical within spheres

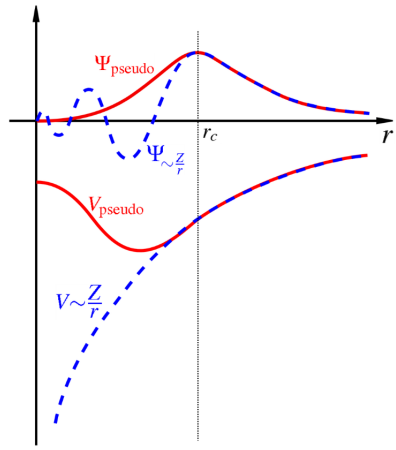

Figure 2.3: Schematic comparison of the real and the pseudo wave functions (blue) and potentials (red), which match from a certain cutoff radius r_c. Taken from Wikipedia, see link: `https://en.wikipedia.org/wiki/Pseudopotential`

surrounding the atoms and constant outside. Within spheres, the wave function is expanded in spherical harmonics and radical solutions. Outside the spheres, the wave function is expanded in plane waves. Thus, the wave function can be written as

$$\psi(\mathbf{r}) = \begin{cases} e^{i\mathbf{k}\cdot\mathbf{r}} & when\ |\mathbf{r}-\mathbf{R}| \geq r_0 \\ U & when\ |\mathbf{r}-\mathbf{R}| < r_0 \end{cases} \tag{2.17}$$

with r_0 is the atoms' core radius and U is the constant spherical potential in the core.

Projector augmented wave method

Projector Augmented Wave Method (PAW), was first developed by Blöchl in 1994.[44,45] It is an approach which generalizes both the pseudopotential and the linear augmented plane wave method in a natural way, and PAW improves first principle calculations with a great computational efficiency. In this method, the physical relevant all electron wave functions, $|\Psi_n\rangle$ have been transformed or

mapped into the computationally convenient, auxiliary wave functions, $|\widetilde{\Psi}_n\rangle$.

$$|\Psi_n\rangle = \hat{\tau}|\widetilde{\Psi}_n\rangle \tag{2.18}$$

where $\hat{\tau}$ is the linear transformation. The transformation of Kohn-Sham Hamiltonian is

$$\widetilde{H} = \hat{\tau}^{\dagger}\hat{H}\hat{\tau} \tag{2.19}$$

the ground state of the $|\widetilde{\Psi}_n\rangle$ can be obtained from

$$\hat{\tau}^{\dagger}\hat{H}\hat{\tau}|\widetilde{\Psi}_n\rangle = \hat{\tau}^{\dagger}\hat{\tau}|\widetilde{\Psi}_n\rangle\epsilon \tag{2.20}$$

When we exploit the characteristics of particular atom types, in order to have $|\tilde{\Psi}\rangle$ and $|\Psi\rangle$ differ only in the regions near the ion cores, the operator has a form "identity plus atomic contributions",

$$\hat{\tau} = 1 + \sum_a \hat{\tau}^a \tag{2.21}$$

where $\hat{\tau}^a$ is non-zero only within some spherical augmentation region Ω_R enclosing atom a.

van der Waals forces

van der Waals Forces or dispersion interactions, are the weak distance-dependant attractive or repulsive forces between atoms or molecules. The term includes: dipole-dipole, dipole-induced dipole and London (instantaneous induced dipole-induced dipole) forces.[46] In this thesis, DFT-D2 approach developed by Grimme[47] was applied. In this method, the correction term for dispersion has the form:

$$E_{disp} = -\frac{1}{2}\sum_{i=1}^{Nat}\sum_{j=1}^{Nat}\sum_{L}{}' \frac{C_{6ij}}{r_{ij,L}^6} f_{d,6}(r_{i,j}, L) \tag{2.22}$$

where the summations are over all atoms N_{at} and all translations of the unit cell $L = (l_1, l_2, l_3)$. C_{6ij} is the dispersion coefficient of the atom pair ij, r_{ij} is the distance between atom i and j. $f(r_{ij})$ is a damping function that is used to scale the force filed. C_{6ij} and $f(r_{ij})$ have the forms of

$$C_{6ij} = \sqrt{C_{6ii}C_{6jj}} \tag{2.23}$$

$$f_{d,6}(r_{ij}) = \frac{S_6}{1 + e^{-d(r_{ij}/(s_R R_{oij})-1)}} \tag{2.24}$$

with R_{0ij} is computed by

$$R_{0ij} = R_{0i} + R_{0j} \tag{2.25}$$

In the calculations of this thesis, s parameters are used the default values and C_{6ii} and R_{oi} are used from values reoptimized in our group.[48]

Table 2.1: C_6 and R_0 parameters used in DFT-D2 calculations in this thesis

Atom	C_6 (Jnm^6/mol)	R_0 (Å)
Ru	4.168	1.639
Cu	2.740	1.562
Pt	7.000	1.750
Pd	5.510	1.690
Ni	2.626	1.357
H	0.14	1.001
C	1.75	1.452
N	1.23	1.397
P	7.84	1.750

Solvation model

As plenty of heterogeneous catalytic reactions take place in the interface between aqueous and catalysts surface, environment contributions such as solvation can not be ignored because of their (de)stabilization effects on the reactants. Therefore, consideration of its effects would further increase our knowledge about the complex reaction networks. In this thesis, solvation contributions to reactants (Figure 2.4) as well as products have been calculated via VASP-Multigrid Continuum Model (VASP-MGCM).[49] In this approach, adding the implicit solvation contributions are based on the solution of the Generalized Poisson Equation (GPE) which governs the behavior of the electrostatic potential of a system.

$$\nabla[\epsilon(\mathbf{r})\nabla\phi(\mathbf{r})] = -4\pi\rho(\mathbf{r}) \tag{2.26}$$

where $\epsilon(\mathbf{r})$ is the known dielectric permittivity. $\phi(\mathbf{r})$ is the gradient of the total electrostatic potential, and ρ is the solute charge density. The electrostatic

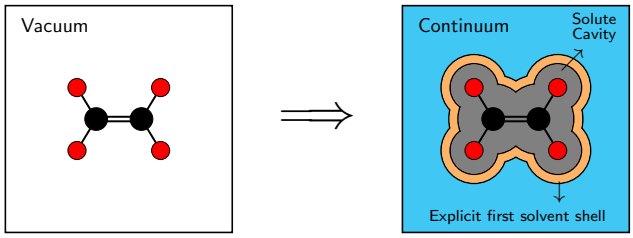

Figure 2.4: Schematic view of implicit solvation. Taken from Ref.[49]

energy of the system can then be calculated by

$$E_{el} = \frac{1}{8\pi} \int \epsilon(\mathbf{r}) |\nabla\phi(\mathbf{r})|^2 d(\mathbf{r}) \tag{2.27}$$

Add this term to the Kohn-Sham effective potential, V_s, the total energy of the system is

$$E_{tot} = T_s[n] + E_{ext}[n] + E_H[n] + E_{xc}[n] + E_{el} + E_{nel} \tag{2.28}$$

where E_{nel} is the non-electrostatic term and has the form

$$E_{nel} = \gamma_{eff} \cdot S \tag{2.29}$$

with γ_{eff} the effective surface tension and S the quantum surface of the solute. Detail information can be traced back to Ref.[50–52] and the Supporting Information of Ref.[49] Calculated sovation energy of the species in H_2O are listed in Table 2.2

DFT study on catalysts

Slab model

For heterogeneous catalysts, their exposed surfaces contains the main reactive sites. Among those exposed surfaces, large fraction is constitute of the low-index surfaces, such as (111), (110), and (0001) for face-centered cubic (FCC), body-centered cubic (BCC) and hexagonal structures, respectively. The practical way of DFT calculations to study the surface reaction mechanisms is to build a slab

Table 2.2: Calculated solvation energy (in eV) of species in water.

Species	E_{sol}
H_2	0.10
O_2	0.01
CO	-0.01
CO_2	-0.19
H_2O	-0.27
CH_2O	-0.21
CH_3OH	-0.20
CH_4	0.00
CHCH	-0.11
CH_2CH_2	-0.02
CH_3CHO	-0.23
CH_3CH_3	0.02
CH_3CH_2OH	-0.19
$HOCH_2CH_2OH$	-0.33
Glycerol	-0.40
Levulinic Acid	-0.27
γ-valerolactone	-0.44
β-Glucose	-0.91

model to simulate the surfaces,[27] see Figure 2.5. In this figure, the model is a $p(3\times3)$ supercell of Ni(111) surface. From the top view, four reaction sites (atop, bridge, fcc (red), and hcp (yellow)) can be distinguished clearly. Repeating the model long with a and b (or x, y) directions, the surface is infinite in two dimensions. In c (z) direction, it is separated by the empty area called vacuum layer to mimic the gas conditions. During calculations, the bottom layers are generally fixed within their bulk parameters and the top layers (two layers in most cases) are full relaxed in three directions. As a result, slab model provides us the way to simulate the reactions at the solid-gas and solid-solution interfaces with reasonable physical and chemical reality.

DFT calculation details

In this thesis, slab calculations were performed using the Vienna *Ab-initio* Simulation Package (VASP),[22,23] The exchange and correlation energies were ob-

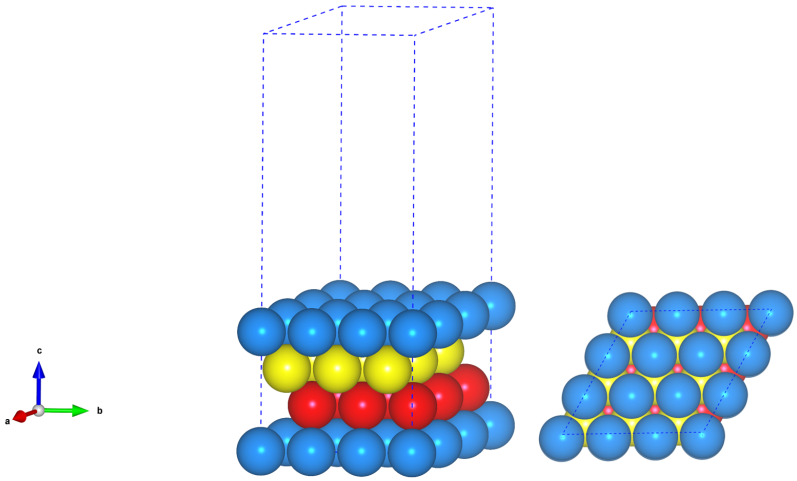

Figure 2.5: Side and top view of $p(3\times3)$ supercell of Ni(111) surface

tained using the PBE functional,[40] The inner electrons were represented by Projector Augmented Wave (PAW) pseudopotentials with cutoff energies of 450 eV.[53,54] All metallic surfaces were modeled by a four-layers slab, where the two upmost layers were fully relaxed and the remaining atoms at the bottom were fixed to the bulk distances. For surface calculations, the Brillouin zone was sampled by a Γ-centered k-points mesh generated through the Monkhorst-Pack method,[55] and the samplings were denser that 0.3 $Å^{-1}$. Since adsorption was performed on one side of the slab, vacuum regions no less than 15 Å were set between slabs to avoid their interaction, dipole correction along z direction[56] was applied to eliminate the spurious contributions arising from the asymmetry of the system. We also included the van der Waals (vdW) corrections for all the calculations in this thesis by applying the Grimme's DFT-D2 method,[47,57] with the C_6 parameters developed in our group.[48] The calculated lattice parameters (Table 2.3) for Ru, Cu, Pd, Pt, Ni agree well with previous experiment results.[58]

All molecules in gas phase in this thesis were relaxed in a box of $20 \times 20 \times 20$ $Å^3$. For small molecules such as methanol, ethanol, ethane, ethylene glycol (EG), and glycerol decompositions on metal surfaces, the cells were built in a $p(3\times3)$ configuration for Ru and Cu. To inspect lateral interactions in reaction

Table 2.3: Calculated lattice parameter (in Å) of catalysts in this thesis and previous experiment values taken from the CRC Handbook of Chemistry and Physics.[58]

Metal	DFT		Exp.	
	$a = b$	c	$a = b$	c
Cu	3.629	3.629	3.615	3.615
Ru	2.712	4.291	2.706	4.282
Pd	3.939	3.939	3.893	3.893
Pt	3.968	3.968	3.924	3.924
Ni	3.517	3.517	3.524	3.524

and activation energies in methanol decomposition studies, we included one or two additional methanol molecules in the $2\sqrt{3} \times 2\sqrt{3} - R30°$ supercell. For large molecules such as glucose, mannose, levulinic, and γ-valerolactone, as well as other related intermediates, the catalyst was modeled by $p(4\times4)$ supercell. Gamma point sampling was used for getting the adsorption geometries and transition states, then their energies were calculated with a denser mesh 0.3 $Å^{-1}$ and the metals were fixed during these processes. An extensive search of potential adsorption conformations was performed following the adsorption rules previously developed in our group.[59] For study in lignin decomposition, because of the size of the molecule, a $p(7\times4)$ supercell with only three layers was used.

Transition state theory

For the potential surface of an elementary chemical reaction, the transition state is a particular configuration which has the highest energy along the reaction coordinate (Figure 2.6). Transition State Theory (TST), which was developed by Eyring and Evans and Polanyi in 1935,[16,17] describes the reaction rate of an elementary chemical reaction. The rate constant can be written as

$$k = \left(\frac{k_B T}{h}\right) \frac{q_0^{\#}}{q} e^{-\frac{E_a}{RT}} \tag{2.30}$$

where k_B and h are Boltzmann and Planck constants, $q_0^{\#}$ and q are partition function respects to their own electronic ground state and E_a is the reaction barrier considered the Zero Point Energy (ZPE) corrections.

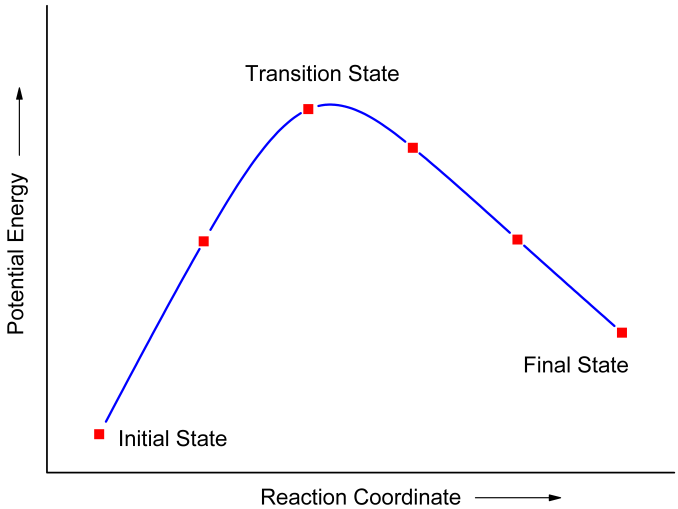

Figure 2.6: System energy varies along with reaction coordination in potential surface.

In a chemical kinetic study of complex system involves plenty of elementary reactions, an efficient approach to determine the reaction mechanism is to compare the reaction barriers of different steps. The overall rate is generally determined by the slowest step, in other words, the one has highest barrier, which is known as the rate determining (limiting) step.

Transition states identification

We employed the Nudged Elastic Band (NEB),[60] Climbing Image-NEB (CI-NEB),[61] and the Improved Dimer Method (IDM),[62] to locate the transition states in the potential surfaces. NEB method is a force based traditional way to find the transition states by extrapolating the initial (IS) and final states (FS) into a few images for searching the minimum energy path (MEP) in potential energy surface. And IDM is a technique for optimizing transition states based on partitioned rational function optimization methods.[62,63] When use this method, the initial dimer direction is provided by calculating the frequencies of transition states from the roughly NEB or CI-NEB results. The optimization thresholds were 10^{-5} eV and 0.015 eV/Å for electronic and ionic relaxations, respectively.

In all cases the saddle point nature of the transition states was assessed by the calculation of the numeric Hessian matrix with a step of 0.02 Å and its diagonalization that rendered a unique imaginary frequency. In the following, all the discussed energies correspond to vdW and ZPE included values unless stated otherwise.

BEP and TSS relationship

Brøsted-Evans-Polanyi relationship (BEP) states that for a set of reactions, there exists a linear correlation between the activation energy (E_a) and reaction energy (ΔE).

$$E_a = \alpha \Delta E + \beta \tag{2.31}$$

where α and β are fitted linear parameters. This relationship was firstly proposed by Brønsted,[18] Bell,[19] and Evans and Polanyi[20] for homogeneous systems.

Even though this relationship provides us a clearly sense to describe the chemical reactions in a quantitative aspect, it was applied to heterogeneous catalysis systems until 2000 (60 years later) by the pioneer studies of Nørskov and coworkers,[64,65] Neurock,[66] and Hu,[67] BEP relationship had became a powerful tool in heterogeneous catalysis studies. Then, Alcalá and Dumesic[68] described another expression of BEP relationship which based on the energies of transition and final states which is the so called transition state scaling (TSS).

$$E_{TS} = \alpha E_{FS} + \beta \tag{2.32}$$

where E_{TS} and E_{FS} are energies of transition and final states taken the initial gas phase energies as reference. As the fitted numbers of α and β have strongly data dependence, plenty of work on the database to improve the precise of α and β values were done by Want et al.[69–72] BEP relationship was reviewed in 2009 by Neurock et al.[73] Further step investigation for its application in predicting and accuracy studies can be referred to the work of Sautet,[74,75] Vlachos,[76–78] Nørskov,[79] Greeley,[80–82] and studies from our group.[59,83]

Energies in this thesis

In this thesis, we studied the methanol, methane, ethylene glycol, ethanol decomposition on four metals (Ru, Cu, Pd, and Pt) to generate the training

database for BEP and TSS relationship and then glycerol decomposition was investigated from the fitted results based on C–C, C–O, C–OH, C–H, and O–H bond breaking types. As the complexity of the systems increases with the C numbers in those alcohols, clear definition of the energies is necessary to be claimed ahead.

Adsorption, activation, and reaction energies

The adsorption, reaction, and activation energies (E_{ads}, ΔE, E_a) were calculated as:

$$E_{ads} = E_{slab}^{ads} - E^{ads} - E_{slab} \tag{2.33}$$

$$\Delta E = \sum E_{products} - \sum E_{reactants} - nE_{slab} \tag{2.34}$$

$$E_a = E_{TS} - E_{IS} \tag{2.35}$$

Where E_{slab}^{ads}, E^{ads} and E_{slab} are the energies of calculated adsorbate-slab, adsorbate in gas phase, and pure slab; $\sum E_{products}$, $\sum E_{reactants}$ are sums of adsorption energies of different species separately on the slab and n is the number difference of species between products and reactants; E_{TS} and E_{IS} are energies of transition states and initial states.

Reference energies in small molecule decomposition systems

In methanol, ethylene glycol (EG), and glycerol decomposition systems, referenced energies are necessary to simplify energy profiles and transition state scalings (TSS). For a given reaction,

$$\mathrm{C_xH_yO_z^* + * \rightarrow C_xH_{y-1}O_z^* + H^*} \tag{2.36}$$

Where, $\mathrm{C_xH_yO_z^*}$ and slab (*) are initial states (IS), $\mathrm{C_xH_{y-1}O_z^*}$ and $\mathrm{H^*}$ are final states (FS), their energies are calculated as :

$$\begin{aligned} E_{IS} &= E_{\mathrm{C_xH_yO_z}} \\ E_{FS} &= E_{\mathrm{C_xH_{y-1}O_z}} + E_H - E_{slab} \end{aligned} \tag{2.37}$$

Reference energy are calculated based on IS, in this case, $\mathrm{C_xH_nO_y}$, with the equation of

$$E_{ref} = (2x + 3 - y) * E_{slab} + E^{gas}_{C_xH_{2x+2}O_z} \tag{2.38}$$

where $E_{C_xH_yO_z}$, E_H, E_{slab} and $E^{gas}_{C_xH_{2x+2}O_z}$ are ZPE corrected energies from direct VASP calculations. $E^{gas}_{C_xH_{2x+2}O_z}$ is taken from a pool containing several fully hydrogenated gas phase molecules (CH_4, CH_3OH, C_2H_6, C_2H_6O, $C_2H_6O_2$, C_3H_8, C_3H_8O, $C_3H_8O_2$, and $C_3H_8O_3$), which share the same x and z numbers with IS structure.

Therefore, referenced energies in one reaction are calculated by following equations:

$$\begin{aligned} E^r_{IS} &= E_{IS} - E_{ref} \\ E^r_{TS} &= E_{TS} - E_{ref} \\ E^r_{FS} &= E_{FS} - E_{ref} \end{aligned} \tag{2.39}$$

where E_{TS} is ZPE corrected transition state energy from VASP calculation.

For glucose and mannose hydrogenations to their linear polyalcohol products, sorbitol and mannitol, and levulinic catalytic conversion to γ-valerolactone, the energies of gas phase molecules (glucose and levulinic acid) and pure slab were taken as the reference energies in reaction coordinates.

Microkinetic model

For simplicity, our microkinetic model describes the behavior of a differential reactor, as shown in Figure 2.7. This is a particular case of a packed-bed reactor where the catalyst has differential thickness.

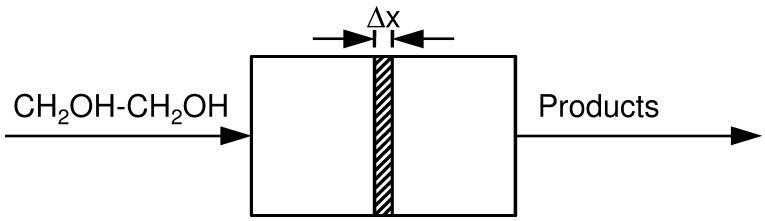

Figure 2.7: Differential reactor used in the microkinetic model

The total adsorption/desorption rate for a specie "C "was modeled using the Knudsen equation:

$$r_{ads_A} = \frac{P_A S_0(T)}{N_0\sqrt{2\pi m_A k_B T}}\theta_* - \frac{k_B T}{h}\exp\left(\frac{E_{ads_A}}{k_B T}\right)\theta_A \tag{2.40}$$

Where:

r_{ads_A}	Rate of adsorption (+) or desorption (–) of "A"
P_A	Pressure of "A" in gas phase
$S_0(T)$	Sticking coefficient
N_0	Density of sites per area
m_A	Molecular mass of "A"
E_{ads_A}	Adsorption energy of "A", from Eq. 2.33

The rate for the i-th reaction in the network is given by:

$$r_i = \frac{k_B T}{h}\, e^{-\frac{E_a}{k_B T}}\theta_{AB^*}\theta_* - \frac{k_B T}{h}\, e^{-\frac{E'_a}{k_B T}}\theta_{A^*}\theta_{B^*} \tag{2.41}$$

Where:

r_i	Rate of i-th reaction
E_a, E'_a	Activation energy for direct and inverse i-th semireactions
θ_j	Surface concentration of species "j"
k_B	Boltzmann constant
T	Temperature

The variation of the surface concentration of species "j" was modeled by a System of "n" Ordinary Differential Equations (SODE), being "n" the total

number of species. These ODE consist in the algebraic sum of the adsorption and reaction rates in which a given surface species "j" participates, as shown in Eq. 2.42.

$$\frac{d\theta_j}{dt} = \sum_{i=1}^{n} r_{ads_j} + s_{ij} r_i \tag{2.42}$$

Where:

s_{ij} Stoichiometric coefficient of species "j" on reaction "i".
t Time

For each time "t", the number of empty sites was calculated with the site balance equation:

$$\theta_* = 1 - \sum_{j=1}^{n} \theta_j \tag{2.43}$$

Table 2.4: Reaction conditions for the microkinetic model for all the processes considered: temperature (T, in K), partial pressures of alcohol, water, and oxygen in the inlet (P_a, P_w, P_o, in atm), and total reaction time (t_x, in s).

Process	Alcohol	T	P_a	P_w	P_o	t_x
Direct decomposition	All	600	1.00	0.00	0.00	10800
Autothermal reforming	Ethanol	950	0.30	0.70	0.10	10800
	Ethylene glycol	950	0.30	0.50	0.05	10800
	Glycerol	950	0.25	0.68	0.07	10800
Steam reforming	Ethanol	800	0.20	0.80	0.00	10800
	Ethylene glycol	800	0.25	0.75	0.00	10800
	Glycerol	800	0.10	0.90	0.00	10800
Aqueous phase reforming	Ethanol	550	20.0	80.0	0.00	10800
	Ethylene glycol	550	25.0	75.0	0.00	10800
	Glycerol	550	10.0	90.0	0.00	10800

The general procedure can be summarized as follows:

1. Define temperature and pressure of reactants, Table 2.4.

2. Calculate the adsorption and reaction constants from equations 2.40 and 2.41.
3. Set the initial concentrations that correspond to a clean surface: $\theta_*(t = 0) = 1$.
4. Calculate adsorption rates for a given time t.
5. Calculate reaction rates.
6. For each species "j", update the surface concentration after a given timestep, Eq. 2.42.
7. Calculate the fraction of empty sites, Eq. 2.43.
8. Back to step 4 and proceed until reaching the desired time, listed in Table 2.4.

Chapter 3

Results

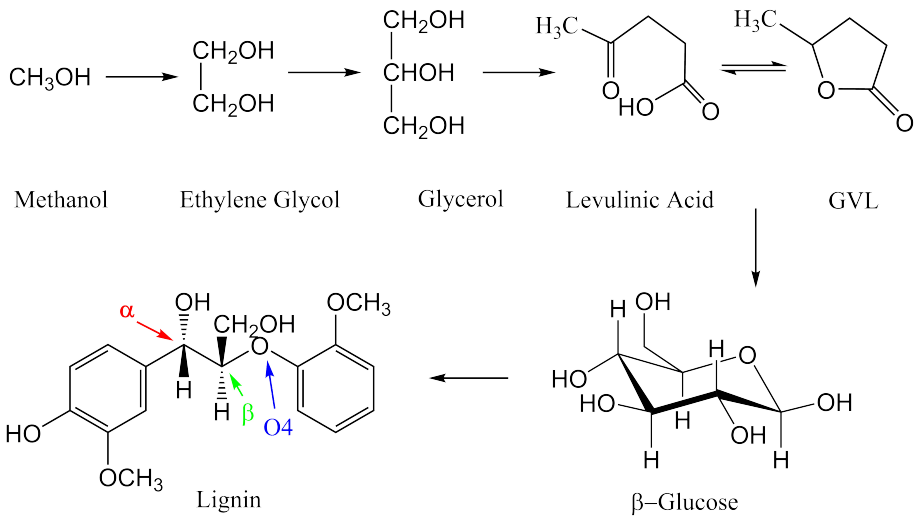

Figure 3.1: Investigated objectives in this thesis

In this chapter, a brief description of the work developed in this thesis has been illustrated, including the background, previous studies, computational process and the main conclusions. Computations (see Figure 3.1) start from methanol

decompositions on Cu(111) and Ru(0001) surfaces, followed by the extension to larger mono-alcohol (ethanol) and di-alcohols (ethylene glycol). All these computational data composed a rich database which paves the way for larger alcohol studies such as glycerol via the linear scaling relationship (LSR) method. *Ab initio* microkinetic dynamics has been employed to study the hydrogen production from direct decomposition (DD), aqueous phase reforming (APR), auto thermal reforming (ATR) and steam reforming (SR) of these alcohols. For biomass conversions, mechanism of levulinic acid conversion to γ-valerolactone on Ru(0001) and HHDMA-Ru(0001) surface have been investigated, our findings show that the interfacial acidity accelerates the reaction rates by changing the adsorption status of initial species, furthermore, in combined with the acidity, structure coverage effects of HHDMA also improve the catalyst's stability. DFT study on glucose and mannose hydrogenation reactions over Ru(0001) have been performed. Calculated reaction mechanisms from linear and cyclic sugar isomers, together with their different adsorption energies and isomers' solution concentrations determine the hydrogenation rates. By employing the Langmuir competitive adsorption model and transition state theory, our results qualitatively repeated the experiment observed rate ratio of mannose/glucose hydrogenation. In the end, mechanisms of lignin depolymerization on both Ni(111) and Ru-decorated Ni(111) surface have been proposed and compared with available experimental studies. Moreover, the stereocenter and Ru effects in the mechanisms were firstly explained.

Paper I: Methanol decomposition on metal surfaces

Background

Methanol is the smallest mono-alcohol which contains three basic bond types: C–H, C–OH and O–H. Unlike methane, methanol is a polar molecule and can be activated easily at low temperatures. Besides, lacking of C–C bond makes its transformation into hydrogen and CO becoming possible under mild conditions.[84] Because of its high H/C ratio, liquid status under ambient temperatures and environmental friendliness, methanol can be used as an ideal H_2 resources in the direct methanol fuel cells (DMFC) and proton exchange membrane fuel cells (PEM). It can also be used as chemical H_2 carrier (hydrogen storage ma-

terial) for long range transportation and then H_2 will be produced in large industry scale via methanol reforming, water gas shift (WGS) reactions and other techniques.[84]

In DMFC, platinum is one the common and most active catalysts in practical applications. However, the main drawback comes from the poison brought by one of its products, CO, which binds on the catalyst strongly and covers the active sites. In the working conditions, the CO concentration have to be limited below 50 ppm.[85] Alloy metallic catalyst by combining Pt and Ru has the lowest sensitivity towards CO among other bimetallic catalysts, such as PtPd, PtIr, PtRh, PtW, et al.[86–89]

Methanol can also be used as fuel in internal combustion engine and as important synthetic compound in chemistry industry. The main product in methanol consumption is CO_2, one of the main green house gases. On the other hand, CO_2 can be utilized as the carbon resources for methanol synthesis by using the commercial catalyst $Cu-ZnO-Al_2O_3$.[90,91] Therefore, the methanol is recovered and CO_2 emission has been controlled in this cycle.[92]

Furthermore, methanol has also been used as an excellent simple model molecule to study the bond selective activations on surface both in experimental and theoretical sides. Hence, understanding the reaction mechanisms and the complete reaction network from an atomic point of view would strengthen our ability to develop catalyst with higher activity and selectivity. Until so far, even there

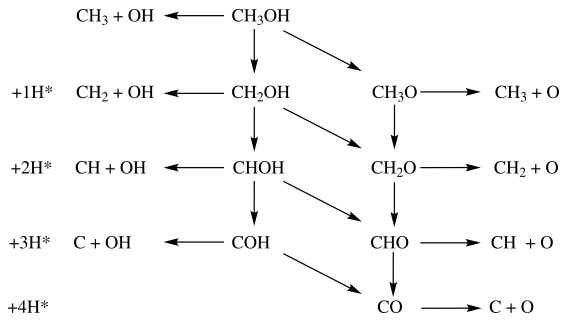

Figure 3.2: Reaction pathways for methanol decomposition on surface

exist a large amount of density functional theory study on methanol decompositions and synthesis, majority of them focus on part of the reaction pathways on specific surfaces and the complete reaction networks have not been fully stud-

ied. For the point view of accuracy, as vdW interactions between atoms on the surface would affects the adsorption energies, higher computational theoretical level such as DFT-D2 method is necessary in the calculations. Moreover, in methanol decomposition network, 10 of 18 reactions in the full methanol decomposition pathways (see Figure 3.2) are H releasing reactions: O–H and C–H scissions. Because of the small hydrogen mass, zero point energy (ZPE) corrections are compulsory.[27] Further data analysis step based on BEP relationships which connect the catalytic behavior and the calculated elementary steps are rare. As this relationship has been proven to be a robust way for scaling the reactions on surfaces and thus is useful for catalysts design and predictions.[64]

Reactions on Cu(111) and Ru(0001)

In this collaboration work, four close packed surfaces of Cu, Ru, Pd, and Pt have been uses as the catalysts models. My calculations correspond to methanol decomposition over Cu(111) and Ru(0001) surfaces for the reason that copper is the well-known and customized catalyst and Ru is the main part in DMFC alloy catalyst to promote the CO resistance. Firstly, complete decomposition network in Figure 3.2 was outlined. Gas phase molecules, and the intermediates and related transition states in the network have been optimized and identified. Energy profiles for methanol decomposition and synthesis (inversed

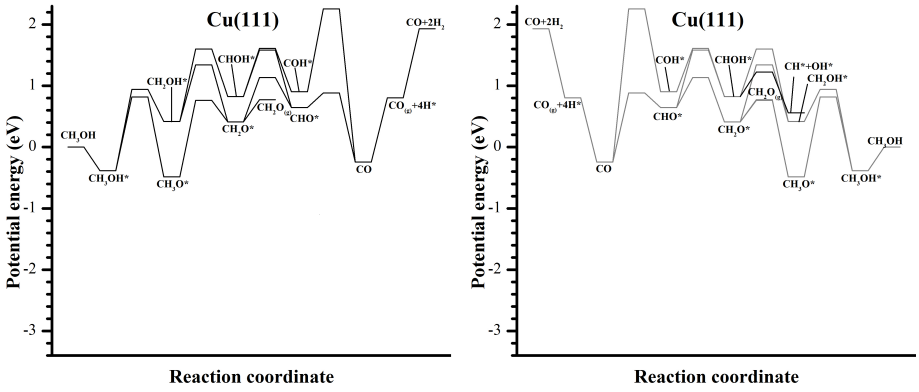

Figure 3.3: Reaction profiles of methanol decomposition and synthesis on Cu(111)

reactions) based on reaction barriers and energies have been generated and analyzed. Similar to previous calculations,[93] mechanism of methanol decomposition on Cu(111) surface goes as:

$$CH_3OH^* \rightarrow CH_3O^* + H^* \rightarrow CH_2O^* + 2H^* \rightarrow$$
$$CHO^* + 3H^* \rightarrow CO^* + 4H^*$$

and the reversed steps are methanol synthesis procedure(see Figure 3.3). However, in decomposition pathway, it is unlikely for further decomposition from formaldehyde CH_2O^* as it desorbs easily. Similarly, in methanol synthesis, formaldehyde would also desorb once it was formed. Hence, high hydrogen pressure are needed for forcing the CH_2O^* hydrogenation to CH_3O^* instead of desorption. Other techniques to enhance formaldehyde adsorption[91,94] are also necessary to benefit methanol synthesis. From CH_2O^*, $CH_3O^* + H^* \rightarrow CH_3OH^*$ is the rate determining step in methanol synthesis. On Ru(0001), two

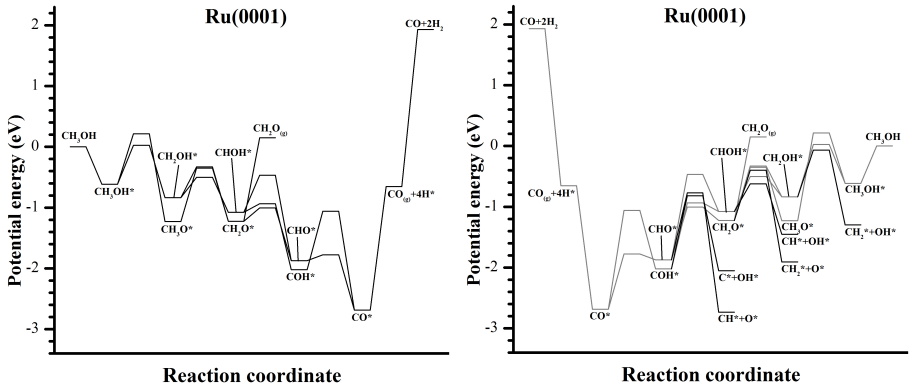

Figure 3.4: Reaction profiles of methanol decomposition and synthesis on Ru(0001)

pathways are observed (see Figure 3.4), one is the same as it on Cu(111), the other one is following:

$$CH_3OH^* \rightarrow CH_2OH^* + H^* \rightarrow CHOH^* + 2H^* \rightarrow$$
$$COH^* + 3H^* \rightarrow CO^* + 4H^*$$

where C–H bond breaks in the first three steps and O–H rupture is in the end of the reaction network. For inverse reactions above, as C–O bond break

competes with other hydrogenation steps, it is unlikely to produce methanol on Ru(0001). The discrepancy between DFT (C–H scission at beginning needs less barrier than that from O–H bond) and experiment results[95](O–H bond breaks at beginning) have been illuminated by considering the coverage effects where two adjacent methanol molecules would form a hydrogen bond to weaken the O–H bond and stabilize the transition states and the C–H bond breaking are impeded by the structure strain brought by the inter-molecule hydrogen bond. Thus, O–H bond scission is more favorable than C–H bond at higher coverages.

BEP and TSS relationships

Transition states scaling applied to O–H, C–H, and C–O bond ruptures have been studied, IS-like results are observed for O–H bond and the the rest hold the FS-like scaling results. It has to be emphasized here is that C–O bond has the worst scaling behavior, showing that further or more detailed classification are probably needed to improve the scaling accuracy.

Paper II: EG and glycerol decompositions on metal surfaces

Background

Glycerol is the main byproduct in bio diesel production, a process which converts lipids (e.g., vegetable oil, soybean oil, and animal fat) via the trans-esterification, is one of useful way to decrease the crud oil dependence. Along with the increasing production of bio diesel, glycerol accumulates and this brings out its over-plus in spite that it has been widely used in food industry, cosmetic, pharmaceutic and personal care applications.[96] Thus, glycerol surplus also affects and limits the development and expanding of bio diesel in return if it is not well disposed.[97] On the other hand, well utilization of those overplus glycerol will promotes and lower the bio diesel production cost.[96] Therefore, economical utilization pathways for glycerol is a must for solving the bottleneck of bio diesel production enhancement in the future.

Among several glycerol applications, hydrogen production would be one possible way for glycerol efficient utilization.[76,98,99] As the large molecules, direct DFT

study for glycerol decomposition network is impossible because there are totally 1945 elementary reactions in the reaction network connected with C_3, C_2 and C_1 species. Plenty of calculations are mainly discussed part of the reaction network and the complete reaction network investigations are still limited.[76,80–82] One compromised way is to use small surrogates to investigate, such as methanol, ethanol, and ethylene glycol. Based on our study about methanol decompositions on metal surfaces described above, a few drawbacks emerges when applying methanol and ethanol as the surrogate to investigate larger molecules related reactions. For example, it is impossible to consider C–C bond in methanol as it forms the basic framework in larger organic molecules, and there is no intramolecular hydrogen bond in ethanol which is known would affect the initial reactions in methanol[83] and ethanol decompositions.[100] Given the similarity of ethylene glycol to glycerol, we select it as the ideal surrogate to investigate its decompositions on catalyst surfaces and then extrapolate these results into the glycerol decomposition system.

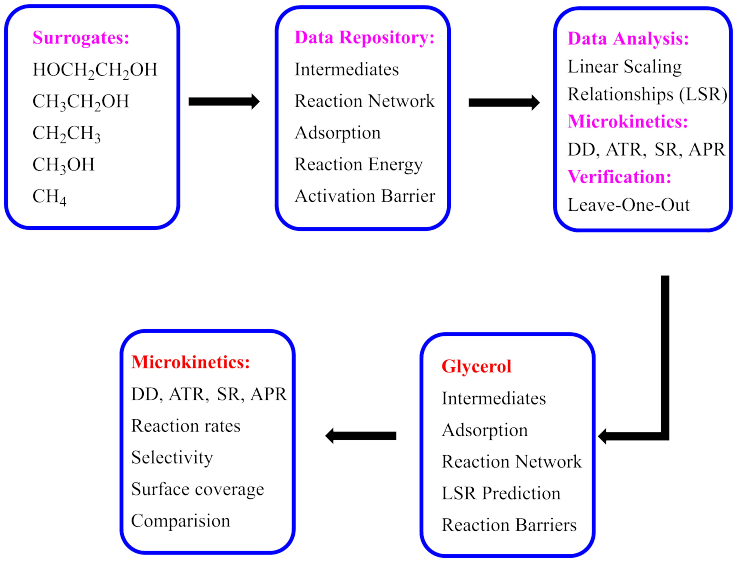

Figure 3.5: Schematic investigation process of this computation study on ethanol, EG and glycerol decompositions on four metals and the following *ab initio* microkinetic study via LSR method.

Database generation

In this study, as illustrated in Figure 3.5, 247 reactions related with ethylene glycol, ethanol, ethane, methanol and methane decompositions have been calculated on four metal surfaces, Cu, Ru, Pd, and Pt. Again, my contributions in this study focus on reactions over Cu and Ru surfaces. The strategy to generate all possible elementary reactions are illustrated in Figure 3.6 where ethylene glycol is taken as the example. Complete DFT calculations were performed on

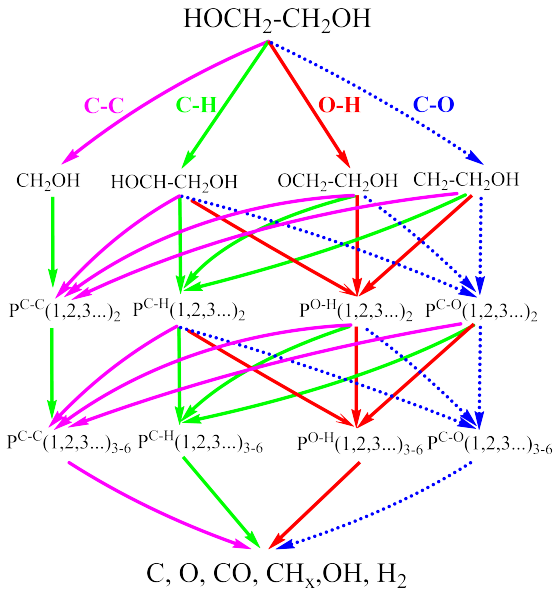

Figure 3.6: Example of elementary steps generation strategy.

these intermediates' optimizations and relevant transition states searching. Empirical binding principle based on oxygen affinity or oxophilicity of these metals have been provided. On Cu(111) and Ru(0001), oxygen terminated structures such as OCH_x-CH_xO are more energetically preferred than $HOCH_{x-1}-CH_xO$ or $HOCH_{x-1}-CH_{x-1}OH$ and this would be reverted on less oxophilic metal surfaces such as Pt(111) and Pd(111). In the decomposition process, C–C bond scission occurs in the late stage when the intermediates has the form of $C_2H_xO_y$ (x=2-4, y=1-2). Especially for $OC-CH_xO_y$ (x=1-2, y= 0-1), C–C bond breaks with

much lower barriers. BEP and TSS relationships were then analyzed to obtain the scaling equations for C–H, C–O, C–OH, C–C, and O–H bonds scissions on individual and all metal surfaces surface. Special structures which deteriorates the TSS relationship have been checked and analyzed in detail. Glycerol decomposition was considered on Ru(0001) surface only as the increasing complexity brought by the third C atom. 270 C_3 intermediates' structures are optimized firstly and followed by applying the TSS relationships (see Figure 3.7) fitted from previous database of ethane, ethanol, and ethylene glycol to predict the reaction barriers.

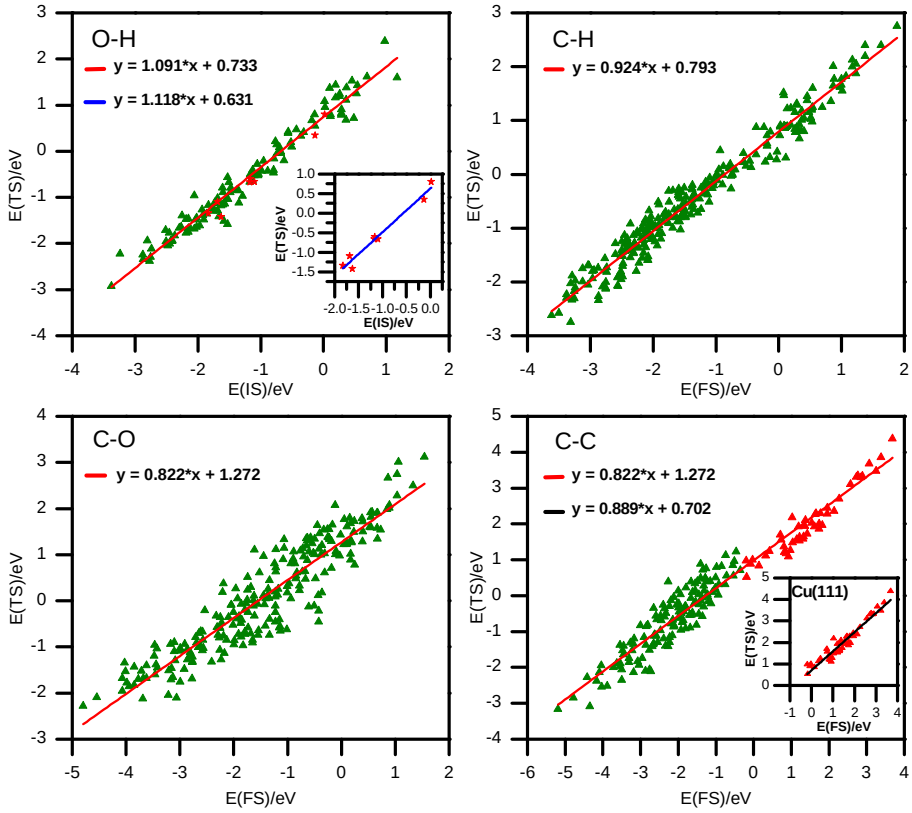

Figure 3.7: Fitted TSS relationship for C–H, O–H, C–O, C–C bond breakings on Cu, Ru, Pd, and Pt metal surfaces.

Ab-initio microkinetics

Finally, *ab-initio* microkinetics study based on previous DFT data have been performed (see Figure 3.8) By comparing the microkinetic studies on ethanol, ethylene glycol, and glycerol under different conditions of DD, SR, ATR, and APR.

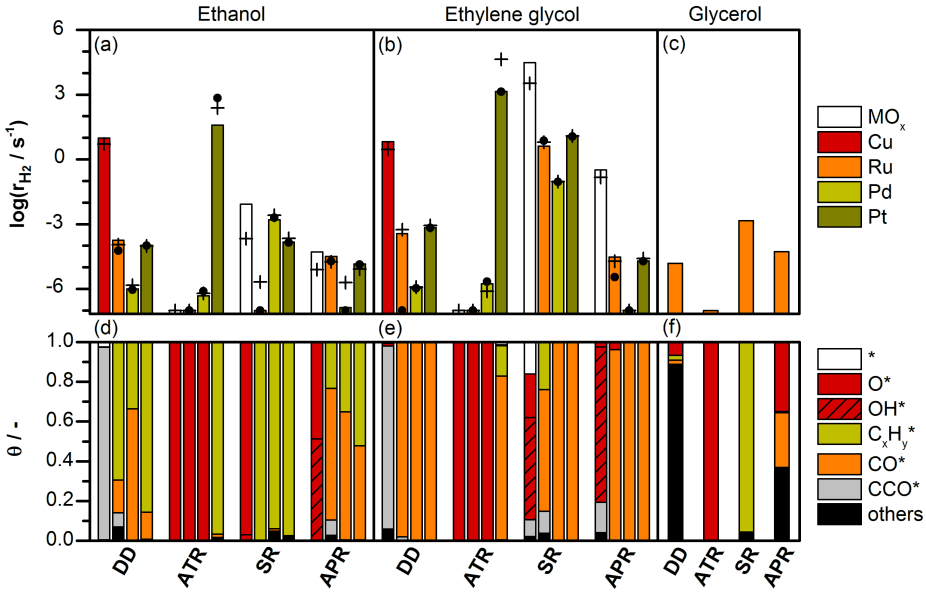

Figure 3.8: Hydrogen production rate during the direct decomposition, and reforming: ATR, SR, and APR of (a) ethanol and (b) ethylene glycol on Cu, Ru, Pd, and Pt. (c) corresponding values for glycerol on Ru. The crosses show the result from MK-DFT, columns from MK-LSR, and dots from the MK-L1O method. White columns stand for configurations where the oxygen content could change the existing catalytic phase. The surface coverages obtained with MK-DFT are shown on panels (d-f).

For ethanol and EG on Cu(111), direct decomposition is the best way to produce H_2, and CCO^* is the most abundant intermediate. For the other reforming techniques, surface oxygen species O^* and OH^* are the most abundant species. On Ru(0001), ethanol direct decomposition has the best hydrogen production

behavior, CCH^*, CO^*, and CCO^* are the main surface species with percentage of 68%, 16%, and 7%. CO and H_2 are the main products with approximate stoichiometric ratio of 2:3. APR has lower H_2 production rate than DD, but much higher than other methods, the most rich species in sequence are CO^*, $C_xH_y^*$ and CCO^*. For ethanol ATR and SR, surface O^* and $C_xH_y^*$ are the main species respectively. When H_2 is produced on Ru(0001), the rates in sequence are SR, DD, APR and ATR. In DD and APR, the surface is almost covered by CO^*. In ATR, surface is covered mostly by O^*. In SR, $C_xH_y^*$, CO^*, and CCO^* are the most abundant surface species. Both EG and Glycerol have the same hydrogen production sequence of SR, DD, APR and ATR. In steam reforming, the activity of EG is 3.5 order of magnitude larger than that of glycerol. The selectivity towards H_2 for EG and glycerol steam reforming on Ru(0001) surface are 84% and 72%, respectively. This observation agrees with previous experimental results on other catalysts. H_2 production in the APR of ethylene glycol is higher than for glycerol on Pt[101] and on Raney catalyst ($Ni_{37}Sn_3$).[102] The longer the alcohol carbon chain (up to C_6), the lower the selectivity towards H_2 and the higher to hydrocarbons and other compounds.[101–103] TSS scaling have been proven to be a robust way for predicting the complex reaction networks on catalyst surfaces.

Paper III: Levulinic acid conversion on Ru(0001)

Background

Levulinic acid (LA, 4-oxopentanoic acid) can be derived from cellulose and hemicellolose in the biorefinery via hydration process of 5-hydroxymethylfuran (HMF).[104–106] Great interests have been paid on this platform molecule as it can be transformed into a series of value added chemicals (see Figure 3.9), fuel additives and hydrocarbon fuels.[107,108] For example, one of the LA derivatives, the intramolecular esterification product, γ-valerolactone (GVL) can be used as solvent,[109–111] fuel additives,[107,108] and chemical intermediates in industries such as perfume, food additives.[112,113] LA is also in the list of top 12 value added chemicals from biomass which was released by the US department of Energy in 2004.[6,7] Ru is an excellent catalyst in aqueous phase carbonyl hydrogenation[114,115] and has been extensively investigated in biomass related reactions, such as glucose and xylose hydrogenation.[4,11,116] For LA hydrogenation

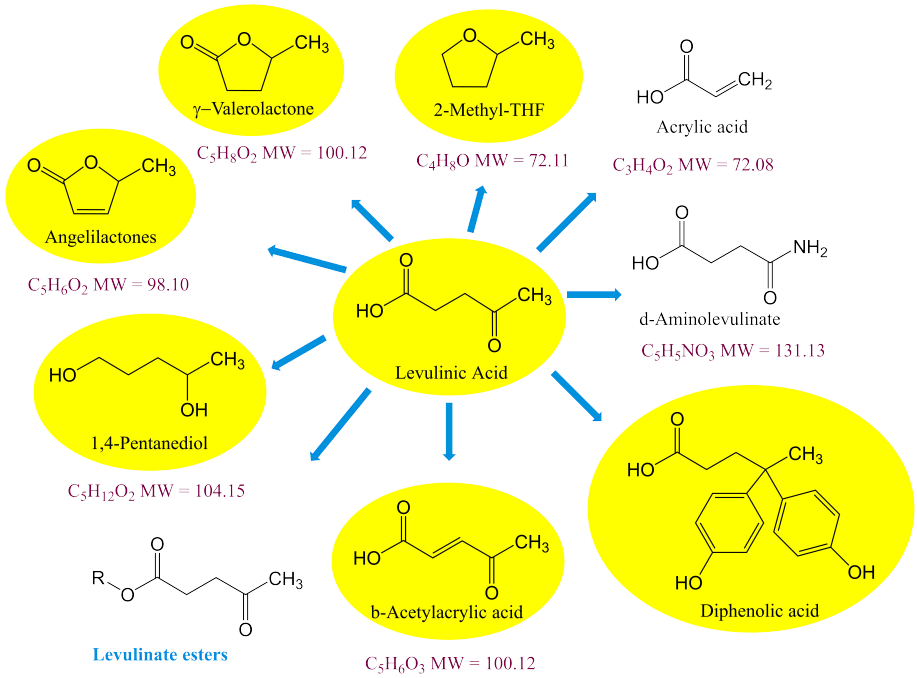

Figure 3.9: Derivatives of levulinic acid. Adapted from Todd et al.[6]

to GVL via solid catalysts, it has been in detailed summarized by Wright[117] and Corma.[107] Among the common used catalysts, such as Ru, Pd, Pt, Ni, Rh, Ir, and Au, Ru holds the superior behaviors (high activity, selectivity) in this conversion.[118–120] Despite of the excellent performance of the conventional Ru/C catalyst, a few drawbacks are still need to be overcome, such as high catalysts loading (5 wt % Ru/C), metal leaching when water is used as solvents, and the deactivation caught by its oxidation into RuO_2.[121,122] To enhance its stability and activity, Ru based bimetallic alloys such as RuRe, RuSn, and RuPd have been investigated.[110,123,124] Also, various of supports such as Metal-Organic Frameworks,, zeolites,[125] TiO_2,[126] and graphene[122] have been considered. Previous studies indicates that the surface acidity would might have positive effects on the decreasing its oxidation tendency and thus making catalysts more robust against deactivation.[127–130]

Developing nanostructured hybrid materials which hold the advantages of homo and heterogeneous catalytic systems has been proven to be an effective strategy for catalysts design.[131–134] Previous studies, Hexadecyl (2-Hydroxyethyl) DiMethyl Ammonium dihydrogen phosphate ligand (HHDMA) have been used to decorate Pd and Pt nanoparticles for alkyne and nitro-group hydrogenation, namely the commercialized Nanoselect^{TM} by BASF.[135–137] The adorption of HHDMA ligand, its effects on tailoring reactants adsorption properties as well as on promoting catalysts behaviors have been investigated by combining experimental and theoretical methods.[138–140]

In the experimental work of this study, HHDMA-Ru catalyst which is used for LA conversion to γ-valerolactone has been synthesized. This catalyst has been well characterized and tested, results (see Figure 3.10) show that HHDMA-Ru has an outstanding four fold higher reaction rate than that of commercial Ru/C catalyst, with the high selectivity remained. Furthermore, it also demonstrated a long time stability in water (no deactivation after 15 h on steam). Density functional theory has been employed to put forward the possible reaction mechanism, interfacial acidity and the stability of this system.

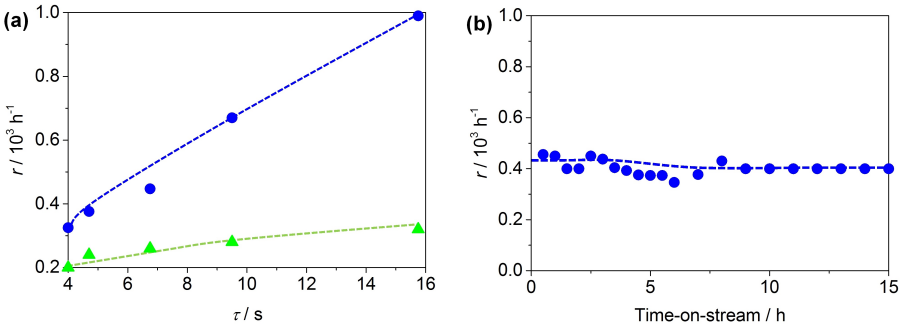

Figure 3.10: (a). Reaction rate (in 103 h^{-1}) as a function of the contact time (τ) in the hydrogenation of LA over HHDMA-Ru/$TiSi_2O_6$ (blue) and Ru/C (green). (b) Stability of HHDMA-Ru/$TiSi_2O_6$ in the hydrogenation of LA. Adapted from Ref.[141]

Reaction mechanism

Levulinic acid conversion on Ru/C catalyst was calculated by using a *p*-4x4 Ru(0001) slab with four layers as the model. As the weak acidity of LA, both levulate anion and LA intact molecule would be exist in the system. For reaction

$$\mathrm{LA} \rightarrow \mathit{Levulate} + \mathrm{H}^{+}$$

on the surface, it is exothermic by 0.69 eV and shows that surface levulate are more stable than its acid form. Hence, the nanoparticle surface would be covered by the anions instead of its carboxylic form. However, the conversion starts from intact LA on the surface are more preferable than that starts from anion. As shown in Figure 3.11. Beside, this intra-molecular esterification mechanism is different from that from the traditional organic chemistry textbook[142] that carboxylic group would be protonated into $\mathrm{R{-}C(OH)_2^+}$ and then followed by the attack (ring formation) and $\mathrm{H_2O}$ elimination. In the mechanism starting from LA, only two steps are related: C–OH breaking from RCOOH and intramolecular ring formation.

Acidity and stability

Because of the intrinsic acidity HHDMA arising from dihydrogen phosphate anion, it can be act as a pH buffer. We assumed that it is the stronger local acidity which protonates the surface levulate into LA and then conversions starts from LA instead of levulate. From experimental point, the local acidity measurement is impossible because probe can not reach to the interface between HHDMA and Ru nanoparticle surface. So, we performed calculations on *p*-(4x4) Ru(0001) surface covered by 4 HHDMA ligands. In order to predict the interface pK_a, a series of acid (formic acid, acetic acid, chloro, dichloro, and trichloro acetic acid) adsorption on HHDMA covered Ru(0001) surface has been calculated. The idea is following: adsorption of those corresponded carboxylates would provide energy for interfacial $\mathrm{H_3O^+}$ to protonates them into their carboxylic acids. In other words, the driving force of protonation step is the adsorption energy of those carboxylates. By using these acid surrogates, the relationship or equation between surface pK_a and energies would be derived.

$$\mathrm{RCOO^-} + * \rightarrow \mathrm{RCOO^*} \tag{3.1}$$

$$\mathrm{H_3O} * + \mathrm{RCOO^*} \rightarrow \mathrm{RCOOH} + \mathrm{H_2O} \tag{3.2}$$

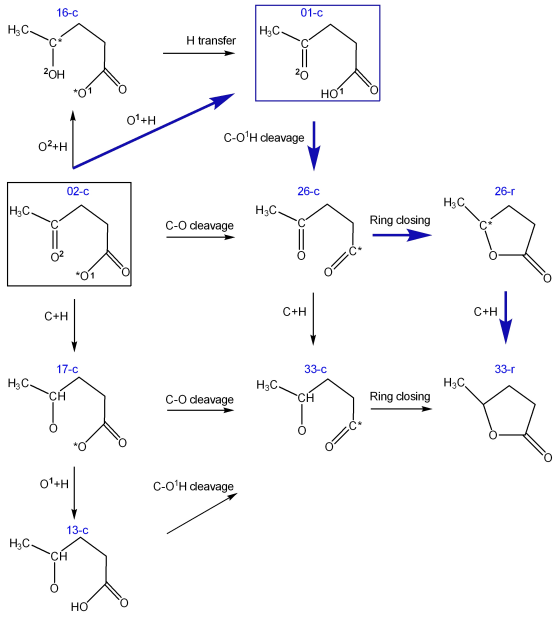

Figure 3.11: DFT calculated reaction mechanism of LA conversion to γ-valerolactone on Ru/C. Adapted from Ref.[141]

with * denotes the surface species. When the adsorption energy equals to the protonation energy, the conversion between carboxylic acid and its carboxylates reaches to the balance. From the scaling equation, pK_a value of the interface is calculated as 1.09, which is strong enough to protonate the leculate to its acid form and thereafter promotes the reactions by changing the mechanisms.

The stability of HHDMA-Ru/$TiSi_2O_6$ has been tested and shown in Figure 3.10. The better behavior of HHDMA-Ru against oxidation to RuO_x attributes to the surface covered HHDMA ligands and the local acidity environment. Oxidation process on the Ru/C and HHDMA-Ru/$TiSi_2O_6$ have been calculated by introducing O atoms into the system, both on the surface and in the sublayer. The average and differential adsorption energies are calculated by the following equations:

$$\begin{aligned} E_{average} &= [E_{(slab+nO)} - E_{(slab)} - n \times E_{(O_2)/2}]/n \\ E_{differential} &= E_{(slab+nO)} - E_{(slab+(n-1)O)} - E_{(O_2)}/2 \end{aligned} \tag{3.3}$$

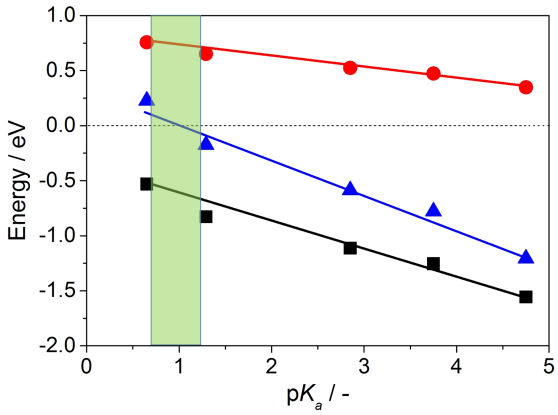

Figure 3.12: Relationship between pK_a and adsorption energy of the corresponding carbohydrate (E_{ads}, black), protonation energies (ΔE, red), as well as the sum of them (E_{ads} + ΔE, blue). Linear fitting: E_{ads} = (-0.23 $\pm$ 0.02) pK_a + (0.44 $\pm$ 0.06), ΔE = (-0.09 $\pm$ 0.01)pK_a + (0.80 $\pm$ 0.02), and E_{ads} + ΔE = (-0.32 $\pm$ 0.03)pK_a + (0.35 $\pm$ 0.08) with r^2 values of 0.97, 0.98, and 0.97, respectively. Estimated pK_a of the interface is 1.09. Adapted form Ref.[141]

with $E_{slab+nO}$, E_{slab}, and $E_{(O_2)}$ are the energy of slab with nO on it, pure slab and gas phase O_2. Calculated oxygen adsorption energies are shown in Figure 3.12. The results show that when surface is decorated with HHDMA, O adsorption becomes less preferable than that on pure Ru(0001) surface. Besides, reaction energy and barrier of O + H $\rightarrow$ OH have been also calculated. On HHDMA-Ru, the reaction becomes less endothermic (0.20 vs 0.57 eV) and has lower barrier (1.22 vs 1.38 eV). This indicates that surface O species are more prone to form OH as H are abundant in the interface and thus the Ru oxidatation trend is reduced.

To sum up, an in-depth molecular analysis by Density Functional Theory demonstrates that the intrinsic acidic properties at the ligand-metal interface under reaction conditions ensure that the less energy demanding path is followed. The reaction does not obey the expected cascade mechanism and intercalates hydrogenation steps, hydroxyl/water eliminations, and ring closings to ensure high selectivity. Moreover, the interfacial acidity increases the robustness of the material against ruthenium oxide formation. These results provide valuable improvements for the sustainable production of GLV and insights for the

rationalization of the exceptional selectivity of Ru-based catalysts.

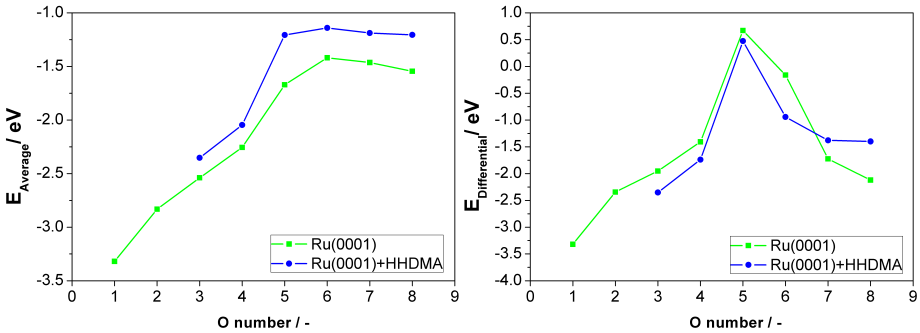

Figure 3.13: Average and differential adsorption energies (in eV) of O on Ru(0001) and Ru(0001)-HHDMA. Adapted from Ref.[141]

Paper IV: Glucose and mannose hydrogenations on Ru(0001)

Background

Sugar alcohols containing five and six C atoms such as mannitol, sorbitol, arabitol, xylitol, are generally the hydrogenation products of sugars such as mannose, glucose, arabinose, and xylose. They are widely used in food chemistry as thickeners and sweeteners, and in organic industry as synthesis materials. From industry, sugar alcohols are typically derived from the corresponding sugars. In fact, some of the sugars (e.g., mannose and ribose) are rare and therein the production are limited. One alternative approach is to hydrogenate a suitable ketose. However, this method suffered the costly separation of the equimolar mixers with different chiralities. For example, hydrogenation of fructose would generate the same amount of mannitol and sorbitol. The other way to get sugar alcohols is directly hydrogenation of the related rare sugars which comes from epimerization process. Reported catalytic epimerization process in this strategy are performed by using Sn-β as catalyst in methanol medium. In the meanwhile

Raney nickel and Ru/C are excellent candidates for the sugar hydrogenation reactions.

H-HPA Ag-HPA Cs-HPA	⇒	H-HPA/HER H-HPA/SiO_2 H-HPA/C	⇒	H-HPA/C Ag-HPA/C Cs-HPA/C	⇒	Cs-HPA/C

Table 3.1: Schematic process for epimerization catalyst design

In the experimental work of this study (Table 3.1), an epimerization catalyst was firstly designed by adsorption of phosphomolybic heteropolyacid (HPA) and its insoluble salt (Ag−HPA and Cs−HPA) on the supports such as silica, activated carbon, and ion-exchange resin (IER). By replacing the proton in HPA with Ag and Cs cations, there exist no significant changes in turn over frequencies (TOF) and the selectivity, showing that protons do not participate in the catalytic process. Mo leaching study showed that Cs−HPA has the highest stability followed by Ag−HPA and HPA is the worst. Support effects on the catalytic process was studies by immobilizing of HPA on IER, SiO_2 and activated C. Results showed that IER has inferior effect, SiO_2 has similar behavior and C doubles the TOF numbers, compared with reactions using HPA only. This is probably because of the higher surface area of activated C which leads to the better dispersion of the catalyst active sites. Given the similar TOF and selectivity of HPA, Ag−HPA and Cs−HPA immobilized on activated C support and the low Mo leaching property, Cs−HPA/C has been designed as a superior epimerization catalyst, such as conversion of glucose to mannose.

Then hydrogenation process was then performed from precious reported Ru/C after test. In this part, different hydrogenation rates were experimentally observed for the mixtures of the epimers, mannose/glucose, xylose/lyxose, and arabinose/ribose, with the later one in each pair has lower apparent activation energies (shown in Figure 3.14).

Linear sugar isomers on Ru(0001)

To illustrate the reason for the different rates of the epimers, we performed DFT calculations. Catalyst is simulated via a *p*-(4×4) slab model of Ru(0001) surface which contains four layers. Glucose and mannose were selected for their hydrogenation calculations. Firstly, the open (linear) structures of glucose and

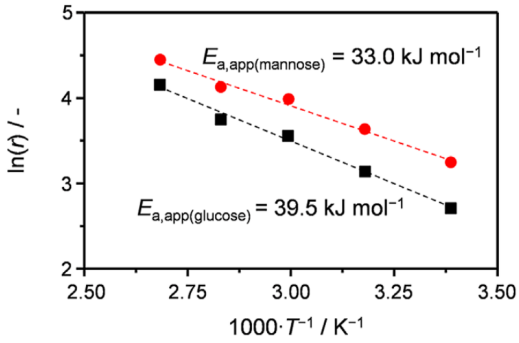

Figure 3.14: Arrhenius plot and the corresponding apparent activation energies for the hydrogenation of glucose and mannose over Ru/C. Adapted from Ref. [143]

mannose were used as model to study the hydrogenations. Our results showed no obvious differences between them in hydrogenation process. (see Figure 3.15) As their very low content (less than 1%) and the nearly same reaction profiles, it is safe to conclude that linear isomers have little effects in the hydrogenation process.

Cyclic sugar isomers on Ru(0001)

Then, four ring structures (α and β isomers) of each epimer have been studied since they are more abundant in the liquid phase with percentage of α-glucose (33%), β-glucose (66%), α-mannose (66%), and β-mannose (33%), respectively. We found that the α isomers have slightly stronger binding energies than β ones as shown in Figure 3.16. Direct and H_2O assistant ring opening reactions and the following C and O hydrogenations have been considered and calculated in the reaction network. We found water associating decreases the barriers in the ring opening steps and β-glucose has lower ring opening barrier than α-mannose. Calculated ring opening and C hydrogenation barriers for α-glucose and β-mannose are much higher than their isomers. Given by the β-glucose and α-mannose having the priority (low barriers) to proceed hydrogenations, the reaction mechanisms from these two molecules are shown in Figure 3.17. H_2O assistant ring-opening step proceeds firstly and then two sides of the broken C–O bond hydrogenated into the corresponding chain structures. The rate determin-

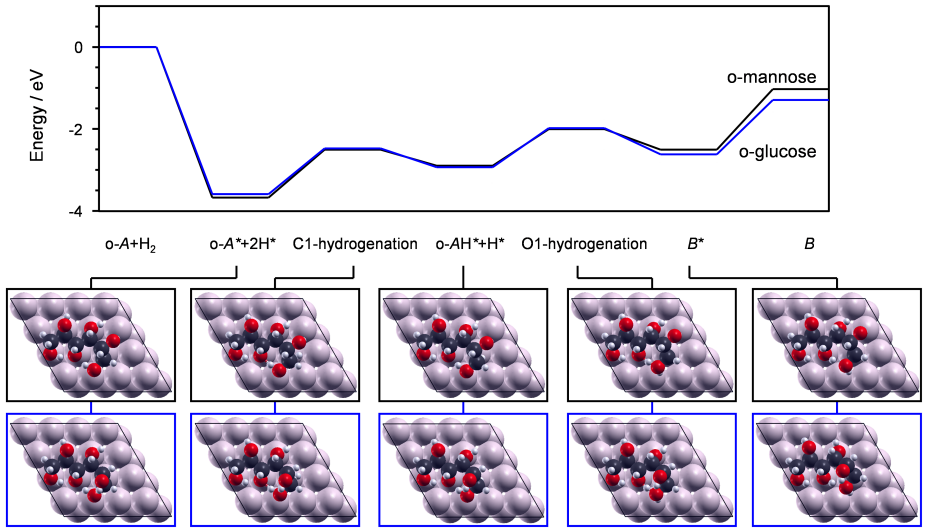

Figure 3.15: Energy profiles for the hydrogenation of the open forms of A = glucose and mannose to B = sorbitol and mannitol, respectively, and the corresponding structures calculated over Ru(0001).

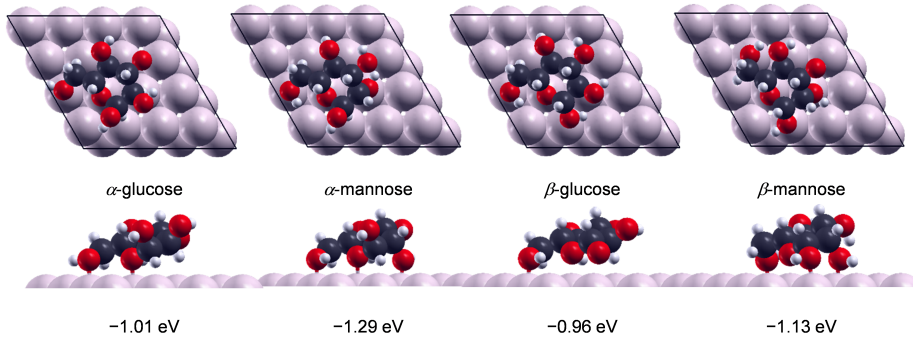

Figure 3.16: Adsorption structures and binding energies (in eV) of the α and β forms of glucose and mannose on Ru(0001).

ing steps for α-mannose and β-glucose are ring-opening and C hydrogenation step, respectively. Kinetic analysis based on Langmuir competitive adsorption

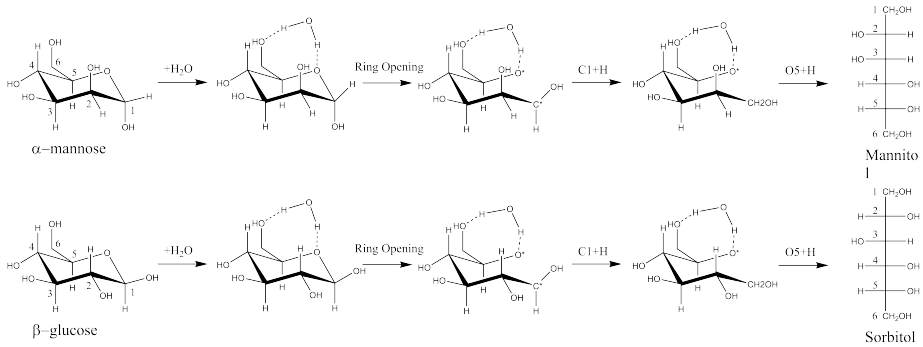

Figure 3.17: Calculated hydrogenation mechanism from mannose and glucose to mannitol and sorbitol. Adapted from Ref.[143]

and transition state theory then was done. Estimated ratio of reaction rates between α-mannose and β-glucose is 11 and this conclusion well interpreted the experiment results, given the approximations in this study.

To sum up, the concentrations of different reactant isomers in the liquid phase, their adsorption nature on the surface, as well as the different rate limiting steps (hydrogenation and ring opening reactions for glucose and mannose) determine the overall reaction rates. This opens a prospective route to the efficient valorization of renewable resources to added-value chemicals.

Paper V: Lignin conversion on Ni(111)

Background

Lignin is widely exist lignocellulosic biomass resources and accounts for 15-30% by weight and up to 40% of the energy.[144] It is the main part of the cell walls and supports plants with its rigidity and strength which originated from its polymer structures formed via C–C and aryl-ether linkages.[145] The well-known basic units in the complex cross-linked polymer are p-hydroxyphenyl, guaiacyl and syringyl, and those related monolignols (See Figure 3.18) are *p*-coumaryl (H), Coniferyl (G), and Sinapyl alcohols (S).[145,146] Lignin is the only nature source to obtain the major aromatic compounds (such as the BTX fraction: benzene,

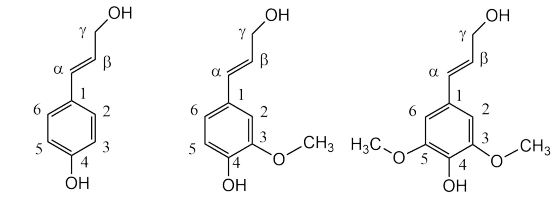

Figure 3.18: Structures of three lignin monomers.

toluene, and the three xylene isomers).[147] Its derived platform chemicals and can be used as renewable materials with agreat potential in polymer industries, food, medical, carbon fiber and so on.[145,148] Because of its highly stability and rigidity, efficient depolymerization methods under low temperatures are still lacking,[8,149,150] and the majority of lignin produced from paper and pulp industry is burned as low-valued materials for heating.[151]

In lignin, there exist different linkages such as β-O-4, β-5, α-O-4, β-β, 5-5, 4-O-5, β-1 and the others.[150] Among them, the most representative linkage is β-O-4, which accounts for 43-50% in softwood and 50-65% in hardwood. Therefore, breaking the β-O-4 bond has the highest priority in catalytic depolymerization and valorization processes. Comprehensive reviews on catalytic lignin transformation were presented by Calvo-Flores,[145] Zakzeski,[149] Zhang,[150] and Behling et al.,[8] focusing on the basic lignin compositions, various lignin valorization approaches in both heterogeneous and homogeneous systems, and the widely potential usages of its products in chemicals, fuels, and materials. Recently, Ni catalyst was observed that exhibits superior activity in aryl-alkyl bond activations in lignin hydrogenolysis, with aromatic moieties keep intact during the catalytic process.[152] Furthermore, by combing Ru into into Ni, Yan et al.[153] found that the bimetallic catalyst has a remarkable catalytic enhancement in aqueous lignin hydrogenolysis, compared with Ni-Rh, and Ni-Pd catalysts, showing the synergistic effects of two metals in catalytic performance (see Figure 3.19).

However, the depolymerization mechanism of lignin on the above mentioned catalysts are still unclear, One of the important reason is the simple model we used for simulating the lignin conversions which can not truly represent the real lignin.[8] From a theoretical point of view, large molecular surrogate structures need compatible large surface area to adsorb, resulting in the large slab model to calculate and heavy computational cost. This impedes the theoreti-

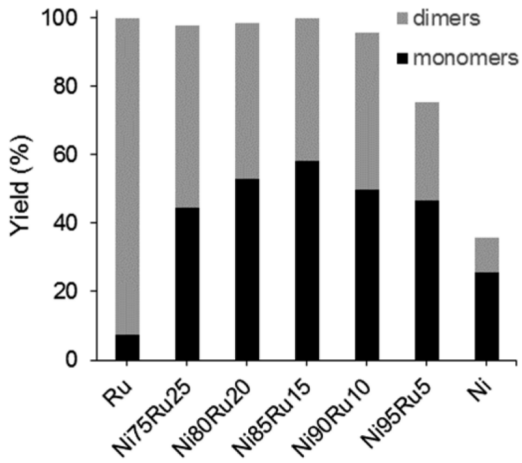

Figure 3.19: Experimental observations of Ru doping effects in promoting Ni catalyst's behavior. Adapted from Ref. [153]

cal investigations. Until now, there are only a few theoretical studies on lignin conversion on metal surfaces, For example, β-O-4 bond scission on Pd(111) [154] and Pt(1111) catalyst, [155] guaiacol hydrodeoxygenation on Pt(111), [156] and their models (lignin monomer and dimers) are very simple.

In fact, numerous lignin linkages with optically active stereocenters are formed between monolignols, [157] but their roles in catalytic conversion are still not considered so far. Besides, as Ni based catalysts generally work above 120 °C [150,153] and exhibits poor activity below this temperature, improvements of catalysts under low temperatures is still needed and understanding the reaction process in atomic level is crucial for this purpose.

Lignin decomposition mechanism on Ni(111)

In this study, adsorption of four isomers with different stereocenters were calculated and A and B were chosen for the lignin dimer model because they have much lower adsorption energies than C and D isomers. Then, possible elementary reactions (Figure 3.20) have been considered and these corresponding transition states were identified.From the calculation of this complex reaction

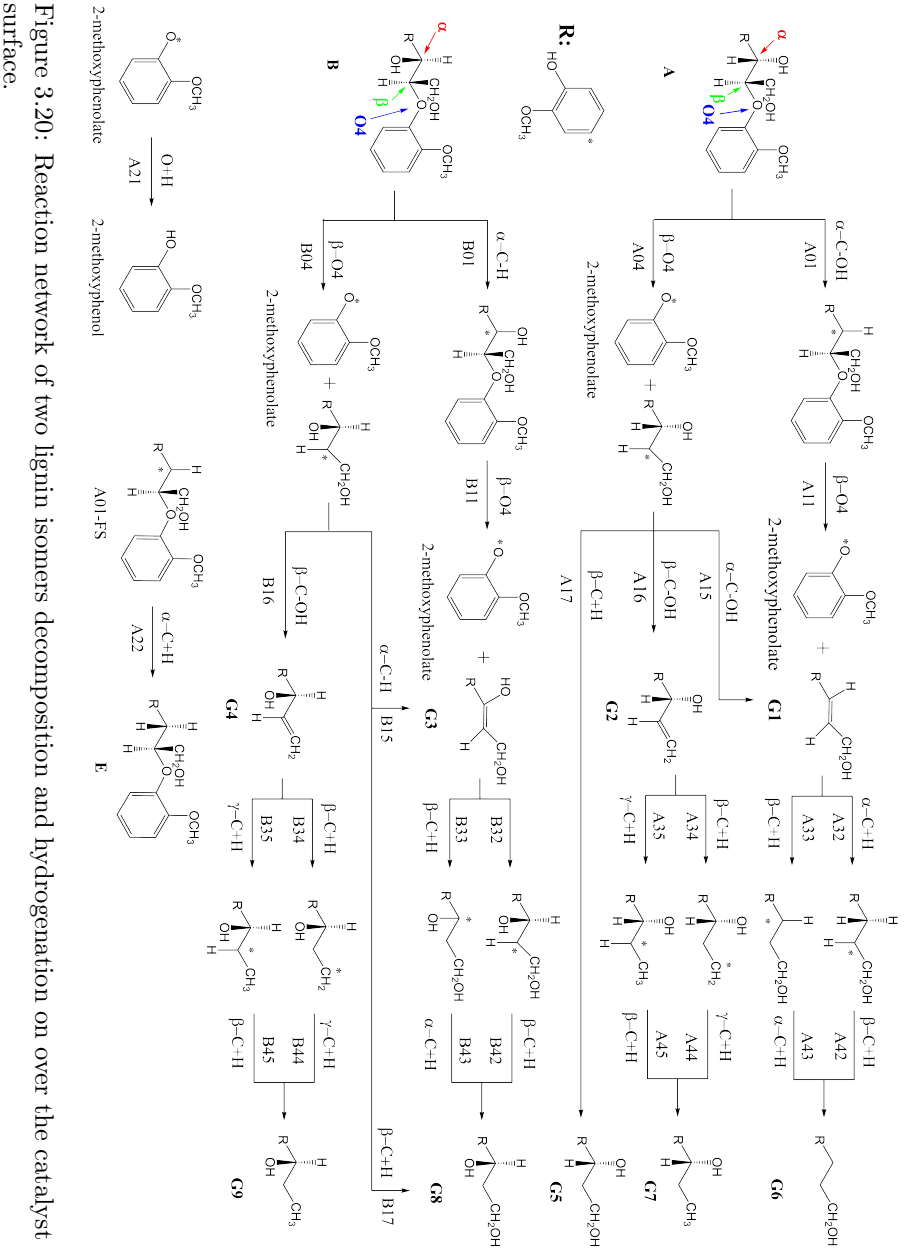

Figure 3.20: Reaction network of two lignin isomers decomposition and hydrogenation on over the catalyst surface.

network, it was found that β-O_4 bond breaks easily after α-C becomes unsaturated, namely after α-C–H or α-C–OH bond ruptures. Because of the stereocenter effects in A and B, the initial steps of decomposition are different and reactions from isomer B seem more kinetically preferable than those from A. Stereocenters also has effects on the production distribution, for instance, G6 and G7 are the main products from A, G8 and G9 from B.

Ru effects on promoting catalysis

Previous study from Zhang et al.[153] demonstrated that doping Ru into Ni based catalysts promotes its behavior and exhibits a volcano curve as shown in Figure 3.19. To elucidate the Ru effects, a set of reactions in the decomposition network were selected firstly, then the surface metal atom beneath the breaking/forming bonds were substituted by the Ru atom. The stability of this substitution model has been confirmed by the solubility of Ru into Ni bulk, segregation and near surface energy, and island formation energy (listed in Table 3.2)

Table 3.2: Calculated stability parameters (in eV): the solubility of Ru into the Ni bulk, E_{sol}, E_{seg}, E_{NS}, E_{isl}

Type	Energy
E_{sol}	0.53
E_{seg}	0.05
E_{NS}	0.00
E_{isl}	0.12

The slab with one Ni replaced by Ru atom was relaxed in the previous step and used for optimizing the transition states. By doing so, Ru effects on different types of reactions can be clearly demonstrated. Our research demonstrates that doping Ru has positive effects on breaking β-O_4 bond via decreasing the barrier by around 0.30 eV. However, introducing Ru into the system would facilitate the species adsorption, both for reactants and the products. As the low Ru content and its penetrating properties in Ni catalysts, Ru atoms consist low fraction on the surface. This has been confirmed by the XPS and XAFS characterizations in the experiment. With low surface Ru content, not only the positive effects on adsorption was observed, on the contrary, Ru would decrease or has little effects on promoting the adsorption process. However, when too much Ru were loaded

in the catalysts, its drawback origins from stronger adsorption appears and deteriorates the catalysts behavior. Our calculations agree well with previous experiment results and those founding such as stereocenters and Ru effects would benefit the future catalyst design.

To sum up, more complex molecular surrogates presenting stereocenters and based on coniferyl alcohol (G) dimers were selected in this work. By performing DFT calculations, the most stable two geometries are identified and the decomposition pathways have been studied on Ni(111) surface. Furthermore, the Ru doping effects were investigated via replacing one of Ni atom by Ru. Our study firstly demonstrate the effects of the stereocenters in decomposition process and the synergistic of Ru and Ni, detailed reaction mechanisms can also provide guideline for the incoming catalysts design.

Chapter 4

Included Papers

Paper I: Methanol on Cu and Ru

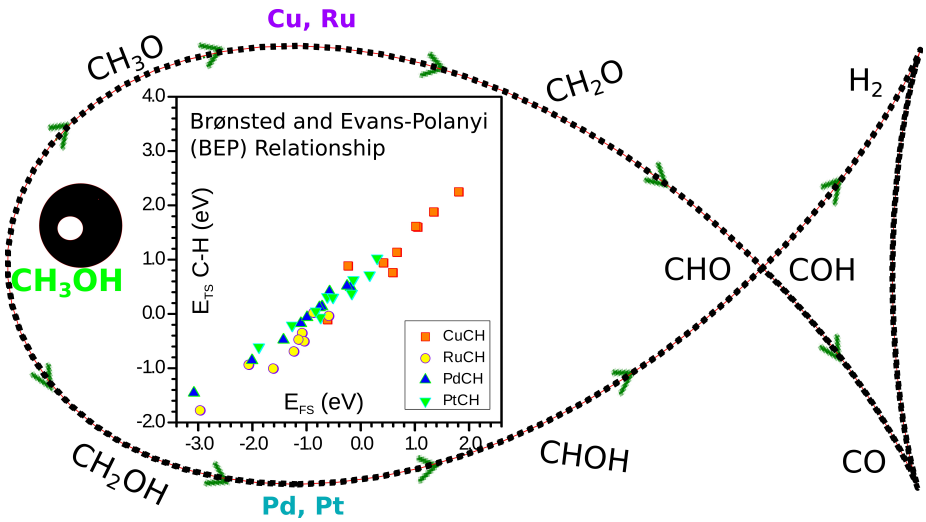

Published in *ACS Catal.* 2015, **5**, 1027-1036.

4.1. Paper I: Methanol on Cu and Ru

Density Functional Theory Comparison of Methanol Decomposition and Reverse Reactions on Metal Surfaces

Rodrigo García-Muelas, Qiang Li, and Núria López*

Institute of Chemical Research of Catalonia (ICIQ), Avgda. Països Catalans 16, 43007 Tarragona, Catalonia, Spain

Supporting Information

ABSTRACT: Methanol decomposition on metals has been subject of several theoretical studies, usually concentrating on a particular set of reactions in the main reaction path. In this work, we present an extensive study that considers all potential elementary steps for four close-packed surfaces including Cu, Ru, Pt, and Pd that shows the different behaviors and alternative routes through which the decomposition can take place by theoretical methods, including dispersion contributions. Decomposition follows different paths on these metals; while Cu would produce CH_2O, CO is the major product for the other metals. In addition, coverage effects might change the first step in Pt and Ru from methylenic to alcohol H activation. Alternatively the reaction network can be inspected for the formation of methanol from CO and hydrogen. Under these conditions, Cu generates CH_2O and only at very high H coverages is methanol likely to appear. On Pd, methanol formation and CHOH dissociation compete, thus leading to an inefficient process. A similar path takes place for Pt. For Ru the lateral paths leading to C−O breaking can occur at several points in the reaction network, never reaching CH_3OH. A compilation of the results with comparable computational setups presents a detailed database that can be added to the thermodynamics and kinetics for other reactions, such as methanation, with which they share a common list of reactions, or employed when analyzing larger alcohols such as those derived from biomass.

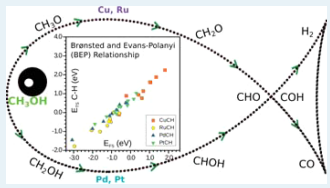

KEYWORDS: *methanol, density functional theory, Brønsted and Evans−Polanyi (BEP) relationships, Pt, Pd, Ru, Cu*

INTRODUCTION

Methanol is the smallest of all alcohols and, as it is a liquid and is easy to store, it has been presented as a potential energy vector that can be employed in new energy approaches. Indeed, the methanol economy concept was coined in the 1990s to account for this possibility.[1] The use of methanol in mobile applications seemed to be the most promising, as it can be directly used as fuel in combustion engines, directly converted to energy in electrochemical cells, or converted into another energy vector such as hydrogen.[2] Several of those approaches are based on its electrochemical transformation and the corresponding energy release, but the problem of direct methanol fuel cells comes from the strong adsorption of one of the subproducts, namely CO. Although methanol is currently produced by hydrogenation of a mixture of CO and CO_2 in a Cu/ZnO catalyst,[3,4] it is also possible to produce it from agricultural products and municipal waste, making it a recycled product. Methanol is also employed as a surrogate for larger biomass-derived alcohols,[5] even if this approach might be overly simple.

Methanol decomposition and synthesis on metal surfaces has been extensively investigated by several authors during the past decade. Greeley and Mavrikakis also investigated methanol decomposition on Cu(111),[6] where the preferred path would start by the dehydrogenation of the hydroxyl group. In the decomposition route on Pt(111),[7,8] the same authors studied a reaction network either starting with the dissociation of the alcohol hydrogen or starting from the methylenic H atoms. According to them, carbon dehydrogenation would be a preferred step, in contrast with the preferential O−H bond breaking found in experimental studies.[9] A recent study by the group of Campbell showed that the methoxy radical adsorbed on Pt(111) is rather unstable, as was predicted by DFT studies.[10] For the same system Neurock and co-workers[11] found that, under ultra-high vacuum conditions, methanol would desorb rather than react, as the activation barriers for the first dehydrogenation are higher than the desorption energy. In the study, two intermediates were discarded due to complexity, CHOH and COH; as we will show, both might belong to the minimum energy path. To rationalize the results for Pt, several attempts have been made. According to the d-band model, the activity of a metal is a function of the d-band center.[12−14] This analysis was employed by Park and co-workers[15] to study the methanol electrooxidation activity of Pt. In parallel, Ferrin and co-workers demonstrated that the catalyst performance for methanol electrooxidation can be described as a function of the free energy of adsorption of CO and OH radicals.[16] However, the adsorption energies and d-band positions are correlated, as the energies are a function of the d-band positions.[14] Yudanov and co-workers focused on C−O bond breaking on Pd nanoparticles, identifying it as a slow side process in the decomposition reaction.[17] On Pd and other metals, the

Received: November 3, 2014
Revised: December 23, 2014
Published: December 31, 2014

4.1. Paper I: Methanol on Cu and Ru

decomposition or dehydrogenation steps have been compiled for a large range of molecules and fragments containing the same heteroatom.[18,19] As for Ru(0001), experiments have shown the coexistence of two paths, one leading to CO and the other one leading to C and O separate fragments, where the second path was identified as responsible for surface poisoning.[20] The reason is that H-assisted reactions have been found to lower the barriers to difficult decompositions such as that of CO.[21]

Completeness at any stage is thus crucial to understand intricate reaction networks that can be intercrossed. As the reaction set becomes quite large, there is a need to describe the fragments to generate a database that can be employed to predict the activation energies of each particular step. Furthermore, the database can be modified to include the particular cases of lateral interactions and/or solvents for a more adequate representation of complex electrocatalytic systems.

This is precisely the aim of the present work. For methanol, we have built a consistent complete reaction network that accounts for crossings between different paths at any time in a way similar to that which we reported for HCN synthesis.[22] The reactions considered in our network are presented in Scheme 1. For this set of reactions we have investigated the following items: (i) we have stablished a common connectivity matrix notation that allows extrapolation to more complex substrates; (ii) we have analyzed the role of different kinetic−thermodynamic relationships to ensure the best form to predict the energies for other metals; (iii) we have described the potential hysteresis in the decomposition/synthesis paths by inspecting the direct and reverse reactions; and (iv) we have analyzed lateral effects for key competitive routes.

Scheme 1. Reaction Network for the Decomposition of Methanol on the Different Surfaces Considered in This Work

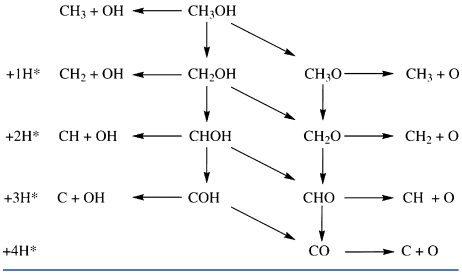

COMPUTATIONAL DETAILS

Slab calculations were performed using the Vienna ab initio simulation package (VASP),[23,24] the PBE density functional,[25] and a kinetic energy cutoff of 450 eV. The inner electrons were represented by projector augmented wave (PAW) pseudopotentials.[26,27] The calculated lattice parameters for Ru, Cu, Pd, and Pt are 2.712, 3.629, 3.939, and 3.968 Å, respectively, and $[c/a]_{Ru}$ = 1.581, in good agreement with experimental values of 2.706, 3.615, 3.893, and 3.924 Å and $[c/a]_{Ru}$ = 1.582.[28−31] The cells were built in a p (3 × 3) configuration for Ru and Cu, with a $2\sqrt{3} \times 2\sqrt{3} - R30°$ supercell. Therefore, the coverages are low and comparable, between 0.08 and 0.11 ML. To inspect lateral interactions in reaction and activation energies, we included one or two additional methanol molecules in the $2\sqrt{3} \times 2\sqrt{3} - R30°$ supercell. All metallic surfaces were modeled by a four-layer slab. The two topmost layers were fully relaxed, and the two bottom layers were fixed to the bulk distances. For surface calculations, the Brillouin zone was sampled by a Γ-centered *k*-point mesh generated through the Monkhorst−Pack method,[32] and the samplings were denser than 0.3 $Å^{-1}$. We included a vacuum region larger than 12 Å and a dipole correction along the *z* direction.[33] We also included the van der Waals (vdW) corrections by applying Grimme's DFT-D2 method,[34,35] with the C_6 parameters developed in our group.[36,37] The van der Waals contributions to adsorption can be found in Table S1 of the Supporting Information. The molecules in the gas phase were relaxed in a box of 20 × 20 × 20 $Å^3$. We employed both the nudged elastic band (CI-NEB) and the improved dimer method, (IDM) to find the transition states.[38−40] The optimization thresholds were 10^{-5} eV and 0.015 eV/Å for electronic and ionic relaxations, respectively. In all cases the saddle point nature of the transition states was assessed by the calculation of the numeric Hessian with a step of 0.02 Å and its diagonalization that rendered a unique imaginary frequency. In the following, all discussed energies correspond to dispersion-containing values including zero-point energy unless stated otherwise.

RESULTS

Description of the Reaction Network. The data for adsorption of key intermediates can be found in Table S1 in the Supporting Information. The contribution of van der Waals dispersion terms has been evaluated for reactants and products. Inclusion of vdW interactions raises (more exothermic) the adsorption values between 0.01 and 0.20 eV. Tests of different adsorption sites and comparison to previous results in the literature are provided in Tables S2−S4 in the Supporting Information. In order to simplify and order all of the intermediates, an identification vector that defines them has been developed (see Table S5 in the Supporting Information) which can be extended to more complex compounds. The vector defines the stoichiometry with the first three numbers (carbon, hydrogen, oxygen), and isomerism is given as a fourth number; thus, methanol corresponds to 1411 and CO to 1011.

In this section we describe all of the potential reaction steps described in Scheme 1 for all four metals in the present study: Cu(111), Ru(0001), Pt(111), and Pd(111). In Figures 1−3, we present top and side perspectives for all of the reaction steps in the paths for the particular case of copper. A complete version of these figures for all metals considered can be found in the final section of the Supporting Information.

The first group of reactions corresponds to the O−H bond breaking and contains four elementary steps starting from methanol (CH_3OH), hydroxymethyl (CH_2OH), hydroxymethylidene (CHOH), and hydroxymethylidyne (COH) (Figure 1). For adsorbed molecules, the initial configuration presents the OH fragment close to the surface and thus bond activation easily occurs. In the case of CH_2OH, both O and C atoms are bonded to the surface but the hydrogen on the OH group is closer to the surface in comparison to the methylenic H; thus, it seems rather straighforward that the OH is more activated at this stage. On the other hand, the CHOH and COH fragments are bonded to the surface by the carbon center (Figure 1), and thus the alcoholic hydrogens are farther away from the surface. Such kinds of configurations would be better activated by

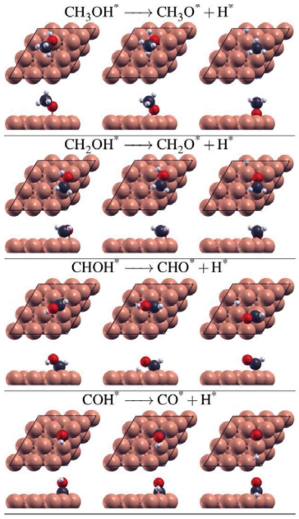

Figure 1. Schematic representation of the reaction steps considered for the decomposition on Cu(111), regarding O−H bond breaking. Large spheres correspond to metal atoms and red, gray, and white spheres to O, C, and H, respectively.

nearby structural defects on the metal surface.[41] Indeed, coordinative unsaturated atoms, such as those present on step sites, could be more effective to catalyze the perpendicularly adsorbed fragments, as they not only are more reactive but also prevent the rotation needed to activate the O−H fragment. In the final positions of methanol and COH decomposition the fragments stand up perpedicular to the surface. In comparison, the fragments with partially dehydrogenated C moieties (CH_2OH and CHOH) either lie on the surface or are just bonded through the C atom. For CH_3OH and CH_2OH, O−H activation implies a change in the coordination of the O atoms from top to fcc sites, Pt being the only exception. For CHOH or COH dehydrogenation, C moves from the bridge to the top site or keeps the fcc site, respectively.

Figure 2 illustrates the dehydrogenation of the carbon atom in six different molecules: CH_3OH, CH_3O, CH_2OH, CH_2O, CHOH, and formyl (CHO). In all cases a change in the coordination of the carbon atom to fulfill the empty valence is found.[42] In some cases, such as the dehydrogenation of CH_2OH, this is accompanied by a reorientation of the final carbon fragment CHOH which leads to O atoms no longer adsorbed to the surface. The rotation is induced by the larger empty valence of C atoms in comparison to O atoms.

The eight elementary steps for the C−O bond breaking are presented in Figure 3, corresponding to CH_3OH, CH_3O, CH_2OH, CH_2O, CHOH, CHO, COH, and CO. It is well-known that the CO decomposition is much easier at steps due to the stand-up nature of the adsorbed CO molecules and the fact that step atoms are more reactive; however, the rest can be analyzed for planar surfaces with a sufficiently high confidence. As we will see later, the obtained barriers are low enough to ensure that the remaining reactions can occur under mild experimental conditions.

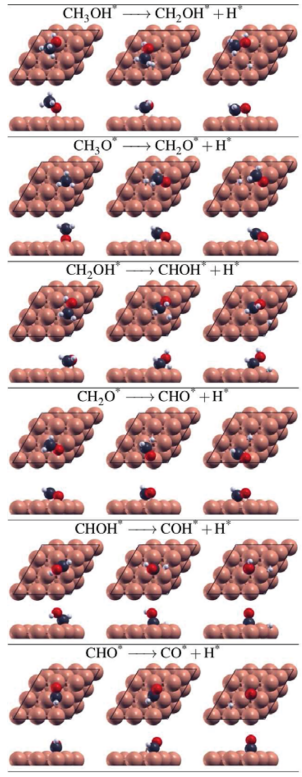

Figure 2. Schematic representation of the reaction steps considered for the decomposition on Cu(111), regarding C−H bond breaking. Large spheres correspond to metal atoms and red, gray, and white spheres to O, C, and H, respectively.

Energy Profiles for Dehydrogenation. The lowest energy paths for methanol decomposition on the different surfaces are shown in Figure 4. Reaction and activation energies are given in Tables S6 and S7 in the Supporting Information, and the structures are depicted in Table S13 in the Supporting Information. On Cu(111), the methanol decomposition pathway follows as $CH_3OH \rightarrow CH_3O \rightarrow CH_2O \rightarrow CHO \rightarrow CO + H_2$. It is the simplest pathway among all of the metals and is also supported by previous theoretical studies.[6,43−45] The first step consists of O−H bond breaking, which is slightly exothermic (−0.22 eV). However, this step presents a rather large energy barrier of 0.98 eV, which is 0.61 eV higher than the desorption energy. CH_3O is acknowledged as the most stable intermediate among all of the species during the decomposition process on Cu(111).[6,44−46] From CH_3O on, all subsequent reactions correspond to C−H breaking. The bond lengths of C−H in sequential TS structures are 1.86, 1.57, and 1.14 Å, respectively, which demonstrates that the C−H bond breaking occurs more easily with further dehydrogenations. In correspondence, the activation energy barriers are 1.04, 0.55,

4.1. Paper I: Methanol on Cu and Ru

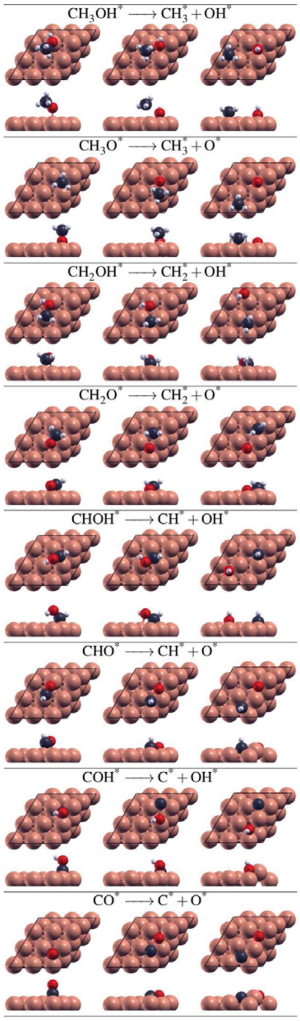

Figure 3. Schematic representation of the reaction steps considered for the decomposition on Cu(111), regarding C−O bond breaking. Large spheres correspond to metal atoms and red, gray, and white spheres to O, C, and H, respectively.

and 0.19 eV. Considering the required energy for O−H scission (0.98 eV), the dehydrogenation from CH_3O to CH_2O, which is also highly endothermic by 0.73 eV, is the most energy-demanding step in the decomposition pathway. The reported reaction (activation) energies for this step in previous theoretical studies are 0.97 (1.42),[6] 0.92 (1.27),[45] 0.85 (1.85),[44] and 1.00 (1.16)[43] eV, respectively. To enhance decomposition, any basic center on the carrier could thus be more adequate than the metal surface itself. Moreover, CH_3O can easily desorb from Cu(111) because its binding energy of 0.31 eV is less than the energy barrier for the dehydrogenation, 0.55 eV. When dehydrogenation continues from formaldehyde, then the C−H bond breaks directly or spontaneously from CHO with a lower energy barrier (0.19 eV) and a highly exothermic path (−0.99 eV). Similar results were obtained by Lim[43] (−0.89 eV) and Zuo[44] (−0.93 eV).

C−O bond breaking could only occur for the CHOH intermediate, but in the direct methanol decomposition path this intermediate is never observed. It has been suggested that in the presence of water the reaction network could continue through the condensation of CH_2O with an adsorbed OH and further oxidation to CO_2.[46]

On Ru(0001) surfaces, there are two competing pathways for methanol decomposition: on one side, $CH_3OH \rightarrow CH_3O \rightarrow CH_2O \rightarrow CHO \rightarrow CO + H_2$, and on the other, $CH_3OH \rightarrow CH_2OH \rightarrow CHOH \rightarrow COH \rightarrow CO + H_2$. The first path is the same as that on Cu(111); the O−H bond breaks first, and then the reaction proceeds for the C−H bonds. However, in the alternative pathway only C−H bond breaking occurs and the O−H bond is retained during the whole process until the final step, which leads to CO and H_2. Starting from methanol, both O−H and C−H bond breakages are exothermic with reaction energies of −0.74 and −0.39 eV and the required bond-breaking energies are 0.60 and 0.48 eV, respectively. Thus, C−H bond splitting is more kinetically preferable, while the O−H bond breaking which leads to the CH_3O is more favored thermodynamically. However, on the basis of experimental studies,[47] only methoxy species were observed in the temperature range from 180 to 340 K. In the first pathway, the dehydrogenation of methoxy to formaldehyde is the step with the highest energy demand, with an energy barrier of 0.90 eV. Unlike the formaldehyde desorption on Cu(111), formaldehyde binds strongly on Ru(0001) with a desorption energy of 1.09 eV, in good agreement with the study by Chiu (1.06 eV).[48] Moreover, the dehydrogenation from CH_2O to CHO occurs easily through a negligible barrier of 0.06 eV. The dehydrogenation of CHO is also almost barrierless (0.04 eV) and is highly exothermic (−0.90 eV). Our results are in good agreement with recent experiments for high methanol coverages, which report that O−H bonds break to form methoxy, which subsequently evolves to CO and hydrogen with no significant C−O bond breaking.[47] In the next section, we will analyze the effect of spectator methanol molecules for the first dehydrogenation reactions on Ru(0001) and Pt(111). Significatively, along the $CH_3OH \rightarrow CH_2OH \rightarrow CHOH \rightarrow COH \rightarrow CO + H_2$ path the three barriers are quite low, although two intermediates are higher in energy than those of the methoxy path. From a thermodynamic perspective, the elementary steps are not as favored as the first path and the first two reactions are only weakly exothermic: −0.39 and −0.43 eV, respectively. Moreover, the last H abstraction from COH to CO, although being exothermic (−0.76 eV), is hindered by a sizable energy barrier of 0.77 eV.

Carbon monoxide binds strongly on Ru(0001), Pd(111), and Pt(111) surfaces, with desorption energies of +1.93, +2.29, and +1.95 eV, respectively. At high methanol pressures, the reaction will proceed until all of these surfaces become covered by carbon monoxide, and further reactions will take place only after carbon monoxide desorbs. This is one of the most common problems for the direct methanol fuel cells that are usually described for Pt. In turn, methanol adsorption on such

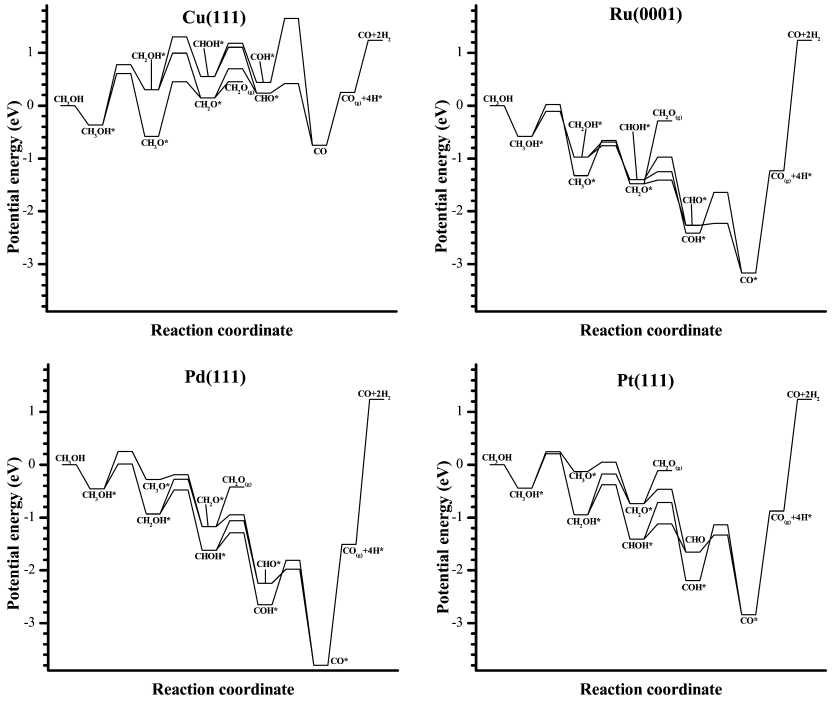

Figure 4. Reaction profiles for the decomposition of methanol to CO and H_2 on different metal surfaces. The minimum energy paths are considered in each particular case.

poisoned surfaces might end up being the observed rate-determining step.

For Pd(111), the lowest energy barrier corresponds to the methylinic dehydrogenation, where the activation energy, 0.47 eV, is on the order of the desorption energy, 0.46 eV. The O−H dehydrogenation has a rather high activation barrier of 0.71 eV and it is thus not feasible. These results are in qualitative agreement with reported values.[49] The main pathway is $CH_3OH \rightarrow CH_2OH \rightarrow CHOH \rightarrow COH \rightarrow CO + H_2$, the subsequent activation barriers being 0.45, 0.34, and 0.84 eV, respectively. Because the last step has a relatively high activation energy, the reaction can also follow the alternative path $CHOH \rightarrow CHO \rightarrow CO + H_2$, with activation energies of 0.56 and 0.26 eV. The energy profile shows the largest energy span[50] among the four surfaces and thus it is the worst to decompose methanol. The experimental decomposition to CO and H_2 was experimentally reported to occur around 250 K.[51] The C−O breaking of methanol was found to be not likely, with a high energy barrier of 1.57 eV, in good agreement with a previous theoretical study (not ZPE corrected 1.78 eV).[52]

For Pt we discuss two routes. The loss of the methylenic hydrogen drives the reaction according to the following elementary steps: $CH_3OH \rightarrow CH_2OH \rightarrow CHOH \rightarrow COH \rightarrow CO + H_2$. Once the first barrier (0.65 eV) is overcome, the reaction will proceed to CO with low energy barriers of 0.57, 0.69, and 1.06 eV. Alternatively, the route $CHOH \rightarrow CHO \rightarrow CO + H_2$ has energy barriers of just 0.28 and 0.32 eV. After full dehydrogenation, CO removal is likely to be the bottleneck, as it can accumulate and poison the surface. Our results are in good agreement with experiments, which determined that the methanol dehydrogenation on Pt(111) occurs at temperatures as low as 140 K,[9] significantly lower than the previously reported 250 K Pd value. Yet, another possible route is $CH_3OH \rightarrow CH_3O \rightarrow CH_2O \rightarrow CHO \rightarrow CO + H_2$. In this route, the first reaction is O−H bond scission, which is also the most demanding energy step with an energy barrier of 0.69 eV, followed by moderate barriers of 0.18, 0.28, and 0.32 eV, which facilates the decomposition reactions. According to these results, an isolated methanol molecule will desorb rather than react on Pt(111),[11] and if any reaction takes place, the C−H dehydrogenation would be preferred to the O−H breaking,[8] given that CH_3O is rather unstable on Pt(111), a fact that has been confirmed by experiments.[10] Nevertheless, experimental observations on the dehydrogenation of methanol and other monoalcohols on Pt(111) detected the methoxy radical as an intermediate, but not CH_2OH.[9,53] The source of this apparent discrepancy is that the former analysis does not consider the effect of neighboring methanol molecules, which might play a significant role in O−H bond breaking (see below).

Role of Lateral Interactions. As we have indicated earlier, there are some apparent contradictions between experimental and theoretical results corresponding to the first stage of

dehydrogenation. Lateral interactions based on hydrogen bonds could be responsible for most of the phenomena regarding O−H groups on metal surfaces.[5,54] Methanol adsorption energy on Cu, Ru, Pd, and Pt is −0.37, −0.59, −0.46, and −0.44 eV, respectively. The hydrogen bond is one of the main lateral interactions between adsorbed methanol molecules, being exothermic by around −0.20 eV. Therefore, under the initial conditions on the clean surfaces, the methanol molecules will approach each other and thus a relatively high coverage even at medium pressures and low temperatures can take place.

In Figure 5 we show that the inclusion of neighboring methanol molecules changes the reaction and activation

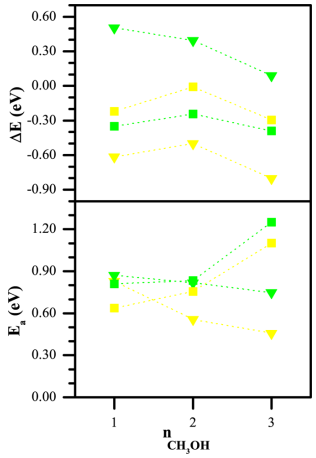

Figure 5. Reaction energies and activation barriers for the dissociation of methanol through the competing O−H (triangles) and C−H (circles) bond breaking, as a function of methanol coverage for Pt(111) (green) and Ru(0001) (yellow).

energies for both O−H and C−H decomposition as follows. On one hand, the nearby OH groups stabilize the methoxy intermediate via hydrogen bonding by around 0.20 eV for each group. They also stabilize the transition state of the O−H decomposition and lower the activation energy by around 0.10−0.20 eV/spectator molecule. On the other hand, the activation barrier for the C−H decomposition increases around 0.10 eV if one spectator methanol molecule is included and then additionally increases by 0.40 eV if a second molecule is incorporated, due to strains in the transition state. The barriers for the competitive reactions at low coverage on Ru favor C−H bond breaking with ΔE_a = 0.19 eV, but at high coverage this value is −0.64 eV, and the values are +0.05 to −0.50 eV for Pt. Therefore, the surrounding methanol molecules will induce a change in the reaction pathway. This is not so clear for Pd, for which the energy difference between both paths is still within the energy change of the lateral hydrogen interactions.

Other intermediates or products can be affected by lateral interactions. For instance, for CO adsorption in dense layers a significant reduction of the average binding energy has been found.[55]

Energy Profiles for the Inverse Reaction: CO Hydrogenation. Over the paths for methanol decomposition, those for synthesis from CO and H_2 without considering the role of CO_2 and/or the water−gas shift reaction can be superimposed to clarify some aspects of methanol synthesis (see Figure 6).

As for the CO hydrogenation, the profiles show that the CHO formation is much more preferable than COH, as the required energies for CHO (COH) formation are 0.17 (2.41) on Cu(111), 0.94 (1.53) on Ru(0001), 1.82 (1.99) on Pd(111), and 1.51 (1.70) eV on Pt(111), respectively. Because of the upright CO adsorption on the four surfaces with C atoms, the interactions between carbon and H atoms are much stronger than those between oxygen and H atoms, which eventually leads to the formation of C−H bonds instead of O−H bonds. For Cu(111) the reaction goes through the adsorption of CO and H_2, forming CHO, which further evolves toward formaldehyde (CH_2O). This formaldehyde preferentially desorbs from the surface. Only if there is a trap for formaldehyde (such as an oxide as in Cu/ZnO[4]) or the amount of H is extremely high could the reaction end up in the formation of methanol. In the modeling of CO_2 electroreduction also some selectivity issues were found on the copper case compatible with our analysis.[56]

The reactions on Ru(0001) are rich, as there are abundant intermediate species and close energy barriers (0.65−0.95 eV) for C−H, C−O, and O−H bond breaking and formation. It should be pointed out here that formaldehyde is the crucial intermediate in the reaction network. The three elementary reactions starting from formaldehyde are $CH_2O \rightarrow CH_3O$, $CH_2O \rightarrow CH_2OH$, and $CH_2O \rightarrow CH_2 + O$. It is interesting to find that they have extremely close barriers of 0.73, 0.70, and 0.72 eV, respectively. Hence, all three reactions can take place in the system. However, the methanol formation from CH_3O is hindered by the largest barrier, 1.34 eV. On the other side, the energy barriers for decomposition from CH_2OH to CHOH (0.21 eV) or CH_2+OH (0.68 eV) are lower than that for methanol formation (0.87 eV). Furthermore, the decomposition from CHOH to CH and OH requires only 0.44 eV and is very exothermic (−1.17 eV). From the above analysis, it is clear to demonstrate that the C−O bond activation reactions are favored on the Ru(0001) surface and, to some extent, methanol formation is unlikely on Ru(0001), as C and O species poison the reactive sites.

On Pd(111), there are two competing reactions from CHOH: $CHOH \rightarrow CH_2OH$ and $CHOH \rightarrow CO + OH$. The barriers (and reaction energies) are 1.14 (0.69) and 1.18 (−0.06) eV, respectively. Therefore, C−O bond scission from CHOH is most favorable thermodynamically despite similar kinetics. In addition to the CHOH formation, as shown in Figure 6, formaldehyde can also be formed, but it is not as favored as CHOH. There are also two ways for formaldehyde to react on the surface, desorption or hydrogenation to CH_2OH, with energy barriers of 0.75 and 0.90 eV. From CH_2OH, the hydrogenation to methanol is favored, as its energy barrier is 0.95 eV, which is lower than that of C−O bond breaking, 1.31 eV. This reaction barrier is in very good agreement with a previous theoretical study (1.30 eV).[57] Hence, although it seems possible to achieve the methanol synthesis from CO and H_2 on Pd(111), the large barrier for the first hydrogenation step would render the process difficult.

On Pt(111), the first likely intermediate for hydrogenation is CHO followed by CHOH upon the second hydrogenation. Then, the reaction goes as $CHOH \rightarrow CH_2OH \rightarrow CH_3OH$ with activation (reaction) energies of 1.03 (0.46) and 1.16 (0.51) eV. Thus, the network is similar to that of Pd(111); CHOH

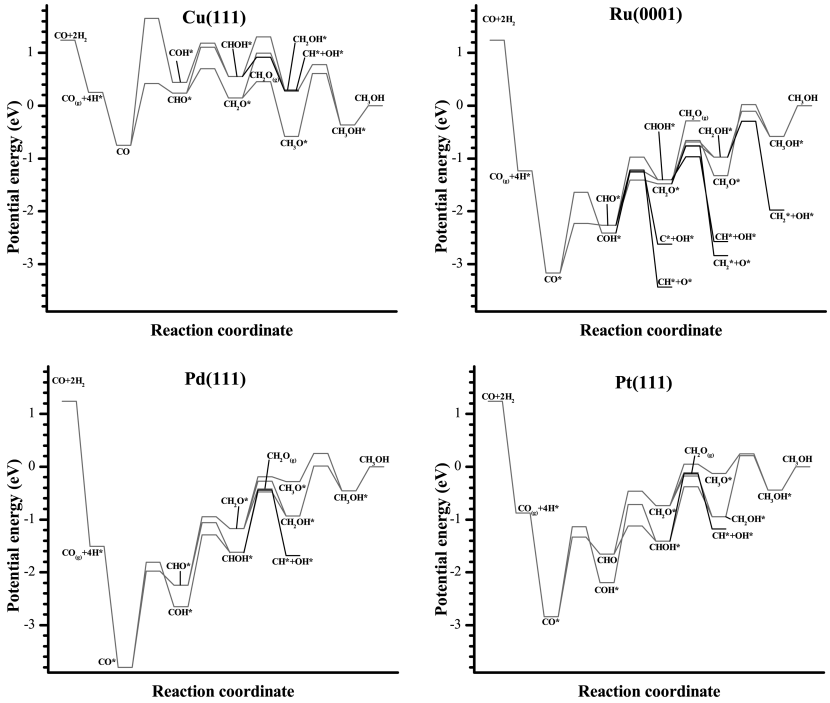

Figure 6. Reaction profiles for the reaction of CO and H_2 on the different surfaces considered here. The minimum energy paths are considered in each particular case.

and CH_3OH are important intermediate species for methanol synthesis. However, it has to be mentioned here that the energy barriers on Pd(111) and Pt(111) are higher than those on other surfaces, and thus these surfaces are less prone to hydrogenate CO.

Kinetic–Thermodynamic Relationships. The relationship between kinetic and thermodynamic parameters was put forward by Brønsted[59] generalized by Evans and Polanyi (BEP),[60] and reintroduced in the density functional theory framework more recently by the groups of Neurock and Nørskov.[61,62] The theory states that the target molecules belonging to a family have similar transition states in nature and thus a change in the thermodynamics of the reaction, i.e. toward more exothermic, is accompanied by a lower activation energy of the direct reaction. If the stability of the intermediates on the surfaces is linked to a single parameter through linear energy scalings,[42] then the BEP relationship directly gives a volcano plot.[63] However, we and others have found that in many cases the BEP relationships represent the dissociation paths better than the associative paths and this behavior has been linked to the early or late-like character of the transition states. An explanation put forward by Hammer[64] indicates that in dissociative paths the interaction between fragments in the transition state resembles that of the final state, provided that this structure corresponds to the fragments sharing some metal atoms in the site ensemble. An alternative formulation of the BEP that allows the systematization for different compounds was presented by Sautet and co-workers.[58,65] These authors employed a general reference and placed the energy of the transition state as a function of either the initial (IS) or the final states (FS). In our case we have employed the two methodologies with the three possible variations (ΔE, IS, FS), to analyze the different classes and deduce the potential relevance of the wide set of data gathered in the present work. The correspoding results are summarized in Figure 7, where all energies contain the ZPE term; to compare only the potential energy values the reader is addressed to Tables S8–S12 and Figures S1–S3 in the Supporting Information.

For the BEP relationships (first column) in Figure 7 it is clear to see that a proper linear dependence is only observed for CH and especially for CO dissociation. In both cases the dispersion is significant in the low energy regime ($\Delta E \leq -1$ eV). In the case of C–H dissociation it seems that the ΔE value is saturated and thus a plateau appears. Indeed, in an understanding of BEP relationships through a Marcus-like approach[66] it becomes clear that for reactions with high endo(exo)thermic energies the values of the activation barrier should be limited by flat areas. The C–H dissociation energies were already reported extensively to show a BEP relationship in the case of the alkyne–alkene–alkane series for a single metal.[18,67] For CO the discrepancy comes from Ru(0001) points that lie at the lowest part of the energy span; in this case the large influence might be

4.1. Paper I: Methanol on Cu and Ru

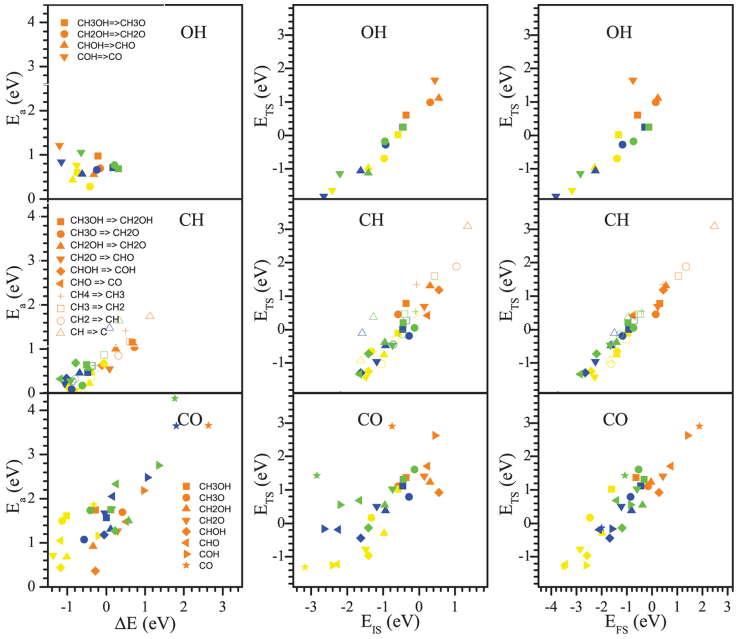

Figure 7. Brønsted–Evans–Polanyi and initial and final state[58] relationships for the different bond breaking reactions: (a) O–H; (b) C–H; (c) C–O. The results of the linear fits are presented in Tables S8–S12 in the Supporting Information.

brought by the strong affinity of Ru toward O atoms (see Table S1 in the Supporting Information).

The situation improves significantly for the dependence on the energy of the initial state, at least for O–H and C–H bond breaking. For O–H a clear line appears with little scattering of around 0.20 eV, the larger being that of Pt (see Figure 7). The values for all metals are distributed quite evenly. The reason for such a good relationship can be traced back to the simple nature of the transition state in this case (Figure 1). A similar, not yet well-defined dependence is found for C–H bonds. In this case the energy span is again large and the points are aligned preferentially on a single line with no semblance of the saturation observed in the BEP plot. However, the point distribution significantly broadens in the central part, where displacements of the individual points to the line can amount up to 0.30 eV. The C–O dissociation class is completely different in this perspective. The list of points is largely scattered, and not even the distribution by individual metals (shown by colors) can illustrate the differences other than from a very qualitative analysis.

Finally, we have considered the dependence of the transition state on the final state energies (third column in Figure 7). For O–H the distribution is no better than that of the initial state. The main reason is the smaller energy span and the appearance of a couple of outliers. When these configurations are analyzed independently, they correspond to Pt and Cu, as in the final state the fragments do not share any metal atoms. In these metals, the FS has no "geometric memory" of the TS, and as described by Hammer[64] the correlation observed for the other points breaks here. For C–H the correlation is excellent and all points show the lowest dispersion from the reference line. The discrepancies are below the 0.20 eV error of DFT, and thus the line can be accepted as presenting an excellent predictive power for this class of reactions. For C–O the final-like transition state nature is nicely captured in the correlation between the transition and final state energies, which gives a good representative character to the BEP line (except for Ru). Since the final states considered here have the fragments sharing same atoms, an even better predicting nature is given to the TS–FS correlation. Discrepancies, for instance the green star at about 0 eV, might be relevant though even on the central part of the point distribution, highlighting that this kind of dissociation, between two heteroatoms that do not differ much in adsorption strength, are the most prone to errors when interpolated.

We note that for several reactions where cooperative, lateral interactions are important, for instance when a web of H bonds is formed, the modification induced by coverage might be much larger than the error made by employing the most suitable kinetic–thermodynamic scaling. Coverage effects in hydroxylic systems might add up an extra 0.15 eV/H bond to the dissociated forms, while the errors of the best prediction curve are around 0.2 eV.

CONCLUSIONS

By means of density functional theory we have investigated the complex networks arising from the decomposition of methanol on four metal surfaces: Cu, Ru, Pd, and Pt. The product

distributions are different on these metals, where Cu preferentially renders CH_2O, while Pt, Pd, and Ru initially generate large amounts of CO that could potentially poison the surface. The initial decomposition state on Pt and Ru has been a subject of discrepancies between experiments and theory, but coverage effects can fine-tune the relative competing routes. On one hand O−H bond breaking is improved at high coverages while the alternative activation of the methylenic H ends up with an intermediate that requires a larger ensemble and thus is more repulsive. The same set of reactions can be employed to understand the reverse reaction of CO hydrogenation. Again differences in the product distribution appear, Cu being quite unique and the reaction leading to CH_2O. For Pt and Pd the routes to form methanol are affected by CO blocking and the large barriers to transfer the first hydrogen. On Ru, the selectivity problem is more acute, as several routes inducing C−O bond breaking appear at different stages of the hydrogenation. For the kinetic−thermodynamic relationships we have explored different routes to obtain the best-predicting representations. C−H bond breaking is the easiest set of reactions to represent, with almost no error in the TS to FS plot. For O−H the initial state representation seems more adequate, the reason being that the H bond is not as different on the metal surfaces. Activation energies for C−O bond breaking are by far the most difficult to be retrieved. In summary, for complex substrates it would be operative to obtain from the kinetic−thermodynamic scalings the first values for C−H and O−H dissociations and evaluate in detail the more complex C−O dissociations. There is a final point regarding the concept of mechanism in heterogeneous catalysis. According to the IUPAC definition, a mechanism is the list of elementary reactions that lead from reactants to products. However, in line with the complexity of the networks that we observe, the total list of reactions involved might contain a richer information indicating that the set of potential steps is common, although due to the energy differences they are manifested in different "mechanisms".

■ ASSOCIATED CONTENT

Supporting Information

The following file is available free of charge on the ACS Publications website at DOI: 10.1021/cs501698w.

Computed adsorption (with van der Waals contribution analysis), reaction, and activation energies, comparison with previous theoretical and experimental studies, Brønsted−Evans−Polanyi, initial state, and final state scalings, and structures of initial, transition, and final states for all of the reactions in the study (PDF)

■ AUTHOR INFORMATION

Corresponding Author

*N.L.: e-mail, nlopez@iciq.es; tel, +34 977920237; fax, +34 977920231.

Notes

The authors declare no competing financial interest.

■ ACKNOWLEDGMENTS

The authors thank the ERC-2010-STG-258406 Bio2Chem-d project and MINECO (CTQ2012-33826) for financial support and BSC-RES for providing generous computer resources.

■ REFERENCES

(1) Olah, G. A. *Angew. Chem. Int. Ed.* **2005**, *44*, 2636−2639.
(2) Nielsen, M.; Alberico, E.; Baumann, W.; Drexler, H.-J.; Junge, H.; Gladiali, S.; Beller, M. *Nature* **2013**, *495*, 85−89.
(3) Gallagher, J. T.; Kidd, J. M. Patent UK1159035, 1966.
(4) Behrens, M.; Studt, F.; Kasatkin, I.; Kühl, S.; Hävecker, M.; Abild-Pedersen, F.; Zander, S.; Girgsdies, F.; Kurr, P.; Kniep, B.-L.; Tovar, M.; Fischer, R.; Norskov, J.; Schlögl, R. *Science* **2012**, *336*, 893−897.
(5) García-Muelas, R.; López, N. *J. Phys. Chem. C* **2014**, *118*, 17531−17537.
(6) Greeley, J.; Mavrikakis, M. *J. Catal.* **2002**, *208*, 291−300.
(7) Greeley, J.; Mavrikakis, M. *J. Am. Chem. Soc.* **2002**, *124*, 7193−7201.
(8) Greeley, J.; Mavrikakis, M. *J. Am. Chem. Soc.* **2004**, *126*, 3910−3919.
(9) Sexton, B. A. *Surf. Sci.* **1981**, *102*, 271−281.
(10) Karp, E. M.; Silbaugh, T. L.; Crowe, M. C.; Campbell, C. T. *J. Am. Chem. Soc.* **2012**, *134*, 20388−20395.
(11) Desai, S. K.; Neurock, M.; Kourtakis, K. *J. Phys. Chem. B* **2002**, *106*, 2559−2568.
(12) Hammer, B.; Nørskov, J. *Surf. Sci.* **1995**, *343*, 211−220.
(13) Greeley, J.; Nørskov, J. K.; Mavrikakis, M. *Annu. Rev. Phys. Chem.* **2002**, *53*, 319−348.
(14) Nørskov, J. K.; Bligaard, T.; Rossmeisl, J.; Christensen, C. H. *Nat. Chem.* **2009**, *1*, 37−46.
(15) Kang, J.; Nam, S.; Oh, Y.; Choi, H.; Wi, S.; Lee, B.; Hwang, T.; Hong, S.; Park, B. *J. Phys. Chem. Lett.* **2013**, *4*, 2931−2936.
(16) Ferrin, P.; Nilekar, A. U.; Greeley, J.; Mavrikakis, M.; Rossmeisl, J. *Surf. Sci.* **2008**, *602*, 3424−3431.
(17) Yudanov, I.; Matveev, A.; Neyman, K.; Rösch, N. *J. Am. Chem. Soc.* **2008**, *130*, 9342−9352.
(18) Andersin, J.; López, N.; Honkala, K. *J. Phys. Chem. C* **2009**, *113*, 8278−8286.
(19) Wang, S.; Petzold, V.; Tripkovic, V.; Kleis, J.; Howalt, J. G.; Skulason, E.; Fernández, E.; Hvolbæk, B.; Jones, G.; Toftelund, A.; Falsig, H.; Björketun, M.; Studt, F.; Abild-Pedersen, F.; J, R.; Nørskov, J.; Bligaard, T. *Phys. Chem. Chem. Phys.* **2011**, *13*, 20760−20765.
(20) Deckert, A.; Brand, J.; Mak, C.; Koehler, B.; George, S. *J. Chem. Phys.* **1987**, *87*, 1936−1947.
(21) Loveless, B. T.; Buda, C.; Neurock, M.; Iglesia, E. *J. Am. Chem. Soc.* **2013**, *135*, 6107−6121.
(22) Gómez-Díaz, J.; López, N. *J. Phys. Chem. C* **2011**, *115*, 5667−5674.
(23) Kresse, G.; Furthmüller, J. *Comput. Mater. Sci.* **1996**, *6*, 15−50.
(24) Kresse, G.; Furthmüller, J. *Phys. Rev. B* **1996**, *54*, 11169−11186.
(25) Perdew, J. P.; Burke, K.; Ernzerhof, M. *Phys. Rev. Lett.* **1996**, *77*, 3865−3868.
(26) Blöchl, P. E. *Phys. Rev. B* **1994**, *50*, 17953−17979.
(27) Kresse, G.; Joubert, D. *Phys. Rev. B* **1999**, *59*, 1758−1775.
(28) Lide, D. *CRC Handbook of Chemistry and Physics*, 84th ed.; CRC Press: Boca Raton, FL, 2003−2004; pp 12(19−21).
(29) Clendenen, R.; Drickamer, H. *J. Phys. Chem. Solids* **1964**, *25*, 865−868.
(30) King, H.; Manchester, F. *J. Phys. F: Metal Phys.* **1978**, *8*, 15−26.
(31) Arblaster, J. *Platinum Met. Rev.* **1997**, *41*, 12−21.
(32) Monkhorst, H. J.; Pack, J. D. *Phys. Rev. B* **1976**, *13*, 5188−5192.
(33) Makov, G.; Payne, M. C. *Phys. Rev. B* **1995**, *51*, 4014−4022.
(34) Grimme, S. *J. Comput. Chem.* **2006**, *27*, 1787−1799.
(35) Bučko, T.; Hafner, J.; Lebegue, S.; Angyán, J. G. *J. Phys. Chem. A* **2010**, *114*, 11814−11824.
(36) Błoński, P.; López, N. *J. Phys. Chem. C* **2012**, *116*, 15484−15492.
(37) Almora-Barrios, N.; Carchini, G.; Błoński, P.; López, N. *J. Chem. Theory Comput.* **2014**, *10*, 5002−5009.
(38) Henkelman, G.; Jónsson, H. *J. Chem. Phys.* **2000**, *113*, 9978−9985.
(39) Henkelman, G.; Uberuaga, B. P.; Jónsson, H. *J. Chem. Phys.* **2000**, *113*, 9901−9904.

4.1. Paper I: Methanol on Cu and Ru

(40) Heyden, A.; Bell, A. T.; Keil, F. J. *J. Chem. Phys.* **2005**, *123*, 224101(1−14).
(41) Lin, S.; Ma, J.; Zhou, L.; Huang, C.; Xie, D.; Guo, H. *J. Phys. Chem. C* **2012**, *117*, 451−459.
(42) Abild-Pedersen, F.; Greeley, J.; Studt, F.; Rossmeisl, J.; Munter, T.; Moses, P. G.; Skulason, E.; Bligaard, T.; Nørskov, J. K. *Phys. Rev. Lett.* **2007**, *99*, 016105(1-4).
(43) Lim, K. H.; Chen, Z.-X.; Neyman, K. M.; Rösch, N. *J. Phys. Chem. B* **2006**, *110*, 14890−14897.
(44) Zuo, Z.-J.; Wang, L.; Han, P.-D.; Huang, W. *Int. J. Hydrogen Energy* **2014**, *39*, 1664−1679.
(45) Gu, X.-K.; Li, W.-X. *J. Phys. Chem. C* **2010**, *114*, 21539−21547.
(46) Lin, S.; Johnson, R. S.; Smith, G. K.; Xie, D.; Guo, H. *Phys. Chem. Chem. Phys.* **2011**, *13*, 9622−9631.
(47) Gazdzicki, P.; Jakob, P. *J. Phys. Chem. C* **2010**, *114*, 2655−2663.
(48) Chiu, C.-C.; Genest, A.; Rösch, N. *Top. Catal.* **2013**, *56*, 874−884.
(49) Jiang, R.; Guo, W.; Li, M.; Fu, D.; Shan, H. *J. Phys. Chem. C* **2009**, *113*, 4188−4197.
(50) Kozuch, S.; Shaik, S. *Acc. Chem. Res.* **2011**, *44*, 101−110.
(51) Davis, J.; Barteau, M. *Surf. Sci.* **1987**, *187*, 387−406.
(52) Zhang, C.; Hu, P. *J. Chem. Phys.* **2001**, *115*, 7182−7186.
(53) Rendulic, K. D.; Sexton, B. A. *J. Catal.* **1982**, *78*, 126−135.
(54) Revilla-Lopez, G.; Lopez, N. *Phys. Chem. Chem. Phys.* **2014**, *16*, 18933−18940.
(55) Loffreda, D.; Simon, D.; Sautet, P. *Surf. Sci.* **1999**, *425*, 68−80.
(56) Peterson, A. A.; Abild-Pedersen, F.; Studt, F.; Rossmeisl, J.; Nørskov, J. K. *Energy Environ. Sci.* **2010**, *3*, 1311−1315.
(57) Lin, S.; Ma, J.; Ye, X.; Xie, D.; Guo, H. *J. Phys. Chem. C* **2013**, *117*, 14667−14676.
(58) Zaffran, J.; Michel, C.; Auneau, F.; Delbecq, F.; Sautet, P. *ACS Catal.* **2014**, *4*, 464−468.
(59) Brönsted, J. *Chem. Rev.* **1928**, *5*, 231−338.
(60) Evans, M.; Polanyi, M. *Trans. Faraday Soc.* **1938**, *34*, 11−24.
(61) Pallassana, V.; Neurock, M. *J. Catal.* **2000**, *191*, 301−317.
(62) Nørskov, J.; Bligaard, T.; Logadottir, A.; Bahn, S.; Hansen, L. B.; Bollinger, M.; Bengaard, H.; Hammer, B.; Sljivancanin, Z.; Mavrikakis, M.; Xu, S. Y.; Dahl; Jacobsen, C. *J. Catal.* **2002**, *209*, 275−278.
(63) Bligaard, T.; Nørskov, J. K.; Dahl, S.; Matthiesen, J.; Christensen, C. H.; Sehested, J. *J. Catal.* **2004**, *224*, 206−217.
(64) Hammer, B. *Phys. Rev. Lett.* **1999**, *83*, 3681−3684.
(65) Loffreda, D.; Delbecq, F.; Vigné, F.; Sautet, P. *Angew. Chem. Int. Ed.* **2009**, *48*, 8978−8980.
(66) Marcus, R. A. *Angew. Chem. Int. Ed.* **1993**, *32*, 1111−1121.
(67) García-Mota, M.; Bridier, B.; Pérez-Ramírez, J.; López, N. *J. Catal.* **2010**, *273*, 92−102.

Paper II: EG and Glycerol on Cu and Ru

Submitted

Microkinetics of alcohol reforming for H_2 production from a FAIR density functional theory database

Qiang Li[1], Rodrigo García-Muelas[1], and Núria López* [1]

[1]Institute of Chemical Research of Catalonia (ICIQ), The Barcelona Institute of Science and Technology, Avgda. Països Catalans 16, 43007, Tarragona, Catalonia, Spain.

Abstract

The production of hydrogen from biomass under technologically relevant conditions is fundamental for a sustainable future. Here, we present a multiscale study of the available technologies based on a Density Functional Theory open database that allows the formulation of linear-scaling relationships and microkinetics. The database fulfills the FAIR criteria: findability, accessibility, interoperability and reusability. Moreover, it contains *ca.* 1000 transition states for the decomposition of C_2 alcohols on closed-packed Cu, Ru, Pd, and Pt surfaces. The microkinetic results for activity, selectivity towards H_2 and stability can be directly mapped to experiments, and the catalytic performance is controlled by various types of poisoning. Linear-scaling relationships provide valid quantitative results that allow the extrapolation to larger compounds like glycerol. Our database presents a robust roadmap to investigate the complexity of biomass transformations through the use of small fragments as surrogates when investigated under different reaction conditions.

*nlopez@iciq.es

4.2. Paper II: EG and Glycerol on Cu and Ru

The conversion of biomass to provide chemicals and energy vectors like H_2 is a fundamental challenge for a sustainable chemical industry based on renewable sources.[1,2] Particularly, to extract hydrogen from biomass, three reforming methodologies as well as direct decomposition (DD) have been put forward, Fig. 1 and Table S1. In the Steam Reforming (SR) process ethanol, sugars, and other oxygenated compounds react on metals and oxides with steam at temperatures around 400–1100 K to produce H_2, CO, CO_2, and CH_4.[3] Autothermal Reforming (ATR) constitutes an improvement over this process as small amounts of oxygen are added along with steam to produce raw syngas. ATR has been tested for ethanol[4] and glycerol[5] on noble metals. However, the high temperatures reached impose limitations to thermal stability related to poisoning. Compared with the former processes, Aqueous Phase Reforming (APR),[6–8] has the advantage of working at temperatures below 650 K, although the process is slow on clean metal surfaces. Only very recently, high turn-over frequencies have been achieved on single-atom catalysts Pt dispersed on α-MoC,[9] but long-term stability of this catalyst might be an issue.

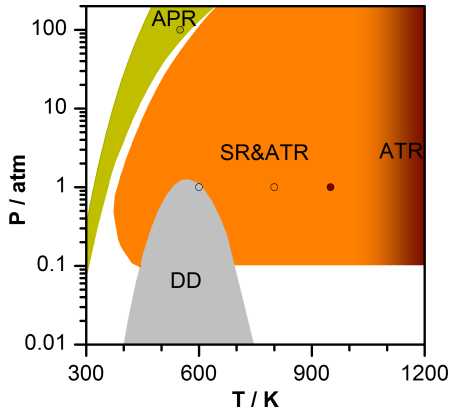

Figure 1: Phase diagram for the engineering conditions of hydrogen production by biomass reforming. Shaded areas correspond to Direct Decomposition (DD), Steam (SR), Autothermal (ATR), and Aqueous-Phase (APR) Reforming. The points correspond to the experimental conditions employed in the simulations and reported in Table S1.

A large number of potential catalysts have been experimentally screened for these reactions, a detailed summary can be found in Table S2, however large scale H_2 production is still costly. A better understanding of the reaction mechanisms and their role when searching a high performance catalyst is needed. Theoretical simulations based on Density Functional Theory (DFT) and micro-kinetic modeling (MK) hold the key for a rational design.[10] The most complete kinetic model on alcohol decomposition analyzed 50 species for ethanol on Pt and about 100 reactions in a correlative

global sensitivity analysis.[3] There, the errors inherent to DFT are correlated due to the similar nature of the oxygenated fragments on the metal surface, thus keeping the predictive value of MK based on DFT data. The complexity of the compounds derived from biomass has prevented an extensive study of full reaction mechanisms (C_6 sugar alcohol decomposition encompasses 10^5 reactions).[11]

As full mechanistic studies by DFT are impractical for large alcohols, divide-and-conquer strategies have been put forward, although their representativity has not been fully assessed. The decomposition of small alcohols including methanol, ethanol, ethylene glycol, glycerol, and other oxygenates has been extensively studied. Thermodynamics for the adsorption of intermediates can be obtained from multivariable scaling based on group additivity rules[12–14] inferred by taking the small molecules as surrogates. The rate coefficients are then extracted from kinetic-thermodynamic relationships[15–21] derived from key (calculated) decomposition steps either on a single metal, or a small group of alcohols. A summary of previous DFT calculations including up to C_3 alcohol decomposition on different metal surfaces is provided in Table S3.

However, the computed data is scarce (only partial networks have been mostly considered), has been generated with differences in the computational setups and thus the FAIR (findability, accessibility, interoperability and reusability) nature of the data is not ensured. This prevents the use of large analysis tools to systematize the available information. To diminish the errors, sparsity, and asymmetries in the computational data, we have developed a full open database that contains all the decomposition steps of C_1–C_2 alcohols: methanol, ethanol, ethylene glycol, together with the complementary steps from the water-gas shift reaction (WGSR) and oxygen adsorption. Initially, the database contains the results for the close packed surfaces, as they are most exposed in the catalytic preparations,[22] but can be extended to include lateral interactions, side reactions, other metals, alloys, undercoordinated sites and supports.[12,23,24] In that case, the linear-scaling relationships previously reported in the literature can also be incorporated.[12,23,24] The database has then been interrogated through microkinetic models to unravel whether the same reaction set is able to reproduce the different experimental behavior on the generation of hydrogen under different reaction conditions, and to predict the best conditions in the reforming of glycerol for one of the metals.

Results and Discussion

We have generated a database that can be retrieved from ioChem-BD,[25] where we have uploaded the computed 55 reaction intermediates and 215 reactions for the C_2 species on each metal.[26] They correspond to 100 dehydrogenations, 55 C–C, and 60 C–O breakings, related to 10, 24, and 21 intermediates in the ethane, ethanol, and ethylene glycol decomposition networks, respectively. Besides, we included 7 reactions to account for the water-gas shift, the O_2 decomposition, and our previous results on methanol.[27] The procedure to generate the full decomposition network of a given

4.2. Paper II: EG and Glycerol on Cu and Ru

species is presented in Figure 2. The species can undergo C–C, C–H, O–H, and C–O bond breakings, and each of these reaction products can further experience these four bond cleavages until the formation of the simplest decomposition products: C*, H*, and O*. The network expanded in Figures S2–S4, and includes lateral paths. The equations used to calculate the energies are shown in Section S1.1, and the computed data are summarized in Table S5-S6.

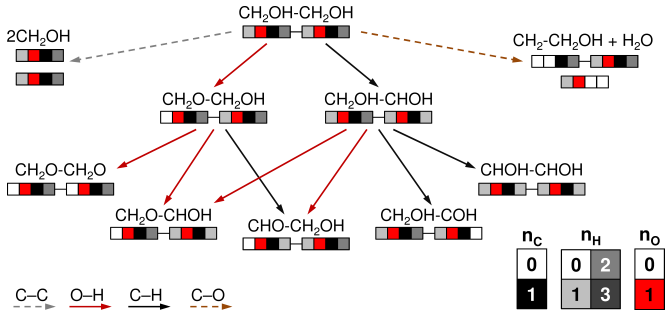

Figure 2: Reaction network for the decomposition of ethylene glycol. Each CH_xOH moiety is shown as a quadruplet whose colours are representative of the stoichiometry. The two central boxes are red (O) and black (C) while the first and last boxes indicate the number of hydrogen atoms attached to them, darker grey stands for higher H content. C–C, O–H, C–H, and C–O bond breakings are displayed as grey, red, black, and brown arrows respectively. C–C breakings lead to the lateral path of methanol decomposition, while C–O breakings lead to the lateral path of ethanol and water dehydrogenation. The full set of reactions is shown in Fig. S2-S4, the same labels have been used in the database.

Based on the reaction database, we tested the predictive power of three types of linear-scaling relationships (LSR): Brønsted-Evans-Polanyi (BEP), Initial-State and Final-State Scalings (ISS, FSS). The reactions were classified according to the type of bond breaking, as O–H, C–H, C–C, C–O, and C–OH. For the O–H bond breaking, the BEP slopes, α, are between 0.07 and 0.24 (Section S3.1 and Table S7). This indicates that the transition states should resemble the initial states.[19] Indeed, the ISS have much better statistics (R^2 and MAE) than the BEP or FSS. For C–H, C–C, C–O, and C–OH bond breakings, the BEP slopes, α, are larger than 0.50, and the FSS are more suitable for the prediction of the transition states energies. The best LSR are presented in Fig. 3 (see Table S8 for the statistics). In the ISS or FSS-relationships the slope, α, was forced to be one. This leads to a simpler yet representative form for the equations, as (i) it eliminates the α regression term avoiding overfitting, (ii) the LSR equations are independent of the energy reference used, see Section S3.1.1. Both conditions are fundamental to use the LSR to predict the activation energies of larger polyalcohols. Cu follows a different behavior than Ru, Pd, and Pt, and therefore it was

treated independently in Fig. 3.

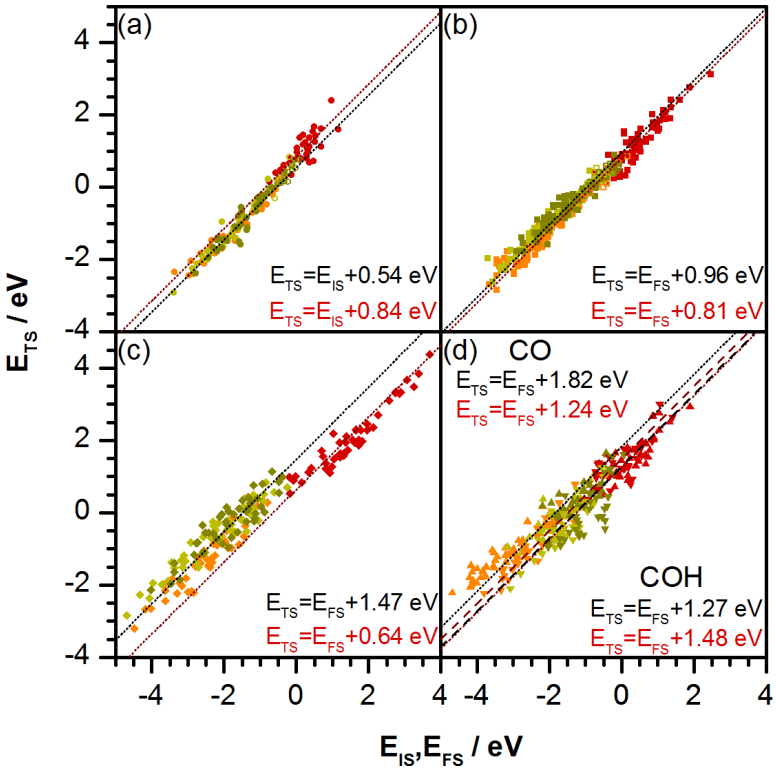

Figure 3: Best Linear Scaling Relationships (LSR) (a) Initial state scaling relationships for O–H bond breaking on Ru, Pd, and Pt (black dotted line) and Cu (red line). Final state scalings for (b) C–H, (c) C–C, and (d) C–O/C–OH bond breakings. The α (slope) values in the LSRs were set to 1.00. Transition states calculated with explicit water molecules and/or the implicit solvation model for methanol are taken from ref. [28] and included as empty symbols showing that the LSRs also hold when solvation is considered.

The complexity of the reaction network can only be described by combining the energy profile with a microkinetic analysis. In Fig. 4 (a) the decomposition of ethanol on Pd is taken as example. To generate this energy profile the transition state with lowest barrier is selected for each intermediate. The rest are only plotted in the figure if their barriers are up to 0.30 eV higher than this reference state. However, in the microkinetic modeling all 246 steps are considered simultaneously. The interpretation of such a complex profile is not straightforward. Microkinetics on the DFT results show that a complex reaction network, as the one shown in Fig. 4 (a), may exhibit several

4.2. Paper II: EG and Glycerol on Cu and Ru

pseudo-stationary states,[29] Fig. 4 (b)-(c) (Supplementary Information Section S3.2). These pseudo-stationary states were identified to obtain the coverages and hydrogen production reported as crosses in Fig. 5 (a-b) and (d-e). Following with the example, in the early stages ($t < 10^0$ s) of ethanol decomposition, Pd dehydrogenates the alcohol moiety, building up a layer of CO and CH poisons, Fig 4 (b). From $t = 10^1 - 10^4$ s, C–O breaking starts to be kinetically relevant, leaving CCH_3 coverages of 30% while the rest is CO (66%). In the meanwhile, most of the CH is consumed. The concentration of CO also increases and reaches a maximum at $t = 10^4$ s (roughly 3 hours), while the desorption rate of H_2 stabilizes in a plateau value around $1.4 * 10^{-6}$ s^{-1}. The surface behavior for $t = 10^4..10^6$ s would be the most representative pseudo-stationary state. After 60 days, the desorption rate of hydrogen will still be significant (30% the initial plateau value) and CCH_2 and CCH_3 will cover most of the surface. The ultimate steady state will be reached at $t = 6.3 * 10^7$ s (two years) where the desorption rate of H_2 is 1% of the previous plateau value. The observed times are only qualitatively meaningful as they have been obtained in a model with no lateral interactions. When those are included, the pseudo-stationary states are the same, both in terms of main products and poisons, but they are reached at shorter reaction times, an example is shown in Figure S9. The expandable nature of our database would allow the incorporation of this type of effects, although this discussion is beyond the scope of the present work. Long equilibration times (in the order of hours) have experimentally been reported for APR of ethylene glycol on Pt.[8] The analysis can then be extended to all metals under all the technical conditions of the reforming. The H_2 production can be found in Fig. 5 (a-b) marked with crosses, along the main surface species, (d-e). The analysis is based on the relevant stationary state reached before 3 h.

The decomposition of ethanol and ethylene glycol on Cu leaves CCO^* as the most abundant intermediate, which covers 97% and 92% of the surface and leave a small fraction of empty sites, 2.4% and 0.6%. For the reforming technologies, the surface coverage of O and OH is very high, adding up to 73-99.9%, thus lowering the productivity of the surface towards H_2. Special care should be taken as for oxygen coverages higher than 0.75 ML suboxides might appear,[30] thus compromising the representability of the metal-only model. Acetaldehyde is the main product of ethanol reforming, while ethylene glycol yields a mixture of CH_2O, CO, and glyoxal. In ATR, the high oxygen coverage strips the hydrogen to generate water and, therefore, no H_2 is produced.

In the ethanol direct decomposition on Ru (the main on-surface species are CCH (68%), CO (16%), and CCO (7%). The main desorption products are CO and H_2, close to the stoichiometric ratio of 2:3. For ethylene glycol C–C bonds can easily break and the surface is strongly poisoned by CO (98%) with minor CCO species. ATR is a very inefficient process on Ru and shows the lowest hydrogen production rate: less than 10^{-10} s^{-1}, as the high O^* coverage consumes all hydrogen. Oxygen is also the most abundant on-surface species for the SR and APR of ethanol on Ru. In the steam reforming of ethanol, CO and CH_3CHO are produced at a 2.3 ratio, but the

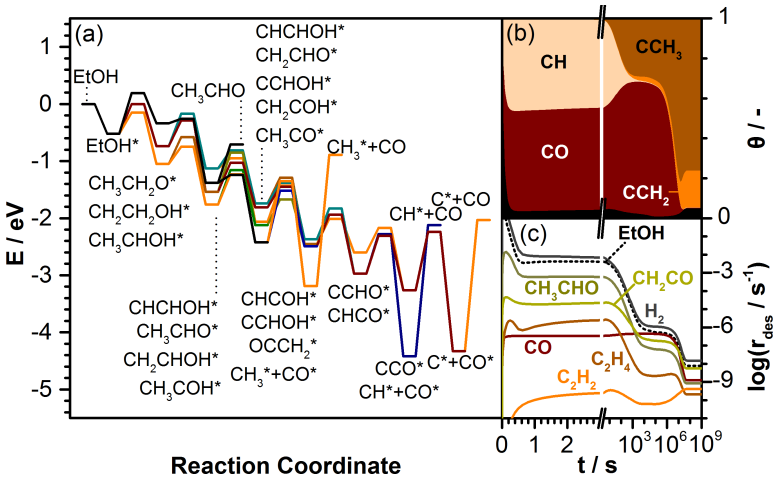

Figure 4: (a) Simplified DFT-Reaction profile for ethanol decomposition on Pd(111) only considering transition states within 0.30 eV energy windows for each TS. MK-DFT: (b) Surface coverages during the decomposition of ethanol on Pd(111) as a function of time at the reaction conditions: $T = 600$ K, $P_{ethanol} = 1$ atm. Main intermediates are labelled, while the black area stands for the small intermediate fractions together with the empty sites. (c) Desorption rate of ethanol and several products as a function of time.

decomposition proceeds slowly and the desorption rate of H_2 is very low. In contrast, CO is the most abundant intermediate for ethylene glycol in SR and APR and the main product along with traces of CO_2. The desorption rate of hydrogen is relatively high for SR.

The direct decomposition of ethylene glycol on Pd produces CO and traces of $HOCH_2CHO$ and other oxygenates. The activity of Pd is low for ATR as the surface is highly covered by O*, which reacts with most of the hydrogen to form water, leading to almost no hydrogen production. The main products from the ATR of ethanol are CO_2 and CH_3CHO in a 8:5 proportion, while ethylene glycol produces glycolaldehyde. In the SR of ethanol and ethylene glycol, the main product is CO, with small traces of C_2H_2 and CH_3CHO. CO accumulates since the high dissociation barrier of water limits the efficiency of the WGSR. On the ethanol steam reforming, three stable carbonaceous species are formed as poisons: CCH_3 (27%), CCH_2 (32%), and CCH (28%), while CO is the main poison for ethylene glycol. In APR, the main on-surface species are CO (65%) and CCH_3 (28%) for ethanol and CO for ethylene glycol. The carbonaceous fragments tend to accumulate rather than desorb.

In the direct decomposition of ethanol on Pt(111), CO is the main desorption product and it is also present on the surface (14%) along CH (42%), CCH_2 (6%), and CCH_3 (37%). CO is the only poison for ethylene glycol, and it is produced along $HOCH_2CHO$

4.2. Paper II: EG and Glycerol on Cu and Ru

in a 2:1 proportion. The ATR has the highest H_2 productivity on Pt compared with any other metal, as the CO poisoning is efficiently removed by oxidation. The H_2:alcohol ratios are 2.8 and 2.9, respectively. The main surface species are all carbonaceous: C (10%), CH (38%), CCH_2 (29%), and CCH_3 (20%), for ethanol and only CH (23%) and CO (66%) for ethylene glycol. The fraction of empty sites is moderate 0.06% and high 3.80% for the mono and di-alcohol. In the SR, the main desorption products are CO and traces of C_2H_4 for ethanol, and glyoxal for ethylene glycol. For ethanol, most of the on-surface species are carbonaceous: CCH_2 (80%), CH (4%), and C (5%), while for ethylene glycol, CO is the main poison. Without CO oxidation, the H_2 production is slower for SR and APR than for ATR (up to 7 orders of magnitude). Nonetheless, a small fraction of water undergoes the WGSR and reduces the CO poisoning. The H_2 productivity is much lower for the APR than for SR of ethanol. For ethanol, CO is the main desorption product, and it is present on the surface along with CH, roughly in 1:1 amounts. Finally, $HOCH_2CHO$ is produced along with CO in the APR of ethylene glycol, but CO is still the main surface intermediate.

To assess the robustness of the linear-scaling relationships in reproducing the full MK-DFT data, we built two different microkinetic models, which differ in the methodology followed to obtain the energies: (i) MK-LSR: The intermediates are taken from DFT, while the activation energies were obtained from the optimum LSR. (ii) MK-L1O: The activation energies were obtained from LSR but employing a Leave-One-Out procedure for the Ru, Pd and Pt triad. These results are shown as bars and dots in Fig. 5 (a-c), respectively.

The general performance of the different models can be found in Fig. 5 (a-b). The agreement between the simplified methodologies and the full DFT results is thus remarkable, particularly as the relative ordering between the different metals is kept and semi-quantitative values can be retrieved. The deviations are within one-two orders of magnitude (similar to the limits identified by Vlachos)[3] for three situations: ATR on Pt and the ethanol SR-Ru and APR-Ru for which higher activities for which the real value is higher than the one obtained from MK-LSR and MK-L1O. Deviations towards higher activities in the MK-LSR model are found only for Cu in the SR of both ethanol and ethylene glycol and to a lesser extent for APR. The production rate of hydrogen is also well reproduced with the MK-L1O methodology, showing differences lower than two orders of magnitude with respect to the MK-DFT results. The direct decomposition of ethylene glycol on Ru is the only process where MK-L1O deviates. The origin of this behavior is that the average activation energies for C–C breakings on Pd and Pt are 0.43 eV higher than the ones from Ru, so the MK-L1O procedure represents a Ru surface that is much less active than for MK-DFT and MK-LSR. This deviation does not appear when taking Pt and Ru or Pd and Ru as sources for the models.

The microkinetic data can be then compared to experimental trends. For instance, the activity for ethylene glycol APR on silica-supported metal catalyst follows the order

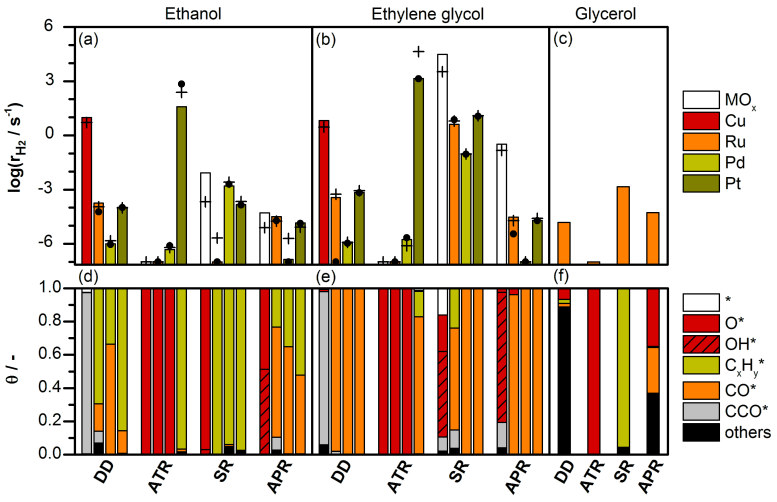

Figure 5: Hydrogen production rate during the direct decomposition, and reforming: ATR, SR, and APR of (a) ethanol and (b) ethylene glycol on Cu, Ru, Pd, and Pt. (c) corresponding values for glycerol on Ru. The crosses show the result from MK-DFT, columns from MK-LSR, and dots from the MK-L1O method. White columns stand for configurations where the oxygen content could change the existing catalytic phase. The surface coverages obtained with MK-DFT are shown on panels (d-f).

Ru>Pt>Pd.[8] This order is well reproduced for MK-LSR and MK-L1O, while the MK-DFT reports Pt>Ru>Pd. This shows that the rules obtained through LSR might avoid accurate convergence issues in transition state searching, thus providing a slightly more robust framework. Still, intrisic DFT errors would require the improvement of the functionals. On the other hand, the production rate of CO_2 follows the order Pt>Ru>Pd.[8] This order is obtained from all three microkinetic models considering together the desorption rates of CO and CO_2.

A detailed comparison to the available literature regarding kinetic parameters (rates, apparent activation energies and reaction orders) has been attempted. Unfortunately the set of experiments is sparse and thus particularly, there is no clear experimental set comparing those similar particle sizes, supports and external conditions for the different materials. In addition, when the catalytic tests are presented together with detailed kinetic analysis, the characterization of the samples before and after reaction is lacking. This is a major handicap when attempting to formulate a robust framework for comparison. However, Table /reft.exp2 shows a summary of the results in the literature. The microkinetic model has been rerun with the experimental conditions reported in Ref. [22,31–33] The systems have been equilibrated to the pseudo-stationary point at t=3h, then a perturbation, either in the temperature or the pressure, has been applied.[34] The results show that the reaction orders and activation energies are properly

4.2. Paper II: EG and Glycerol on Cu and Ru

reproduced except for when a relevant role of the support can be anticipated, CeO_2. The activation barriers show a larger deviation but are qualitative in the same range.

Table 1: Experimental apparent activation energies, E_a^{app} (in eV), and reaction orders with respect to ethanol and water, n_a and n_w (dimensionless), for the steam reforming of ethanol. The experimental results (indicated by "exp") and the calculations are performed under the same conditions. The conditions for temperature, T (in K), and partial pressures of ethanol and water, P_a and P_w (in atm), are also shown.

Ref.	Metal	T	P_a	P_w	n_a^{exp}	n_a	n_w^{exp}	n_w	$E_a^{app,exp}$	E_a^{app}
31	Ru/γ-Al_2O_3	923	0.042	0.420	1.0	1.0	0.0	0.0	0.99	0.66
22	Pd/γ-Al_2O_3	575	0.125	0.375	-	0.9	-	0.0	0.49	0.54
22	Pt/γ-Al_2O_3	575	0.125	0.375	-	1.1	-	0.0	0.59	0.71
32	Pt/γ-Al_2O_3	575	0.125	0.375	0.8	1.1	-	0.0	0.48	0.71
33	Pt/CeO_2	575	0.005	0.015	0.5	1.0	0.0	0.0	0.19	0.69

Finally, the MK-LSR methodology was used to predict the reactivity for glycerol on Ru as, experimentally, it has been a better catalyst in steam reforming than Pd or Pt.[35] The full decomposition network comprises 349 on-surface species and 1944 reaction steps. The MK-LSR was applied as follows: (i) the energies for the C_3 intermediates were obtained by DFT, (ii) with these energies the ISS and FSS from Fig. 3 were applied (Table S12) and employed in the MK setup. The coverages and hydrogen production can be seen in Fig. 5. The results show that most suitable technology to produce hydrogen from glycerol is SR, as APR is considerably less active. The activity for the glycerol steam reforming is 3.5 orders of magnitude smaller than that of ethylene glycol. This observation agrees with previous experimental results on other catalysts. H_2 production in the APR of ethylene glycol is higher than for glycerol on Pt[6] and on Raney catalyst ($Ni_{37}Sn_3$).[7] The longer the alcohol carbon chain (up to C_6), the lower the selectivity towards H_2 and the higher to hydrocarbons and other compounds.[6,7,36] This is correctly reproduced by the simulations as we obtained 84% of selectivity towards H_2 for ethylene glycol and 72% for glycerol with the MK-LSR scheme.

We would like to summarize our present results to highlight their importance in further catalytic design. First of all, setting up a FAIR database accessible to other researchers, allowing its extension to consider lateral interactions, low-coordinated sites, other metals, and supports within the same computational framework. Second, the common nature of many elementary steps that can then easily be transferred, inherited, and expanded to investigate other reactions in the same metals, thus preventing repetitive computations. Third, the completeness in the decomposition path ensures that no intermediates/products are discarded as has been done in the literature, where many times only the selective path was identified, this would allow effective machine learning implementations as those in Ref. [37]. We hope that the standard set by the present approach is adopted by other practitioners in the field and accelerates the comparison of the catalytic properties of different materials and provides robust design

guidelines from a accumulated databases.

Conclusions

We have investigated the complex reaction networks arising from the decomposition of ethanol and ethylene glycol on Cu, Ru, Pd, and Pt, through a multiscale method encompassing microkinetic modelling on the energies obtained through Density Functional Theory. To this end an open database has been set up to provide the most robust sets of Linear Scaling Relationships that allow the evaluation of different catalysts. With this scheme, activity, selectivity towards H_2 and stability under a variety of technical reforming conditions have been derived and compared to experiments. The present work paves the way towards an open, accessible, interoperable, and reusable database for simulations of catalytic properties that can speed up the identification of better performing catalysts in the transformation of biomass compounds.

Methods

The Density Functional Theory calculations were performed with the Vienna Ab-initio Simulation Package (VASP).[38,39] The functional of choice was PBE[40] and the van der Waals (vdW) contributions were obtained through the DFT-D2 method,[41,42] with our reparameterization of C_6 coefficients.[43] This setup has been proven to predict the experimental adsorption energies of several mono- and poly-alcohols accurately.[14] The inner electrons were represented by Projector-Augmented Wave pseudopotentials (PAW)[44,45] and the monoelectronic states were expanded in plane waves with a kinetic energy cutoff of 450 eV. Metal surfaces were modeled by a four-layers slab and at least $p(3 \times 3)$ supercells, where the two uppermost layers were fully relaxed and the rest fixed to the bulk distances. In the surface calculations, the Brillouin zone was sampled by a Γ-centred k-points mesh from the Monkhorst-Pack method,[46] and the k-point samplings were denser than 30 $Å^{-1}$. The vacuum between the slabs was at least 13 Å, and the adsorbates were placed only on one side of the slab and thus a dipole correction was applied to remove spurious contributions arising from this asymmetry.[47] The molecules were placed in a cubic box of 20 Å sides. Transition states were located by a combination of the Nudged Elastic Band and the Improved Dimer Methods.[48–50] In all cases, the nature of the saddle points was assessed by the diagonalization of the numerical Hessian generated by 0.02 Å displacements for each coordinate. All TS structures have a single imaginary frequency. In all cases the optimization thresholds were 10^{-5} eV and 0.02 eV/Å for electronic and ionic relaxations, respectively. The decomposition reactions can be used to explore all the experimental conditions including water and oxygen effects as: (i) Water gas-shift related reactions are explicitly included in the reaction pool; (ii) O-assisted breaking C-H require higher energies than the C-H counterparts by 0.60-1.00 eV as shown in Table S6; (iii) Proton abstraction in alcohols

4.2. Paper II: EG and Glycerol on Cu and Ru

by oxygen molecules is barrierless[28] on metals. In addition, the formulations of the catalyst are typically supported on carriers with acid/base characteristics[8] thus, when compared to experiments with active supports (Table 1), these reactions have been considered to occur on the support and to be barrierless. Finally, as for the water-assisted reactions two groups can be made: on unreactive metals the LSR are kept as shown by explicit/implicit continuum models,[28] Supplementary Information Figure S7; for reactive metals (Ru) hydroxyl groups are present render proton abstraction from the alcohols barrierless.[28,51]

The microkinetic model explores hydrogen production on the closed packed surfaces of Cu, Ru, Pd, and Pt under four reaction conditions: DD at constant temperature, ATR, SR, and APR, which are presented in Fig. 1 and Table S1. The reason to chose the (111) surface ((0001) in the case of Ru) is because it presents the lowest energy surface and thus is more represented in the equilibrium structure of the active metal nanoparticles. Moreover, most of the catalyst preparation results in active nanoparticles larger than 5 nm in diameter.[22] In addition, choosing (111) presents the advantage that the cells are smaller than for other open surfaces, are easier to compare to previous computational data. Since our database is expandable, adding the results from low-coordinated sites, alloys, lateral effects, and carriers would be possible.[23,24] The procedure, detailed in the Supplementary Information Section S1.2, can be summarized as follows: A stream containing the alcohol, water, and oxygen in variable proportions was fed into an isothermal differential reactor. The reactor operates in transient state and the initial coverages correspond to a clean surface, while the temperatures and pressures resemble typical experimental conditions. The adsorption rates were obtained from the Knudsen equation,[34] the rate coefficients from Transition State Theory,[34] and the activation energies from DFT calculations. The mass balance for each species "i" comes from the sum of rates "j" in which species "i" participates. Site balance equation was also included. The system of ordinary differential equations was solved in Maple.[52] A reaction was considered to reach a relevant stationary state when the surface concentrations and reaction rates varied less than 0.01%/s.

References

[1] Corma, A., Iborra, S., and Velty, A. *Chem. Rev.* **107**(6), 2411–2502 (2007).

[2] Guo, N., Caratzoulas, S., Doren, D. J., Sandler, S. I., and Vlachos, D. G. *Energy Environ. Sci.* **5**(5), 6703–6716 (2012).

[3] Sutton, J. E., Guo, W., Katsoulakis, M. A., and Vlachos, D. G. *Nat. Chem.* **8**, 331–337 (2016).

[4] Deluga, G. A., Salge, J. R., Schmidt, L. D., and Verykios, X. E. *Science* **303**(5660), 993–997 (2004).

[5] Dauenhauer, P. J., Salge, J. R., and Schmidt, L. D. *J. Catal.* **244**(2), 238–247 (2006).

[6] Cortright, R. D., Davda, R. R., and Dumesic, J. A. *Nature* **418**(6901), 964–967 (2002).

[7] Huber, G. W., Shabaker, J. W., and Dumesic, J. A. *Science* **300**(5628), 2075–2077 (2003).

[8] Davda, R. R., Shabaker, J. W., Huber, G. W., Cortright, R. D., and Dumesic, J. A. *Appl. Catal. B* **43**(1), 13–26 (2003).

[9] Lin, L., Zhou, W., Gao, R., Yao, S., Zhang, X., Xu, W., Zheng, S., Jiang, Z., Yu, Q., Li, Y.-W., Shi, C., Wen, X.-D., and Ma, D. *Nature* **544**(7648), 80–83 (2017).

[10] Nørskov, J. K., Bligaard, T., Rossmeisl, J., and Christensen, C. H. *Nat. Chem.* **1**(1), 37–46 (2009).

[11] Sutton, J. E. and Vlachos, D. G. *Chem. Eng. Sci.* **121**, 190–199 (2015).

[12] Abild-Pedersen, F., Greeley, J., Studt, F., Rossmeisl, J., Munter, T. R., Moses, P. G., Skúlason, E., Bligaard, T., and Nørskov, J. K. *Phys. Rev. Lett.* **99**(1), 016105 (2007).

[13] Salciccioli, M., Chen, Y., and Vlachos, D. G. *J. Phys. Chem. C* **114**(47), 20155–20166 (2010).

[14] García-Muelas, R. and López, N. *J. Phys. Chem. C* **118**(31), 17531–17537 (2014).

[15] Ferrin, P., Simonetti, D., Kandoi, S., Kunkes, E., Dumesic, J. A., Nørskov, J. K., and Mavrikakis, M. *J. Am. Chem. Soc.* **131**(16), 5809–5815 (2009).

[16] Wang, S., Petzold, V., Tripkovic, V., Kleis, J., Howalt, J. G., Skúlason, E., Fernández, E. M., Hvolbæk, B., Jones, G., Toftelund, A., Falsig H, B. M., Studt, F., Abild-Pedersen, F., Rossmeisl, J., Nørskov, J. K., and Bligaard, T. *Phys. Chem. Chem. Phys.* **13**(46), 20760–20765 (2011).

[17] Wang, S., Temel, B., Shen, J., Jones, G., Grabow, L. C., Studt, F., Bligaard, T., Abild-Pedersen, F., Christensen, C. H., and Nørskov, J. K. *Catal. Lett.* **141**(3), 370–373 (2011).

[18] Wang, S., Vorotnikov, V., Sutton, J. E., and Vlachos, D. G. *ACS Catal.* **4**(2), 604–612 (2014).

[19] Zaffran, J., Michel, C., Auneau, F., Delbecq, F., and Sautet, P. *ACS Catal.* **4**(2), 464–468 (2014).

[20] Rangarajan, S., Brydon, R. R. O., Bhan, A., and Daoutidis, P. *Green Chem.* **16**(2), 813–823 (2014).

[21] Zaffran, J., Michel, C., Delbecq, F., and Sautet, P. *J. Phys. Chem. C* **119**(23), 12988–12998 (2015).

[22] Basagiannis, A. C., Panagiotopoulou, P., and Verykios, X. E. *Top. Catal.* **51**(1-4), 2–12 (2008).

[23] Calle-Vallejo, F., Loffreda, D., Koper, M. T. M., and Sautet, P. *Nat. Chem.* **7**(5), 403–410 (2015).

[24] Calle-Vallejo, F., Tymoczko, J., Colic, V., Vu, Q. H., Pohl, M. D., Morgenstern, K., Loffreda, D., Sautet, P., Schuhmann, W., and Bandarenka, A. S. *Science* **350**(6257), 185–189 (2015).

[25] Álvarez-Moreno, M., De Graaf, C., López, N., Maseras, F., Poblet, J. M., and Bo, C. *J. Chem. Inf. Model.* **55**(1), 95–103 (2014).

[26] Li, Q., García-Muelas, R., and López, N.
http://dx.doi.org/10.19061/iochem-bd-1-37
Embargoed link for rewievers:
https://iochem-bd.iciq.es/browse/review-collection/100/2347/50e1ec03e8af71571cd3f664.

[27] García-Muelas, R., Li, Q., and López, N. *ACS Catal.* **5**(2), 1027–1036 (2015).

[28] Garcia-Ratés, M., García-Muelas, R., and López, N. *J. Phys. Chem. C* **121**, 13803–13809 (2017).

[29] Jørgensen, M. and Grönbeck, H. *ACS Catal.* **6**(10), 6730–6738 (2016).

[30] Gattinoni, C. and Michaelides, A. *Surf. Sci. Rep.* **70**(3), 424–447 (2015).

[31] Vaidya, P. D. and Rodrigues, A. E. *Ind. Eng. Chem. Res.* **45**(19), 6614–6618 (2006).

[32] Sutton, J. E., Panagiotopoulou, P., Verykios, X. E., and Vlachos, D. G. *J. Phys. Chem. C* **117**(9), 4691–4706 (2013).

[33] Ciambelli, P., Palma, V., and Ruggiero, A. *Appl. Catal., B* **96**(1), 190–197 (2010).

[34] Chorkendorff, I. and Niemantsverdriet, J. W. *Concepts of modern catalysis and kinetics*. John Wiley & Sons, (2006).

[35] Hirai, T., Ikenaga, N.-o., Miyake, T., and Suzuki, T. *Energy & Fuels* **19**(4), 1761–1762 (2005).

[36] Huber, G. W., Cortright, R. D., and Dumesic, J. A. *Angew. Chem. Int. Ed.* **43**(12), 1549–1551 (2004).

[37] Ulissi, Z. W., Medford, A. J., Bligaard, T., and Nørskov, J. K. *Nat. Comm.* **8**, 14621 (2017).

[38] Kresse, G. and Furthmüller, J. *Comput. Mater. Sci.* **6**(1), 15–50 (1996).

[39] Kresse, G. and Furthmüller, J. *Phys. Rev. B* **54**(16), 11169–11186 (1996).

[40] Perdew, J. P., Burke, K., and Ernzerhof, M. *Phys. Rev. Lett.* **77**(18), 3865–3868 (1996).

[41] Grimme, S. *J. Comput. Chem.* **27**(15), 1787–1799 (2006).

[42] Bučko, T., Hafner, J., Lebegue, S., and Angyán, J. G. *J. Phys. Chem. A* **114**(43), 11814–11824 (2010).

[43] Almora-Barrios, N., Carchini, G., Błoński, P., and López, N. *J. Chem. Theory Comput.* **10**(11), 5002–5009 (2014).

[44] Blöchl, P. E. *Phys. Rev. B* **50**(24), 17953–17979 (1994).

[45] Kresse, G. and Joubert, D. *Phys. Rev. B* **59**(3), 1758–1775 (1999).

[46] Monkhorst, H. J. and Pack, J. D. *Phys. Rev. B* **13**(12), 5188–5192 (1976).

[47] Makov, G. and Payne, M. C. *Phys. Rev. B* **51**, 4014–4022 (1995).

[48] Henkelman, G. and Jónsson, H. *J. Chem. Phys.* **113**(22), 9978–9985 (2000).

[49] Henkelman, G., Uberuaga, B. P., and Jónsson, H. *J. Chem. Phys.* **113**(22), 9901–9904 (2000).

[50] Heyden, A., Bell, A. T., and Keil, F. J. *J. Chem. Phys.* **123**(22), 224101(1–14) (2005).

[51] Bellarosa, L., García-Muelas, R., Revilla-López, G., and Lopez, N. *ACS Cent. Sci.* **2**(2), 109–116 (2016).

[52] Waterloo Maple Inc. Waterloo, Ontario.

4.2. Paper II: EG and Glycerol on Cu and Ru

425 **Acknowledgements**

426 The authors thank the ERC-2010-StG-258406 Bio2chem-d, ERC-2015-PoC-680900
427 BigData4Cat, MINECO CTQ2012-33826, and MINECO CTQ2015-68770-R projects
428 for financial support. The authors gratefully acknowledge the generous computing time
429 and assistance provided by the Barcelona Supercomputing Center and the Spanish
430 Supercomputing Network. The authors thank Moisés Álvarez-Moreno for technical
431 support in the ioChem-BD database management.

432 **Author contributions**

433 Q.L. and R.G.-M. performed the numerical calculations and contributed equaly to this
434 work. N.L. supervised the project. All authors contributed to analyze the data and to
435 write the manuscript.

436 **Competing financial interest**

437 The authors declare no competing financial interests.

438 **Corresponding author**

439 Correspondence to: Núria López. nlopez@iciq.es

440 **Supplementary Information**

441 Derivation of the equations, review of previous theoretical and experimental studies,
442 detailed reaction networks, adsorption energies for all intermediates on Cu, Ru, Pd, and
443 Pt, reaction and activation energies for all reactions, analysis of the energy profiles,
444 scalings and analysis of stationary states. The structures of all intermediates and
445 transition states can be downloaded from DOI: 10.19061/iochem-bd-1-37.[26]

Paper III: LA conversion to GVL

Published in *Green Chem.*, 2017, **19**, 2361-2370

Green Chemistry

PAPER

View Article Online
View Journal

Cite this: DOI: 10.1039/c6gc02586b

Interfacial acidity in ligand-modified ruthenium nanoparticles boosts the hydrogenation of levulinic acid to gamma-valerolactone†

Davide Albani,‡[a] Qiang Li,‡[b] Gianvito Vilé,[a] Sharon Mitchell,[a] Neyvis Almora-Barrios,[b] Peter T. Witte,[c] Núria López*[b] and Javier Pérez-Ramírez*[a]

Gamma-valerolactone (GVL), a versatile renewable compound listed among the top 10 most promising platform chemicals by the US Department of Energy, is produced *via* hydrogenation of levulinic acid (LA). The traditional high-loading ruthenium-on-carbon catalyst (5 wt% Ru) employed for this transformation suffers from low metal utilisation and poor resistance to deactivation due to the formation of RuO_x species. Aiming at an improved catalyst design, we have prepared ruthenium nanoparticles modified with the water-soluble hexadecyl(2-hydroxyethyl)dimethylammonium dihydrogen phosphate (HHDMA) ligand and supported on $TiSi_2O_6$. The hybrid catalyst has been characterised by ICP-OES, elemental analysis, TGA, DRIFTS, H_2-TPR, STEM, EDX, ^{31}P and ^{13}C MAS-NMR, and XPS. When evaluated in the continuous-flow hydrogenation of LA, the Ru-HHDMA/$TiSi_2O_6$ catalyst (0.24 wt% Ru) displays a fourfold higher reaction rate than the state-of-the-art Ru/C catalyst, while maintaining 100% selectivity to GVL and no sign of deactivation after 15 hours on stream. An in-depth molecular analysis by Density Functional Theory demonstrates that the intrinsic acidic properties at the ligand–metal interface under reaction conditions ensure that the less energy demanding path is followed. The reaction does not obey the expected cascade mechanism and intercalates hydrogenation steps, hydroxyl/water eliminations, and ring closings to ensure high selectivity. Moreover, the interfacial acidity increases the robustness of the material against ruthenium oxide formation. These results provide valuable improvements for the sustainable production of GLV and insights for the rationalisation of the exceptional selectivity of Ru-based catalysts.

Received 15th September 2016,
Accepted 3rd October 2016

DOI: 10.1039/c6gc02586b

www.rsc.org/greenchem

Introduction

The necessity of more sustainable products and processes has led to the use of new methodologies which result in a low carbon footprint. This implies, in line with the 12 principles of green chemistry,[1,2] the utilisation of biomass-derived reactive substrates, non-toxic solvents (*e.g.*, water), sustainable heterogeneous catalysts based on low precious metal loadings, and continuous-flow processes.[3] Gamma-valerolactone (GVL), for example, has been recognised by the US Department of Energy as an important bio-derived platform chemical.[4–8] This compound can be used for the manufacture of a number of important commodities such as transportation fuels, polymer intermediates, pharmaceuticals, food ingredients, or it can be directly applied as a renewable organic solvent. Gamma-valerolactone is synthesised from levulinic acid *via* a two-step process involving selective hydrogenation and intramolecular dehydration.[8,9] Ruthenium-based catalysts are widely applied for this reaction,[10] due to the intrinsic ability of this metal to selectively hydrogenate the C=O bond without reducing other unsaturated functionalities.[11] Nonetheless, conventional catalysts, such as 5 wt% Ru/C, have some drawbacks, including the high metal content, possible metal leaching in water-based solvents, and oxidation to RuO_2 that can lead to severe activity losses.[12,13] In order to increase stability, some authors have proposed the utilisation of RuRe, RuSn, and RuPd alloys.[14–16] Similarly, it has been postulated that acidic moieties surrounding the catalytically active surface could be beneficial to reduce the extent of deactivation.[17–20]

Alternative active phases to Ru, such as Cu,[21] Pt,[22] Ni,[23], Pd,[24] Ir,[24] and Au,[25] are much less selective, yielding 2-methyl-

[a]*Institute for Chemical and Bioengineering, Department of Chemistry and Applied Biosciences, ETH Zurich, Vladimir-Prelog-Weg 1, 8093 Zurich, Switzerland. E-mail: jpr@chem.ethz.ch*
[b]*Institute of Chemical Research of Catalonia (ICIQ), Av. Països Catalans 16, 43007 Tarragona, Spain. E-mail: nlopez@iciq.es*
[c]*BASF Nederland BV, Strijkviertel 67, 3454PK De Meern, The Netherlands*
†Electronic supplementary information (ESI) available: Additional characterization of the catalysts, reaction mechanism, and calculated properties of Ru (0001) and Ru(0001) + HHDMA. See DOI: 10.1039/c6gc02586b and DOI: 10.19061/iochem-bd-1-15
‡These authors contributed equally to this work.

4.3. Paper III: LA conversion to GVL

tetrahydrofuran and 1,4-pentandiol, and/or require harsher reaction conditions to reach the same conversion level. Applications of nanostructured hybrid materials in catalysis are continuously expanding due to the unique properties that can arise from the interaction of the organic and inorganic components.[26–28] In fact, their chemical versatility makes these materials attractive for the possibility to combine the advantages of heterogeneous catalysts (*e.g.*, easy separation of the catalyst from the reaction mixture) with the intrinsic selectivity encountered over homogeneous catalysts.[29] In the last few years, a key development in the application of hybrid materials for selective hydrogenations was the identification of hexadecyl(2-hydroxyethyl)dimethylammonium dihydrogen phosphate (HHDMA) as a suitable ligand for the synthesis of metal nanoparticles.[30,31] This molecule integrates both stabilising and reducing properties and can be applied in aqueous medium, eliminating many hurdles which have long hampered the industrial exploitation of other routes to prepare hybrid nanoparticles (*e.g.*, the need to use low-boiling point solvents, the fast addition of expensive or toxic reductants). This enabled the production of hybrid Pd-HHDMA and Pt-HHDMA catalysts for alkyne and nitro-group hydrogenation, respectively, commercialised by BASF under the trademark NanoSelect.[32–35] Due to the presence of a dihydrogen phosphate anion, the HHDMA ligand acts as a pH buffer, controlling the local acidity. This can be utilised for attaining beneficial effects in terms of reaction rate, while retaining high selectivity levels. Since the selective hydrogenation of levulinic acid requires catalyst acidity to improve the performance, we decided to prepare and catalytically explore for the first time HHDMA-modified Ru nanoparticles.

From a process viewpoint, the hydrogenation of levulinic acid to GVL has been traditionally conducted in batch reactors,[21–25,36] mainly due to the simplicity of the equipment. However, it is now widely recognised that continuous-flow reactors offer important benefits in terms of process intensification, safety, evaluation of deactivation phenomena, and kinetic analysis in steady state.[37] For these reasons, in recent times, several authors have explored the selective hydrogenation of levulinic acid in continuous mode.[13,25,38–41]

Herein, we report the synthesis of Ru-HHDMA colloids displaying a narrow particle size distribution centred at 1.5 nm, and the subsequent deposition onto a $TiSi_2O_6$ carrier. Characterisation by inductively coupled plasma optical emission spectroscopy, elemental analysis, scanning transmission electron microscopy, energy dispersive X-ray mapping, ^{31}P and ^{13}C magic angle spinning nuclear magnetic resonance, X-ray photoelectron spectroscopy, diffuse reflectance infrared spectroscopy, and temperature-programmed reduction with H_2 confirms the desired interaction of the ligand and the metal nanoparticle in the resulting catalyst. In order to explore the advantages of ligand modification in comparison with the state-of-the-art Ru/C material, the catalyst performance has been evaluated in the continuous-flow three-phase hydrogenation of levulinic acid to γ-valerolactone in water at different temperatures, pressures, and flow rates. Density Functional Theory has been employed to derive mechanistic understanding of the high selectivity to GVL achieved over Ru-based catalysts and the enhanced activity of the ligand-modified nanoparticles.

Experimental

Catalyst preparation

As depicted in Fig. 1, an aqueous solution of HHDMA (7 cm^3, 30%) was diluted in deionised water (200 cm^3) and mixed with an aqueous solution of $RuCl_3$ (2 cm^3, 0.5 M) and HCl (0.5 cm^3, 33%). The resulting mixture, containing 0.5 mg Ru per cm^3, was heated to 368 K and stirred at this temperature for 2 h to form colloidal metal nanoparticles of approximately 1.5 nm. The colloidal solution was added to a suspension consisting of $TiSi_2O_6$ (Aldrich, 30 g) and deionised water (300 cm^3). The suspension was stirred for 1 h, filtered extensively with deionised water, and dried overnight at 333 K. The Ru/C catalyst (Sigma-Aldrich, ref.: 24888169) was commercially available. Prior to use, this material was reduced at 473 K for 1 h under flowing 10 vol% H_2/N_2 (20 cm^3 min^{-1}) using a heating rate of 10 K min^{-1}.

Catalyst characterisation

The ruthenium content in the catalysts was determined by inductively coupled plasma-optical emission spectrometry (ICP-OES) using a Horiba Ultra 2 instrument equipped with a photomultiplier tube detector. The C, H, N, and P contents were determined by infrared spectroscopy using a LECO CHN-900 combustion furnace. Nitrogen isotherms were obtained at 77 K using a Micrometrics ASAP 2020, after evacuation of the samples at 393 K for 3 h. High-angle

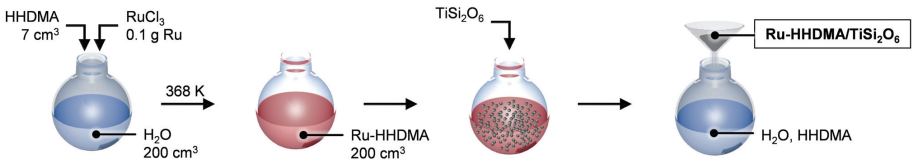

Fig. 1 Synthetic steps involved in the preparation of the Ru-HHDMA/$TiSi_2O_6$ catalyst.

annular dark field scanning transmission electron microscopy (HAADF-STEM) images and elemental maps by energy dispersive X-ray (EDX) spectroscopy were acquired using an FEI Talos S200 microscope operated at 200 kV, with a 70 mm C2 aperture and 0.4 nA beam current. The catalysts were dispersed as dry powders on lacey carbon coated copper grids. The particle size distribution was assessed by counting more than 150 individual Ru nanoparticles. H_2 chemisorption was performed using a Thermo TPDRO 1100 unit. The samples were treated in He (20 cm^3 min^{-1}) at 393 K for 60 min and reduced to 5 vol% H_2/N_2 (20 cm^3 min^{-1}) at 423 K for 30 min. Then, pulses of 5 vol% H_2/N_2 (0.344 cm^3) were dosed to the catalyst at 308 K every 4 min. The ruthenium dispersion was calculated from the amount of chemisorbed H_2, considering an atomic surface density of 1.57×10^{19} atoms per m^2 and an adsorption stoichiometry Ru/H_2 = 2.[42] Temperature-programmed reduction with hydrogen (H_2-TPR) was performed using a Micromeritics Autochem II 2920 unit connected to a MKS Cirrus 2 quadrupole mass spectrometer. The samples (0.1 g) were treated under a He flow (20 cm^3 min^{-1}) at 393 K for 1 h, cooled down to 308 K, and finally heated to 1273 K (10 K min^{-1}) while monitoring the consumption of H_2. X-ray photoelectron spectroscopy (XPS) was conducted with a Physical Electronics Instruments Quantum 2000 spectrometer using monochromatic Al Kα radiation generated from an electron beam operated at 15 kV and 32.3 W. The spectra were recorded under ultra-high vacuum conditions (residual pressure = 5×10^{-8} Pa) at a pass energy of 50 eV. In order to compensate for charging effects, all binding energies were referenced to the C 1s at 288.2 eV. Thermogravimetric analysis was performed using a Mettler Toledo TGA/DSC 1 Star system. Prior to measurement, the samples were dried in N_2 (40 cm^3 min^{-1}) at 393 K for 1 h. The analysis was performed in air (40 cm^3 min^{-1}), heating the sample from 298 K to 1173 K at a rate of 10 K min^{-1}. ^{13}C and ^{31}P magic-angle spinning nuclear magnetic resonance (MAS NMR) spectra were recorded on a Bruker AVANCE III HD NMR spectrometer at a magnetic field of 16.4 T corresponding to a ^1H Larmor frequency of 700.13 MHz. A 4 mm double resonance probe head at a spinning speed of 10 kHz was used for all experiments. The ^{13}C spectra were acquired using the cross polarization mode with a contact time of 2.00 ms and a recycle delay of 1 s. A total of 64×10^3 scans were added for each sample. The ^{31}P experiments used a single pulse excitation sequence with a recycle delay of 1 s. Between 39×10^3 and 96×10^3 scans were acquired depending on the sample. Both ^{13}C and ^{31}P experiments used high-power ^1H decoupling during acquisition with the SPINAL-64 sequence. Fourier transform infrared (FTIR) spectroscopy was performed using a Bruker Optics Vertex 70 spectrometer equipped with a high temperature cell, ZnSe windows, and a mercury–cadmium–telluride (MCT) detector. The cell was filled with a powdered catalyst diluted with KBr in a weight ratio of 1 : 10 and carefully levelled to minimise reflection from the sample surface. The spectra were recorded in He (20 cm^3 min^{-1}) at 473 K, accumulating 64 scans in the 4000–1000 cm^{-1} range with a resolution of 4 cm^{-1}.

Catalyst testing

The hydrogenation of levulinic acid (ABCR, 98%) was carried out in a fully-automated flooded-bed reactor (ThalesNano H-Cube Pro™), in which the gaseous hydrogen produced *in situ via* electrolysis of Millipore water and the liquid feed (containing 5 wt% of the substrate and deionised water as the solvent) flowed concurrently upward through a cylindrical cartridge of an approximately 3.5 mm internal diameter. The latter contained a fixed bed composed of the catalyst (0.1 g of Ru-HHDMA/$TiSi_2O_6$ or 0.05 g of Ru/C) well mixed with inert titanium silicate as diluent (0.12 g, Sigma-Aldrich, 99.8%), both with a particle size of 0.2–0.4 mm. The reactions were conducted at various temperatures (373–423 K), total pressures (1–60 bar), and liquid flow rates (0.3–1.2 cm^3 min^{-1}, resulting in contact times (τ) between 4 and 16 s), keeping the H_2 flow rate constant (56 cm^3 min^{-1}). For every experimental condition, three data points were averaged. In particular, the products were collected after 20 min under each experimental condition; this was appropriate, considering that, in our continuous-flow microreactor, steady-state operation is reached in 5–10 min. The product composition was analysed offline by high-performance liquid chromatography (HPLC), using a Merck LaChrome system equipped with a HPX-87H column, refractive index and UV-vis detectors. A 0.005 M aqueous H_2SO_4 solution flowing at 0.600 cm^3 min^{-1} was used as the eluent. The conversion (X) of a given substrate was determined as the amount of the reacted levulinic acid divided by the amount of the substrate at the reactor inlet. The reaction rate (r) was expressed as the mole of LA reacted per hour and mole of Ru in the catalyst. The selectivity (S) to each product was quantified as the amount of the particular product divided by the amount of reacted levulinic acid.

Computational details

Density Functional Theory (DFT) calculations were performed using the Vienna *ab initio* Simulation Package (VASP),[43,44] employing the generalised gradient approximation with the Perdew–Burke–Ernzerhof exchange–correlation functional.[45] Since van der Waals (vdW) contributions are required to effectively model large molecules such as LA and HHDMA, the Grimme DFT-D2 method[46,47] modified with C6 parameters developed in our group has been applied.[48] The interaction between valence and core electrons was described by the projector augmented wave (PAW) pseudopotentials[49,50] with a cut-off energy of 450 eV. The calculated lattice parameters for Ru (2.712 Å with c/a = 1.582) agree well with the experimental one (2.706 Å with c/a = 1.584).[51] Gas-phase molecules such as LA and GVL were optimised in a simulation box of 20 × 20 × 20 $Å^3$. The Ru/C catalyst (Ru(0001)) was modelled using periodic slabs with a thickness of four layers and in a $p(4 \times 4)$ supercell, while for the Ru-HHDMA four dihydrogen phosphates and the corresponding cationic head groups of the surfactant were included.[33] The slabs were separated from the neighbouring ones through a vacuum gap of 20 Å to avoid lateral interactions. In particular, the two upmost layers were

completely relaxed, whereas the atoms in the remaining layers were fixed to mimic the bulk. The calculation of the adsorption and transition state energies was performed with a 3 × 3×1 *k*-point. Dipole corrections were introduced to eliminate the spurious contributions arising from the asymmetry of the system. Solvation contributions for the molecules in the liquid phase were also considered using the MGCM methodology.[52] The climbing image nudged elastic band (CI-NEB)[53,54] and improved dimer method (IDM)[55] were employed to locate the transition states in the potential surfaces. The transition states were confirmed by having only one imaginary value from frequency analysis.

Results and discussion

Catalyst properties

Table 1 shows the bulk composition and morphological characteristics of the materials prepared. ICP-OES analysis of the Ru/C and Ru-HHDMA/$TiSi_2O_6$ catalysts reveals a total ruthenium content of 5 and 0.24 wt%, respectively. In particular, for the latter material, the presence of a ligand is confirmed by C, H, N, and P analysis. Considering the stoichiometry of the surfactant ($C_{20}H_{46}NO_5P$), it is possible to estimate a total ligand concentration of *ca*. 10 wt%. The inspection of the scanning transmission electron micrographs reveals that the ruthenium nanoparticles possess a uniform spherical shape, with an average particle diameter of around 1.5 nm in both cases (Fig. 2). As reported by Philippot *et al.*,[56] this is unsurprising since small Ru particles readily form due to the strong interaction of this metal with a variety of C, Ti, and Si-based supports. The nanoparticles are well distributed and no evidence of particle agglomeration is observed. Characterisation by N_2 sorption confirms the distinct textural properties of the two catalysts (Fig. S1†). In particular, the Ru-HHDMA catalyst exhibits the typical total surface area (200 m^2 g^{-1}) of titanium silicate carriers, and a high (meso)porosity. The corresponding pore size distribution derived by the Barrett–Joyner–Halenda model evidences a discrete range of pore sizes centred around 10 nm. In contrast, the Ru/C catalyst displays the surface area as 755 m^2 g^{-1}, owing to the high microporosity evidenced by the high uptake in the N_2 adsorption isotherm at low relative pressures. To confirm the microporous nature of the carbon support, an NLDFT model assuming slit-pore geometry has been employed, which evidenced a pore size distribution centred at 0.8 nm. In order to characterise the ligand distribution over the catalyst, EDX mapping was

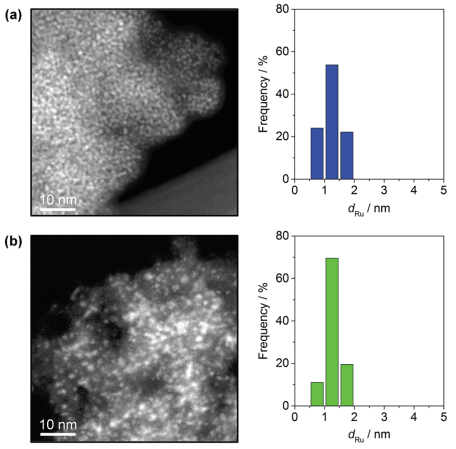

Fig. 2 Scanning transmission electron micrographs and particle size distributions of Ru-HHDMA/$TiSi_2O_6$ (a) and Ru/C (b).

performed over Ru-HHDMA/$TiSi_2O_6$ (Fig. 3). Interestingly, phosphorus appears to be mainly localised in the areas where Ru is also present, corroborating previous hypotheses that the ligand is bound to the metallic nanoparticle through the phosphate and to the carrier through N–OH.[31] This clear partition between the type of ligand adsorbed on the nanoparticles and that on the support enables, for the first time, the direct estimation of the ligand content per nanoparticle. Assuming an hcp unit cell with an atomic packing of 0.76,[57] and considering the dispersion of Ru, we have first calculated the moles of surface Ru atoms. The ratio between the moles of P obtained by elemental analysis and those of surface Ru provided the number of HHDMA molecules per nanoparticle (*ca*. 250 HHDMA molecules per nanoparticle). To determine the thermal stability of the ligand shell, thermogravimetric analysis in air was conducted (Fig. 4a). In line with the previous results,[33–35] the ligand decomposition started at 500–550 K, confirming that the metal–ligand interaction is independent of the metal identity. To further elucidate the chemical identity of the ligand molecule, DRIFT spectra were acquired on both the Ru-HHDMA/$TiSi_2O_6$ catalyst and the $TiSi_2O_6$ support (Fig. 4b). The spectrum of the catalyst shows, between 3000 and 2800 cm^{-1}, the C–H vibrational mode of the aliphatic

Table 1 Characterisation data of the catalysts

Catalyst	Ru[a]/wt%	C[b]/wt%	H[b]/wt%	N[b]/wt%	P[b]/wt%	Weight loss[c]/%	S_{BET} [d]/m^2 g^{-1}	V_{pore} [e]/cm^3 g^{-1}	d_{Ru} [f]/nm
Ru-HHDMA/$TiSi_2O_6$	0.24	4.5	1.8	0.3	0.9	12	281	0.21	1.3
Ru/C	5.0	95	—	—	—	—	755	0.65	1.5

[a] Inductively coupled plasma optical emission spectroscopy. [b] Elemental analysis. [c] Thermogravimetric analysis. [d] BET method. [e] Volume of N_2 at $p/p_0 = 0.95$. [f] H_2 chemisorption.

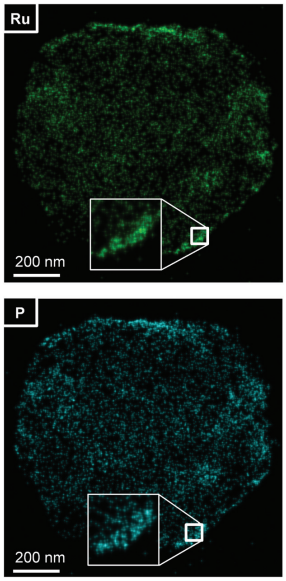

Fig. 3 Energy dispersive X-ray maps of Ru and P in Ru-HHDMA/$TiSi_2O_6$. The insets show a zoom of 4 times.

chain of the ligand and, between 1200 and 1100 cm^{-1}, the stretching mode of the phosphate group. In addition, the broad band at 3500 cm^{-1}, which is present in both the support and catalysts, is attributed to the stretching of O–H groups associated with the surface of the $TiSi_2O_6$ support.

The sample was further characterised by solid-state ^{13}C and ^{31}P MAS NMR. The ^{31}P MAS NMR spectra (Fig. 5a) display a single, broad isotropic signal at around 0 ppm, which is consistent with the presence of an orthophosphate anion. This peak is flanked on either side by a spinning sideband giving a rough estimate of the chemical shift anisotropy of about 50 ppm. Contrarily, the peaks in the ^{13}C MAS NMR spectra (Fig. 5b) can be assigned in analogy with the signals observed in the solution state NMR spectra. The signals above 40 ppm all originate from carbon positions in close proximity to the nitrogen. These resonances display a markedly increased linewidth when compared to many of the peaks below 40 ppm, which mainly correspond to positions in the aliphatic tail of the molecule. These observations are consistent with previous findings,[35] indicating a reduced mobility (on the NMR timescale) of the head-group with respect to the tail, for which the signals are dynamically equilibrated. In fact, the ^{31}P peak with a full width at the half height of approximately 2 kHz seems to be inhomogeneous in nature and this is indicative of a statically disordered environment.

Notwithstanding the determination of the atomic state of Ru-based materials is not straightforward for carbon supported materials, due to the overlapping of the Ru 3d core level signal with C 1s one, a feature centred at 281.3 eV indicative of the presence of RuO_x species for the Ru/C sample was

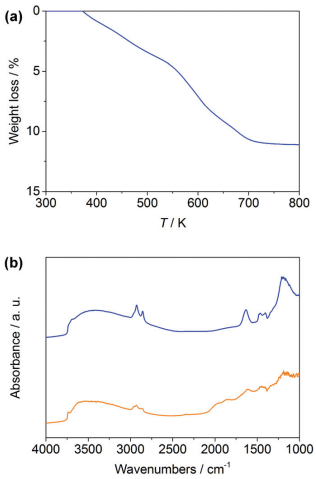

Fig. 4 Thermogravimetry of Ru-HHDMA/$TiSi_2O_6$ in air (a). DRIFT spectra of the Ru-HHDMA/$TiSi_2O_6$ catalyst (blue) and the $TiSi_2O_6$ carrier (orange) (b).

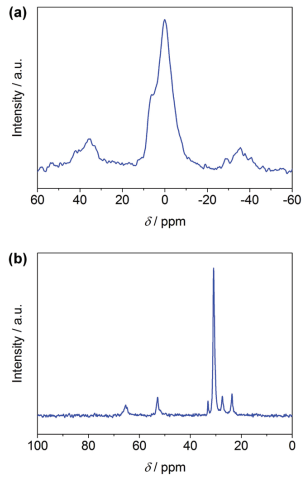

Fig. 5 ^{31}P (a) and ^{13}C (b) magic-angle spinning nuclear magnetic resonance spectroscopy of Ru-HHDMA/$TiSi_2O_6$.

4.3. Paper III: LA conversion to GVL

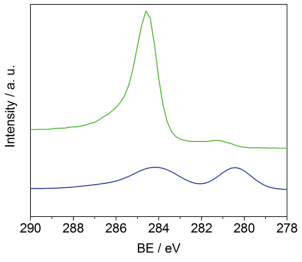

Fig. 6 Ru 3d core level X-ray photoelectron spectra of the Ru-HHDMA/$TiSi_2O_6$ (blue) and Ru/C (green).

observed.[58] In the case of Ru-HHDMA/$TiSi_2O_6$, a single Ru $3d_{5/2}$ core level at 280.2 eV was displayed (Fig. 6), confirming that the ruthenium surface is fully metallic.[58,59] An additional tool to further prove the oxidation state of the Ru catalysts is H_2-TPR (Fig. S2†). Apart from the decreased signal intensity observed at room temperature due to the stabilisation of the MS filament, Ru-HHDMA/$TiSi_2O_6$ did not show any hydrogen consumption peak at around 400 K, the expected temperature of reduction of RuO_x species to Ru^0.[60] In contrast, the Ru/C sample shows two peaks at 400 and 560 K. The first is attributed to the reduction of oxidic Ru species to metallic Ru, whereas the second represents the H_2 consumption due to the formation of methane catalysed by Ru.

Hydrogenation of levulinic acid

The performance of the Ru-based catalysts has been assessed in the continuous hydrogenation of levulinic acid in water (Fig. 7 and 8). The contour maps in Fig. 7 show the effect of temperature and pressure on levulinic acid conversion and on the selectivity to γ-valerolactone for Ru-HHDMA/$TiSi_2O_6$ and Ru/C. An excellent selectivity degree (>95%) was obtained at all temperatures and pressures investigated for both catalysts, highlighting the intrinsic selectivity of Ru-based materials for these types of chemical transformations (*vide infra*).

1,4-Pentanediol was also formed in the reaction, but with a selectivity lower than 5%. In terms of reaction rate, the ligand-modified catalyst exhibits, at 403 K and 20 bar, a fourfold higher activity compared to the state-of-the-art catalyst, indicating that the combination of inorganic and organic counterparts boosts the catalytic activity (this important aspect is elaborated below). We have also studied the effect of the contact time (τ) on the reaction rate (r) for both catalysts. A linear increase of r with the contact time is observed in both cases (Fig. 8a). Note that, even with four times longer residence times, high selectivity levels were retained. In order to verify the stability against leaching of the hybrid catalyst, a long-term test was conducted. The catalyst was stable for 15 h on stream, displaying no signs of deactivation (Fig. 8b). To further prove that both the ligand and the metal were retained after the reaction, elemental analysis of the used catalyst was conducted,

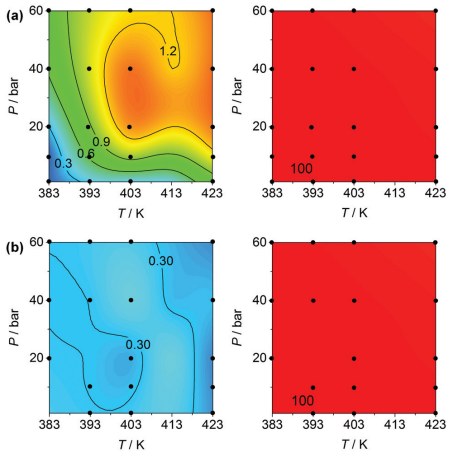

Fig. 7 Reaction rate (in 10^3 h^{-1}, left) and selectivity to γ-valerolactone (in %, right) as a function of temperature and pressure in the hydrogenation of levulinic acid over Ru-HHDMA/$TiSi_2O_6$ (a) and Ru/C (b). Conditions: F_L(levulinic acid + water) = 0.3 cm^3 min^{-1}, and $F_G(H_2)$ = 54 cm^3 min^{-1}. The contour maps were obtained through spline interpolation of the experimental points indicated by black dots.

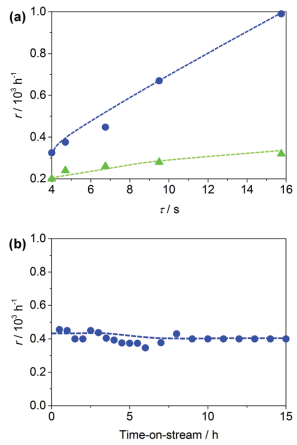

Fig. 8 Reaction rate (in 10^3 h^{-1}) as a function of the contact time (τ) in the hydrogenation of levulinic acid over Ru-HHDMA/$TiSi_2O_6$ (blue) and Ru/C (green) (a). Stability of Ru-HHDMA/$TiSi_2O_6$ in the hydrogenation of levulinic acid (b). Conditions: T = 403 K, P = 10 bar, F_L(levulinic acid + water) = 0.3–1.2 cm^3 min^{-1}, and $F_G(H_2)$ = 54 cm^3 min^{-1} (a); T = 393 K, P = 20 bar, F_L(levulinic acid + water) = 0.3 cm^3 min^{-1}, and $F_G(H_2)$ = 54 cm^3 min^{-1} (b).

showing negligible differences in the loading of both Ru and ligand with respect to the fresh catalyst. Additionally, STEM micrographs of the used catalysts have been acquired to verify if the ligand can hinder the sintering of the Ru nanoparticles. Interestingly, as depicted in Fig. S3,† the average particle size was retained upon hydrogenation. Contrarily, as reported elsewhere,[61] extensive particle sintering is typically observed for Ru/C, confirming that the Ru nanoparticles are susceptible to clustering if not effectively shielded in the presence of water.

Mechanism over bare Ru nanoparticles

To obtain molecular insights into the mechanism of the reaction over Ru and Ru-HHDMA surfaces, DFT calculations were conducted. Fig. 9 depicts the generally accepted cascade mechanism for the conversion of LA to GVL.[6,62] LA would either undergo hydrogenation to produce 4-oxopentanal and 4-hydroxypentanoic acid, or intramolecular esterification to produce angelica lactone. It is important to highlight that this pathway only provides a macroscopic framework for the reaction. When considering the reaction from the microscopic viewpoint, the mechanism for LA and levulinate to GVL consists of numerous and much more complex elementary steps, including C–O bond cleavage, hydrogenation (protonation) of the oxygen atoms, hydrogenation of carbon in the ketone group, and ring closing steps. To construct a solid theoretical model, we have considered all 34 intermediates generated from the 68 corresponding elementary steps (see the ESI, Fig. S4 and S5†). The sequence of these reactions could affect the result, determining the most preferable pathway. Due to the complexity of the reaction network, all aforementioned steps have been first computed for a bare Ru surface representing the naked nanoparticle, and then extrapolated these results to understand the Ru-HHDMA case (*vide infra*). To maximise the relevance of the theoretical calculations, DFT calculations using dispersion interactions have been applied. Besides, to determine the nature of the interaction between LA and the surface, we have also considered that the reactions take place in water, suggesting that LA, which is an acid with a pK_a of 4.5, is prevalent in the anionic state in aqueous solution. The first step of the reaction is hydrogen dissociation on the Ru metal surface, which is barrierless and exothermic (0.68 eV per atom). This step is followed by the adsorption of levulinate on the surface (black box in Fig. 10 and ESI†). As shown in Fig. 10, once the levulinate is in the adsorbed state, several paths can follow: C–O cleavage, followed by ring closure, or hydrogenation. From the analysis of the reaction energies and energy barriers of all possible steps (see the ESI†), it emerges that mainly the hydrogenation of the ketonic group leading to 17-c is likely to occur. In fact this step needs a relatively low energy barrier (0.57 eV) compared to the competitive protonation of O^1 and O^2 (1.34 and 1.33 eV, respectively). Besides, the

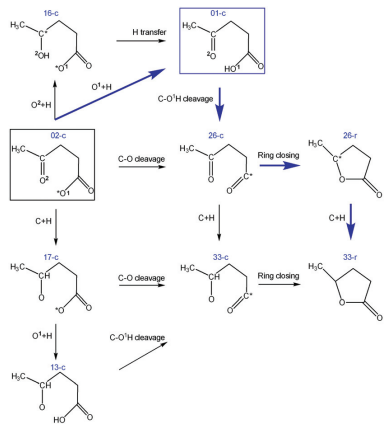

Fig. 10 Reaction network for levulinic acid (blue)/levulinate to γ-valerolactone. Blue arrows describe the path for levulinic acid on Ru-HHDMA. Contrarily, all the steps are possible in the levulinate transformation on the bare Ru(0001) surface.

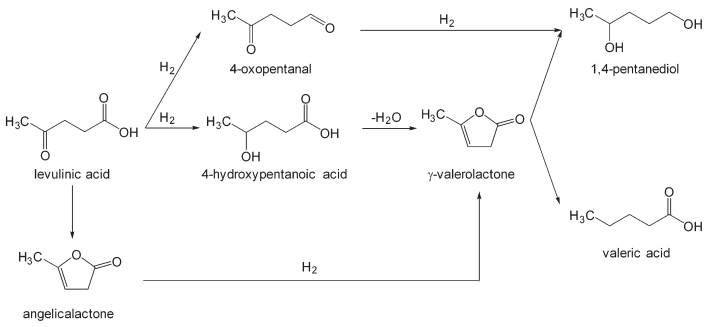

Fig. 9 Cascade process for the hydrogenation of LA to GVL, 1,4-pentanediol, and valeric acid.

4.3. Paper III: LA conversion to GVL

protonation of O^1 and O^2 is highly endothermic (0.69 and 1.13 eV). C–O cleavage of LA is also unlikely to occur. In fact, the direct C–O bond scission from the carboxylate group of levulinate (structure 02-c) and 17-c needs large energy barriers (1.56 and 1.39 eV, respectively). These high barriers arise from the strong interaction of the metal surface with the bidentate O atoms from COO^- which is η^2-O,O coordinated to the surface. Since the reaction is carried out in water, we have investigated the possibility that the solvent assists the C–O cleavage,[63] resulting in a barrier decrease to 1.08 and 1.17 eV, respectively. Since these barriers remain pretty large, only moderate contributions from ring closing reactions are expected from R–COO^- species, due to the strong binding of the O of the carboxyl group, inhibiting the internal C–O bond formation. Thus, after the formation of 17-c, the water-assisted C–O cleavage takes place, leading to the formation of 33-c that gives the final product, GVL (33-r) *via* ring closing. The C–O bond breaking is the rate determining step of the whole process. Note, however, that the reaction network can encompass other species, like those shown in Fig. 9, and that a complete reaction rate analysis with the contribution of the different paths under different conditions would require a full microkinetic analysis including coverage effects.

The thermodynamic selectivity concept, which refers to the energy difference between the adsorption of the reactants and that of the products, is the simplest descriptor that can be used to rationalise activity–selectivity patterns of challenging hydrogenation reactions.[64–66] High thermodynamic selectivity requires that the reactants are much more strongly adsorbed to the catalyst surface than the products. This concept can be applied here to rationalise the high product selectivity obtained in the reaction. Specifically, GVL over-hydrogenation cannot occur since the calculated barrier for this step is approximately 1.36 eV. This is higher than the desorption barrier for GVL (1.22 eV, which reduces to 0.80 eV once solvation is taken into account). Thus, once GVL is formed, it easily desorbs from the surface.

Mechanism over Ru-HHDMA

Since the reaction network is very complex, the role of the Ru-HHDMA can be inferred from the Ru(0001) network, and complemented with a few calculations on the modelled Ru-HHDMA interface. The preferred path on Ru-HHDMA is highlighted by the blue arrows in Fig. 10. The major molecular difference in the mechanism of reaction over the Ru-HHDMA surface is in the activation of molecular H_2. Due to the presence of HHDMA ligands, hydrogen dissociation is barrierless and exothermic on the Ru-HHDMA interface (0.45 eV per atom). This facilitated hydrogen activation produces a buffer of hydrogen atoms that at high coverage can be stabilised between the phosphate anions and co-adsorbed water. Particularly, part of these hydrogen atoms can be trapped in the form of hydronium (H_3O^+) species. These protons being more acidic than LA reverse the equilibrium of the reactant towards its acidic form (LA), instead of the anionic intermediate described above. This trapping is almost thermoneutral (+0.12 eV). Thus, when adsorbing the levulinate to the Ru-HHDMA, the proton buffered at the interface is transferred, converting the levulinate adsorbate into LA (01-c, see the blue box in Fig. 10). Due to the absence of hapticity (that is, the coordination of a ligand to a metal *via* a contiguous series of atoms), LA has a weaker interaction with the surface than $RCOO^-$ (02-c), and therefore the C–OH breaking from R–COOH (01-c to 26-c) features a lower barrier (0.46 eV) than any other reaction (*ca.* 1.0 eV). This enhanced C–OH cleavage results in a fourfold increase in the reaction rate observed experimentally (Table 2). After that, the ring closing takes place with a small barrier (0.44 eV), followed by the hydrogenation of 26-r to 33-r (0.87 eV).

To further characterise the intrinsic acidity of the surface, we have employed a set of small compounds: formic acid, acetic acid, chloro, dichloro, and trichloro acetic acid. In Fig. 11, the adsorption energy of the corresponding anions (red) and the energy required to protonate them (black) have been calculated with respect to the anions in solution. The difference of these gives the adsorption energy of the acid (blue line). This energy is equal to zero when the acid/anion are identical, enabling the determination of the intrinsic pK_a of the Ru-HHDMA interface. From our calculations, the interface is buffered around pK_a = 1, indicating that reactions featuring molecules of a lower pK_a would not benefit in terms of reaction rate. Similarly, Ru nanoparticles stabilised on reduced graphene oxide (GO) have also shown a fourfold increase in

Table 2 Main elementary steps in the mechanisms for LA hydrogenation to GVL on Ru(0001) and Ru-HHDMA surface

	Ru(0001)	Ru-HHDMA
Step 1	Adsorption of levulinate	Adsorption of levulinate
Step 2	C^2 hydrogenation	Protonation of levulinate to LA
Step 3	C–O breaking from R–COO	C–OH breaking from R–COOH
Step 4	Ring closing to GVL	Ring closing
Step 5	GVL desorption	C^2 hydrogenation to GVL
		GVL desorption

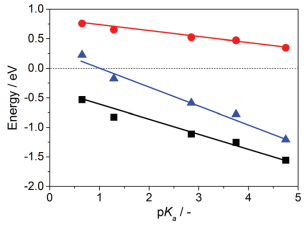

Fig. 11 Relationship between pK_a and adsorption energy of the corresponding carboxylate (E_{ads}, black), protonation energies (ΔE, red), as well as the sum of them ($E_{ads} + \Delta E$, blue). Linear fitting: $E_{ads} = (-0.23 \pm 0.02)$ pK_a + (0.44 ± 0.06), $\Delta E = (-0.09 \pm 0.01)pK_a$ + (0.80 ± 0.02), and $E_{ads} + \Delta E = (-0.32 \pm 0.03)pK_a$ + (0.35 ± 0.08) with r^2 values of 0.97, 0.98, and 0.97, respectively. Estimated pK_a of the interface is 1.09.

the activity when compared with standard Ru formulations.[12] Since in GO supports some acidic centres are retained even upon reduction, we believe that these centres can act as promoters in the same way as the interface does in Ru-HHDMA. This concept can be further transposed to any reaction catalysed by ionic liquids with sulfonate terminations.[67] The pH control at the interface adds to recent electrochemical effects found for other NanoSelect catalysts.[68]

In order to rationalise the outstanding selectivity of the Ru-based catalyst in breaking C–O bonds, a comparison with other metals could also be crucial. For instance, C–OH bond breaking on less oxophilic metals, such as Pd(111) and Pt(111) surfaces, presents high barriers (1.28 and 0.84 eV, respectively), while the competitive hydrogenations exhibit barriers of *ca.* 1 eV. Therefore, on these metals, the selectivity levels achieved are much lower since the activation energy window is very narrow.

Finally, considering that the main issue of Ru catalysts for biomass conversion is the relative instability against the formation of oxidic phases (RuO_x),[12] the ligand-modified catalyst was tested in a stability test (Fig. 8b) and complemented with the analysis of oxygen adsorption. We have found that the adsorption of large quantities of oxygen on the Ru-HHDMA nanoparticles is inhibited due to the repulsion of the orthophosphate group (see the ESI, Table S3 and Fig. S6†). Under a H_2 atmosphere, the interface acidity modulates the oxidative effect of the oxygens and converts them into hydroxyls that are less prone to oxide formation. These computational results give the key for the outstanding selectivity of the Ru-based catalyst in the conversion of LA to GVL, indicating that acid properties at the interface improve the activity and the stability of the Ru-HHDMA nanoparticles.

Conclusions

We have prepared and characterised a new type of hybrid Ru nanoparticle using HHDMA as a modifier. ICP-OES, elemental analysis, TGA, DRIFTS, H_2-TPR, STEM, EDX, ^{31}P and ^{13}C MAS-NMR, and XPS have been used for confirming the ligand–metal interaction and determining the textural and spectroscopic features of the catalyst. The catalyst was evaluated in the continuous-flow hydrogenation of LA in water. Under all conditions screened (T = 373–423 K, P = 1–60 bar, and τ = 4–16 s), Ru-HHDMA/$TiSi_2O_6$ displays an outstanding fourfold higher reaction rate than that of the benchmark 5 wt% Ru/C catalyst, and full selectivity to GVL. Since the Ru/C catalyst is known to deactivate easily in water, a stability test over the ligand-modified catalyst has been carried out, showing no sign of deactivation for 15 h on stream. Density Functional Theory has unravelled the reasons behind this remarkable activity and intrinsic selectivity of the Ru-HHDMA catalyst in the selective hydrogenation of levulinic acid. In particular, the metal/surfactant/water interface causes a local increase in the pH that can protonate the levulinate anion, resulting in a reaction network featuring low barriers and a fourfold reaction rate increase. Due to the structure of the nanocatalysts, this enhancement is maintained, demonstrating the robustness of the catalytic system. The high selectivity is of thermodynamic nature, meaning that once GVL is formed, it is easily desorbed from the surface, avoiding further hydrogenation. Contrary to the deactivation suffered by the Ru/C catalyst due to surface oxidation, the formation of RuO_x compounds on the ligand-modified catalyst is impeded for two reasons: the phosphate anions at the surface shield the nanoparticle, thus reducing the oxygen uptake from by-products, and the high pH at the interface does not allow the formation of the oxide.

Acknowledgements

Financial support from ETH Zurich, ICIQ Foundation, and the Spanish Ministerio de Economía y Competitividad (CTQ2012–33826 and "Ayuda formación Posdoctoral" Fellowship (N. A.-B.)) is acknowledged. Dr Roland Hauert (EMPA, Dubendorf) and Dr Réne Verel are acknowledged for the XPS analyses, and ^{13}C and ^{31}P MAS-NMR, respectively. ScopeM of the Swiss Federal Institute of Technology is acknowledged for providing access to its facilities. BSC-RES is thanked for generous computational resources. Dr. M. García-Ratés is acknowledged for the solvation values.

References

1 P. Anastas and N. Eghbali, *Chem. Soc. Rev.*, 2010, **39**, 301.
2 C. O. Tuck, E. Pérez, I. T. Horváth, R. A. Sheldon and M. Poliakoff, *Science*, 2012, **337**, 695.
3 R. A. Sheldon, *Green Chem.*, 2014, **16**, 950.
4 D. M. Alonso, S. G. Wettstein and J. A. Dumesic, *Green Chem.*, 2013, **15**, 584.
5 I. T. Horváth, H. Mehdi, V. Fábos, L. Bode and L. T. Mika, *Green Chem.*, 2008, **10**, 238.
6 M. Besson, P. Gallezot and C. Pinel, *Chem. Rev.*, 2014, **114**, 1827.
7 R. Palkovits, *Angew. Chem., Int. Ed.*, 2010, **49**, 4336.
8 F. D. Pileidis and M.-M. Titirici, *ChemSusChem*, 2016, **9**, 562.
9 A. Corma, S. Iborra and A. Velty, *Chem. Rev.*, 2007, **107**, 2411.
10 W. R. H. Wright and R. Palkovits, *ChemSusChem*, 2012, **5**, 1657.
11 C. Michel and P. Gallezot, *ACS Catal.*, 2015, **5**, 4130.
12 C. Xiao, T.-W. Goh, Z. Qi, S. Goes, K. Brashler, C. Perez and W. Huang, *ACS Catal.*, 2016, **6**, 593.
13 O. A. Abdelrahman, A. Heyden and J. Q. Bond, *ACS Catal.*, 2014, **4**, 1171.
14 S. G. Wettstein, J. Q. Bond, D. M. Alonso, H. N. Pham, A. K. Datye and J. A. Dumesic, *Appl. Catal., B*, 2012, **117**, 321.
15 D. J. Braden, C. A. Henao, J. Heltzel, C. C. Maravelias and J. A. Dumesic, *Green Chem.*, 2011, **13**, 1755.
16 W. Luo, M. Sankar, A. M. Beale, Q. He, C. J. Kiely, P. C. A. Bruijnincx and B. M. Weckhuysen, *Nat. Commun.*, 2016, **6**, 6540, DOI: 10.1038/ncomms7540.

17 C. Moreno-Marrodan and P. Barbaro, *Green Chem.*, 2014, **16**, 3434.
18 V. V. Kumar, G. Naresh, M. Sudhakar, C. Anjaneyulu, S. K. Bhargava, J. Tardio, V. K. Reddy, A. H. Padmasri and A. Venugopal, *RSC Adv.*, 2016, **6**, 9872.
19 A. M. R. Galletti, C. Antonietti, V. De Luise and M. Martinelli, *Green Chem.*, 2012, **14**, 688.
20 X. Zhang, P. Murria, Y. Jiang, W. Xiao, H. I. Kenttämaa, M. M. Abu-Omar and N. S. Mosier, *Green Chem.*, 2016, **18**, 5219.
21 A. M. Hengne and C. V. Rode, *Green Chem.*, 2012, **14**, 1064.
22 M. Sudhakar, V. V. Kumar, G. Naresh, M. L. Kantam, S. K. Bhargava and A. Venugopal, *Appl. Catal., B*, 2016, **180**, 113.
23 Z.-p. Yan, L. Lin and S. Liu, *Energy Fuels*, 2009, **23**, 3853.
24 L. E. Manzer, *Appl. Catal., A*, 2004, **272**, 249.
25 X.-L. Du, Q.-Y. Bi, Y.-M. Liu, Y. Cao and K.-N. Fan, *ChemSusChem*, 2011, **4**, 1838.
26 G. E. Oosterom, J. N. H. Reek, P. C. J. Kamer and P. W. N. M. van Leeuwen, *Angew. Chem., Int. Ed.*, 2001, **40**, 1828.
27 V. I. Pârvulescu and C. Hardacre, *Chem. Rev.*, 2007, **107**, 2615.
28 A. Kaushik, R. Kumar, S. K. Arya, M. Nair, B. D. Malhora and S. Bhansali, *Chem. Rev.*, 2015, **115**, 4571.
29 M. A. Boles, D. Ling, T. Hyeon and D. V. Talapin, *Nat. Mater.*, 2016, **15**, 141.
30 P. T. Witte, P. H. Berben, S. Boland, E. H. Boymans, D. Vogt, J. W. Geus and J. G. Donkervoort, *Top. Catal.*, 2012, **55**, 505.
31 P. T. Witte, S. Boland, F. Kirby, R. van Maanen, B. F. Bleeker, D. A. M. de Winter, J. A. Post, J. W. Geus and P. H. Berben, *ChemCatChem*, 2013, **5**, 582.
32 E. H. Boymans, P. T. Witte and D. Vogt, *Catal. Sci. Technol.*, 2015, **5**, 176.
33 G. Vilé, N. Almora-Barrios, S. Mitchell, N. López and J. Pérez-Ramírez, *Chem. – Eur. J.*, 2014, **20**, 5926.
34 G. Vilé, N. Almora-Barrios, N. López and J. Pérez-Ramírez, *ACS Catal.*, 2015, **5**, 3767.
35 D. Albani, G. Vilé, S. Mitchell, P. T. Witte, N. Almora-Barrios, R. Verel, N. López and J. Pérez-Ramírez, *Catal. Sci. Technol.*, 2016, **6**, 1621.
36 A. Yepez, S. De, M. S. Climent, A. A. Romero and R. Luque, *Appl. Sci.*, 2015, **5**, 532.
37 M. Irfan, T. N. Glasnov and C. O. Kappe, *ChemSusChem*, 2011, **4**, 300.
38 A. S. Piskun, J. E. de Haan, E. Wilbers, H. H. van de Bovenkamp, Z. Tang and H. J. Heeres, *ACS Sustainable Chem. Eng.*, 2016, **4**, 2939.
39 R. A. Bourne, J. G. Stevens, J. Ke and M. Poliakoff, *Chem. Commun.*, 2007, 4632.
40 J.-P. Lange, R. Price, P. M. Ayoub, J. Louis, L. Petrus, L. Clarke and H. Gosselink, *Angew. Chem., Int. Ed.*, 2010, **49**, 4479.
41 J. M. Bermudez, J. A. Menéndez, A. A. Romero, E. Serrano, J. Garcia-Martinez and R. Luque, *Green Chem.*, 2013, **15**, 2786.
42 J. Okal, M. Zawadzki, L. Kępiński, L. Krajczyk and W. Tylus, *Appl. Catal., A*, 2007, **319**, 202.
43 G. Kresse and J. Furthmüller, *Comput. Mater. Sci.*, 1996, **6**, 15.
44 G. Kresse and J. Furthmüller, *Phys. Rev. B: Condens. Matter*, 1996, **54**, 11169.
45 J. P. Perdew, K. Burke and M. Ernzerhof, *Phys. Rev. Lett.*, 1996, **77**, 3865.
46 S. Grimme, *J. Comput. Chem.*, 2006, **27**, 1787.
47 T. Bučko, J. Hafner, S. Lebègue and J. G. Ángyán, *J. Phys. Chem. A*, 2010, **114**, 11814.
48 N. Almora-Barrios, G. Carchini, P. Błoński and N. López, *J. Chem. Theory Comput.*, 2014, **10**, 5002.
49 P. E. Blöchl, *Phys. Rev. B: Condens. Matter*, 1994, **50**, 17953.
50 G. Kresse and D. Joubert, *Phys. Rev. B: Condens. Matter*, 1999, **59**, 1758.
51 D. Lide, *CRC Handbook of Chemistry and Physics*, CRC Press, Boca Ranton, 84th edn, 2003–2004.
52 M. Garcia-Ratés and N. López, *J. Chem. Theory Comput.*, 2016, **12**, 1331.
53 G. Henkelman and H. Jónsson, *J. Chem. Phys.*, 2000, **113**, 9978.
54 G. Henkelman, B. P. Uberuaga and H. Jónsson, *J. Chem. Phys.*, 2000, **113**, 9901.
55 A. Heyden, A. T. Bell and F. J. Keil, *J. Chem. Phys.*, 2005, **123**, 224101.
56 L. M. Martínez-Prieto, A. Ferry, L. Rakers, C. Richter, P. Lecante, K. Philippot, B. Chaudret and F. Glorius, *Chem. Commun.*, 2016, **52**, 4768.
57 A. B. Ellis, M. J. Geselbracht, B. J. Johnson, G. C. Linsensky and W. R. Robinson, *Teaching General Chemistry: A Material Science Companion*, American Chemical Society Publication, 1st edn, 1993, p. 103.
58 A. M. Ruppert, M. Jędrzejczyk, O. Sneka-Płatek, N. Keller, A. S. Duman, C. Michel, P. Sautet and J. Grams, *Green Chem.*, 2016, **18**, 2014.
59 D. J. Morgan, *Surf. Interface Anal.*, 2015, **47**, 1072.
60 I. Rossetti, N. Pernicone and L. Forni, *Appl. Catal., A*, 2003, **248**, 97.
61 E. P. Maris, W. C. Ketchie, V. Oleshko and R. J. Davis, *J. Phys. Chem. B*, 2006, **110**, 7869.
62 M. J. Climent, A. Corma and S. Iborra, *Green Chem.*, 2014, **16**, 516.
63 C. Michel, J. Zaffran, A. M. Ruppert, J. Matras-Michalska, M. Jędrzejczyk, J. Grams and P. Sautet, *Chem. Commun.*, 2014, **50**, 12450.
64 Y. Segura, N. López and J. Pérez-Ramírez, *J. Catal.*, 2007, **247**, 383.
65 M. García-Mota, B. Bridier, J. Pérez-Ramírez and N. López, *J. Catal.*, 2010, **273**, 92.
66 G. Vilé, D. Albani, N. Almora-Barrios, N. López and J. Pérez-Ramírez, *ChemCatChem*, 2016, **8**, 21.
67 J. Julis, M. Hölscher and W. Leitner, *Green Chem.*, 2010, **12**, 1634.
68 N. Almora-Barrios, G. Vilé, M. García-Ratés, J. Pérez-Ramírez and N. López, *ChemCatChem*, 2016, DOI: 10.1002/cctc.200161134.

Paper IV: Glucose and mannose conversions

Published in *ChemSusChem*, 2016, **9**, 3407-3418

Catalyst and Process Design for the Continuous Manufacture of Rare Sugar Alcohols by Epimerization–Hydrogenation of Aldoses

Giacomo M. Lari,[a] Olivier G. Gröninger,[a] Qiang Li,[b] Cecilia Mondelli,*[a] Núria López,*[b] and Javier Pérez-Ramírez*[a]

Sugar alcohols are applied in the food, pharmaceutical, polymer, and fuel industries and are commonly obtained by reduction of the corresponding saccharides. In view of the rarity of some sugar substrates, epimerization of a readily available monosaccharide has been proposed as a solution, but an efficient catalytic system has not yet been identified. Herein, a molybdenum heteropolyacid-based catalyst is developed to transform glucose, arabinose, and xylose into less-abundant mannose, ribose, and lyxose, respectively. Adsorption of molybdic acid onto activated carbon followed by ion exchange to the cesium form limits leaching of the active phase, which greatly improves the catalyst stability over 24 h on stream. The hydrogenation of mixtures of epimers is studied over ruthenium catalysts, and it is found that the precursor to the desired polyol is advantageously converted with faster kinetics. This is explained by density functional theory on the basis of its more favorable adsorption on the metal surface and the lower energy barrier for the addition of a hydrogen atom to the primary carbon atom. Finally, different designs for a continuous process for the conversion of glucose into mannitol are studied, and it is uncovered that two reactors in series with one containing the epimerization catalyst and the other containing a mixture of the epimerization and hydrogenation catalysts increases the mannitol/sorbitol ratio to 1.5 from 1 for a single mixed-bed reactor. This opens a prospective route to the efficient valorization of renewables to added-value chemicals.

Introduction

Sugar alcohols, particularly those with C_5 and C_6 backbones, are an important class of carbohydrate derivatives. Pentose-derived polyols include arabitol, xylitol, and ribitol, whereas mannitol and sorbitol are the most relevant representatives of hexose-derived alcohols, which comprise a higher number of molecules owing to the presence of an additional stereocenter. All these molecules have multiple uses in the fine chemical, pharmaceutical, and food industries.[1] Specifically, they improve the nutritional profile of food preparations, as they are often incompletely absorbed by the intestine,[2] marginally alter blood sugar levels,[3] and appear to limit the formation of body fat.[4] They are also added to toothpaste and chewing gum formulations for their anticaries effect, as oral bacteria cannot ferment them.[5] Additionally, they are relevant and versatile monomers for the manufacture of highly performing biodegradable and biocompatible materials[6] and renewable feedstocks for the preparation of chemicals[7] and fuels.[8] Notably, arabitol has recently entered the list of the top-12 biobased chemicals.[9]

Sugar alcohols are rarely isolated from natural products and are more commonly obtained by hydrogenation of the corresponding carbohydrates. This has mostly been achieved by means of enzymes,[10] although chemocatalytic technologies have also been proposed.[11] The latter systems feature a lower environmental and economic impact owing to the possibility of processing reactants at higher concentrations and of operating over wider pH and temperature ranges.[12] Aldoses are the substrates of choice,[13] as the formation of a hydroxyl group from a primary carbonyl function does not generate a stereocenter and the reaction can proceed with high selectivity. Nevertheless, the very low availability of certain sugars (e.g., mannose and ribose) limits the feasibility of obtaining some of the polyols at a large scale.[14] Two approaches have been proposed to overcome this problem. The first comprises the use of a suitable ketose, as in the case of fructose for the preparation of mannitol.[15] Here, the drawback is the formation of approximately equimolar mixtures of mannitol and sorbitol, which have to be separated by costly crystallization or chromatography techniques.[16] Indeed, attempts to increase the selectivity to mannitol by modification of the catalyst[17] or by the addition of a chiral organic co-catalyst[18] have only led to moderate success. Alternatively, the abundant epimeric form of

[a] G. M. Lari, O. G. Gröninger, Dr. C. Mondelli, Prof. J. Pérez-Ramírez
Institute for Chemical and Bioengineering
Department of Chemistry and Applied Biosciences
ETH Zurich
Vladimir-Prelog-Weg 1, 8093 Zurich (Switzerland)
E-mail: cecilia.mondelli@chem.ethz.ch
jpr@chem.ethz.ch

[b] Q. Li, Prof. N. López
Institute of Chemical Research of Catalonia, ICIQ
The Barcelona Institute of Science and Technology
Av. Països Catalans 16, 43007 Tarragona (Spain)
E-mail: nlopez@iciq.es

Supporting Information and the ORCID identification number(s) for the author(s) of this article can be found under http://dx.doi.org/10.1002/cssc.201600755.

4.4. Paper IV: Glucose and mannose conversions

a rare sugar could be chosen as the starting material, and the desired polyol could be obtained by combining epimerization and hydrogenation steps.[19] Remarkably, this strategy could be applied to sugars such as pentoses, for which the ketonic form is infrequent. Raney nickel and Ru/C have been shown to be effective hydrogenation catalysts,[11] whereas the best heterogeneous epimerization materials reported so far have shown limitations with respect to the concentration of the substrate owing to the requirement of using methanol as the medium (Sn-β)[20] or to their level of activity (layered niobium molybdate).[21] Besides, only few catalytic data are available for solids prepared by immobilizing the highly active but water-soluble[22] phosphomolybdic heteropolyacid (HPA) through adsorption onto activated charcoal[23] or by precipitation in the form of an insoluble salt.[24] Most relevantly, the combination of the two reactions has never been studied in detail, and the application of industrially more amenable reactors in flow mode instead of vessels in batch mode has not been explored.

Herein, we target the preparation of rare sugar alcohols by epimerization followed by hydrogenation. In particular, we focus on the synthesis of mannitol from glucose, ribitol from arabinose, and arabitol from xylose. We initially confront various methods for the immobilization of HPA by evaluating the epimerization activity of the silica-supported, carbon-supported, and ion-exchange-resin-supported materials obtained and by investigating their compositional and structural changes upon use in continuous-flow catalytic runs. After selecting an efficient and stable hydrogenation catalyst based on ruthenium, we investigate the relative hydrogenation rates of the starting sugars and their epimers by combining kinetic tests and density functional theory (DFT) simulations. Finally, we study the overall performance of a continuous process by comparing different arrangements of the catalysts in single and series reactor configurations.

Results and Discussion

Design of the epimerization catalyst

Bulk and supported molybdenum-based catalysts were prepared to evaluate their activity and stability in sugar epimerization (Scheme 1). The first group included phosphomolybdic acid in its protonic form and as its silver and cesium salts.[24] The second set was obtained by adsorption of the acid or the salt on silica, activated carbon,[23] or an ion-exchange resin (IER).[25] Compositional data (Table 1) confirmed the expected molybdenum contents in the bulk solids. In the case of the supported catalysts, high metal loadings were observed that corresponded to up to 75% uptake of the precursor applied in the preparation. The Mo/P ratio was used to estimate the preservation of the heteropolyacid nature (Scheme 1) of the active phase upon synthesis. The typical value of phosphomolybdic acid (12) was obtained in most cases. A notable exception was the material prepared by using the IER, which lost part of the phosphoric acid groups. This was ascribed to the limited stability of the heteropolyacid at pH > 3, which resulted in depletion of its Keggin-type structure and the formation of molybdate and phosphate ions.[26] Finally, the Mo/*M* ratio (*M* = Ag, Cs) was considered to evaluate the efficiency of the proton exchange.

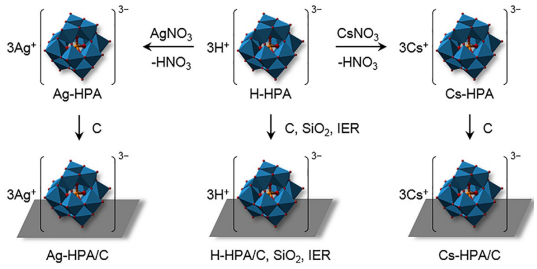

Scheme 1. Preparation of bulk and supported heteropolyacid catalysts.

Table 1. Characterization data and epimerization activity of the molybdate-based catalysts.[a]

Catalyst	Mo[b] [wt%]	Mo/P[c]	Mo/*M*[c]	S_{BET}[d] [$m^2 g^{-1}$]	V_{pore}[e] [$mL g^{-1}$]	TOF[f] [h^{-1}]	S_M[g] [%]	Mo leaching[b] [%]
MoO_3	73.5	–	–	15	0.21	1.8	95.7	100
H-HPA	65.6	12.8	–	7	0.06	28.9	93.6	100
Ag-HPA	48.1	10.9	3.5	41	0.18	31.1	89.9	21
Cs-HPA	49.7	11.5	3.8	61	0.16	29.1	89.4	13
H-HPA/IER	12.2	15.9	–	21	0.07	15.4	91.5	3
H-HPA/SiO_2	18.6	11.8	–	105	0.35	35.4	95.1	61
H-HPA/C	25.5	12.4	–	581	0.41	51.8	93.4	16
Ag-HPA/C	20.1	12.6	5.2	629	0.45	60.7	92.8	4
Cs-HPA/C	16.1	13.1	5.5	654	0.42	55.4	90.2	2

[a] Reaction conditions: $T = 333$ K, [glucose] = 0.28 M, glucose/Mo = 50, $t = 30$ min. [b] ICP-OES. [c] XRF. [d] BET method. [e] Volume of N_2 adsorbed at $p/p_0 = 0.99$. [f] Based on Mo. [g] Selectivity to mannose.

This was close to the theoretical value of 4 for the bulk Ag-HPA and Cs-HPA, whereas it was significantly higher for the carbon-supported materials, indicating that part of the exchanged metal was lost (Table 1). This can be explained by the ionic nature of the interaction between the support and the active phase, as hinted by previous reports describing that positively charged sites on the carbon surface act as cations displacing the Ag^+ and Cs^+ species.[23] The porous properties of the catalysts were determined by nitrogen sorption. The data evidence that H-HPA possessed an even lower specific surface area (S_{BET}) than the reference material MoO_3, whereas the S_{BET} values of Ag-HPA and Cs-HPA were markedly higher.[27] Carbon-supported catalysts displayed high porosity (V_{pore}) and total surface areas (S_{BET}) greater than 500 $m^2 g^{-1}$. Nevertheless, it should be noted that these values are substantially lower than those of the bare carbon (V_{pore} = 0.61 $mL g^{-1}$ and S_{BET} = 1100 $m^2 g^{-1}$). This points to significant pore blockage upon deposition of large quantities of the heteropolyacid. The same was observed in the case of the silica-supported material. Incorporation of the active phase reduced the S_{BET} of the bare support by 20 $m^2 g^{-1}$ and its V_{pore} by 0.15 $mL g^{-1}$. In the case of the IER-supported solid, no differences were observed relative to the pristine carrier. H-, Ag-, and Cs-HPA deposited on carbon were amorphous, as no distinctive reflections were observed by X-ray diffraction (Figure S1a in the Supporting Information). On the other hand, H-HPA/SiO_2 and the bulk materials showed typical reflections of the Keggin-type phosphomolybdic acid. The very sharp diffraction lines point to crystals >100 nm in size Taking into account the substantially different loadings of the elements, energy-dispersive X-ray spectroscopy (EDS) mapping of the Cs-HPA/C catalyst (Figure 1a) displayed homogeneous distributions of Cs, Mo, and P on the carbon support, in line with a high dispersion of the active phase. Additionally, the absence of areas enriched in Mo or P pointed to a preserved heteropolyacid structure.

The catalytic activities of the prepared materials were tested in the batch epimerization of glucose to mannose. The heteropolyacid-based catalysts exhibited better performances than the bulk molybdenum oxide (Table 1 and Table S1), as expected on the basis of previous evidence.[22] Interestingly, the exchange of protons by cesium or silver cations did not influence the reaction rate significantly, in line with the fact that protons do not partake in the reaction,[28] but the material became less soluble and only 13–21% of the molybdenum leached from the solids into the reaction mixture.

The immobilization of molybdic acid onto solid supports led to inferior (IER carrier), similar (SiO_2 carrier), or doubled (C carrier) activity. The enhancement in the turnover frequency (TOF) in the latter case (Table 1) is possibly due to a better dispersion of the active phase. The amount of Mo leached varied over a very broad range. Specifically, the maximum (61%) was observed in the case of the silica-supported solid and the minimum (3%) for H-HPA/IER. This indicates that ionic interactions, which were expected to be the only means for immobilization onto the IER, are most beneficial to anchor the active phase in a stable manner, whereas weak dipolar interactions, such as those acting in the case of silica, are ineffective. Both mechanisms likely play a role in the deposition of HPA on carbon,[23] which rationalizes the intermediate leaching observed by using this carrier. Immobilization of the ion-exchanged HPAs produced catalysts showing activities and selectivities comparable to those shown by H-HPA/C, in line with the testing of the bulk materials featuring different counterions. Still, these solids were more stable, as metal depletion was similar to that of the robust H-HPA/IER. Also in this case, the presence of a different counterion did not significantly alter the activity or selectivity. On the basis of its high activity and robustness, Cs-HPA/C was chosen to investigate the temperature dependence of the reaction and the catalyst stability upon repeated use. Regarding the first aspect, a negligible glucose conversion was observed below 313 K, whereas it steadily increased between 333 and 373 K (Figure 2a). The Mo leaching over 10 cycles was higher than 80% in the case of H-HPA/C but was limited to only 35% in the case of Cs-HPA/C (Figure 2b). Notably, in both cases, the Mo/P ratio did not change, which likely indicates that the Keggin-type structure was maintained. On the basis of these results, Cs-HPA/C was tested in continuous mode under industrially relevant, that is, high-conversion, conditions (Figure 2c). A minor activity loss was observed over the first 12 h on stream, whereas deactivation became more pronounced in the subsequent 12 h of the test. The major reason for the activity loss seems to be the substantial (45%) depletion of the Mo content, as determined by elemental analysis. It should be noted that, despite significant deactivation, the stability of this optimized catalyst was found to be greatly superior to that of

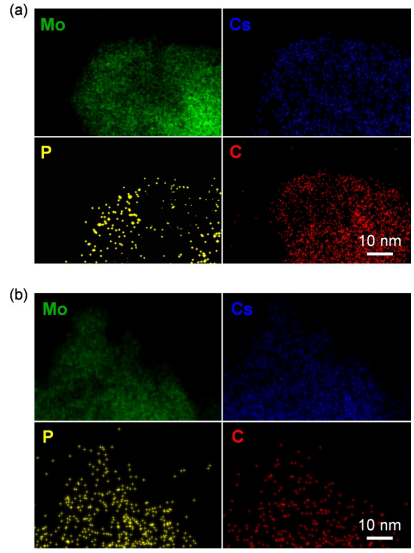

Figure 1. EDS mapping of Mo, Cs, P, and C for Cs-HPA/C in (a) fresh and (b) used forms.

4.4. Paper IV: Glucose and mannose conversions

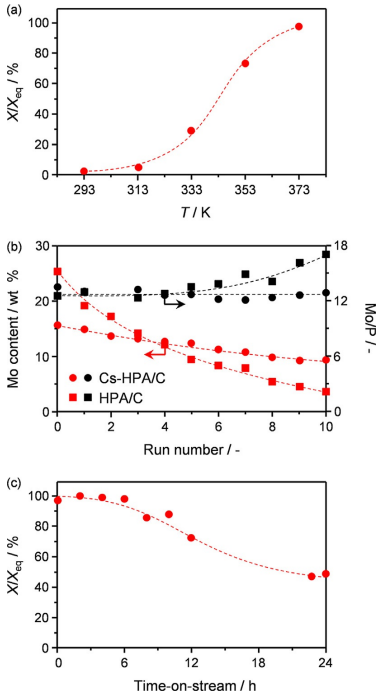

Figure 2. (a) Glucose conversion (relative to the equilibrium) as a function of temperature over Cs-HPA/C. (b) Variation in the molybdenum content and the molar molybdenum-to-phosphorous ratio upon consecutive batch runs over H-HPA/C and Cs-HPA/C at 333 K. (c) Glucose conversion (relative to the equilibrium) versus time-on-stream during continuous experiments over Cs-HPA/C at 363 K.

previously reported materials. The used catalyst was analyzed by transmission electron microscopy (TEM)-EDS (Figure 1 b), which showed that the fine distribution of the active phase was preserved. The slightly decreased intensity of the Cs, Mo, and P signals in the map of the used sample is in line with leaching (Table 1). Finally, Cs-HPA/C was evaluated in the epimerization of arabinose to ribose and of xylose to lyxose. In both cases, high selectivities were attained (Table 2), and the turnover frequencies were similar to that obtained in the conversion of glucose, which confirmed the versatility of this catalyst with respect to the nature of the saccharide substrate.

Design of the hydrogenation catalysts

For the hydrogenation of glucose/mannose, xylose/lyxose, and arabinose/ribose mixtures obtained by epimerization of the first more naturally abundant sugar over molybdate-based materials, the catalyst selection relied on literature studies on the reduction of fructose to mannose. Ruthenium supported on carbon has been reported to display the highest activity in this reaction, although its selectivity to mannitol is limited by the sustained formation of the epimeric alcohol sorbitol. A more selective process has been attained by alloying this element with other metals.[17] To choose the most suitable material, we thus prepared a 5 wt% Ru/C catalyst as well as bimetallic systems comprising the same amount of Ru and 1 wt% Sn, Cr, La, or Pd by incipient wetness. As shown in Table 3, the actual metal loadings were determined to be close to the nominal values. The porous properties of the support were not substantially modified upon deposition of the active phase. No reflections attributed to any of the metals were observed in the XRD patterns of the solids (Figure S1 b), which was indicative of high dispersion. The latter was determined for Ru to be in the 54–67% range on the basis of CO chemisorption. Additionally, TEM analysis of Ru/C (Figure 3 a) visualized very small metallic particles with diameters less than 5 nm.

Testing of these catalysts in the hydrogenation of fructose surprisingly revealed that the presence of any of the second metals did not improve the mannitol/sorbitol ratio (Figure 3 b) and reduced the activity. The discrepancy between our data and earlier evidence may originate from the different reaction conditions applied.[17] On the basis of these results, further studies were conducted over the simple Ru/C catalyst. Firstly, the dependence of mannitol selectivity on the temperature and hydrogen pressure was explored. Although very different operating conditions were investigated (Figure 3 c), only slight changes in the mannitol selectivity were observed, which was the highest below 0.7 MPa and at 313–343 K. On the other hand, the conversion increased monotonously with the tem-

Table 2. Performance of Cs-HPA/C in the epimerization of arabinose and xylose.[a]

Reaction	X_{eq} [b] [%]	TOF[c] [h^{-1}]	S_{epimer} [d] [%]
arabinose↔ribose	41.2	54.3	96.6
xylose↔lyxose	52.7	48.2	98.1

[a] Reaction conditions: $T = 333$ K, [arabinose, xylose] = 0.28 M, (arabinose, xylose)/Mo = 50, $t = 30$ min. [b] Equilibrium conversion obtained at $t = 16$ h. [c] Based on Mo. [d] Selectivity to ribose or lyxose from arabinose and xylose, respectively.

Table 3. Characterization data of the ruthenium-based catalysts.

Catalyst	Ru[a] [wt%]	M[b] [wt%]	V_{pore} [c] [mL g^{-1}]	S_{BET} [d] [m^2 g^{-1}]	D_{CO} [e] [%]
Ru/C	4.8	–	0.58	912	61
RuSn/C	5.1	1.0	0.61	956	54
RuCr/C	4.9	0.9	0.53	988	58
RuLa/C	4.8	1.0	0.55	973	60
RuPd/C	5.0	1.0	0.57	934	67

[a] ICP-OES. [b] XRF. [c] Volume of N_2 adsorbed at $p/p_0 = 0.99$. [d] BET method. [e] Ru dispersion determined by CO pulse chemisorption.

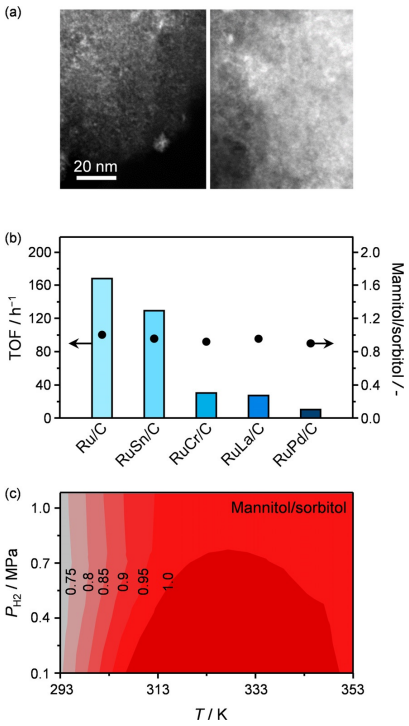

Figure 3. (a) HAADF-STEM micrographs for the fresh (left) and used (right) Ru/C catalyst. (b) Effect of metal modifiers on the fructose hydrogenation activity and selectivity to mannitol of Ru/C at 333 K. The TOF was calculated on the basis of the exposed Ru sites. (c) Mannitol/sorbitol ratio upon fructose hydrogenation versus temperature and H_2 pressure.

perature or the pressure (Figure S2). Subsequent testing of the hydrogenation of the mixtures of epimers was conducted in these ranges. Batch experiments performed at low conversion levels proved that the hydrogenation of one of the two epimers proceeded more readily for all mixtures (Table 4). In particular, mannose, lyxose, and ribose were reduced to the corresponding sugar alcohols 2–3 times faster than their isomers. To further investigate this effect, kinetic tests were performed to derive the apparent activation energies for the conversion of the two hexoses. On the basis of the Arrhenius plots (Figure 4a), the hydrogenation of mannose was found to be less impeded than that of glucose by 6.5 kJ mol^{-1}.

Table 4. Reaction rates for the hydrogenation of glucose/mannose, xylose/lyxose, and arabinose/ribose on Ru/C.[a]

Sugar mixture (*i*/*j*)	TOF_i [h^{-1}]	TOF_j [h^{-1}]
glucose/mannose	13.4	25.1
xylose/lyxose	10.9	23.6
arabinose/ribose	19.1	48.1

[a] Reaction conditions: T = 333 K, [glucose, xylose, arabinose] = [mannose, lyxose, ribose] = 0.14 M, (glucose + mannose, xylose + lyxose, arabinose + ribose)/Ru = 100, t = 15 min, P_{H_2} = 0.1 MPa.

This significant difference implies that, assuming first-order reaction kinetics, the maximum theoretical mannitol/sorbitol formation rate ratio is between 4 and 2.5 in the 293–373 K range (Figure 4b), as confirmed by the experimental data. This hints at the possibility of overcoming, after adequate engineering of the catalyst and the process, the approximately 1:1 sugar ratio obtained upon epimerization. Ultimately, the two-step process would thus enable an overall higher selectivity than that obtained by direct hydrogenation of the typically rare ketose. The analogous differences in the reaction rate observed during the hydrogenation of mixtures of aldopentose epimers likely find the same origin. Indeed, the stereochemical configuration of the two carbon atoms in proximity to the carbonyl group is the same for glucose, arabinose, and xylose (2*R*,3*S*) and for mannose, ribose, and lyxose (2*S*,3*S*), which exhibited slower and faster reaction rates, respectively.

The stability of the hydrogenation catalyst was evaluated in 24 h runs (Figure 5a–c). The catalyst lost 15–35% of its original activity in the conversion of the three mixtures. This evidence is in line with previous hydrogenation studies for which Ru/C catalysts were used and for which the deactivation was ascribed to fouling or poisoning by adsorption of trace amounts

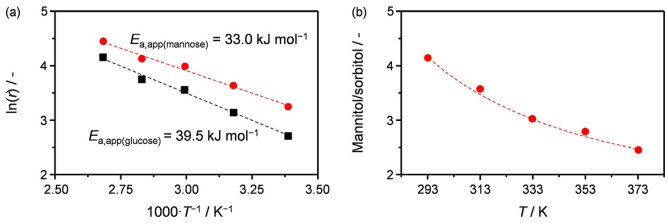

Figure 4. (a) Arrhenius plot and the corresponding apparent activation energies for the hydrogenation of glucose and mannose over Ru/C. (b) Mannitol/sorbitol ratio versus temperature. The red line represents the theoretical values obtained from the activation energies.

4.4. Paper IV: Glucose and mannose conversions

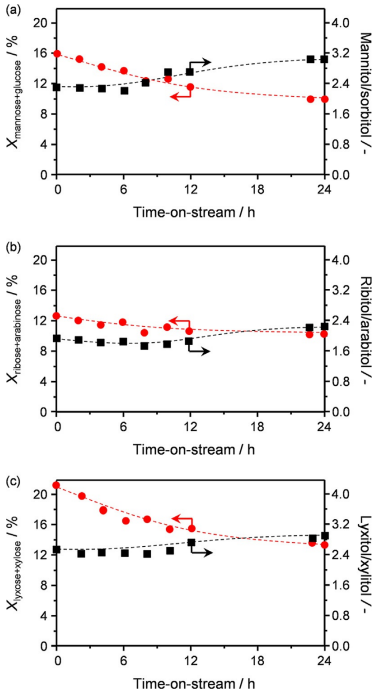

Figure 5. Total conversion and ratio of sugar alcohols for the hydrogenation of (a) glucose/mannose, (b) ribose/arabinose, and (c) lyxose/xylose mixtures over Ru/C at 333 K

of gluconic/mannonic acids formed upon exposure of the starting saccharide solutions to air.[29] An increase in the sugar alcohol ratio was observed in parallel to the decrease in activity. This is explained by the fact that, at higher conversion levels, the concentration of the slower reacting sugar is greater than that of the faster reacting one, which lowers the difference between their actual hydrogenation rates. Aiming at a more robust process, the catalyst could be periodically washed with a suitable solvent to restore its functionality or the liquid feed could be isolated under an inert atmosphere. Additionally, the sugar alcohol ratio was slightly altered in favor of mannitol, ribitol, and arabitol with time on stream. This is explained by the fact that the more reactive sugar is consumed more rapidly than the more inert epimer. Accordingly, keeping a low conversion level ensures a higher amount of mannose, ribose, and lyxose available as substrates, which promotes the formation of the desired alcohol.

DFT was applied to unravel the molecular reason for the different reactivities of the sugars and epimers towards hydrogenation by considering the case of glucose and mannose. First, the adsorption modes of these two saccharides on a metallic Ru(0 0 0 1) surface were studied. In the liquid phase, their cyclic α and β forms dominate over their open structures (denoted as *o*-glucose and *o*-mannose). Specifically, α-glucose, β-glucose, α-mannose, and β-mannose are more abundant (33, 66, 66, and 33 %, respectively) than *o*-glucose and *o*-mannose, which only account for less than 1 % each.[30] Nevertheless, both configurations were considered. The adsorption geometries obtained in the screening are reported in Figure S3, and the adsorption energies relative to the most stable configuration are reported in Table S2. The calculated energy of water solvation for β-glucose (−87.8 kJ mol^{-1}) is in reasonable agreement with previous reports (−77.2 kJ mol^{-1}).[31]

Thereafter, activation energies for the hydrogenation reactions were computed. Those obtained for the linear forms (Table S3 and Figure S4) are not able to explain the difference in rate determined experimentally, probably because of their negligible concentration in solution. The results for the ring structures (Figure 6) show that the α forms have lower adsorption energies than the β forms for both glucose (−97.4 vs. −92.6 kJ mol^{-1}) and mannose (−124.5 vs. −109.0 kJ mol^{-1}) with energy differences of 4.8 and 15.5 kJ mol^{-1}, respectively. Moreover, they indicate that both α- and β-mannose adsorb on the catalyst more strongly than α- and β-glucose. The different stereochemical configuration of the C2 in mannose (*S*) relative to that in glucose (*R*) increases the number of sugar interactions

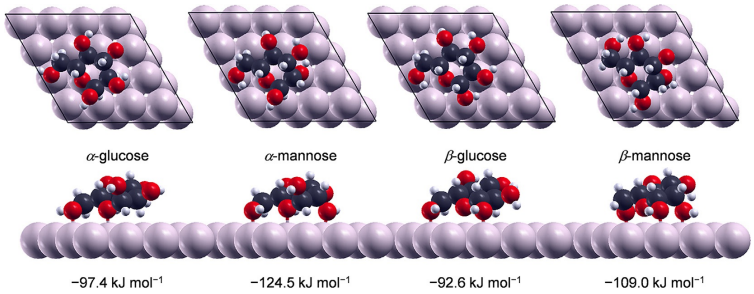

Figure 6. Adsorption structures and binding energies of the α and β forms of glucose and mannose on Ru(0 0 0 1).

with Ru through O atoms by one, which, as reported earlier, is the primary contributor to adsorption.[32] After interaction with the metal, the molecules can react with water, which leads to *o*-glucose and *o*-mannose, or with adsorbed H atoms. For both glucose and mannose, the transition states relative to ring opening[33] and the following hydrogenation reaction were initially studied in the absence of water (Table 5). The energy barriers for ring opening (C–O cleavage, see Scheme 2) are comparably high for β-glucose and α-mannose (150.5 and 144.7 kJ mol^{-1}, respectively) and are lower than the energy barriers of the other two isomers, α-glucose (193.9 kJ mol^{-1}) and β-mannose (174.6 kJ mol^{-1}). Regarding hydrogenation, two sites are present that can accept H atoms (C1 and O5). For both glucose and mannose, O5 hydrogenation is associated with higher barriers than C1 hydrogenation. The energy demand of the latter is lower for α- and β-mannose (162.1 and 205.9 kJ mol^{-1}) than for α- and β-glucose (297.2 and 260.5 kJ mol^{-1}), which points to the positive effect of the additional interaction between the surface and the C2 or C1 hydrogenation. On the basis of the values obtained, it appears that the different configuration of C2 determines that the reactive conformation is α in the case of mannose and β in the case of glucose. In view of the distance between C2 and O5, the impact of Ru–C2 bonding is not effective in lowering the O5 hydrogenation barrier. Additional theoretical simulations were performed considering the presence of a water molecule to attain a more realistic representation of the catalytic system. The results (Figure 7) indicate that the presence of the solvent promotes ring opening by lowering the energy demand by 55.0 and 5.9 kJ mol^{-1} for β-glucose and α-mannose, respectively. The beneficial impact of water is twofold: it provides an H atom for O5 protonation and stabilizes the transition states by hydrogen bonding (Scheme 2). In spite of a lower ring-opening barrier, the activation energy for C1 hydrogenation is higher for *o*-glucose than for *o*-mannose (116.7 vs. 91.7 kJ mol^{-1}). Hence, the rate-determining steps are C1 hydrogenation for β-glucose and ring opening for α-mannose.

Table 5. Activation barriers (E_a) for ring-opening and hydrogenation reactions for glucose and mannose in the presence or absence of H_2O.

Species	E_a [kJ mol^{-1}]				
	C–O	C1+H	O5+H	C–O(H_2O)	C+H
α-glucose	193.9	297.2	321.3	194.9	–
β-glucose	150.5	260.5	235.4	95.5	116.7
α-mannose	144.7	162.1	247.0	131.2	91.7
β-mannose	174.6	250.9	272.1	159.2	–

To explain the experimental results, a kinetic model based on Langmuir competitive adsorption and transition state theories was built.[34] The coverage of surface species was estimated by Equation (1) and (2):

$$\theta_{i-A} = \frac{K_{i-A}^{ads} \cdot [i-A]}{1 + \sum_i K_{i-A}^{ads} \cdot [i-A]} \quad (1)$$

for which

$$K_{i-A}^{ads} = exp\left(\frac{-\Delta G_{i-A}^{ads}}{RT}\right) \quad (2)$$

and K_{i-A}^{ads} is the equilibrium constant for the adsorption of *i*–*A*, ΔG_{i-A}^{ads} is the Gibbs energy of the adsorption, and [*i*–*A*] is the concentration of glucose or mannose in the form *i* (α or β) in solution. The expression for the hydrogenation rate is [Eq. (3)]:

$$r_{i-A} = k_{i-A} \cdot \theta_{i-A} \cdot \theta_H = A_{i-A}\left(\frac{-E_{i-A}^{A}}{RT}\right) \cdot \theta_{i-A} \cdot \theta_H \quad (3)$$

in which k_{i-A} is the rate coefficient, A_{i-A} is the pre-exponential factor for the hydrogenation reaction, E_{i-A}^{a} is the energy barrier for the rate-limiting process (i.e., ring opening or hydrogenation), and θ_H is the surface coverage of H (which is treated as a constant; i.e., $\theta_H = 1$). According to the analysis of the transition states, only β-glucose and α-mannose would be hydro-

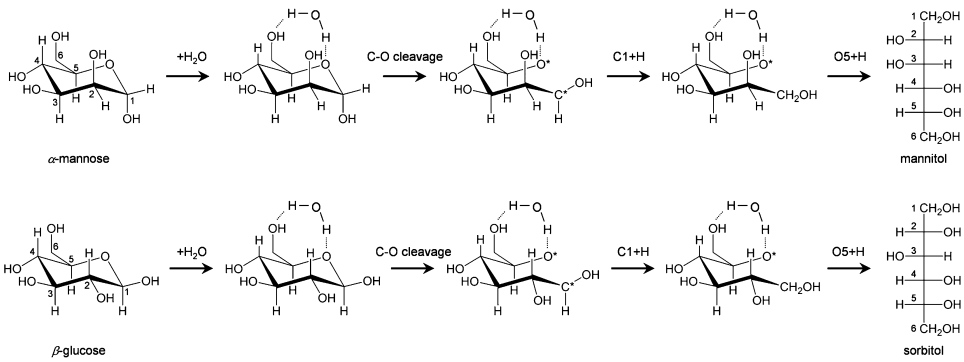

Scheme 2. Reaction mechanisms for the hydrogenation of α-mannose to mannitol (top) and β-glucose to sorbitol (bottom).

4.4. Paper IV: Glucose and mannose conversions

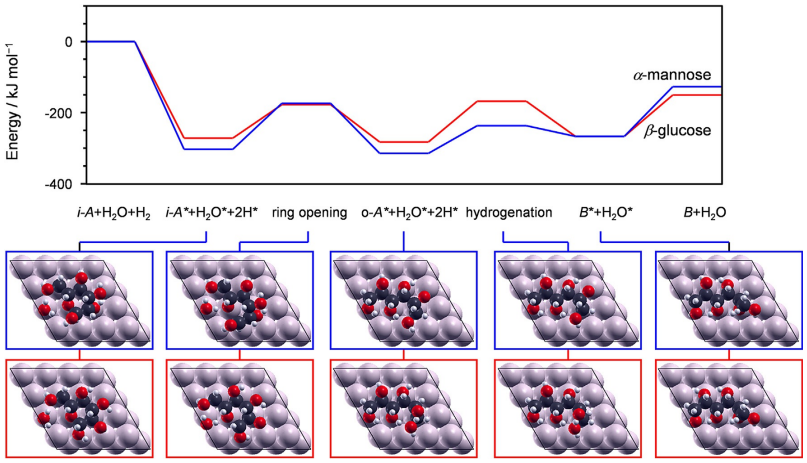

Figure 7. Energy profiles for the hydrogenation of β-glucose to sorbitol (red) and of α-mannose to mannitol (blue) and the corresponding structures calculated over the Ru(0001) surface.

genated with lower energy barriers. The most energy-demanding steps are different for α-mannose (step 2) and β-glucose (step 3), as shown in Table 6. The relative rates for glucose and mannose hydrogenation can be written as follows, for which C–O refers to the ring-opening reaction and C+H to C1 hydrogenation [Eq. (4)]:

$$\frac{r_{\alpha-\text{mannose}}}{r_{\beta-\text{glucose}}} \approx \frac{r_{\alpha-\text{mannose,C-O}}}{r_{\beta-\text{glucose,C+H}}} = \frac{k_{\alpha-\text{mannose,C-O}} \cdot \theta_{\alpha-\text{mannose}}}{k_{\beta-\text{glucose,C+H}} \cdot \theta_{o-\text{glucose}} \cdot \theta_H}$$
$$\approx \frac{k_{\alpha-\text{mannose,C-O}} \cdot \theta_{\alpha-\text{mannose}}}{k_{\beta-\text{glucose,C+H}} \cdot K^{\text{C-O}}_{\beta-\text{glucose}} \cdot \theta_{\beta-\text{glucose}}}$$
$$= exp\left(-\frac{E^{a}_{\alpha-\text{mannose}} + \Delta G^{ads}_{\alpha-\text{mannose}} - E^{a}_{\beta-\text{glucose}} - \Delta G^{ads}_{\beta-\text{glucose}}}{RT}\right)$$
$$\cdot \frac{[\alpha-\text{mannose}]}{K^{\text{C-O}}_{\beta-\text{glucose}} \cdot [\beta-\text{glucose}]}$$
$$= \frac{1}{K^{\text{C-O}}_{\beta-\text{glucose}}} exp\left(-\frac{E^{a}_{\alpha-\text{mannose}} + \Delta G^{ads}_{\alpha-\text{mannose}} - E^{a}_{\beta-\text{glucose}} - \Delta G^{ads}_{\beta-\text{glucose}}}{RT}\right) \quad (4)$$

in which $\theta_{o\text{-glucose}}$ is the surface coverage of open glucose and $K^{\text{C-O}}_{\beta-\text{glucose}}$ is the equilibrium constant of the β-glucose ring-opening reaction. Given that mannose can be practically obtained from glucose by an equilibrium-limited epimerization reaction with [glucose]/[mannose] ≈ 2 [Eq. (5)]:

$$\frac{[\alpha-\text{mannose}]}{[\beta-\text{glucose}]} = \left(\frac{2}{3}[\text{mannose}]\right) / \left(\frac{1}{3}[\text{glucose}]\right) \approx 1 \quad (5)$$

Using the calculated adsorption and activation energies, the ratio of reaction rates between α-mannose and β-glucose was estimated to be approximately 11. Considering that the DFT simulations were performed with several approximations, including the use of only one adsorption configuration for the reactants and the use of a single molecule of water in the ring-opening step and excluding solvation effects when the molecule was adsorbed, the qualitative agreement between this estimate and the value derived experimentally (2.7) is remarkable. In this perspective, even the order of magnitude of the relative activity is meaningful. Notice that the error associated with the difference in the computed and experimentally estimated energy barriers corresponds to only 0.04 eV.

Table 6. Steps for the hydrogenation of α-mannose and β-glucose on Ru(0001).[a]

Step	α-Mannose	β-Glucose
1	α-mannose+*↔α-mannose*	β-glucose+*↔β-glucose*
2	α-mannose*→*o*-mannose*[a]	β-glucose*↔*o*-glucose*[a]
3	*o*-mannose*+H*↔mannitol*+*	*o*-glucose*+H→sorbitol*+*
4	mannitol*↔mannitol+*	sorbitol*↔sorbitol+*

[a] *o*-Mannose* and *o*-glucose* correspond to the linear structures of mannose and glucose, respectively.

Process design

The identification of efficient epimerization and hydrogenation catalysts suitable for use under flow conditions opens the door to realize a continuous two-step process for the conversion of glucose into mannitol. To this end, the configuration of the catalytic bed(s) and the operation temperature comprise the main parameters to be tuned. Initially, the performance of a single bed constituted by a physical mixture of the two cata-

lysts was evaluated. In this case, the temperature was set to 363 K, as the epimerization catalyst Cs-HPA/C cannot produce a high concentration of mannose under milder conditions (Figure 2a), as discussed before. At the initial stages of the reaction, the mannitol/sorbitol ratio was approximately 1 (Figure 8a and Table S4). This is a remarkable result, as the value is equivalent to that obtained in the reduction of fructose.[11] Still,

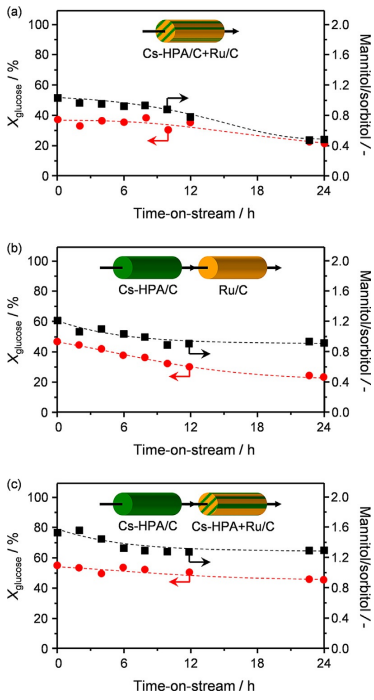

Figure 8. Glucose conversion and mannitol/sorbitol ratio by using different reactor configurations: (a) a single reactor with a mixture of Cs-HPA/C and Ru/C at 363 K, (b) two series reactors containing Cs-HPA/C at 363 K and Ru/C at 333 K, respectively, and (c) two series reactors containing Cs-HPA/C at 363 K and a mixture of Cs-HPA/C and Ru/C at 333 K, respectively.

during the course of the reaction, the glucose conversion decreased by approximately 30% and the mannitol/sorbitol ratio was reduced to approximately 0.4. The two observations are likely related, that is, the lower amount of mannitol formed as a result of the deactivation of the epimerization catalyst caused a reduction in the mannitol production rate, similar to the case of the hydrogenation of equimolar mixtures of epimers (Figure 5). Moreover, the hydrogenation catalyst was operated at an excessively high temperature, which could trigger additional deactivation phenomena (Figure 4b). Hence, an improved process was achieved by separating the epimerization and the hydrogenation catalysts into two distinct reactors. In this case, the temperature applied to the latter could be lowered by 50 K, which theoretically should enable an increase in the mannitol/sorbitol ratio by approximately 40%. In this configuration, the polyols ratio was raised to 1.2 (Figure 8b and Table S4) and, owing to the milder conditions in the second reactor, remained significantly more stable than in the first scenario. The glucose conversion and the deactivation rate were similar to those observed in the previous case. Still, further optimization of the process was envisaged on the basis of the following reasoning. Even if the hydrogenation catalyst is operated at its optimal temperature, concentration gradients will develop along the bed. Specifically, the portion of catalyst located closer to the reactor outlet will be contacted with a solution containing much less mannose, as a great part of it will have already been converted over the fraction of catalyst placed at the beginning of the bed. Thus, the formation of mannitol will decrease along the bed. Consequently, a third configuration was explored, in which the first reactor was dedicated solely to epimerization at high temperature (363 K) and the second reactor contained a mixture of Ru/C and Cs-HPA/C, operated at a lower temperature (333 K). In this way, the mannose concentration, which decreases during the course of the hydrogenation reaction, could be restored continuously. Remarkably, the mannitol/sorbitol ratio increased even further to approximately 1.6 (Figure 8c and Table S4). Additionally, the glucose conversion was constant over 1 day, possibly thanks to the overall increased mass of the Cs-HPA/C catalyst. In line with that observed in the second process design, the mannitol selectivity remained more stable over the same timeframe as well.

This continuous chemocatalytic technology stands as a promising alternative to the batch biocatalytic preparation of sugar alcohols. In fact, it allows for higher operational flexibility and for reduced waste production, as sugar feeds featuring a less constrained composition and a higher concentration can be applied. Moreover, it is foreseen that the continuous-flow reactors can be scaled up easily and that energy can be saved through heat integration between units, that is, heat recovered from the reactors can produce energy to operate the separation units. These elements are expected to substantially lower the economic and environmental footprint of the production of polyols.

Conclusions

We successfully demonstrated a chemocatalytic continuous process for the preparation of sugar alcohols from the epimers of their corresponding aldoses. Targeting the preparation of mannitol from glucose, ribitol from arabinose, and arabinol from xylose, an improved epimerization catalyst was initially developed. In this regard, activated carbon was uncovered as a support offering higher stability to the immobilized phosphomolybdic acid phase. Ion exchange of the heteropolyacid from the protonic form to the cesium form limited its large solubility even further, which led to partial retention of the original catalyst performance even after 24 h on stream. Thereafter, the hydrogenation of mixtures of epimers over a ruthenium

catalyst was studied. Interestingly, the reaction rate was found to be dependent on the stereochemical configuration of the sugar. Density functional theory simulations showed that the latter strongly influences the adsorption and activation energies for the hydrogenation of the carbon atom. Finally, the process design was optimized through the selection of the most efficient reactor configuration. The use of two series flow reactors brought considerable advantages with respect to a single reactor. In particular, the mannitol yield was maximized if the first reactor contained the epimerization catalyst and the second reactor contained a mixture of the epimerization and hydrogenation solids. In addition to improved selectivity, the possibility of optimizing the operation temperature in each reactor led to a remarkable increase in catalyst stability. Overall, this process enables a rather straightforward method for the preparation of rare polyols starting from widely available sugars. The use of a fully chemocatalytic technology, in contrast to fermentation, shall grant reduced waste production, continuous operation, easier scalability, and, possibly, improved ecological and economic metrics.

Experimental Section

Catalyst preparation

Hydrated phosphomolybdic acid (Sigma–Aldrich, >99%, denoted H-HPA) and MoO_3 (Sigma–Aldrich, 99.5%) were used as received. Silver and cesium phosphomolybdates were prepared by coprecipitation of H-HPA (0.01 M aqueous solution) with $AgNO_3$ (ABCR, 99.9%) and $CsNO_3$ (Acros Organics, 99.99%), respectively, which were added in 50% molar excess. The solids were separated by filtration, washed with deionized water (≈100 mL per gram of dried material), and dried (338 K, 16 h). They were labeled Ag-HPA and Cs-HPA. Supported HPA catalysts were prepared by using silica (Sipernat 120, code SiO_2), an anionic ion-exchange resin (Amberlyst A26, Sigma–Aldrich, code IER), and granulated activated carbon (Norit Cabot RX 1.5 Extra, 0.2–0.4 mm sieve fraction, code C). The supports (2.0 g) were added to a solution of H-HPA (0.5 g) in water (50 mL), and the suspension was magnetically stirred for 2 h. Thereafter, the solids were separated by filtration, washed with deionized water (≈100 mL per gram of dried support), and dried (338 K, 16 h). They were labeled H-HPA/SiO_2, H-HPA/IER, and H-HPA/C. Two additional C-supported samples (Ag-HPA/C and Cs-HPA/C) were produced through the same procedure by adding $AgNO_3$ or $CsNO_3$ to the suspension. A supported 5 wt% Ru/C catalyst was synthesized by impregnation of the C support with an aqueous solution of $RuCl_3{\cdot}H_2O$ (ABCR, 99.9%), followed by drying (338 K, 16 h) and reduction in hydrogen flow (20 vol% H_2/N_2, 100 mL min^{-1}, 723 K). Bimetallic 5 wt% Ru/1 wt% M/C catalysts (M = Sn, Cr, La, or Pd) were prepared through the same method by additionally using $SnSO_4$, $Cr(NO_3)_3{\cdot}9H_2O$ (Sigma–Aldrich, 99%), $LaCl_3$ (ABCR, 99.9%), or $PdCl_2$ (ABCR, 99.9%) as the precursor of the second metal upon impregnation.

Catalyst characterization

The Mo and Ru contents in the catalysts were determined by inductively coupled plasma optical emission spectroscopy (ICP-OES) by using a Horiba Ultra 2 instrument equipped with a photomultiplier tube detector. The Sn, Cr, La, and Pd contents and the Mo/P ratio were determined by X-ray fluorescence (XRF) spectroscopy by using an EDAX Orbis Micro-XRF analyzer equipped with a Rh source operated at a voltage of 35 kV and a current of 500 μA. Powder X-ray diffraction (XRD) was performed by using a PANalytical X'Pert PRO-MPD diffractometer with Ni-filtered CuK_α radiation ($\lambda = 0.1541$ nm), acquiring data in the $2\theta = 5–70^\circ$ range with a step size of 0.05° and a counting time of 8 s per step. N_2 sorption at 77 K was conducted by using a Micromeritics TriFlex analyzer. Prior to the measurements, the samples were degassed at 573 K under vacuum for 3 h. High-angle annular dark field scanning transmission electron microscopy (HAADF-STEM) images and energy dispersive spectroscopy (EDS) elemental maps were acquired by using a FEI Talos instrument operated at 200 kV. Powdered samples were deposited on Cu grids. HAADF images were collected before and after the EDS measurements to corroborate the absence of morphological changes. CO chemisorption was performed by using a Micromeritics AutoChem II 2920 chemisorption analyzer. The samples were heated at 393 K under a He flow (50 mL min^{-1}) for 60 min and were then reduced at 523 K under a flow of 5 vol% H_2/He (20 mL min^{-1}) for 30 min. Afterwards, 1 mL of 1 vol% CO/He was pulsed over the catalyst bed at 308 K every 4 min. The Ru dispersion was calculated on the basis of the amount of CO chemisorbed, considering an adsorption stoichiometry of 1.

Catalytic testing

Batch epimerization experiments were performed under autogenous pressure in 15 mL, thick-walled glass vials (Ace, pressure tubes, front seal) dipped in an oil bath heated at 303–353 K. The vials were loaded with approximately 10 mL of a 0.28 M aqueous solution of glucose, arabinose, or xylose. Then, the appropriate amount of molybdate-based catalyst was added to achieve a substrate/Mo molar ratio of 50. The mixture was allowed to react under vigorous stirring for 30 min. Thereafter, the reaction was quenched by using an ice bath, and the catalyst removed by means of a Chromafil Xtra 0.25 μm syringe filter. Batch hydrogenation experiments were performed under 1.0 MPa hydrogen (Messer, 99.999%) in 10 mL autoclaves (Endeavor) at 303–393 K. The vials were loaded with 5 mL of a 0.28 M fructose (Sigma–Aldrich, >99%), a 0.14 M glucose (Sigma–Aldrich, 99.5%)–0.14 M mannose (Sigma–Aldrich, >99%), a 0.14 M arabinose (ABCR, 99%)–0.14 M ribose (ABCR, 98%), or a 0.14 M lyxose (ABCR, 99%)–0.14 M xylose (Sigma–Aldrich, >99%) solution in deionized water. Then, the appropriate amount of Ru/C or modified Ru/C catalyst was added to achieve a substrate/Ru molar ratio of 100 and hydrogen was introduced. The mixture was heated to the desired reaction temperature and allowed to react under 1000 rpm stirring for 1 h. Then, the reaction was quenched, and the catalyst was removed by using a Chromafil Xtra 0.25 μm syringe filter.

Continuous catalytic tests were performed by using a homemade flow reactor setup comprising: one, an HPLC pump (Gilson-306); two, a mass flow controller; three, stainless-steel tubular reactors (Swagelok SS-T4-S-035, o.d. = 6 mm, i.d. = 4.6 mm) placed in tubular ovens; four, a backpressure regulator (Swagelok, LH2981001). In the case of epimerization reactions, the reactor was loaded with the catalyst (0.2–0.3 g, sieve fraction = 0.2–0.4 mm) and diluted with quartz (0.5 g, sieve fraction = 0.2–0.4 mm). After heating at the desired temperature, a liquid feed (0.5 mL min^{-1}, 0.28 M glucose, arabinose, or xylose aqueous solution) was admitted, and the system was pressurized at 1.0 MPa. For hydrogenations of glucose/mannose, arabinose/ribose, and xylose/lyxose mixtures, the reactor was loaded with the catalyst (0.2–0.3 g, sieve fraction = 0.2–0.4 mm, diluted with 0.5 g quartz of the same sieve fraction). The combination of the epimerization and hydrogenation steps was

studied by using a mixed catalyst bed or two separate catalytic beds operated at different temperatures. In the former case, the reactor was loaded with a mixture of the two catalysts (0.2 g Ru/C, 0.2 g Cs-HPA/C, diluted with 0.4 g quartz). In the latter case, the two reactors were loaded with Cs-HPA/C (0.4 g, diluted with 0.4 g quartz) and Ru/C (0.2 g, diluted with 0.6 g quartz), respectively. Alternatively, the second reactor was filled by using a mixture of the two catalysts (0.2 g Ru/C, 0.2 g Cs-HPA/C, diluted with 0.4 g quartz). The hydrogenation and combined epimerization–hydrogenation reactions were started by following the same protocol as that for the epimerization reaction but adding a gas feed of 50 mL_{H_2} min^{-1}. In all tests, liquid samples were periodically collected at the outlet of the reactor.

Reaction products were isolated by high-performance liquid chromatography (HPLC) in an Agilent 1260 system equipped with a Biorad Aminex HPX-87C column heated at 338 K and a refractive index detector set at 303 K by using water (0.450 mL min^{-1}) as the eluent. Quantification was attained on the basis of the absolute peak areas. Calibration curves were measured in the 0.05–0.3 M range for the sugars and the corresponding sugar alcohols sorbitol (Sigma–Aldrich, >98%), mannitol (Fluka, 99%), arabitol (Acros Organics, 99%), xylitol (ABCR, 99%), and ribitol (Sigma–Aldrich, >99%). The conversion of substrate i (X_i) and selectivity to the product k (S_k) were calculated as follows [Eqs. (6) and (7)]:

$$X_i = 1 - \left(\frac{n_{i,1}}{n_{i,0}}\right) \quad (6)$$

$$S_k = \frac{n_{k,1}}{n_{i,0} - n_{i,1}} \quad (7)$$

in which n refers to the moles of i or k and 0/1 to the reaction beginning/end. The conversion of the mixtures of sugars was obtained by summing the conversions of the two aldose epimers. The epimerization equilibrium conversions for glucose, ribose, and arabinose were determined as the conversion observed after 16 h of reaction by using Cs-HPA as the catalyst and were 35.0, 41.2, and 52.7%, respectively, in good agreement with the literature data.[35]

Computational details

DFT was employed to study the ruthenium-catalyzed reduction of glucose and mannose by using the Vienna Ab Initio Simulation Package (VASP).[36] The exchange and correlation energies were obtained by using the PBE functional.[37] As glucose, mannose, and other intermediates as well as their hydrogenation products sorbitol and mannitol are large molecules, van der Waals correction was performed by using the Grimme's DFT-D2 method[38] with the C6 parameters developed in our group.[39] The inner electrons were represented by projector augmented wave (PAW) pseudopotentials[40] with cutoff energies of 450 eV. The calculated lattice parameter for Ru was 2.712 Å (c/a = 1.581), which agrees well with the known experimental value of 2.706 Å (c/a = 1.584).[41] Gas molecules were calculated in a box of 20×20×20 $Å^3$. The Ru/C catalyst was modeled by a four-layer ruthenium slab with a $p(4\times4)$ supercell, for which the two upmost layers were fully relaxed and the remaining atoms at the bottom were fixed to mimic the bulk. A 20 Å thick vacuum region was set between each slab to avoid their interaction. Given that adsorption was performed on one side of the slab, dipole correction was applied to eliminate the spurious contributions arising from the system's asymmetry. Gamma point sampling was used to obtain the adsorption geometries and transition states, and then their energies were calculated with a denser mesh than 30 $Å^{-1}$. The metal atoms were fixed during these processes. An extensive search of potential adsorption conformations was performed by following the adsorption rules previously developed in our group. Solvation contributions for the molecules in the liquid phase were investigated through the multigrid-based (MGCM) methodology.[42] The climbing image nudged elastic band (CI-NEB)[43] and improved dimer method (IDM)[44] were employed to locate the transition states in the potential surfaces. All transition states were confirmed with only one imaginary value in the frequency analysis. The most relevant structures were uploaded to the ioChem-BD database.[45]

Acknowledgements

This work was sponsored by the Swiss National Science Foundation (Project Number 200020–159760). Dr. S. Mitchell and E. Vorobjeva are thanked for the microscopic analyses. N.L. and Q.L. are grateful to MINECO (CTQ2015–68770-R) for financial support and to the Barcelona Supercomputing Centre (BSC-RES) for providing the computational resources.

Keywords: epimerization · flow chemistry · heterogeneous catalysis · hydrogenation · sugar alcohols

[1] a) Y.-C. Park, E. J. Oh, J.-H. Jo, Y.-S. Jin, J.-H. Seo, *Curr. Opin. Biotechnol.* **2016**, *37*, 105–113; b) P. Mäki-Arvela, B. Holmbom, T. Salmi, D. Y. Murzin, *Catal. Rev.* **2007**, *49*, 197–340.
[2] A. M. Langkilde, H. Andersson, T. F. Schweizer, P. Würsch, *Eur. J. Clin. Nutr.* **1994**, *48*, 768–775.
[3] T. M. S. Wolever, A. Piekarz, M. Holland, K. Younker, *Can. J. Diabetes* **2002**, *26*, 356–362.
[4] T. Matsuo, Y. Baba, M. Hashiguchi, K. Takeshita, K. Izumori, H. Suzuki, *J. Clin. Biochem. Nutr.* **2001**, *30*, 55–65.
[5] M. Fontana, C. González-Cabezas, *Adv. Dent. Res.* **2012**, *24*, 123–128.
[6] F. Zamora, K. Hakkou, A. Alla, J. L. Espartero, S. Muñoz-Guerra, J. A. Galbis, *J. Polym. Sci. Part A* **2005**, *43*, 6394–6410.
[7] E. L. Kunkes, D. A. Simonetti, R. M. West, J. C. Serrano-Ruiz, C. A. Gärtner, J. A. Dumesic, *Science* **2008**, *322*, 417–421.
[8] a) J. C. Serrano-Ruiz, J. A. Dumesic, *Energy Environ. Sci.* **2011**, *4*, 83–89; b) M. Rose, R. Palkovits, *ChemSusChem* **2012**, *5*, 167–176.
[9] T. Werpy, G. R. Petersen, *Top Value Added Chemicals from Biomass: Vol. I–Results of Screening for Potential Candidates from Sugars and Synthesis Gas*, DOE/GO-102004-1992,Department of Energy, Washington, DC, **2004**.
[10] O. Akinterinwa, R. Khankal, P. C. Cirino, *Curr. Opin. Biotechnol.* **2008**, *19*, 461–467.
[11] a) C. Luo, S. Wang, H. Liu, *Angew. Chem. Int. Ed.* **2007**, *46*, 7636–7639; *Angew. Chem.* **2007**, *119*, 7780–7783; b) J. V. Karabinos, A. T. Ballun, *J. Am. Chem. Soc.* **1953**, *75*, 4501–4502.
[12] M. Morales, P. Y. Dapsens, I. Giovinazzo, J. Witte, C. Mondelli, S. Papadokonstantakis, K. Hungerbühler, J. Pérez-Ramírez, *Energy Environ. Sci.* **2015**, *8*, 558–567.
[13] A. K. Sirkar, *US Pat. 4380678*, **1983**.
[14] T. Ona, T. Sonoda, K. Itoh, M. Shibata, *Holzforschung* **1997**, *51*, 396–404.
[15] J. Wisnlak, R. Simon, *Ind. Eng. Chem. Prod. Res. Dev.* **1979**, *18*, 50–57.
[16] a) R. A. Hales, US Pat. 3484492, 1969; b) H. J. Bart, R. C. Messenböck, C. H. Byers, A. Prior, J. Wolfgang, *Chem. Eng. Process.* **1996**, *35*, 459–471.
[17] A. W. Heinen, J. A. Peters, H. van Bekkum, *Carbohydr. Res.* **2000**, *328*, 449–457.
[18] M. A. Veksler, Y. I. Petrov, N. G. Geling, E. I. Klabunovskii, *Bull. Acad. Sci. USSR Div. Chem. Sci. (Engl. Transl.)* **1974**, *23*, 45–49.
[19] W. M. Kruse, *US Pat. 4029878*, **1977**.
[20] R. Bermejo-Deval, R. Gounder, M. E. Davis, *ACS Catal.* **2012**, *2*, 2705–2713.

[21] A. Takagaki, S. Furusato, R. Kikuchi, S. T. Oyama, *ChemSusChem* **2015**, *8*, 3769 – 3772.
[22] F. Ju, D. Van der Velde, E. Nikolla, *ACS Catal.* **2014**, *4*, 1358 – 1364.
[23] M. A. Schwegler, P. Vinke, M. van der Eijk, H. van Bekkum, *Appl. Catal. A* **1992**, *80*, 41 – 57.
[24] R. Sheikh, M.-S. Choi, J.-S. Im, Y.-H. Park, *J. Ind. Eng. Chem.* **2013**, *19*, 1413 – 1419.
[25] T. Baba, Y. Ono, *Appl. Catal.* **1986**, *22*, 321 – 324.
[26] a) J. A. R. van Veen, O. Sudmeijer, C. A. Emeis, H. de Wit, *J. Chem. Soc. Dalton Trans.* **1986**, 1825 – 1831; b) Z. Zhu, R. Tain, C. Rhodes, *Can. J. Chem.* **2003**, *81*, 1044 – 1050.
[27] M. Langpape, J. M. M. Millet, U. S. Ozkan, M. Boudeulle, *J. Catal.* **1999**, *181*, 80 – 90.
[28] V. Bílik, L. Petruš, V. Farkaš, *Chem. Zvesti* **1975**, *29*, 690 – 693.
[29] a) Z. Yan, L. Lin, S. Liu, *Energy Fuels* **2009**, *23*, 3853 – 3858; b) M. Besson, P. Gallezot, *Catal. Today* **2003**, *81*, 547 – 559.
[30] Y. Zhu, J. Zajicek, A. S. Serianni, *J. Org. Chem.* **2001**, *66*, 6244 – 6251.
[31] C. O. da Silva, B. Mennucci, T. Vreven, *J. Org. Chem.* **2004**, *69*, 8161 – 8164.
[32] R. García-Muelas, N. López, *J. Phys. Chem. C* **2014**, *118*, 17531 – 17537.
[33] W. Plazinski, A. Plazinska, M. Drach, *Phys. Chem. Chem. Phys.* **2015**, *17*, 21622 – 21629.
[34] I. Chorkendorff, J. W. Niemantsverdriet, *Concepts of Modern Catalysis and Kinetics*, Wiley-VCH, Weinheim, **2006**.
[35] S. J. Angyal, *Angew. Chem. Int. Ed. Engl.* **1969**, *8*, 157 – 166; *Angew. Chem.* **1969**, *81*, 172 – 182.
[36] a) G. Kresse, J. Furthmüller, *Comput. Mater. Sci.* **1996**, *6*, 15 – 50; b) G. Kresse, J. Furthmüller, *J. Phys. Rev. B* **1996**, *54*, 11169 – 11186.
[37] J. P. Perdew, K. Burke, M. Ernzerhof, *Phys. Rev. Lett.* **1996**, *77*, 3865 – 3868.
[38] a) S. Grimme, *J. Comput. Chem.* **2006**, *27*, 1787 – 1799; b) T. Bučko, J. Hafner, S. Lebegue, J. G. Angyán, *J. Phys. Chem. A* **2010**, *114*, 11814 – 11824.
[39] N. Almora-Barrios, G. Carchini, P. Błoński, N. López, *J. Chem. Theory Comput.* **2014**, *10*, 5002 – 5009.
[40] a) P. E. Blöchl, *Phys. Rev. B* **1994**, *50*, 17953 – 17979; b) G. Kresse, D. Joubert, *Phys. Rev. B* **1999**, *59*, 1758 – 1775.
[41] D. Lide, *CRC Handbook of Chemistry and Physics*, 84th ed., CRC, Boca Raton, FL, **2003–2004**, pp. 12(19 – 21).
[42] M. Garcia-Ratés, N. López, *J. Chem. Theory Comput.* **2016**, *12*, 1331 – 1341.
[43] a) G. Henkelman, H. Jónsson, *J. Chem. Phys.* **2000**, *113*, 9978 – 9985; b) G. Henkelman, B. P. Uberuaga, H. Jónsson, *J. Chem. Phys.* **2000**, *113*, 9901 – 9904.
[44] A. Heyden, A. T. Bell, F. J. Keil, *J. Chem. Phys.* **2005**, *123*, 224101 – 224114.
[45] M. Álvarez-Moreno, C. de Graaf, N. López, F. Maseras, J. M. Poblet, C. Bo, *J. Chem. Inf. Model.* **2015**, *55*, 95 – 103.

Received: June 7, 2016
Revised: September 2, 2016
Published online on October 14, 2016

Paper V: Lignin depolymerization

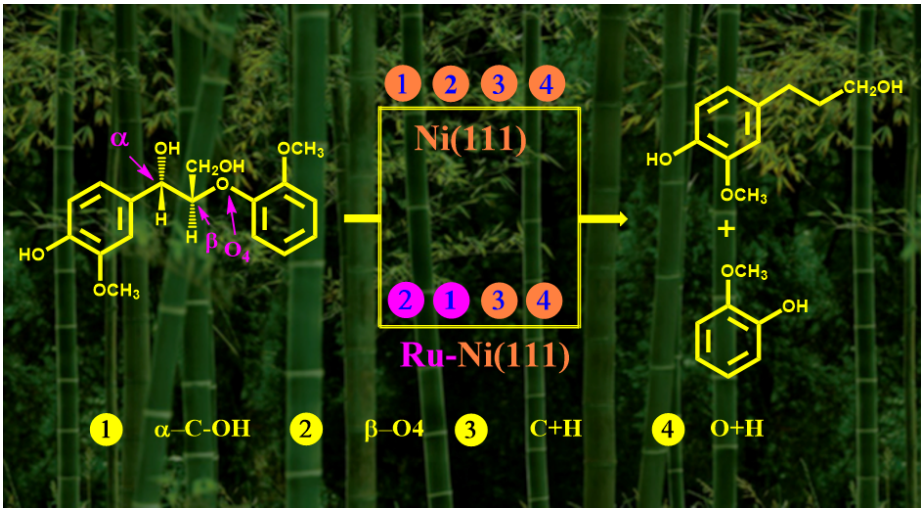

In preparation

On the role of stereocenters and rigidity in lignin depolymerization on nickel and nickel doped catalysts: a fundamental perspective

Qiang Li* and Núria López*

Institute of Chemical Research of Catalonia (ICIQ), The Barcelona Institute of Science and Technology, Avgda. Països Catalans 16, 43007, Tarragona, Catalonia, Spain

E-mail: qli@iciq.es; nlopez@iciq.es

Phone: +34 977920237. Fax: +34 977920231

Abstract

Efficient lignin depolymerization is crucial to achieve a positive economical return in biorefineries. However, due to the complex cross-polymerized network among the aromatic lignols, catalysts that can work at low temperatures perform insufficiently both in terms of activity and selectivity. Recently reported Ni-based catalysts hold a superior catalytic behavior in lignin valorization but the mechanism of the depolymerization remains unclear. In the present study, we employed Density Functional Theory to investigate lignin decomposition on pure and Ru doped Ni(111) surfaces to unravel the key issues that limit the performance. The reaction network was screened by using complex lignin models containing different sterocenters, thus presenting a better representation of the complexity of the parent compound. Our results show that on Nickel, adsorption is relative independent of the α stereocenter but the preferred reaction paths are different depending on the chirality of the center. In addition, the rigidity of the β-O-4 link is also responsible for reactivity found. Finally, the presence of small amounts of Ru on the surface simplifies the reaction as they act as preferential points for β-O-4 bond cleavage via the weakened C–O bond that is induced by the increasing the metal–O bond strength.

1 Introduction

Lignin is a complex cross-linked phenolic polymer which widely exists in the cell walls and supports plants via its strength and rigidity. It is one of the main components in lignocellulosic biomass resources, and accounts for 15-30% by weight and up to 40% of the energy.[1] But due to its highly stability efficient depolymerization methods are lacking,[2–4] and 98% lignin produced from paper and pulp industry was considered a low-valued material and burned for heating still at the beginning of the 21^{st} century.[5]

In a close future, and due to the oil depletion, lignin has been seen as a new source to provide the major aromatic compounds (such as the BTX fraction: benzene, toluene, and the three xylene isomers)[6] or directly to provide some synthetic intermediates that are used in the industry. Altogether the derived platform chemicals could be used as renewable materials in polymer industries with a great potential in food, medical, carbon fiber and so on.[7,8] However, the optimal processing of lignin is far from being solved. Hence, developing catalysts with high efficiency and selectivity for the depolymerization is the key to allow its applications in high value-added chemicals and improve the economics of the biorefinery process.[9,10]

One of the added difficulties in the chemical treatment of lignin is its variable compositions when different raw materials, such as hardwood, softwood and grass, are feed in the bioconfinery process.[3] The proportions of the monomeric units and linkages depends on the lignin origin.[3] The most common monolignols steaming from the depolymerization are *p*-coumaryl (H), coniferyl (G), and sinapyl alcohols (S)[11] and different linkages topologies connecting these monomers have been identified: β-O-4, β-5, α-O-4, β-β, 5-5, 4-O-5, β-1 and the others (see Figure S1). For instance, the most representative linkage is β-O-4, which accounts for 43-50% in softwood and 50-65% in hardwood and happens to be the most labile among the linkages. Therefore, breaking the β-O-4 bond has the highest priority in catalytic depolymerization and valorization processes.

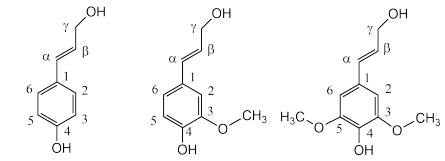

Figure 1: Structures of three lignin monomers.

Some compounds have been proposed as homogeneous depolymerization catalyst but heterogeneous catalytic lignin transformation holds the advantages of continuity,[12,13] production separation and catalyst recycle ability and are suitable for large industry scale pro-

cesses. Comprehensive reviews on the advances in the area were presented by Calvo-Flores,[7] Zakzeski,[2] Zhang,[3] and Behling et al.,[4] focusing on the basic lignin compositions, various lignin valorization approaches in both heterogeneous and homogeneous systems, and the widely potential usages of its products in chemicals, fuels, and materials. The majority of catalysts investigated are transition metal based, including Mn, Co, Ni, Ru, Pd, and Pt. Other multicomponent catalysts like transition metal (Ti, Mo, Nb, W) nitrides, have been applied by Chen et. al[14] and Ti-N was identified to be a promising catalyst for partial lignin depolymerization. Titanium-Nitride-Nickel catalyst (TiN-Ni) has also been used under mild reaction conditions by Valerio et al.,[15] and exhibited comparable performance to Raney Ni catalyst, which is a well-known catalysts for hydrogenation processes.

Among the transition metal catalysts, Ni exhibits superior activity in aryl-alkyl bond activations in lignin hydrogenolysis, with aromatic moieties keep intact during the catalytic process, both in homogeneous[13] and heterogeneous[16] processes. Still, Ni-based catalysts exhibit poor activity below 120 °C,[17] and thus improvements in the catalytic performance to reduce working temperatures are desirable. By combing Pd and Ni into a bimetallic nanoparticle catalyst, Zhang et al.[18] observed a remarkable catalytic enhancement compared with only Ni and Pd. Previous study of Yan et al.[17] shows that Ni-Ru bimetallic catalyst exist excellent behavior in aqueous lignin hydrogenolysis, compared with Ni-Rh, and Ni-Pd catalysts. Both studies show the synergistic effects of two metals in catalytic performance.

Density Functional Theory (DFT) approaches to understand the reaction network for the depolymerization are rather scarce. By combining DFT calculations and experiments, Lu et al.[19] investigated the β-O-4 bond scission on Pd catalyst. In this study, lignin model was represented by 2-phenoxy-1-phenylethanol and its β-O-4 bond cleavage mechanism on Pd(111). In addition, Hamou et al.[20] studied the adsorption and decomposition mechanism of lignin on Pt(111) by using a simple model (2-phenoxyethanol). However, because of the simple representative models used both in theoretical and experiment studies,[4] some of crucial effects would be artificially ignored or hiden. For example, numerous lignin linkages with stereocenters are formed between monolignols,[21] and the steric effect of methoxy or other groups in the *meta* and *para* aromatic substitution positions would also have impact on the interactions between molecules and the surface and further affect the reaction network.[22]

Besides, in order to improve the design further understanding the reaction process in atomic level is needed. The depolymerization mechanism of lignin even on the most simple of these catalysts, Ni is lacking. This is due to several factors including: (i) the large size of lignin that has prompted the use of small surrogates[4] that does not account for key aspects like chirality of the linkers; (ii) the complex reaction networks that involve various products; (iii) the variety of metal catalysts and complexity of advanced materials like TiN-Ni.[15] In view of these fundamental complexity we have employed DFT calculations on slab

models representing the simplest of these materials (Ni and Ru doped Ni) but considered large molecular surrogates that have stereocenters (dimers ($C_{17}H_{20}O_6$) of the most abundant monolignols coniferyl alcohol (G)) and an extensive reaction network that accounts for many of the potential transformations. Our results firstly reveal the effects of the stereocenters in decomposition mechanism and the synergistic effects in the Ru doped Ni catalyst, and can also provide guideline for the incoming catalysts design.

2 Computational Details

In this work, slab model calculations were performed by using the Vienna Ab-initio Simulation Package (VASP),[23,24] The exchange and correlation energies were obtained via the PBE functional.[25] We also included the van der Waals (vdW) corrections by applying the Grimme's DFT-D2 method,[26,27] with the C_6 reparameterized by our group.[28] The inner electrons were represented by Projector Augmented Wave (PAW) pseudopotentials with cutoff energies of 450 eV.[29,30] The Brillouin zone was sampled by a Γ-centered k-points mesh generated through the Monkhorst-Pack method.[31] The calculated Ni and Ru lattice parameter of 3.517 and 2.712 Å ($[c/a] = 1.581$) agree well with previous experiment results of 3.524 and 2.706 Å ($[c/a] = 1.582$).[32]

The adsorption of small species such as H_2O, H, CO, O, OH were studied on a p-(3×3) supercell with four layers and gamma centered 5×5×1 sampling kpoints were used. In slab optimization step, Ni(111) and Ru(0001) surface were modeled by a four-layers slab with p-(7×4) supercells, the two uppermost layers were fully relaxed and the remaining atoms at the bottom were fixed to the bulk distances. Then the last bottom layers were removed and the rest three layers were fixed and used for adsorption and transition states calculations via Γ point sampling, then these structures were taken as the initial inputs for reoptimization via the denser mesh of (2×3×1). This method is a trade-off between computational demands for the large system and achieving the accuracy compared with the traditional method in which the denser kpoints sampling were used for surface reaction studies directly. Since adsorption was performed on one side of the slab, a 15 Å-thick vacuum region was set between each slab to avoid their interaction, dipole correction along z direction[33] was also applied to eliminate the spurious contributions arising from the system's asymmetry.

In the reaction mapping, we employed both Climbing Image Nudged Elastic Band Method (CI-NEB),[34] and the Improved Dimer Method (IDM)[35] to locate the transition states in the potential surfaces. The optimization thresholds were 10^{-5} eV and 0.03 eV/Å for electronic and ionic relaxations, respectively. In all cases the saddle point nature of the transition states was assessed by the calculation of the numeric Hessian with a step of 0.02 Å and its diagonalization that rendered a unique imaginary frequency.

All molecules in gas phase were relaxed in a box of $20 \times 20 \times 20$ Å^3. Four coniferyl alcohol dimers (named as A, B, C, and D) with different chiralities were used as lignin model in this study, as shown in Figure S2. The alphatic side chain on the right aromatic moiety was removed in order to reduce the molecule length and also the surface length in y direction. Solvation energies of those closed-shell molecules both in ethylene glycol and water (Table S1) have been calculated via MGCM methodology (MultiGrid Continuum Model).[36]

In order to study the Ru doping effects, system's stability in this work was investigated firstly via a few aspects following the procedures as in ref.[37] The solubility was calculated in a cubic bulk box containing 32 Ni atoms, segregation and near surface energies are calculated via p-(2×2) slab with six layers and the top four layers were relaxed during calculation, island formation energy was calculated on a p-(3×3) slab with four layers and the top two layers were relaxed. As listed in Table S2, calculated energy of one Ru atom dissolved into Ni bulk is 0.53 eV, implying the a relative instability in forming the alloy. However, the endothermic energy would compensated by the entropy contributions as Ru can replace Ni atoms from three directions and the higher disorder corresponds to higher entropy and therefore the lower free energy.[37,38] Small exothermic segregation energy (-0.05 eV) implies that Ru penetrating into the bulk is slightly preferable and can be exist both on surface and in the bulk. From the positive island formation energy (0.12 eV), it safe to derive that Ru dispersion on the surface is preferred.

According to this analysis, Ru effects have been investigated by substituting the Ni atom under the breaking bonds with Ru on the top layer. In other words, the activate site Ni atoms for variety types of bond breakages as well as adsorption structures have been replaced by the Ru atoms specifically, depending on the reaction types.

3 Results and Discussion

3.1 Adsorption

Four isomers of the lignin model with different α and β chiralities were selected to study the adsorption properties (see Figure S2). The adsorption energies listed in Table S1 show that structures with β-S (A and B) are more stable than those have β-R configurations (C and D). Adsorption energies of A and B are at least 0.40 eV lower than those of C and D, hence C and D are not further considered in the decomposition network. For isomer-A (α-S, β-S) and isomer-B (α-R, β-S), since the adsorption energies are very close, -2.25 vs -2.27 eV, decompositions from these two structures were both considered and compared in the reaction paths. Adsorption structures of products containing for unsaturated (G1-G4) and six saturated (G5-G10) molecules in lignin hydrogenolysis reaction network have been

calculated, see Figure 2 and Figure S3, S4. Their adsorptions on Ni(111) and Ru(0001) surfaces have been calculated and compared (Table S1). Results show that the adsorption of these species on Ru(0001) surface are stronger than that on Ni(111) surface. Strong adsorption activity would impede the desorption steps where products leave surface and new active sites need to be regenerated for next reaction cycles. All these structure geometries labeled as the same names in this work are freely accessible from the iochem-BD database.[39]

3.2 Reaction Network

In the reaction network, since reported experiment results show that aromatic parts are undisturbed during the catalytic process by using activated carbon supported Ni (Ni/AC) catalyst,[16] only reactions related with α and β-C were considered and the full decomposition path ways are plotted in Figure S3 and S4. (α-S, β-S) and (α-R, β-S) are denoted as structure A and B (Figure 1). From α-C side in A, two reactions are possible, C-OH bond and O–H bond breakings. Two C–C bonds, C_α-$C_{aromatic}$ and C_α-C_β, need higher barriers to proceed because the lacking interaction between C sides and the surface resulting into the unactivated C–C bond. The model molecules can be treated as the H atom from the two C sides in ethylene glycol replaced by aromatic moieties and CH_2OH, previous studies show that C–C bond breaks in the late dehydrogenation steps.[40] Therefore, this assumption is reasonable and reliable in lignin decomposition path. From β-C side in A and B, direct β-O-4 and C–H bond ruptures have been studied. These four reactions have been compared firstly and the following steps from the one with highest barriers were not further considered. For α-C side in B, there is only C–H bond breaking. Figure 2 and 3 are the reaction networks and profiles of the most preferable reactions extracted from the complete reaction network.

3.3 Discussion

3.3.1 Reaction profiles from isomer A

Reaction profiles are shown in Figure 3 and Figure S5. From A, there are two competing reactions from α-C positions, the C–OH and O–H bond breakings with barriers of 0.86 and 1.00 eV. The former one is more exothermic by -0.34 eV. It has to be mentioned here is that α-C–O breaks with low barriers and high exothermic energies of 0.33 and -1.10 eV after the initial O–H bond scission. As a result, all reactions above bring out the same main product as OH abstraction from α-C side. Then, β-O-4 bond breaks easily both kinetically (with barrier of 0.38 eV) and thermodynamically prefered (exothermic by -0.82 eV). Such a lower barrier for C–O bond is attributed to the formation of a highly conjugated product (G1). α-C hydrogenation step (A22) after C–O bond scission has been calculated, this step has an activation barrier of 0.86 eV and is nearly thermoneutral by 0.08 eV. The inverse

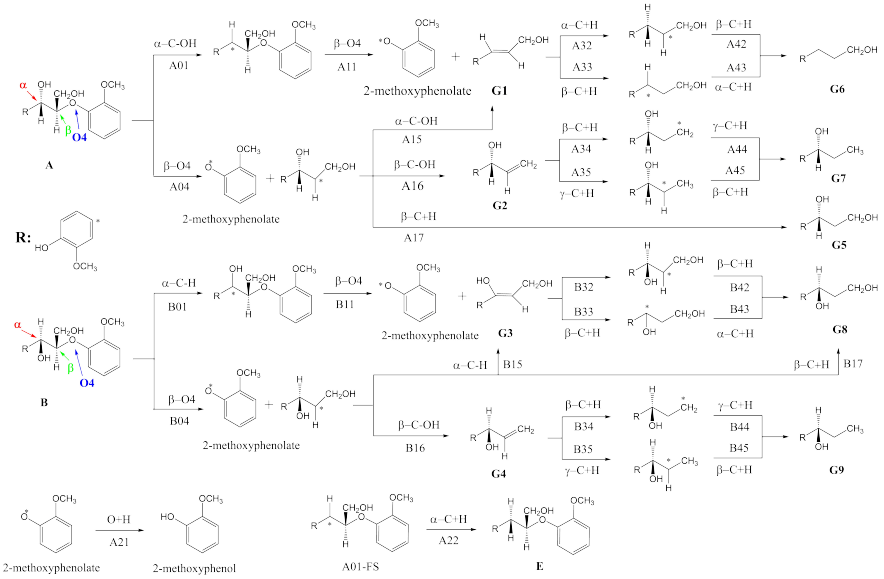

Figure 2: Reaction pathways for dimer models of A and B decompositions on Ni(111) surface

reaction of A01 is difficult to proceed due to its higher barrier of 1.20 eV, compared with the lower barrier of 0.86 eV in step A01. Hence, once C–OH bond breaks, the reverse reaction can not compete with the hydrogenation step or β-O-4 bond breakings. The products of the β-O-4 bond rupture consist one neutral molecule, G, one building unit of lignin and methoxy-phenolate. The reaction step related to another product is the 2-methoxy-phenolate hydrogenation to 2-methoxy-phenol. This step has close barrier (0.82 eV) to the first C–OH scission and endothermic by 0.37 eV. Conifery alcohol (G1) and methoxy-phenol would need to overcome the desorption energies of 2.33 and 1.25 eV, respectively.

For reactions from β-C, β-C–H and direct β-O-4 bond breaking were calculated. β-C–H bond scissions in the reaction network are blocked by much higher barriers and endothermic energies compared with other reactions (see A02, B02, A13 and B13 reactions in Table S2). This is because of the rigidity of the lignin structure which prevents the rotation of C-C chain around the two aromatic units. Hence, the reactions in the chain after the β-C–H step have not been considered anymore. Direct β-O-4 bond breaking would also compete the C–OH and O–H bond breakings in spite of its relatively barrier of 1.08 eV. The product could undergo C–OH breakage with reasonable barriers from either α (0.87 eV) and β (0.77 eV) side to produce G1 and its isomer G2. Besides, the product can also undergo the

hydrogenation step directly and produces G5, which requires 1.62 eV to desorb. After G1 and G2 produced, their desorption would be impeded by the high desorption energies of 2.33 and 2.05 eV, respectively. Hydrogenation steps (from A32 to A35, and from A42 to A45) can continue to form the saturated structures, G6 and G7, their desorptions require lower energies of 1.56 and 1.43 eV.

Furthermore, C–OH and β-O-4 scission can effect each other when they proceed in different order. For example, C–OH bond breaking in the first step facilitates the subsequent β-O-4 bond rupture significantly because of forming the conjugated structures. Direct β-O-4 bond breakage also facilitates the following C–OH bond breakage, but to a smaller extent. In turn, β-C–H bond scission is prohibited. As C–OH bond scission needs barriers similar to the hydrogenation step on carbon side, we can expect that OH groups in G6 and G7 would be replaced by H atom in the H abundant reaction process and the ultimate product would be R$-$CH$_2-$CH$_2-$CH$_3$ (G10 in Figure S2).

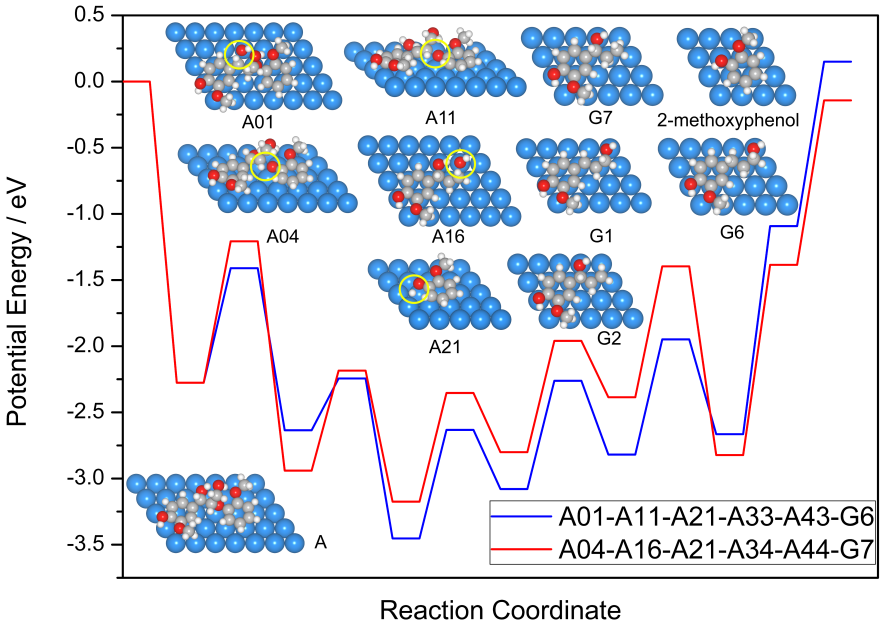

Figure 3: Reaction profiles of lignin model A decompositions on Ni(111) surface

3.3.2 Reaction Profiles from B isomer and Stereo effects

Reactions starting from B, behave similarly to those from A, β-C–H rupture needs highest barrier among all reactions, showing that the chirality changing from α-C does not effects on the C–H scission from β-C side. Besides, the α-C–H bond breaking proceeds with lower barrier of 0.66 eV and almost thermodynamically neutral (-0.09 eV). Considering the large energies to overcome in other reactions, this one is the most preferable step to start the reaction network. After α-C–H bond breaks, β-O-4 scission step is greatly promoted with barrier of only 0.14 eV and has high exothermic by -0.75 eV. This indicates that conjugated structures again plays significant role in reducing the barrier to break β-O-4 bond . The low barrier can be regarded as the effect of substituting H by OH on α side, which origins from the stereo effects. One product, methoxy-phenolate repeats the last hydrogenation step from A and produces methoxy-phenol. The other product, denoted as G3, is a neutral molecule and its desorption requires 1.66 eV.

When β-O-4 bond breaks directly, the barrier increased by 0.15 eV and less exothermic by -0.28 eV, compared with this reaction from A. Although the changing H and OH position on α C side has little effects on the adsorption energies. Lacking surface–O interaction in B might be the reason for the slightly increased barrier and decreased reaction energy. After β-O-4 bond breaks, the product would undergo three possible reactions, α-C–H, β-C–OH bond breakings and β-C hydrogenation, to produce G3, G4 and G8. The barriers and released energies for decompositions are very close for these two reactions, 0.89 *vs* 0.91 eV and -0.34 *vs* -0.42 eV. Compared with them, β-C hydrogenation to G8 competes with lower barrier of 0.77 eV and slightly endothermic energy of 0.16 eV. G3 and G4 also require high energy to desorb (2.05 and 1.75 eV) and hydrogenation steps would occur to form related saturated structures G8 and G9, followed by desorption with barriers of 1.19 and 1.30 eV.

For initial reactants, A and B, stereo effect on the adsorption energies is small, -2.25 and -2.27 eV for A and B, respectively. However, as mentioned above, it would change the first reaction step from C–OH to C–H and results into different intermediates and products. For example, C–OH bond scission from α-C side in B isomer is unlikely because the lack of interaction of C–OH with the surface leads to the unactivated C–OH bond. Thus, OH group in α-C side of reactant B remains during the reaction network. Besides, chirality in the α-C side would also affect the reaction rates by producing the precursor of the conjugated products. By comparing reaction barriers of A01 and B01 step, its clear to see that C–H breaking with barrier of 0.66 eV proceeds easier than C–OH bond which has barrier of 0.86 eV. Given by the lower barriers in the first two steps (C–H and β-O-4 scissions), lignin decomposition from reactant B would proceed much faster than that from reactant A, demonstrating that stereocenters affect the complex reaction networks in lignin.

3.3.3 Ru effects

Previous experiment study from Yan et al.[17] demonstrated that bimetallic NiRu exhibited superior activity in hydrogenolysis of lignin in water. By combining XPS and X-ray absorption spectroscopy methods, it was found that the Ni is surfaced-enriched in the catalyst. In this study, the Ru effects was studied via a simple model by replacing one surface Ni with Ru atom, then the adsorption properties and transition states were optimized. Reaction barriers and energies before and after Ru doping are listed in Table 1.

Table 1: Comparison of activation barriers E_a and reaction energies ΔE (both in eV) on pure Ni(111) and Ru doped Ni(111) surfaces

	Ni(111)		Ni(111)+Ru	
Label	E_a	ΔE	E_a	ΔE
A01	0.87	-0.36	0.78	-0.12
A04	1.07	-0.66	0.77	-0.39
A11	0.39	-0.82	0.29	-1.20
A15	0.86	-0.45	1.01	-0.39
A16	0.76	-0.23	0.72	-0.04
A21	0.82	0.37	1.06	0.74
B01	0.67	-0.06	0.74	-0.09
B04	1.15	-0.40	0.96	-0.18
B11	0.15	-0.78	0.05	-1.18
B15	0.89	-0.33	0.56	-0.68
B16	0.90	-0.42	0.87	-0.20

When α-C-OH bond breaks (A01) over the substituted Ru atom, the barrier decreases slightly by 0.09 eV and becomes less exthermic by 0.24 eV. Large differences are observed in direct β-O-4 bond scission (A04) with barrier decreasing from 1.07 to 0.77 eV and reaction energy being less exothermic by 0.28 eV. Ru has little effect on the barrier of β-O-4 in the second step (A11) but large effect on the reaction energy (from -0.82 to -1.20 eV). α-C-OH breaking step (A15) after A04 needs 0.15 eV more energy to proceed after Ru doped and the reaction energy changes slightly. Barrier of another α-C-OH scission step (A16) changes slightly by 0.04 eV and turns to be thermoneutral. Furthermore, for 2-methoyxphenolate hydrogenation to 2-methoxyphenol (A21), Ru on the surface also increases the barrier by 0.24 eV and the reaction becomes more endothermic from 0.37 to 0.74 eV.

For reactions from isomer B, Ru also decreases the barrier by 0.16 eV for direct β-O-4 bond scission (B01). Larger energy release from the second β-O-4 bond (B04) has been observed again, in agreement with reaction from A. It is interesting to observe that for B15, C–H bond breaking after B04 step, is also more activated by 0.33 eV and more thermodynamically favorable by -0.68 eV. This is the another case in reactions from A that

A15 becomes more difficult to proceed as stated above, demonstrating the synergistic effect of sterocenters and the Ru doping. For C–OH bond in B16, the barrier is slightly reduced from 0.90 to 0.87 eV and reaction is less exothermic by energy of 0.23 eV, which is similar to the A situation. Thus, for C–OH bond breaking, Ru has little (for A16 and B16) or negative (for A15) effects on the reaction barriers and reactions become more endothermic by energies between 0.20 to 0.30 eV. For β-O-4 bond breaking in the first and second step, doping Ru facilitates the reaction by reducing the barrier by maximum of 0.30 eV with reactions becoming less exothermic. In the final step, the introduced Ru arises the barrier and energy for phenolate hydrogenation into phenolic by 0.27 and 0.35 eV. This can be attributed to the stronger O affinity of Ru than that of Ni which stabilizes the phenolate specie. In spite that, this step can be promoted by the high surface H concentration and H_2O via the formation of hydrogen bonds.

As Ru have stronger adsorption ability than Ni, for one intermediate, its adsorption energy on Ru decorated Ni(111) surface would be between that on pure Ni(111) and Ru(0001) surface. This has been confirmed by the adsorption energies on Ru-Ni(111) surface. When A and B approach to the Ru-Ni(111) surface, the adsorption energies depend on their motifs above the Ru atom (see Table S1). Structures with aromatic part above on the Ru atom (denoted as Ar_{Ru}) are more stable than those with O (from β-O-4) above the Ru atom (O_{Ru}). For example, Ar_{Ru} and O_{Ru} structures of A have adsorption energies of -2.28 and -2.15 eV. However, the β-O-4 bond breakage barrier of Ar_{Ru} is 0.13 eV higher than that of O_{Ru}. This implies that Ru participates into lowering the C–O cleavage barriers. To confirm this assumption, single O atom adsorption on atop Ni and Ru atoms were studied. The Ni–O distance and adsorption energies respected to the gas O_2 energy are 1.678 Å and -0.54 eV on top Ni atom of pure Ni(111) surface, and -1.734 Å and -1.51 eV on top Ru atom of Ru doped Ni(111) surface. The more negative O adsorption energy on top Ru indicates that Ru–O bond is much stronger than Ni–O bond. This demonstrates that more electron density are localized between O and Ru thus weakening the β-O-4 bond when A and B adsorb on the surface. This weaken bond can also be indicated by the earlier transition state C–O bond length of 2.103 Å on Ru-Ni(111), compared with the longer bond distance of 2.242 Å on Ni(111). Stronger Ru–O interaction can also be implied via comparison of the O adsorption energies on Ru(0001) and Ni(111), -2.98 *vs* -2.45 eV. Therefore, the doped Ru strengthens the metal–O bond and weakens the β-O-4 and promotes the C–O bond cleavage.

Local surface environment and rigidity from lignin would accounts for the the weaker O_{Ru} adsorptions. The Ni atoms surrounding Ru have been pull up by 0.02 Å, and Ru is 0.06 Å above the surface. The local surface unflatness push the atoms above them up slightly, compared with the flat Ni(111) surface. For example, when A adsorption on Ru-Ni(111) and Ni(111) surfaces, the Ru–O and Ni–O bonds are 2.177 and 2.111 Å, respectively. O

coordination in z direction on Ru-Ni(111) is 0.132 Å higher than that on Ni(111). The carbon atoms from the benzene ring connecting the O atom also shift upwards slightly with range from 0.003-0.098 Å. However, the benzene ring far from the O atom nearly keeps its structure unaltered, and this rigidity might bring out the intra-molecule strain and thus increase the structure energies.

Besides, for all species, their adsorption energies are more negative on Ru(0001) than those on Ni(111) surface (Table S1). Such strong adsorption property would also impede the reactions by covering the active sites. It has to be emphasized here is that Ru also has the strong ability in hydrogenation of the arenes.[41] Therefore, doping small percentage of Ru into the Ni catalyst would benefit the catalytic process. When Ru contents increase, more Ru-species interactions would stabilize the intermediates and make the surface poisoned.This has been demonstrated before via the experiment results from Yan et al.[17] in which a volcano-like behavior exist when varying the Ru percentages in the Ni based catalyst.

4 Conclusions

In this study, DFT calculations of more complex lignin dimer β-O-4 bond models over Ni(111) and Ru doped surfaces were performed. Reaction network accompanied by the stereo and Ru doping effects have been investigated. Our results show that β-O-4 bond breakage would be promoted or accelerated by unsaturated the α-C side (α-C-H and α-C-OH breaks ahead) because this would benefit the conjugated products formation. Stereo centers have two effects on the network, Structurally, it can control the the final products by interaction of H or OH in α-C side. Different structures can then have impacts on the reaction rates with lower barriers and reactions from reactant B are expected faster than these from reactant A. Ru has both positive and negative effects on the catalytic behavior. On one hand, it can promotes the direct β-O-4 bond scission by lower the reaction barriers via strengthen the Metal-O bond and make it competitive to the first C–H or C–OH bond scissions. On the other hand, when surface Ru content is small, local surface unflatness and the structure rigidity would have negative effects on adsorption energies. As the stronger adsorption properties of Ru towards the reactants, too much percentage of Ru would lead to less active surface sites by covering the intermediates and impede the total behavior of catalyst as a consequence. Our study firstly considered the stereocenter effects on the reaction network and the doping effects interpret the previous results on Ru-Ni experiment reasonably.

Acknowledgement

The authors thank MINECO (CTQ2015-68770-R) for financial support and Barcelona Supercomputing Centre (BSC-RES) for providing generous computer resources via Centro de Supercomputación y Visualización de Madrid, Universidad Politécnica de Madrid. The authors also appreciate the kind discussion of Frank Abild-Pedersen from SLAC.

Supporting Information Available

Structures and decomposition network considered in this work, computed adsorption energies of close shell structures, reaction barriers, reaction energies and stability calculation details. This material is available free of charge via the Internet at `http://pubs.acs.org/`.

References

(1) Perlack, R. D.; Wright, L. L.; Turhollow, A. F.; Graham, R. L.; Stokes, B. J.; Erbach, D. C. *Biomass as feedstock for a bioenergy and bioproducts industry: the technical feasibility of a billion-ton annual supply*; 2005.

(2) Zakzeski, J.; Bruijnincx, P. C.; Jongerius, A. L.; Weckhuysen, B. M. *Chem. Rev.* **2010**, *110*, 3552–3599.

(3) Li, C.; Zhao, X.; Wang, A.; Huber, G. W.; Zhang, T. *Chem. Rev.* **2015**, *115*, 11559–11624.

(4) Behling, R.; Valange, S.; Chatel, G. *Green Chem.* **2016**, *18*, 1839–1854.

(5) Thielemans, W.; Can, E.; Morye, S.; Wool, R. *J. Appl. Polym. Sci.* **2002**, *83*, 323–331.

(6) Delidovich, I.; Hausoul, P. J.; Deng, L.; Pfützenreuter, R.; Rose, M.; Palkovits, R. *Chem. Rev.* **2015**, *116*, 1540–1599.

(7) Calvo-Flores, F. G.; Dobado, J. A. *ChemSusChem* **2010**, *3*, 1227–1235.

(8) Kai, D.; Tan, M. J.; Chee, P. L.; Chua, Y. K.; Yap, Y. L.; Loh, X. J. *Green Chem.* **2016**, *18*, 1175–1200.

(9) Ragauskas, A. J. et al. *Science* **2014**, *344*, 1246843.

(10) Alonso, D. M. et al. *Sci. Adv.* **2017**, *3*, e1603301.

(11) Chakar, F. S.; Ragauskas, A. J. *Ind. Crops Prod.* **2004**, *20*, 131–141.

(12) Roberts, V.; Stein, V.; Reiner, T.; Lemonidou, A.; Li, X.; Lercher, J. A. *Chem. Eur. J.* **2011**, *17*, 5939–5948.

(13) Sergeev, A. G.; Hartwig, J. F. *Science* **2011**, *332*, 439–443.

(14) Chen, L.; Korányi, T. I.; Hensen, E. J. *Chem. Commun.* **2016**, *52*, 9375–9378.

(15) Molinari, V.; Clavel, G.; Graglia, M.; Antonietti, M.; Esposito, D. *ACS Catal.* **2016**, *6*, 1663–1670.

(16) Song, Q.; Wang, F.; Xu, J. *Chem. Commun.* **2012**, *48*, 7019–7021.

(17) Zhang, J.; Teo, J.; Chen, X.; Asakura, H.; Tanaka, T.; Teramura, K.; Yan, N. *ACS Catal.* **2014**, *4*, 1574–1583.

(18) Zhang, J. W.; Cai, Y.; Lu, G. P.; Cai, C. *Green Chem.* **2016**, *18*, 6229–6235.

(19) Lu, J.; Wang, M.; Zhang, X.; Heyden, A.; Wang, F. *ACS Catal.* **2016**, *6*, 5589–5598.

(20) Ould Hamou, C. A.; Réocreux, R.; Sautet, P.; Michel, C.; Giorgi, J. B. *J. Phys. Chem. C* **2017**, *121*, 9889–9900.

(21) Calvo-Flores, F. G.; Dobado, J. A.; Isac-García, J.; Martí-Martínez, F. J. *Lignin and lignans as renewable raw materials: chemistry, technology and applications*; John Wiley & Sons, 2015.

(22) He, J.; Zhao, C.; Lercher, J. A. *J. Am. Chem. Soc.* **2012**, *134*, 20768–20775.

(23) Kresse, G.; Furthmüller, J. *Comput. Mater. Sci.* **1996**, *6*, 15–50.

(24) Kresse, G.; Furthmüller, J. *Phys. Rev. B* **1996**, *54*, 11169–11186.

(25) Perdew, J. P.; Burke, K.; Ernzerhof, M. *Phys. Rev. Lett.* **1996**, *77*, 3865–3868.

(26) Grimme, S. *J. Comput. Chem.* **2006**, *27*, 1787–1799.

(27) Bučko, T.; Hafner, J.; Lebegue, S.; Angyán, J. G. *J. Phys. Chem. A* **2010**, *114*, 11814–11824.

(28) Almora-Barrios, N.; Carchini, G.; Błoński, P.; López, N. *J. Chem. Theory Comput.* **2014**, *10*, 5002–5009.

(29) Blöchl, P. E. *Phys. Rev. B* **1994**, *50*, 17953–17979.

(30) Kresse, G.; Joubert, D. *Phys. Rev. B* **1999**, *59*, 1758–1775.

(31) Monkhorst, H. J.; Pack, J. D. *Phys. Rev. B* **1976**, *13*, 5188–5192.

(32) Lide, D. *CRC Handbook of Chemistry and Physics*, 84th ed.; CRC press LLC: Boca Raton London New York Washington, D.C., 2003–2004; pp 12(19–21).

(33) Makov, G.; Payne, M. C. *Phys. Rev. B* **1995**, *51*, 4014–4022.

(34) Henkelman, G.; Uberuaga, B. P.; Jónsson, H. *J. Chem. Phys.* **2000**, *113*, 9901–9904.

(35) Heyden, A.; Bell, A. T.; Keil, F. J. *J. Chem. Phys.* **2005**, *123*, 224101(1–14).

(36) Garcia-Ratés, M.; López, N. *J. Chem. Theory Comput.* **2016**, *12*, 1331–1341.

(37) López, N.; Vargas-Fuentes, C. *Chem. Commun.* **2012**, *48*, 1379–1391.

(38) Soto-Verdugo, V.; Metiu, H. *Surf. Sci.* **2007**, *601*, 5332–5339.

(39) Álvarez-Moreno, M.; De Graaf, C.; López, N.; Maseras, F.; Poblet, J. M.; Bo, C. *J. Chem. Inf. Model.* **2014**, *55*, 95–103.

(40) Salciccioli, M.; Vlachos, D. G. *ACS Catal.* **2011**, *1*, 1246–1256.

(41) Dwivedi, A. D.; Rai, R. K.; Gupta, K.; Singh, S. K. *ChemCatChem* **2017**, *9*, 1930–1938.

Chapter 5

Conclusions

DFT approach has been provided to be a robust method to understand catalytic processes on the surface and has the ability to describe the reaction mechanisms accurately, which strengthens our knolwdge in the atomic size and benefits the catalysts designment. In the end of the thesis, several meaningful results and insights about objective molecules such as methanol, EG, glycerol, levulinic acid, linear and cylic glucose, mannose, and lignin dimers are summarized and listed as below.

- Density Functional Theory Comparison of Methanol Decomposition and Reverse Reactions on Metal Surfaces
    1. Detail methanol decomposition network has been computed on the Cu(111) and Ru(0001) surfaces
    2. On Cu(111), H_2 and CH_2O are the products and the decomposition process goes as:

       $$CH_3OH^* \rightarrow CH_3O^* + H^* \rightarrow CH_2O^* + 2H^* \rightarrow CH_2O_{gas} + 2H^*$$

       Further decomposition are not favored because of the weak adsorption energy of CH_2O.
    3. Similarly, methanol formation process (reverse reaction steps) would stop when formaldehyde forms because of its trends to desorb. Hence, high H coverage is likely to promote the formaldehyde hydrogenations

to methanol. From CH_2O to CH_3OH, $CH_3O + H \rightarrow CH_3OH$ is the rate determining step.

4. On Ru(0001), CO and H_2 are the finally products and the process goes as:

   $$CH_3OH^* \rightarrow CH_3O^* + H^* \rightarrow CH_2O^* + 2H^* \rightarrow CHO^* + 3H^* \rightarrow CO^* + 4H^*$$

5. On Ru(0001), it is impossible to produce methanol as C–O bond breaks much easier from the intermediates than their hydrogenations.

6. Biased initial C–H and O–H competition in the first decomposition step between DFT calculations and experiment observations have been discussed by taking account of the lateral hydrogen bond interactions between two methanol molecules.

7. Inter molecule hydrogen bond formation stabilizes both the initial and transition states for O–H bond breaking. In the meanwhile, it also increases the rigidity for the methyl group bending to interaction with the surface and leads to larger C–H bond breaking barriers.

8. BEP and TSS relationships have been obtained and analyzed. O–H, C–H, and C–O bond breakages exhibit the IS, FS, and FS-like relationships, and C–O has the worst scaling results due to the significant structure changes.

- Microkinetics of alcohol reforming for H_2 production from a FAIR density functional theory database

1. Complete decomposition network of ethanol, ethylene glycol, and glycerol have been calculated.

2. 350 structures including C_0 (7), C_1 (18), C_2 (55), and C_3 (270) have been optimized on Ru(0001) and C_{0-2} (80) on Cu(111) and 250 transition states for C_1 and C_2 species on each metal have been found in this work.

3. An empirical principle description of the stability for O or OH terminated structures based on the metal oxophility was displayed.

4. BEP and TSS relationships have been extrapolated and the factors that affect the scaling behaviors have been analyzed in detail.

5. O–H has the best IS-like TSS results, and the rest bond breaking (C–H, C–C, C–OH and C–O) have FS-like types, the scaling behaviors are followed by the C–H, C–O, C–C, and C–OH.

6. Reaction network of glycerol decomposition (1698 reactions) have been mapped and the transition states' energy were predicted via the scaling method (TSS) from the optimized intermediates' energies.

7. *ab initial* microkinetics study of hydrogen production from ethanol, ethylene glycol and glycerol have been performed.

8. For ethanol and EG on Cu(111), direct decomposition is the best way to produce H_2, and CCO^* is the most abundant intermediate.

9. For the other reforming techniques, surface oxygen species O and OH are the most abundant species.

10. For ethanol on Ru(0001), direct decomposition has the best hydrogen production behavior, CCH^*, CO, and CCO^* are the main surface species with percentage of 68%, 16%, and 7%. CO and H_2 are the main products with approximate stoichiometric ratio of 2:3.

11. APR has lower H_2 production rate than DD, but much higher than other methods, the most rich species in sequence are CO^*,$C_xH_y^*$ and CCO^*.

12. For ethanol ATR and SR, surface O^* and $C_xH_y^*$ are the main species respectively.

13. For EG Ru(0001), the H_2 production rates in sequence are SR, DD, APR and ATR. In DD and APR, the surface is almost covered by CO. In ATR, surface is covered mostly by O^*. In SR, $C_xH_y^*$, CO^*, and CCO^* are the most abundant surface species.

14. Both EG and Glycerol have the same hydrogen production sequence of SR, DD, APR and ATR.

15. In steam reforming, the activity of EG is 3.5 order of magnitude smaller than that of glycerol.

16. The selectivity towards H_2 for EG and glycerol steam reforming on Ru(0001) surface are 84% and 72%, respectively.

- Interfacial acidity in ligand-modified ruthenium nanoparticles boosts the hydrogenation of levulinic acid to gamma-valerolactone

  1. Intra-molecule esterification of levulinic acid to γ-valerolactone over Ru(0001) surface have been calculated.
  2. Mechanisms starting from levulinic acid and its lactate form have been calculated in detail, our results show that when conversion starts from the surface levulinic acid form, it is more kinetic preferable than that from levulate form.
  3. By using a series of probe acid molecules, the estimated interfacial acidity (pH) is around 1.0, and this is strong enough to protonate the levulate into levulinic acid and change the reaction path, thus making the HHDMA-Ru(0001) better than pure Ru(0001) for LA conversion.
  4. The anti-oxidation ability of the interfacial has been studied by adsorption 6 and 8 oxygen atoms on HHDMA-Ru(0001) and pure Ru(0001) surface. Our results imply that oxygen adsorption on HHDMA decorated Ru(0001) surface is less thermodynamic preferable than on pure Ru(0001).
  5. Interfacial acidity and the coverage effect from the HHDMA ligands also inhibits the oxygen adsorption and insertion into the Ru bulk, which results into the higher stability towards anti oxidation.

- Catalyst and Process Design for the Continuous Manufacture of Rare Sugar Alcohols by Epimerization Hydrogenation of Aldoses

  1. Glucose and mannose hydrogenation to their alcohols over Ru(0001) surface have been calculated.
  2. Reactions from linear isomers of glucose and mannose have been studied and the differences in the reaction coordinate are small, Given the low concentration of them less than 1% in the liquid phase, the different reaction rates can not be explained from the linear structures.
  3. Cyclic isomers of glucose and mannose adsorption have been calculated and exist obvious adsorption sequence of α-mammnose $>$ β-mammnose $>$ α-glucose $>$ β-glucose.
  4. α-glucose and β-mannose have much higher reaction barriers than their isomers.

5. Water associates in the ring opening steps and β-glucose has lower ring opening barrier than α-mannose.
6. The rate determining step is hydrogenation reaction (C + H) from β-glucose and is the ring opening from α-mannose,
7. Different solution concentration of their isomers, adsorption energies and different rate determining steps control the overall hydrogenations rates.
8. Surface kinetic analysis based on Langmuir-Hinshelwood mechanism have been employed and the outcome qualitatively agrees with experimental results.

- Lignin decomposition on pure and Ru doped Ni(111) surfaces: density functional theory study on stereo and synergistic effects.
  1. More complex coniferyl alcohol dimers models containing the sterocenters at α and β carbon positions have been built.
  2. Adsorption of these models have been calculated and the stability were compared.
  3. Complete decomposition and hydrogenation of lignin conversion have been calculated. The α-C–OH or α-C–H bond breaking firstly, followed by the β-O_4 bond breaking and then the hydrogenation steps.
  4. Sterocenter effects on reaction kinetics have been discussed, changing the OH and H positions in the α-C would promote the reaction by lower reaction barriers.
  5. Ru doping effects in promoting the Ni catalysts have been investigated. In the doping model, one surface Ni atom was replaced bu Ru atom and the stability of this model has been verified by the segregation and near surface energies, and island formation energy.
  6. On one side, Ru facilitates the β-O_4 bond breaking via lowering the barrier by 0.20 eV. This is due the the stronger Ru–O interaction which weakens the β-O_4 bond. On the other side, as Ru has stronger binding ability towards the species than Ni, doping too much Ru would deteriorate the catalyst behavior by the poisoning effects. Thus, will increasing the doping amount of Ru into the Ni catalyst, experimentalist observed a volcano curve.

Chapter 6

Appendix

Article VI: Hydrogen production from ammonia-borane

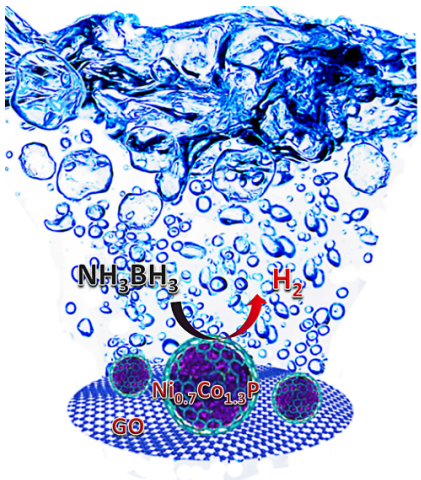

Published in *Energy Environ. Sci.*, 2017, **10**, 1770-1776

Environmental Science

COMMUNICATION

View Article Online
View Journal | View Issue

Cite this: *Energy Environ. Sci.*, 2017, **10**, 1770

Received 6th June 2017,
Accepted 25th July 2017

DOI: 10.1039/c7ee01553d

rsc.li/ees

Ternary Ni–Co–P nanoparticles as noble-metal-free catalysts to boost the hydrolytic dehydrogenation of ammonia-borane†

Chun-Chao Hou,‡[ab] Qiang Li,‡[c] Chuan-Jun Wang,[ab] Cheng-Yun Peng,[ab] Qian-Qian Chen,[ab] Hui-Fang Ye,[ab] Wen-Fu Fu,*[ad] Chi-Ming Che,[e] Núria López*[c] and Yong Chen*[ab]

The development of high-efficiency and low-cost catalysts for hydrogen release from chemical hydrogen-storage materials is essential for the hydrogen-economy paradigm. Herein, we report a facile and controllable method to fabricate a series of Co-doped nickel phosphides and their corresponding nanohybrids with graphene oxide (GO) as highly efficient, robust and noble-metal-free catalysts for ammonia borane hydrolysis. The incorporation of Co into Ni_2P effectively optimizes the electronic structures of $Ni_{2-x}Co_xP$ catalysts to enhance their interaction with AB and simultaneously facilitate the hydroxyl activation of AB, resulting in the reduction of the reaction energy barrier and thus substantial improvement of the catalytic rate.

Broader context

The chemical storage and release of hydrogen under mild conditions are of importance to the hydrogen-economy paradigm. Ammonia-borane (AB) has been regarded as a competitive candidate for chemical hydrogen storage because of its high hydrogen content, non-toxicity, and long-term stability under ambient temperature. Fast hydrogen evolution from AB has been achieved using noble metal nanoparticles (*e.g.* Rh and Pt) as the catalyst. However, all non-noble metal catalysts (*e.g.* Fe, Co, Ni nanoparticles) still display relatively poor catalytic activity; the TOF is usually less than 70 min^{-1} at room temperature for these systems. Therefore, the development of high-efficiency and noble-metal-free catalysts for hydrogen release is highly desirable. Metal phosphides with partial charge transfer from metal to P have been discovered to be promising catalysts for AB hydrolysis. However, the specific mechanism regarding how the electronic structure of metal phosphide influences the catalytic performance and why the presence of extra OH^- can dramatically improve the activity are unclear. In this work, ternary Ni–Co–P nanoparticles with various metal elemental ratios and electronic structures are firstly used as catalysts for AB hydrolysis. The incorporation of Co into Ni_2P effectively optimizes the electronic structures of $Ni_{2-x}Co_xP$ catalysts to enhance their interaction with AB and simultaneously facilitate the hydroxyl activation of AB, resulting in the reduction of the reaction energy barrier and thus substantial improvement of the catalytic rate.

Hydrogen, a renewable clean and abundant energy vector, is well recognized as one of the most ideal candidates to replace conventional fossil fuels in the future, but this prospect meets some intractable obstacles including the storage, transportation and release of hydrogen for practical application due to its low boiling point and volumetric density under air conditions.[1–4] The development of safe and efficient chemical storage and release of hydrogen under mild conditions is thus necessary for the sake of the well-known hydrogen-economy paradigm.[5–9] Ammonia-borane (AB) which has the advantages of a low molecular weight but high hydrogen content (19.6 wt%, 146 g L^{-1}), long-term stability under ambient temperature, and non-toxicity, is regarded as a competitive candidate for chemical hydrogen storage.[10–12] Fast hydrogen evolution from AB has been achieved using homogeneous molecular systems and metallic nanoparticles (MNPs), especially Pt, Ru-based noble metals and/or their alloys, as the catalyst.[13–16] However, the exorbitant prices and global reserve scarcity of these precious metals limit their extensive usage. It is highly required to develop robust and noble-metal-free catalysts with high and controllable activities which can operate under ambient conditions.[17–20]

In this respect, Xu and co-workers reported that low-cost MNPs (Ni, Co and Cu) immobilized on various supports with ample surface areas showed good catalytic performances for AB hydrolysis in 2006.[21] Following this, they found that amorphous Fe NPs generated *in situ* through reduction of $FeSO_4$ by $NaBH_4$ exhibited high catalytic activity, which overwhelmingly hinges on the aspects of morphology, dispersion, size and electronic structure.[22]

[a] *Key Laboratory of Photochemical Conversion and Optoelectronic Materials and HKU-CAS Joint Laboratory on New Materials Technical Institute of Physics and Chemistry, Chinese Academy of Sciences, Beijing 100190, P. R. China. E-mail: chenyong@mail.ipc.ac.cn*
[b] *University of Chinese Academy of Sciences, Beijing 100049, P. R. China*
[c] *Institute of Chemical Research of Catalonia, ICIQ. The Barcelona Institute of Science and Technology, Av. Països Catalans, 16, 43007, Tarragona, Spain. E-mail: nlopez@iciq.es*
[d] *College of Chemistry and Engineering, Yunnan Normal University, Kunming 650092, P. R. China. E-mail: fuwf@mail.ipc.ac.cn*
[e] *State Key Laboratory of Synthetic Chemistry and Department of Chemistry, The University of Hong Kong, Pokfulam Road, Hong Kong, P. R. China*
† Electronic supplementary information (ESI) available. See DOI: 10.1039/c7ee01553d
‡ The authors contributed equally.

6.1. Article VI: Hydrogen production from ammonia-borane

Quite recently, Zhong, Lee and co-workers developed a nanostructured $Cu_xCo_{1-x}O$/GO bi-metallic synergistic system to verify that the catalytic activity largely depends on the electronic structure changes in the metal nanoparticles (MNPs).[23] Through the *in situ* XAS experiments, they managed to find that by screening the ratio of Cu–Co in the MNPs deposited on GO, the B–N bond in AB could be weakened due to the interaction of the modified surface of the catalysts with AB, which eventually accelerates the hydrolysis of AB but is still suboptimal with respect to widespread applications. It has become the general trend, even though still a daunting challenge, to develop highly efficient catalysts through regulation of their electronic structures to facilely adsorb and weaken the B–N bonds.[24–27]

Recently, metal phosphide NPs with suitable charge transfer from metal to P facilitating the Proton-Coupled Electron Transfer (PCET) process have been widely used as photo- and electrocatalysts for water splitting.[28–31] In light of the above unique feature and their high chemical stability over a wide range of pH 0–14, Ni_2P NPs were firstly applied to AB hydrolysis by our group and achieved a moderate TOF at room temperature.[32] However, the specific mechanism regarding how the electronic structure of metal phosphide influences the catalytic performance and why the presence of extra OH^- could dramatically improve the activity was unclear. With this in mind, herein we firstly use ternary Ni–Co–P nanoparticles with various metal elemental ratios and electronic structures as catalysts for AB hydrolysis in order to deeply understand the electronic structure–catalytic activity relationship of metal phosphides and thus to further promote their catalytic performance. Among the $Ni_{2-x}Co_xP$ catalysts, the optimized $Ni_{0.7}Co_{1.3}P$ displays the best catalytic performance with an initial TOF value of 58.4 mol(H_2) mol($Ni_{0.7}Co_{1.3}P$)$^{-1}$ min^{-1} at ambient temperature. Furthermore, when $Ni_{0.7}Co_{1.3}P$ was uniformly distributed on GO as a hybrid catalyst, an unprecedentedly high TOF value of 153.9 mol(H_2) mol($Ni_{0.7}Co_{1.3}P$)$^{-1}$ min^{-1} for AB hydrolysis was achieved under ambient conditions. As far as we know, this TOF value is the highest one ever reported for noble-metal-free heterogeneous systems. This superior catalytic performance can be ascribed to collective factors including the ternary Ni–Co–P synergistic effect, high dispersibility, improved surface area and the interfacial interaction between $Ni_{0.7}Co_{1.3}P$ and GO. The experimental results and mechanistic interpretation presented here are expected to stimulate further research efforts on metal phosphides for AB hydrolysis in the future.

The clean-surface $Ni_{2-x}Co_xP$ NP catalysts were prepared using a facile two-step strategy without addition of strong reducing agents like $NaBH_4$ and organic stabilizers (Fig. S1, ESI†). First, the $Ni_{1-0.5x}Co_{0.5x}(OH)_2$ precursors were obtained through a co-precipitation method by virtue of the similar K_{sp} of $Co(OH)_2$ and $Ni(OH)_2$. Then, the precursors were converted into ternary Co–Ni–P nanohybrids *via* a solid-state phosphorization reaction. When $Ni(OH)_2$ alone was used as the precursor, the XRD analysis indicates the formation of the hexagonal phase of Ni_2P (JCPDS No. 65-3544) (Fig. S2 and S3, ESI†). With the increase of the Co-doping content, the positions of the XRD peaks shift toward higher diffraction angles corresponding to hexagonal NiCoP (JCPDS No. 71-2336), suggesting successful Co-doping into the lattice of Ni_2P. Note that the XRD profiles are exactly the same as NiCoP when the x value is larger than 1.0. It has been reported that Co–Ni–P solid solutions, NiCoP (ICDD No. 04-001-4562), $Co_{1.49}Ni_{0.51}P$ (ICDD No. 04-019-5182), $Co_{1.4}Ni_{0.6}P$ (ICDD No. 04-005-5616) and others,[33–35] all show very similar XRD patterns probably due to their same crystal structures and very similar lattice parameters.

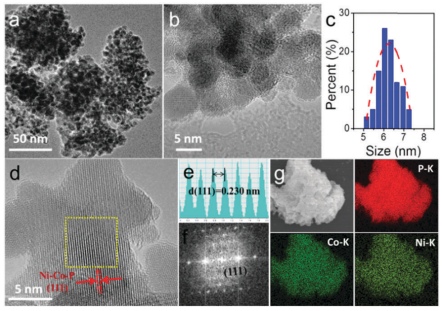

Fig. 1 (a) TEM and (b) magnified TEM images of the as-prepared $Ni_{0.7}Co_{1.3}P$ nanoparticles. (c) The size distribution diagram. (d) The HRTEM image, (e) the spacing of the crystal lattice, (f) the FFT pattern of the corresponding area in (d), and (g) the corresponding EDX elemental mapping of Co, Ni and P for the $Ni_{0.7}Co_{1.3}P$.

TEM and magnified TEM images of $Ni_{0.7}Co_{1.3}P$ (Fig. 1a and b) reveal the formation of well-distributed sphere-shaped nanoparticles with a diameter of 5–7 nm. The HRTEM image taken for one $Ni_{0.7}Co_{1.3}P$ nanocrystal reveals distinct lattice fringes with a spacing of about 0.230 nm corresponding to the (111) plane of $Ni_{0.7}Co_{1.3}P$ (Fig. 1d and e), which is consistent with the SAED pattern (Fig. 1f). The presence of Ni, Co and P elements is confirmed by energy-dispersive X-ray spectroscopy (EDX) (Fig. S4, ESI†) and inductively coupled plasma-optical emission spectroscopy (ICP-OES). The latter also enabled the accurate elemental analysis of the as-prepared samples (Table S1, ESI†). As evidenced by the corresponding EDX elemental mappings, the Ni, Co and P elements are uniformly distributed throughout the $Ni_{0.7}Co_{1.3}P$ nanocrystals (Fig. 1g). The chemical states of Ni, Co and P for $Ni_{0.7}Co_{1.3}P$ are further characterized by X-ray photoelectron spectroscopy (XPS). As shown in Fig. S5 (ESI†), two peaks are apparent in the Ni (2p) region at 853.7 and 856.6 eV and the Co (2p) region at 779.0 and 781.9 eV, respectively, along with another two peaks in the P (2p) region at 129.7 and 133.7 eV. The peaks at 853.7, 779.0 and 129.7 eV are attributed to the binding energies (BEs) for Ni, Co and P of $Ni_{0.7}Co_{1.3}P$, respectively. The peaks at about 856.6, 781.9 and 133.7 eV are assigned to the oxidized Ni, Co and P species, resulting from inevitable surface oxidation of $Ni_{0.7}Co_{1.3}P$.[36–38]

The H_2-generating reaction by hydrolysis of AB with various Ni–Co–P catalysts was carefully evaluated under ambient conditions in a sealed home-made flask equipped with a magnetic stirrer. Control experiments showed that in the absence of catalysts, the AB aqueous solution has long-term stability without any H_2 release.

6.1. Article VI: Hydrogen production from ammonia-borane

As shown in Fig. 2a and b, the $Ni_{0.7}Co_{1.3}P$ catalyst demonstrated the highest activity for hydrogen release from AB amongst a series of Ni–Co–P catalysts. The generated H_2 gas was identified using gas chromatography (Fig. S6, ESI†) and was monitored by a water-filled burette. All the hydrolysis experiments approximately generated 3 mole of H_2 gas per mole of AB, indicating that the decomposition of AB proceeded according to reaction (1) (see ref. 39):

$$H_3NBH_3 + 4H_2O \rightarrow NH_4^+ + B(OH)_4^- + 3H_2 \qquad (1)$$

This process was further confirmed by ^1H NMR and ^{11}B NMR spectra before and after the reaction (Fig. S7–S10, ESI†). Then the effects of $Ni_{2-x}Co_xP$ catalysts, the amount of AB and temperature on the hydrogen-generating rate were measured to interpret the kinetics of AB hydrolysis. As shown in Fig. 2c and Fig. S11–S13 (ESI†), upon varying the molar ratio of $Ni_{0.7}Co_{1.3}P$/AB by changing either the catalyst or the AB concentration, we found that the hydrogen-generating rate is dependent on $[Ni_{0.7}Co_{1.3}P]$, following first-order kinetics with respect to catalyst concentration (Fig. S11, ESI†). In contrast, the reaction rate is much less dependent on [AB] (Fig. S13, ESI†), but nevertheless it does not follow zero-order kinetics due to the interactions between the catalysts and OH^-/H_2O. The $Ni_{0.7}Co_{1.3}P$ catalyst at an optimized cat/AB molar ratio of 0.026 displays the highest catalytic activity

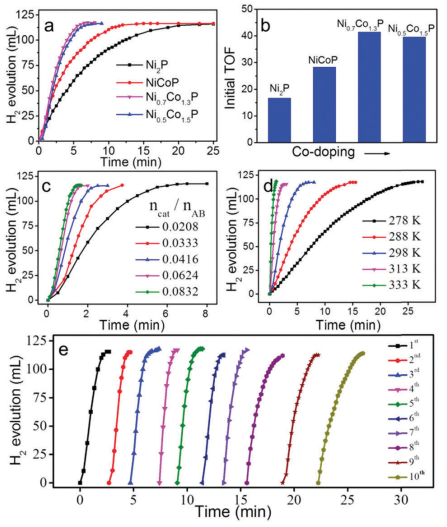

Fig. 2 (a) Stoichiometric hydrogen evolution in 0.5 M NaOH solution (5 mL) containing 1.62 mmol AB catalyzed by Ni_2P, NiCoP, $Ni_{0.7}Co_{1.3}P$ and $Ni_{0.5}Co_{1.5}P$ nanoparticles at 298 K. (b) The corresponding TOFs. (c) The relationship between the H_2 generation rate and $Ni_{0.7}Co_{1.3}P$/AB ratios and (d) temperature. (e) Recycling of the $Ni_{0.7}Co_{1.3}P$ catalyst (10 mg) in 0.5 M NaOH solution (5 mL), with addition of AB (1.62 mmol) to the system at 298 K in each cycle.

with an initial TOF value of 58.4 $mol_{(H_2)}$ $mol_{(Ni_{0.7}Co_{1.3}P)}^{-1}$ min^{-1} at ambient temperature.

As shown in Fig. 2d and Fig. S14 (ESI†), we also investigated the temperature dependence of the catalytic reaction in the range of 278–333 K. The activation energy is estimated to be 43.2 kJ mol^{-1} through an Arrhenius plot. This value is favourably comparable to those of Ru-based bimetallic catalysts.[40,41] The durability of this catalyst is further tested under ambient atmosphere at 298 K. As depicted in Fig. 2e, the $Ni_{0.7}Co_{1.3}P$ catalyst retained 95.2% of its initial activity even after 7 cycles and still kept good activity after 10 cycles, demonstrating its good recyclability. The slight drop in activity might be ascribed to the aggregation of NPs, degraded crystallinity and inevitable surface oxidation during repeated experimental operations (Fig. S15, ESI†).

To get an in-depth understanding of the improved catalytic performance of ternary Ni–Co–P catalysts, X-ray photoelectron spectroscopy (XPS) and X-ray absorption fine structure spectroscopy (XAFS) measurements were performed. Fig. S16 (ESI†) shows XPS spectra of $Ni_{2-x}Co_xP$ in the Co 2p, Ni 2p and P 2p windows. It is clear that the BEs of both Ni 2p and Co 2p positively shift with the increase of Co-doping concentration, whereas the one of P 2p shifts negatively. These findings indicate that more charge transfer from metal to P centres occurred. The variation of electronic states can be further corroborated by the XAFS results. As shown in Fig. 3a, the Ni K-edge XANES spectra of all Ni–Co–P solid solutions are broadly similar to a distinct pre-edge peak that is characteristic of metal phosphides and differs from the pure Ni foil or NiO_x.[42–44]

However, with the increase of Co-doping content into Ni_2P, both the Ni absorption edge of XANES (Fig. 3a and b) and the Co K-edge (Fig. S17, ESI†) slightly shifted toward higher energy, indicating a change in the average Ni and Co oxidation state to a higher value. Furthermore, the arrow in Fig. 3b shows a clear shift in absorption intensity (μt) with the increase of Co-doping.[45–47] As the white line is indicative of the unoccupied electronic states, the increment of the white line peak at about 8350 eV indicates the increase of unoccupied electronic states, which could be achieved by weak oxidation and in other words, electron transfer occurs from Ni to P centres. A similar situation is also observed in Co K-edge XANES spectra as shown in Fig. S17 (ESI†). Based on the above discussions, we are convinced that charge transfer from metal to P centres occurred. Indeed the DFT calculations show a P charge in the range of −0.35 to −0.42 $|e^-|$ (see Table S2, ESI†).

The Ni K-edge extended XAFS (EXAFS) $k^3\chi(k)$ oscillation curve for the $Ni_{0.7}Co_{1.3}P$ is comprised of an oscillation region in 2.5–8 $Å^{-1}$ due to the Ni–P contribution and another one beyond 8 $Å^{-1}$ assigned to the Ni–Ni contribution (Fig. 3c). This profile reveals a noticeable difference in comparison to that of Ni_2P, implying the structural difference in the coordination environment surrounding the Ni atoms.[42–44] A similar situation can be found for a Co atom (Fig. S16, ESI†), which coordinately provides evidence for the successful Co-incorporation. The R space plot for the Ni–Co–P NPs is characterized by two main peaks centred at 1.78 Å and 2.20 Å, which roughly correspond to

6.1. Article VI: Hydrogen production from ammonia-borane

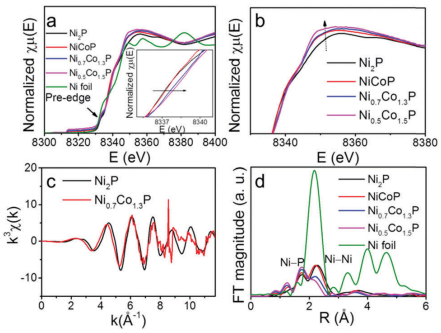

Fig. 3 (a) Ni K-edge and (b) magnified XANES spectra of Ni_2P, NiCoP, $Ni_{0.7}Co_{1.3}P$ and $Ni_{0.5}Co_{1.5}P$ nanocatalysts. (c) Ni K-edge EXAFS $k^3\chi(k)$ oscillation functions of the Ni_2P and $Ni_{0.7}Co_{1.3}P$ NPs and (d) the corresponding FT curves of Ni_2P, NiCoP, $Ni_{0.7}Co_{1.3}P$, $Ni_{0.5}Co_{1.5}P$ NPs and pure Ni foil for comparison (inset: the magnified curves of the Ni–Co–P solid solution).

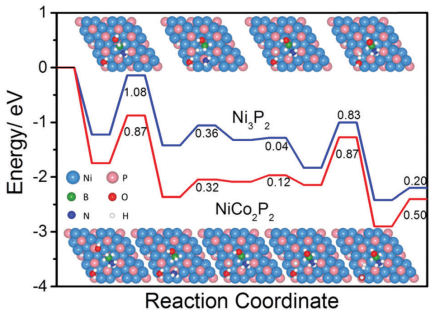

Fig. 4 Energy profiles of AB hydrolytic dehydrogenation on Ni_3P_2(0001) and $NiCo_2P_2$(0001) surfaces with the same initial hydroxyl concentration. The 3D models in the upper panels denote transition states, while those at the bottom correspond to the intermediates.

the Ni–P and neighbouring Ni–Ni configurations, respectively. Compared to Ni foil, the Ni–Co–P NPs all showed decreased intensity, which was ascribed to the nano-size effect. As for Co-doping, the phase-shift-free Fourier transform (FT) showed an increased intensity of Ni–P and a decrease in the Ni–Ni feature together with slight phase changes, implying that the Co-doping induces a relatively higher coordination number of Ni–P and a smaller coordination number of the second pair (Ni–Ni).[48] All of these results revealed that Co was successfully incorporated into the crystal lattice of Ni_2P and occupied partially the initial place of Ni atoms, implying the formation of a Co–P bond with decreasing long-range order.

The aforementioned results provide strong evidence for the promotion of electron transfer from metal to P centres in these ternary Ni–Co–P solutions, finally resulting in strong adsorption of AB, which can effectively activate the B–N bonds in AB, therefore decreasing the reaction energy barrier and accelerating hydrogen evolution. This point was further corroborated by DFT modeling with the PBE functional.[49] The specific details are provided in the ESI† and Tables S3–S6. In view of the basic reaction conditions where the reaction takes place, an S_N2 mechanism where surface OH* attacks the adsorbed BH_3NH_3 was found (Fig. 4, Scheme S1 and Table S4, ESI†). As shown in the energy profile, the reaction starts from both AB and H_2O adsorbed on the surface of the catalyst. This adsorption process is exothermic by 1.75 eV for $NiCo_2P_2$, and only 1.23 eV for Ni_3P_2, indicating the stronger interaction between them (solvent contributions would reduce adsorption by about 0.65 eV).[50] The results are consistent with XPS and XAFS results.

Following the S_N2 reaction in which surface OH* attacks the BH_3 group, B–N bond breaking is induced ($OH^* + BH_3NH_3^* \rightarrow BH_3OH^* + NH_3^*$, see video S_N2.avi, ESI†). This reaction is exothermic on Ni_3P_2 and $NiCo_2P_2$ by −0.20 and −0.62 eV, respectively, showing that the doped system is more thermodynamically favourable. From the kinetic point of view, the reaction barrier on the doped surface is also favoured as the barrier on $NiCo_2P_2$ (0.87 eV) is 0.21 eV lower than that on Ni_3P_2 (1.08 eV). The product, BH_3OH^* has been widely regarded as the key intermediate in borohydride and ammonia borane oxidation reactions.[51] After B–N bond scission, one of the hydrides leaves the B atom with small barriers (0.36 and 0.32 eV) ($BH_3OH^* \rightarrow BH_2OH^* + H^*$, see video B–H bond-breaking.avi, ESI†) on both surfaces and this is then followed by the almost barrierless B–N bond regeneration (0.04 and 0.12 eV) ($BH_2OH^* + NH_3^* \rightarrow HOBH_2{-}NH_3^*$, see video B–N regeneration.avi, ESI†). A second S_N2 cycle was calculated, $HOBH_3^* + OH^* \rightarrow BH_2(OH)_2^* + H^*$, and the higher barrier required (1.01 eV) shows that this step cannot compete with the direct B–H bond breaking from BH_3OH^*. In the B–N bond formation step, electrostatic interaction between B and N atoms would contribute to the low B–N bond regeneration barrier. Bader charge analysis[52] (Table S5, ESI†) shows that B and N atoms are positively and negatively charged by 1.26 and 1.20 $|e^-|$ in BH_2OH and NH_3. Possible side reactions were also calculated (Table S4, ESI†) but they cannot compete with this step. The hydride group on the surface can then attack H_2O to generate H_2 (see video H_2O splitting.avi, ESI†). The barriers of this step are close to each other for the two surfaces (0.83 and 0.87 eV), and the process is slightly more exothermic (by 0.17 eV) on the Co-containing one. The last step concerns H_2 desorption which is slightly easier on Ni_2P but the energies for desorption are low and will be surpassed by the molecular entropy gain. After one reaction cycle ($BH_3NH_3 + H_2O \rightarrow HOBH_2NH_3 + H_2$), when the species left on the surface are $HOBH_2{-}NH_3$, it will repeat the previous steps twice and produce two more H_2 molecules from $BH_2(OH)_2^*$ and $BH(OH)_3^*$. These species and their importance in reaction mechanisms have been proposed by Chatenet *et al. via in situ* Fourier transform infrared spectroscopy studies on borohydride[53] and ammonia borane oxidation reactions.[54] Our mechanism based on DFT matches well with these results. We should note that the S_N2 step is the rate-limiting step in AB hydrolytic dehydrogenation, which could rationalize the common phenomenon that the presence of OH^-

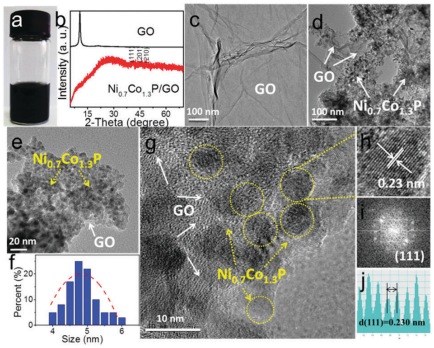

Fig. 5 (a) The photograph of $Ni_{0.7}Co_{1.3}P$/GO dispersed in water. (b) XRD patterns. The TEM images of (c) GO and (d) the $Ni_{0.7}Co_{1.3}P$/GO nanohybrid. (e) The magnified TEM and (g) HRTEM images of $Ni_{0.7}Co_{1.3}P$/GO. (f) The size distribution. (h) The single NPs, (i) the FFT pattern of the corresponding area in (h) and (j) the spacing of the crystal lattice.

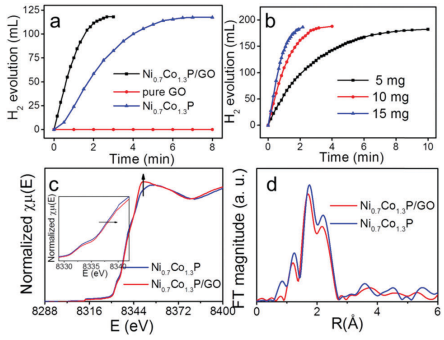

Fig. 6 (a) Stoichiometric hydrogen evolution in 0.5 M NaOH solution (5 mL) containing 1.62 mmol AB catalyzed by pure GO, $Ni_{0.7}Co_{1.3}P$ and the $Ni_{0.7}Co_{1.3}P$/GO nanohybrid at 298 K. (b) The relationship between the H_2 generation rate and various amounts of the $Ni_{0.7}Co_{1.3}P$/GO nanocatalyst. (c) Ni K-edge XANES spectra and (d) the corresponding FT curves of the $Ni_{0.7}Co_{1.3}P$ NPs and $Ni_{0.7}Co_{1.3}P$/GO nanohybrid.

could dramatically improve the catalytic properties and shorten the induction period. The lower barrier on the Co-containing surface explains why TOF values are higher for these materials. The observed improvement in the catalytic activity implies the fine tuning of the electronic structure at the Ni–Co surface as can be inspected from the d-band center position (see Table S6, ESI†). In the Ni–Co system the Ni centres are slightly more reactive than the Ni-only counterpart while the Co *d*-states are slightly less reactive than the Co-only compound. Thus the formation of the intermetallic bond is crucial for adjusting the chemical properties of the surface.

In an effort to further improve the catalytic activity, a $Ni_{0.7}Co_{1.3}P$/GO nanohybrid material was prepared according to a modified procedure (see the ESI†). As displayed in the TEM images in Fig. 5 and Fig. S18–S20 (ESI†), $Ni_{0.7}Co_{1.3}P$ NPs with a size of about 5 nm is uniformly deposited on the surface of GO due to the anchoring effect of the oxide-GO. The formation of the hybrid material is further confirmed by XRD, ICP-OES, XPS and BET (Fig. S21, S22 and Table S7, ESI†) *etc.* Then the catalytic activity of the $Ni_{0.7}Co_{1.3}P$/GO in the hydrolysis of AB was evaluated under the same conditions. Control experiments showed that pure GO has no catalytic activity for AB hydrolysis, while the $Ni_{0.7}Co_{1.3}P$/GO sample exhibited exceedingly higher catalytic performance compared to the single $Ni_{0.7}Co_{1.3}P$ alone. The dramatically improved activity can be attributed to the good dispersion and hence the enlarged surface area of nanoparticles on the GO surface with good electrical activity, therefore, creating an additional synergistic effect between the connection.[55–58] The interaction between $Ni_{0.7}Co_{1.3}P$ and GO was confirmed by XAFS (Fig. 6). The rising edge of the $Ni_{0.7}Co_{1.3}P$/GO sample shifts to a higher energy, implying slight electron transfer may occur from $Ni_{0.7}Co_{1.3}P$ to the GO, which was also corroborated by XPS (Fig. S21, ESI†). Both experimental results indicate a bonding relationship between the two materials.

The stability of the $Ni_{0.7}Co_{1.3}P$/GO sample is also probed by the recycling experiment. As shown in Fig. S23 (ESI†), the $Ni_{0.7}Co_{1.3}P$/GO sample maintains 93.0% of its initial activity after 5 cycles. It is worth mentioning that the recovered sample in the second cycle demonstrates an extraordinary activity with a TOF value of about 153.9 $mol_{(H_2)}$ $mol_{(Ni_{0.7}Co_{1.3}P)}^{-1}$ min^{-1}, which is much higher than that in the first cycle (TOF = 93.3 $mol_{(H_2)}$ $mol_{(Ni_{0.7}Co_{1.3}P)}^{-1}$ min^{-1}). Such a phenomenon is also observed for the pure $Ni_{0.7}Co_{1.3}P$ sample and for other metal phosphides reported in our previous studies.[32,59] This can be reasonably explained by the *in situ* reduction of some surface oxidized Ni–Co–P species in this reductive NH_3BH_3 system. As far as we know, this achieved TOF of 153.9 (109.4 based on the total mole number of metal) represents one of the highest values ever reported for all noble-metal-free based catalysts (Table S8, ESI†).

Conclusions

In summary, we have successfully achieved a feasible, viable and scalable way to synthesize Co-doped nickel phosphide NPs and their nanohybrid with graphene oxide (GO) as excellent catalysts for hydrolysis of AB. Benefitting from the ternary Ni–Co–P synergistic effect, high dispersibility, improved surface area and the interfacial interaction between $Ni_{0.7}Co_{1.3}P$ and GO, the $Ni_{0.7}Co_{1.3}P$/GO shows a high initial turnover frequency (TOF) of up to 153.9 $mol_{(H_2)}$ $mol_{(Ni_{0.7}Co_{1.3}P)}^{-1}$ min^{-1} at ambient temperature, which is an unprecedented value higher than those ever reported for noble-metal-free catalytic systems, and a good sustainability maintaining 93.0% activity after 5 cycles. The promotion is rationalized through Density Functional Theory indicating that hydroxyl activation of the AB bond is enhanced when Co is present. These findings not only enrich

the family of noble-metal-free catalysts for AB hydrolysis, but also provide significant and promising insights into modulating the electronic structures of metal phosphides for hydrogen storage and related applications.

Acknowledgements

The financial support from the National Key Basic Research Program of China (973 Program 2013CB834800 and 2013CB632403) and the Strategic Priority Research Program of the Chinese Academy of Sciences (XDB17030300) are deeply acknowledged. This work was partially supported by the Natural Science Foundation of China (21371175) and CAS-Croucher Funding Scheme for Joint Laboratories. Y. C. is thankful of support from the Chinese Academy of Sciences (100 Talents Program). Q. L. and N. L. are grateful to MINECO (CTQ2015-68770-R) for financial support and to the Centro de Supercomputación y Visualización de Madrid, Universidad Politécnica de Madrid for providing the computational resources through the BSC-RES. We also thank BSRF for synchrotron beamtime.

Notes and references

1 Q.-L. Zhu and Q. Xu, *Energy Environ. Sci.*, 2015, **8**, 478–512.
2 Ö. Metin, V. Mazumder, S. Özkar and S. H. Sun, *J. Am. Chem. Soc.*, 2010, **132**, 1468–1469.
3 F. A. de Bruijn, *ChemSusChem*, 2008, **1**, 782–783.
4 J. Yang, A. Sudik, C. Wolverton and D. Siegel, *Chem. Soc. Rev.*, 2010, **39**, 656–675.
5 J. Wang, X. B. Zhang, Z. L. Wang, L. M. Wang and Y. Zhang, *Energy Environ. Sci.*, 2012, **5**, 6885–6888.
6 J. Wang, Y. L. Qin, X. Liu and X. B. Zhang, *J. Mater. Chem.*, 2012, **22**, 12468–12470.
7 J. M. Yan, X. B. Zhang, T. Akita, M. Haruta and Q. Xu, *J. Am. Chem. Soc.*, 2010, **132**, 5326–5327.
8 J. M. Yan, X. B. Zhang, H. Shioyama and Q. Xu, *J. Power Sources*, 2010, **195**, 1091–1094.
9 J. M. Yan, X. B. Zhang, S. Han, H. Shioyama and Q. Xu, *J. Power Sources*, 2009, **194**, 478–481.
10 S. K. Singh, A. K. Singh, K. Aranishi and Q. Xu, *J. Am. Chem. Soc.*, 2011, **133**, 19638–19642.
11 H.-L. Jiang, S. K. Singh, J.-M. Yan, X.-B. Zhang and Q. Xu, *ChemSusChem*, 2010, **3**, 541–549.
12 Q. Xu and M. Chandra, *J. Alloys Compd.*, 2007, **446–447**, 729–732.
13 W. Chen, J. Ji, X. Duan, G. Qian, P. Li, X. Zhou, D. Chen and W. Yuan, *Chem. Commun.*, 2014, **50**, 2142–2144.
14 M. Zahmakiran and S. Özkar, *Top. Catal.*, 2013, **56**, 1171–1183.
15 M. Rakap, *Appl. Catal., A*, 2014, **478**, 15–20.
16 S. Wang, D. Zhang, Y. Ma, H. Zhang, J. Gao, Y. Nie and X. Sun, *ACS Appl. Mater. Interfaces*, 2014, **6**, 12429–12435.
17 T. J. Clark, G. R. Whittell and I. Manners, *Inorg. Chem.*, 2007, **46**, 7522–7527.
18 J.-M. Yan, X.-B. Zhang, S. Han, H. Shioyama and Q. Xu, *Inorg. Chem.*, 2009, **48**, 7389–7393.
19 Z.-H. Lu, H.-L. Jiang, M. Yadav, K. Aranishi and Q. Xu, *J. Mater. Chem.*, 2012, **22**, 5065–5071.
20 X. Ma, Y.-X. Zhou, H. Liu, Y. Li and H.-L. Jiang, *Chem. Commun.*, 2016, **52**, 7719–7722.
21 Q. Xu and M. Chandra, *J. Power Sources*, 2006, **163**, 364–370.
22 J.-M. Yan, X.-B. Zhang, S. Han, H. Shioyama and Q. Xu, *Angew. Chem., Int. Ed.*, 2008, **47**, 2287–2289.
23 K. Feng, J. Zhong, B. Zhao, H. Zhang, L. Xu, X. H. Sun and S.-T. Lee, *Angew. Chem., Int. Ed.*, 2016, **55**, 11950–11954.
24 M. Mahyari and A. Shaabani, *J. Mater. Chem. A*, 2014, **2**, 16652–16659.
25 J. Hu, Z. Chen, M. Li, X. Zhou and H. Lu, *ACS Appl. Mater. Interfaces*, 2014, **6**, 13191–13200.
26 Y.-Z. Chen, Q. Xu, S.-H. Yu and H.-L. Jiang, *Small*, 2015, **11**, 71–76.
27 H. Zhang, X. Wang, C. Chen, C. An, Y. Xu, Y. Huang, Q. Zhang, Y. Wang, L. Jiao and H. Yuan, *Int. J. Hydrogen Energy*, 2015, **40**, 12253–12261.
28 D. R. Weinberg, C. J. Gagliardi, J. F. Hull, C. F. Murphy, C. A. Kent, B. C. Westlake, A. Paul, D. H. Ess, D. G. McCafferty and T. J. Meyer, *Chem. Rev.*, 2012, **112**, 4016–4093.
29 J. Q. Tian, Q. Liu, A. M. Asiri and X. P. Sun, *J. Am. Chem. Soc.*, 2014, **136**, 7587–7590.
30 Q. Liu, J. Q. Tian, W. Cui, P. Jiang, N. Y. Cheng, A. M. Asiri and X. P. Sun, *Angew. Chem., Int. Ed.*, 2014, **53**, 6710–6714.
31 S. Cao, Y. Chen, C. J. Wang, P. He and W. F. Fu, *Chem. Commun.*, 2014, **50**, 10427–10429.
32 C. Y. Peng, L. Kang, S. Cao, Y. Chen, Z. S. Lin and W. F. Fu, *Angew. Chem., Int. Ed.*, 2015, **54**, 15725–15729.
33 Z. Wang, X. Q. Cao, D. Liu, S. Hao, G. Du, A. M. Asiri and X. P. Sun, *Chem. Commun.*, 2016, **52**, 14438–14441.
34 W. Li, X. F. Gao, X. G. Wang, D. Xiong, P. Huang, W. G. Song, X. H. Bao and L. F. Liu, *J. Power Sources*, 2016, **330**, 156–166.
35 W. Li, D. Xiong, X. F. Gao, W. G. Song, F. Xia and L. F. Liu, *Catal. Today*, 2017, **1**, 122–129.
36 J. Q. Li, M. Yan, X. M. Zhou, Z.-Q. Huang, Z. M. Xia, C.-R. Chang, Y. Y. Ma and Y. Q. Qu, *Adv. Funct. Mater.*, 2016, **37**, 6785–6796.
37 J. Yu, Q. Q. Li, Y. Li, C. Y. Xu, L. Zhen, V. P. David and J. S. Wu, *Adv. Funct. Mater.*, 2016, **26**, 7644–7651.
38 P. Zhang, Y. Chen, M. Wang, Y. Yang, J. Jiang, B. Zhang, L. Duan, Q. Daniel, F. Li and L. C. Sun, *J. Mater. Chem. A*, 2017, **5**, 7564–7570.
39 W. Y. Chen, D. Li, Z. J. Wang, G. Qian, Z. J. Sui, X. Z. Duan, X. G. Zhou, I. Yeboah and D. Chen, *AIChE J.*, 2017, **1**, 60–65.
40 G. Chen, S. Desinan, R. Rosei, F. Rosei and D. Ma, *Chem. – Eur. J.*, 2012, **18**, 7925–7930.
41 N. Mohajeri, A. T-Raissi and O. Adebiyi, *J. Power Sources*, 2007, **167**, 482–485.
42 Y. K. Lee and S. T. Oyama, *J. Catal.*, 2006, **239**, 376–389.
43 T. Kawai, K. K. Bando, Y. K. lee, S. T. Oyama, W. J. Chun and K. Asakura, *J. Catal.*, 2006, **241**, 20–24.
44 H.-R. Seo, K.-S. Cho and Y.-K. Lee, *Mater. Sci. Eng., B*, 2011, **176**, 132–140.
45 S. T. Oyama, T. Gott, K. AsaKura, S. TakaKusagi, K. Miyazaki, Y. Koike and K. K. Bando, *J. Catal.*, 2009, **268**, 209–222.
46 Y. Chen, C. Li, J. Zhou, S. Zhang, D. Rao, S. He, M. Wei, D. G. Evans and X. Duan, *ACS Catal.*, 2015, **5**, 5756–5765.

47 L. Zhou, M. Shao, C. Zhang, J. Zhao, S. He, M. Rao, M. Wei, D. G. Evans and X. Duan, *Adv. Mater.*, 2016, 1604080.
48 K. Xu, H. Ding, H. F. Lv, P. Z. Chen, X. Lu, H. Cheng, T. Zhou, S. Liu, X. J. Wu, C. Z. Wu and Y. Xie, *Adv. Mater.*, 2016, **28**, 3326–3332.
49 J. P. Perdew and K. Burke; M. Ernzerhof, *Phys. Rev. Lett.*, 1996, **77**, 3865–3868.
50 M. Garcia-Ratés and N. López, *J. Chem. Theory Comput.*, 2016, **12**, 1331–1341.
51 T. Maiyalagan and V. S. Saji, *Electrocatalysts for Low Temperature Fuel Cells: Fundamentals and Recent Trends*, John Wiley & Sons, 2017.
52 G. Henkelman, A. Arnaldsson and H. Jónsson, *Comput. Mater. Sci.*, 2006, **36**, 254.
53 B. Molina Concha, M. Chatenet, F. Maillard, E. A. Ticianelli, F. H. B. Lima and R. B. de Lima, *Phys. Chem. Chem. Phys.*, 2010, **12**, 11507–11516.
54 B. Molina Concha, M. Chatenet, F. H. B. Lima and E. A. Ticianelli, *Electrochim. Acta*, 2013, **89**, 607–615.
55 P. Xi, F. Chen, G. Xie, C. Ma, H. Liu, C. Shao, J. Wang, Z. Xu, X. Xu and Z. Zeng, *Nanoscale*, 2012, **4**, 5597–5601.
56 L. Yang, N. Cao, C. Du, H. Dai, K. Hu, W. Luo and G. Cheng, *Mater. Lett.*, 2014, **115**, 113–116.
57 K. Gungörmez and Ö. Metin, *Appl. Catal., A*, 2015, **494**, 22–28.
58 N. S. Ciftci and Ö. Metin, *Int. J. Hydrogen Energy*, 2014, **39**, 18863–18870.
59 Z. C. Fu, Y. Xu, S. L. F. Chan, W. Wang, F. Li, F. Liang, Y. Chen, Z. S. Lin, W. F. Fu and C.-M. Che, *Chem. Commun.*, 2017, **53**, 705–708.

Article VII: Shape control in concave metal nanoparticles by etching

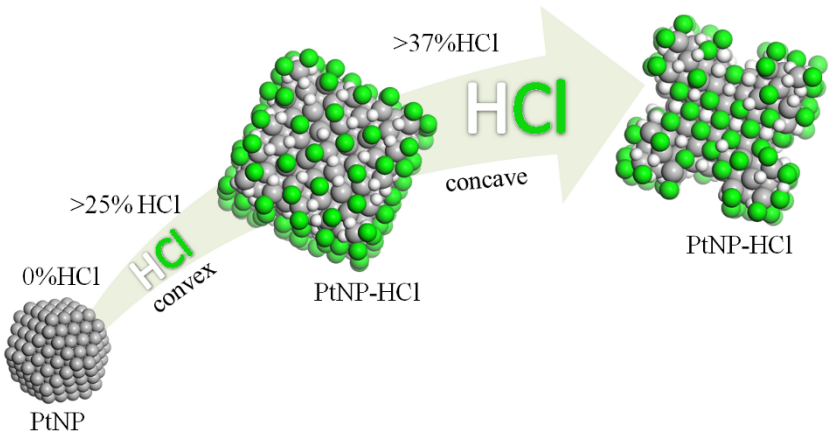

Published in *Nanoscale*, 2017, **9**, 13089-13094

6.2. Article VII: Shape control in concave metal nanoparticles by etching

Nanoscale

PAPER

View Article Online
View Journal | View Issue

Cite this: *Nanoscale*, 2017, **9**, 13089

Shape control in concave metal nanoparticles by etching†

Qiang Li, [a] Marcos Rellán-Piñeiro, [a] Neyvis Almora-Barrios, [a] Miquel Garcia-Ratés, [a] Ioannis N. Remediakis [b] and Núria López *[a]

Received 1st June 2017,
Accepted 30th July 2017

DOI: 10.1039/c7nr03889e

rsc.li/nanoscale

The shape control of nanoparticles constitutes one of the main challenges in today's nanotechnology. The synthetic procedures are based on trial-and-error methods and are difficult to rationalize as many ingredients are typically used. For instance, concave nanoparticles exhibiting high-index facets can be obtained from Pt with different HCl treatments. These structures present exceptional capacities when are employed as catalysts in electrochemical processes, as they maximize the activity per mass unit of the expensive material. Here we show how atomistic simulations based on density functional theory that take into account the environment can predict the morphology for the nanostructures and how it is even possible to address the appearance of concave structures. To describe the control by etching, we have reformulated the Wulff construction through the use of a geometric model that leads to concave polyhedra, which have a larger surface-to-volume ratio compared to that for nanocubes. Such an increase makes these sorts of nanoparticles excellent candidates to improve electrocatalytic performance.

Introduction

The properties of noble metal nanoparticles depend on their morphology and surface crystalline orientation and, thus, the specific control of the architectures is one of the major challenges in nanotechnology.[1–7] Shape control has been achieved and several synthetic methods allow the production of selected polyhedra limited by convex surfaces (cubes, octahedra, tetrahedra, and rods).[8–10] Many of the synthetic processes are based on the generation of a seed by a fast reduction of a metal salt, which is then grown on a solution containing halides and/or surfactants with a milder reductive agent. Recent studies have shown the efficiency of biomolecules in recognizing specific crystallographic facets and affecting nanocrystal shapes.[11,12] The mechanism of shape control has been proposed to be kinetic or thermodynamic and is a consequence of the solution ingredients and conditions.[13] In recent years, there has been considerable interest in the synthesis of concave nanoparticles (see Fig. 1).[2,14] These structures have unique potential in electrocatalysis because of their exposed high-index facets[5,15] that encompass a larger surface area compared to that in convex systems and result in more active sites.[14–19] In wet chemistry, two strategies have been proposed to generate concave nanocrystals of active metals: (i) directionally controlled overgrowth[20,21] and (ii) site-specific dissolution.[22] Overgrowth relies on the fact that capping agents, bound to specific facets, modify the relative growth rates leading to concave polyhedra. This is the case of Pt octapods exhibiting the {411} facets, or Ag nanostructures that are formed when amines or Cu^{2+} ions are added.[15,23] Octapods were also indicated to appear by kinetically controlled overgrowth in the case of Rh with bromide as a capping agent.[24]

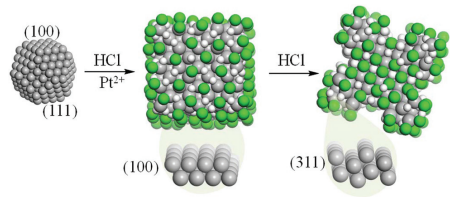

Fig. 1 Atomic representation of the structures formed during the synthetic process of Pt nanoparticles based on the fast reduction of a metal salt that grows in a solution with a different amount of HCl. The insets highlight the most stable surfaces in each stage of the process. The scheme is adapted from ref. 2. Color code for the surface atoms: Pt in grey, Cl in green, and H in white.

[a]*Institute of Chemical Research of Catalonia, ICIQ, The Barcelona Institute of Science and Technology, Av. Països Catalans, 16, 43007 Tarragona, Spain. E-mail: nlopez@iciq.es*
[b]*Department of Materials Science and Technology, University of Crete, and Institute of Electronic Structure and Laser, FORTH, Heraklion, 71003, Greece*
†Electronic supplementary information (ESI) available: Calculated surface and binding energies, resulting Wulff structures, and details on the *ab initio* thermodynamics formalism and on the geometric model. See DOI: 10.1039/c7nr03889e

6.2. Article VII: Shape control in concave metal nanoparticles by etching

Alternatively, concave nanoshapes can be formed by partial dissolution of a larger nanoparticle. The region that experiences the faster dissolution evolves into a concave surface. Therefore, the strength of the etchants needs to be finely tuned in order to obtain the desired shape.[25]

Halides and hydrogen halides form dense phases on metal surfaces.[26] For Au and Ag, halides are employed as structure directing coatings that show a large preference for the {100} planes, and thus for cubes.[27] This has been recently confirmed computationally, showing a thermodynamic control of the nanoparticle shape.[28] Experiments on more reactive metals, like Pt or Pd, have found that hydrogen halides at certain concentrations lead to the formation of concave nanoparticles.[2,3,29] In these cases, the process of the formation of high-index facets requires available low index-planes like {100} and {111} surfaces that serve as templates.[14]

The morphology of nanoparticles can be explored through the systematic use of theoretical tools based on Density Functional Theory, DFT, coupled with the Wulff construction, either in the continuum[30,31] or atomistic versions,[32,33] or by creating the environment through first-principles thermodynamics.[34] In the experiments, concave nanoparticles are produced in an acid/watery environment, in open air and with the Pt precursor in the solution. The full theoretical study would require addressing all the stages from nucleation to growth and including all the reactive ingredients which make the prediction of the shape computationally unaffordable. Alternatively, we have shown previously[28,35] that a much better understanding of the shape controlling factors can be obtained by addressing the problem of the nanoparticle shape through first principles and by sequentially increasing the level of complexity (*i.e.* with the presence of the solvent, additives). The lack of a methodology equivalent to the Wulff construction for concave objects poses an additional challenge. In this study, we aim at describing the formation of cubic Pt nanoparticles and how they lead to concave structures when HCl concentration increases and at describing an alternative to the Wulff construction for concave structures.

Methods

We have performed DFT calculations with the Vienna *ab initio* simulation package code (VASP version 5.3.3)[36,37] with the Perdew–Burke–Ernzerhof (PBE) exchange–correlation functional.[38] Inner electrons were represented by projector augmented wave (PAW) potentials[39,40] with a kinetic cutoff energy of 400 eV, and dispersion contributions with D2 parameters complemented with our reparametrized values for metals.[41,42] The corresponding *k*-point samplings were denser than 0.3 $Å^{-1}$. We considered several low-index planes, (100), (111), and (110), and also the open surfaces that might be present in particle-etched concave structures, that is, (211), (311), (411) and (511) planes which contain the {111} steps and the {100} terraces. The models for all the Pt surfaces were constructed with 5–9 layers depending on the degree of openness of the surfaces to ensure convergence in all cases. The topmost 2–4 layers were relaxed during optimization, while the remaining layers were kept fixed to mimic the bulk. The structures were interleaved under 12 Å vacuum. HCl was adsorbed only on the topmost surface and the dipole correction was employed to correct potential spurious terms arising from the asymmetry of the slabs.[43] We used *ab initio* atomistic thermodynamics to understand the effect of the concentration of different adsorbed species on the stability and growth of Pt nanoparticle surfaces.[34] Solvent contributions were added *via* the VASP-MGCM (VASP-Multigrid Continuum Model).[44] To illustrate how theoretical simulations can account for the etching of Pt nanoparticles, we have generated a finite cubic model of 16 Å side, representing the most likely growth morphology. The surface was completely covered with HCl and the total stoichiometry was 365 Pt atoms and 148 HCl units in the form of a monolayer of a rock-salt-like structure (see Fig. S2†). The so-built structure was then allowed to relax and during this step some HCl molecules were formed and left the surface due to the repulsion between them. These molecules were then removed from the simulation box leaving the final Pt-cube structure surrounded by 119 HCl units. Pitting was then tested at different positions of the naked Pt_{365} and $Pt_{365}(HCl)_{119}$: in the middle of a facet, in the edge, and at the corner positions. Finally, we computed the change in energy due to the addition of an extra Pt atom to the Pt_{365} and $Pt_{365}(HCl)_{119}$ at the face positions. A data-set collection of computational results is available in the ioChem-BD repository.[45]

Results and discussion

Experiments have evidenced that Pt nanoparticles present concave faces upon exposure to high concentrations of HCl.[2] Simulations have been carried out to explain these observations. The present simulations might seem simple but we would like to point out the following: (i) this is the first ever approach that involves the use of density functional theory to explore the appearance of concave nanoparticles by etching. (ii) Solvent contributions are employed when needed through a continuum model. Although this is not the best situation, because explicit water molecules could have a role, it simplifies the chemical approach whilst avoiding a discussion based only on gas-phase energies. (iii) The contribution of oxidants (O_2) that might be present in the solution has not been considered. Again, a proper representation of the full phenomena of shape control would be needed to integrate the mechanistic contribution of these species. (iv) However, even if the models presented here are rather simple, they do allow the formulation of a concave version of the Wulff construction. The Wulff construction has served to understand the equilibrium structure of nanoparticles since 1901. To our knowledge, this is the first attempt to predict the theoretically concave shapes of nanoparticles in a generalized framework.

The first point that is addressed in the simulations is the estimation of the adsorption energy of HCl molecules on all

6.2. Article VII: Shape control in concave metal nanoparticles by etching

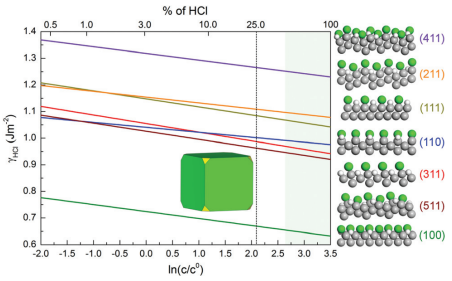

Fig. 2 (Left) Surface energy for different planes as a function of the HCl concentration (c^0 = 1 M) at room temperature and (right) side view of the different surfaces with the densest HCl coverage. The inset represents the nanoparticle morphology, as derived from the Wulff construction at 25% of HCl (dashed line). The shaded area corresponds to HCl concentrations where pitting occurs, as calculated from our kinetic model. Color code for the Pt surfaces: (100) green, (110) blue, (111) olive, (211) orange, (311) red, (411) purple and (511) wine. Atomic color code as in Fig. 1.

relevant Pt surfaces. These quantities are needed to predict the equilibrium shape of the nanoparticle in an interacting environment using the Wulff construction method.[30] The interaction of HCl on these surfaces with the densest coverage was calculated with respect to the solvated molecules. The results for adsorption energies and atom–atom distances are summarized in section S2.† Fig. 2 (right) shows the side view of the densest HCl packing on low-index facets, such as (100), (110), and (111), and also on stepped surfaces (211), (311), (411) and (511). The HCl molecules have been found to adsorb preferentially on the (100) Pt surfaces, resulting in a large value for the binding energy per HCl molecule (−1.11 eV per HCl). Note that the adsorption of NaCl also considered in ref. 2 is almost thermoneutral, so the nanoparticle shape control would only be induced by Cl^- adsorption as in the case of Ag@Au[28] (therefore, we do not discuss it further). In this surface, the Cl and H atoms are placed on the bridge sites of the Pt surface at a distance of 1.934 Å and 1.011 Å from the surface, respectively. Surface energies calculated with DFT methods are known to deviate from experimental data.[46] However, DFT-based results for binding energies are not affected in the same way.[42]

To predict the shape of the nanoparticles in the HCl–water environment, we have adopted an *ab initio* thermodynamics framework,[34] see section S4,† that allows the estimation of the surface energy for each of the surfaces as a function of the acid concentration, c. For this purpose, we considered the chemical potential of the species as the reference in solution at room temperature. The results for the surface energy for the HCl-covered Pt surfaces, γ_{HCl}, at different HCl concentrations are shown in Fig. 2 (left). The range of HCl concentrations corresponds to values between 0.5% and 100% (see Table S5†).

The *ab initio* thermodynamics indicates that the preferred configurations are dense phases with high concentrations of adsorbed HCl. The general trend shown in Fig. 2 is that the (100) surface is the most stable over the whole range of concentrations. With regard to the remaining surfaces, it is important to note that, although the (311) and (511) faces are less stable than the (110) surface at low HCl concentrations, the situation is the opposite for large HCl amounts. In order to validate our approach, we repeated the calculations for the (100) surface considering the system solvated by the continuum model in water. The largest deviation in the calculated γ_{HCl} with respect to the same quantity for the systems in vacuum is lower than 1%. Therefore, unsolvated surface energies were employed and solvation was considered only for the reference HCl molecule (section S2†), in the definition of the binding energy. The inset in Fig. 2 shows that the application of the Wulff construction at 25% of HCl concentration results in a nanocube (see section S3†).

Increasing the acid concentration led to the erosion of the cubes. Experiments showed that at a HCl concentration of 37%[2] the corresponding structure obtained from our Wulff construction is no longer valid. Increasing the HCl concentration further causes the formation of bone-like structures without increasing the nanoparticle size.[2] This is due to the effect of the acid. As the deposition rate starts to become lower than the etching one, and therefore pitting starts.[3] In order to understand how pitting occurs, we calculated the reaction energies for dissolution at relevant acid concentrations. We started by studying this dissolution process on the thermodynamically preferred surface: (100), and on a high-index plane: the (311) facet. The removal of a Pt atom from the (100) surface is 0.21 eV easier than that from the (311) one. This energy difference relies on the different HCl configuration that we have on both the surfaces. In the case of the (100) facet, H and Cl atoms are placed at the bridge positions between Pt atoms, whereas for the (311) surface, H and Cl atoms are placed on top of the Pt atoms (see Fig. 3a and b). When a Pt atom is removed from both the surfaces, there is no change in the configuration of the HCl network in the (100) facet, whereas for the (311) facet, a Cl atom occupies the hollow left by Pt. Thus, although for this last surface the Cl atom approaches a Pt atom, the HCl network is distorted locally and leads to a less favorable situation in terms of energy compared to the pitting in the (100) facet.

Similarly, for the Pt_{365} nanoparticle, we calculated the energy gain to depositing an isolated Pt atom together with the energy cost to remove a Pt atom from the corner, step and the (100) facet. In the case of naked Pt nanoparticles, the easiest Pt removal corresponds to the lowest atom coordination, the corners being 1.75 eV more thermodynamically easy to be removed than the atoms at the face centers (see Table S6†). The situation changes for HCl-covered nanoparticles (see Fig. 3c and d). In this case, the pitting at the edge and facet positions is almost equivalent and the corresponding configurations are 0.94 eV more stable than removing one atom at the corner, thus the stability goes as: corner > edge

6.2. Article VII: Shape control in concave metal nanoparticles by etching

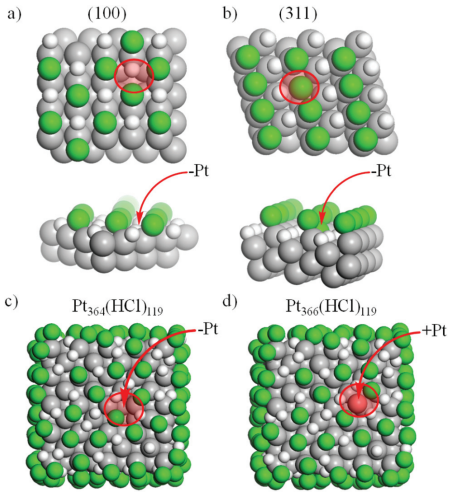

Fig. 3 Optimized structures after a Pt atom removal of HCl on (a) the Pt(100), (b) Pt(311) surfaces, as well as on (c) the $Pt_{365}(HCl)_{119}$ nanocube, and (d) after a Pt atom addition in the later system. Atomic color code as in Fig. 1. The positions of the removed and added Pt atoms are highlighted with a red circle.

≈ facet. However, for a cube with side length a and N atoms side, the number of edge atoms N_e is linear with N, while the number of face atoms N_f is quadratic. Therefore, N_f is one order of magnitude larger than N_e and, thus, the pitting shall start readily at the facets.

Although the presence of oxidative agents and explicit water models would be needed to have a complete picture of the synthesis and shape control of the nanoparticles, the computed results have already provided some hints on these phenomena.

With the calculated values, we propose a kinetic model to identify at which HCl concentration the pitting starts. The energy references have been taken as soluble H_2PtCl_6 units. This model relies on two equations:

$$\text{Deposition } Pt_{365} + H_2PtCl_6 + 4H_3O^+ \rightarrow Pt_{366} + 6HCl + 4H_2O$$

$$\text{Elimination } Pt_{365} + 6HCl \rightarrow Pt_{364} + H_2PtCl_6 + 4H^+$$

The kinetic coefficients[47] for deposition and elimination can be traced back to the values for deposition (−4.63 eV at the facet of the HCl-decorated Pt_{365}) and elimination (4.17 eV from the facet of the HCl-decorated Pt_{365}). For simplicity, we consider the kinetics of the above equations to be governed by power-low rates. Solvent effects are only considered through the continuum model. Although an atomistic insight[48] would be relevant to unravel the specific effect of the solvent, this point is beyond the aim of the present work. At a given value for the HCl concentration, when pitting starts, the deposition and elimination rates shall be equal and we can write the following equation

$$k_{dep}[Pt_{365}][H_2PtCl_6][H_3O^+]^4 = k_{el}[Pt_{365}][HCl]^6$$

Considering the experimental conditions: room temperature and the concentration of Pt in the solution, $[H_2PtCl_6]$ = 0.1 M and pH = 0, the [HCl] concentration at which the pitting starts is 43% HCl. Experimentally, the transition between Pt nanocubes and bonelike structures is observed at 37%.[2] Given the simplicity of our model, the agreement between the two thresholds for the pitting is remarkable. In addition, our results qualitatively agree with the increase in the (100) surface area of up to 25% HCl (43% in our case) and with its decrease for higher concentrations. From that point onwards, the surface area of surfaces like the 311 and 511 (which involve a higher number of steps and defects) increases.[2]

As the Wulff theorem always results in convex objects, we devised a new procedure to consider etched nanostructures obtained: (i) its final shape, (ii) surface(s) exposed, and (iii) the surface-to-volume ratio. Starting from the nanocube limited {100} planes and given that the pitting starts at the center of the facet, the formation of the convex structure can be found as a volume excavation from this pitting point.[15] Therefore, the process of forming a high-index faceted concave nanoparticle consists of the removal of an object (in our case, a tetragonal pyramid), made of the {hll}-like planes from each face of a nanocube (h, k, and l are Miller indices with $k = l$ and $h > k$, see Fig. 4a). Varying the concentration of HCl would then correspond to a different degree of intersection between solids. In the beginning, the facet excavated structures resemble the bonelike ones reported in ref. 2. In the limit where the {100} planes are completely excavated out, the resulting structure is an octapod containing, in our case, only the {311} planes (Fig. 4b). As mentioned above, it is important to point out that a concave nanoparticle containing just the {311} planes can only be obtained if the pitting occurs at the center of the {100} faces. If it occurred either at the corners or at the edge centers, the resulting structures would always contain the {100} and {311} planes simultaneously, and would never have sharp corners. A full derivation of the nanostructure formation, bonelike to octapods in this case, is presented in section S6.†

The final effect of the degree of penetration of the etching volume (red in Fig. 4) is represented by the δ parameter, which is the shortest distance between the corners of the pyramidal pit and the edges of the cubic particle (see Fig. 4b). The parameter δ depends on the concentration c of HCl (see section S6.2†). Therefore, for low etching values, the surface area of the nanoparticle does not change much (Fig. 4c). At intermediate values, the composition of the surface is 50% that of the {100} and {311} stepped surfaces, and only when the octapods appear, the total surface area decreases by about 45% of the initial value, being mostly of the {311} type. The effect on the volume is more pronounced. Although at $\delta = 0$ the volume is

6.2. Article VII: Shape control in concave metal nanoparticles by etching

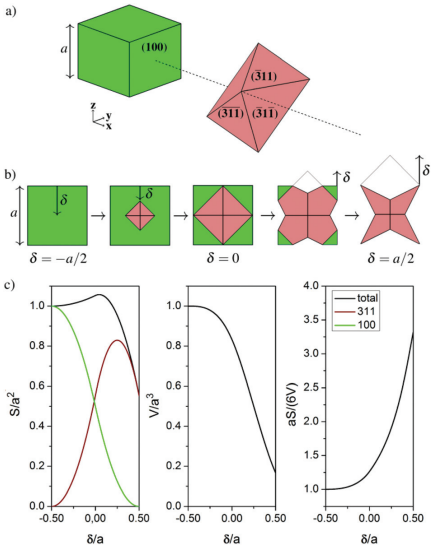

Fig. 4 (a) The formation of etched nanoparticles exhibiting the {311} planes can be described as a process where a tetragonal pyramid composed of the {311} planes intersects a cube at each face center. (b) Resulting structures for different HCl concentrations in the *y*–*z* plane (concentration increases from left to right). The gray line corresponds to the intersection between the tetragonal pyramid with the plane $x = a/2$. The parameter δ (see section S6†), which is shown for some of the cases, is measured from the edge of each face. (c) Surface area (left), volume (middle) and surface-to-volume ratio (right) for the nanoparticles as a function of δ. All quantities are scaled by the respective values for a cube with side length *a*. The color code for the surfaces is the same as shown in Fig. 2.

about 80%, when the octapod is formed the volume is only around 20% that of the nanocube. The most striking characteristic of these nanoobjects is the increase in the surface-to-volume ratio upon etching. At intermediate values of δ, the effect is not pronounced (marginal 10% increase), but it exponentially grows for δ/a larger than 0.25. Thus, after this severe etching (represented by the fourth structure in Fig. 4b), the surface-to-volume ratio is doubled and, under the most favorable conditions, it reaches a 3–4-fold increase. Such atom economy is essential to improve electrocatalytic performance.

To sum up, the acid control on the shape of the nanoparticle works as follows. Firstly, the nanostructures grow exhibiting the {100} surfaces as predicted from *ab initio* thermodynamics and reinforced by the Wulff construction. Once the chemical potential of the acid in the solution is too high, the deposition and consequent growth are no longer preferred over elimination and etching. This can be inferred by considering the chemical potential in the corresponding microkinetic equations. Here, the starting pitting point is important as it determines the final nanoparticle shape. A detailed balance between the number of potential pitting points – corners, edges, and facets – and the thermodynamic demand for this particular elimination is required to obtain the etched shape. Once the starting pitting point, in our case the face center, has been determined, the final equilibrium structure can be obtained by a geometrical model involving the intersection of our nanoobject with a polyhedron composed of the next stable surface at the pitting point. The impact on the geometric parameters can then be described through a model which, in our particular case, results in a surface-to-volume enhancement of up to 3–4-fold which improves the atom economy in these types of materials.

Conclusions

Theoretical calculations hold the key for an atomistic understanding of the control in the synthesis of nanostructures even when concave structures are generated. We have presented a formulation that describes the formation of concave Pt nanoparticles in the HCl–water environment. Our results based on *ab initio* thermodynamics predict cubic nanoparticles for any HCl concentration. However, at a certain HCl concentration, the gain for adding an extra Pt atom to the nanoparticle equilibrates with that of etching. Therefore, pitting starts at the most favorable elimination position, the facets. From this point, a geometric model based on the intersection of a nanocube and a polyhedron made of the {*hll*} planes predicts the equilibrium nanoparticle shape as a function of the degree of intersection, δ, between both the figures. When this parameter, which can be correlated with HCl concentration, adopts its maximum value, the structures are the octapods but resemble bonelike for smaller values as in the experiments. For the limiting case of octapods made of the {311} planes, the volume decreases 80% with respect to that for the cubic nanoparticle and the surface-to-volume ratio reaches a 3–4-fold increase. The resulting insights advance the understanding of the role of additives during metal nanoparticle growth and etching and can be extended to other metals and structures, thus opening a new perspective in understanding the control of new shapes and architectures.

Conflicts of interest

There are no conflicts of interest to declare.

Acknowledgements

The authors acknowledge the MINECO (project CTQ2015-68770-R and grants FPDI-2013-16194, SEV-2013-0319, and SEVP-2014-068237) for financial support. We are grateful to Professors J. M. Feliu and L. M. Liz-Marzan, for useful discussions.

References

1 E. C. Dreaden, A. M. Alkilany, X. H. Huang, C. J. Murphy and M. A. El-Sayed, *Chem. Soc. Rev.*, 2012, **41**, 2740–2779.

2 R. A. Martínez-Rodríguez, F. J. Vidal-Iglesias, J. Solla-Gullón, C. R. Cabrera and J. M. Feliu, *J. Am. Chem. Soc.*, 2014, **136**, 1280–1283.

3 T. Yu, D. Y. Kim, H. Zhang and Y. Xia, *Angew. Chem., Int. Ed.*, 2011, **50**, 2773–2777.

4 X. Xie, G. Gao, Z. Pan, T. Wang, X. Meng and L. Cai, *Sci. Rep.*, 2015, **5**, 8515.

5 H. Mistry, A. S. Varela, S. Kühl, P. Strasser and B. R. Cuenya, *Nat. Rev. Mater.*, 2016, **1**, 16009.

6 H. Heinz, C. Pramanik, O. Heinz, Y. Ding, R. K. Mishra, D. Marchon, R. J. Flatt, I. Estrela-Lopis, J. Llop, S. Moya and R. F. Ziolo, *Surf. Sci. Rep.*, 2017, **72**, 1–58.

7 Y. Xia and X. Yang, *Acc. Chem. Res.*, 2017, **50**, 450–454.

8 C. Burda, X. B. Chen, R. Narayanan and M. A. El-Sayed, *Chem. Rev.*, 2005, **105**, 1025–1102.

9 M. Grzelczak, J. Pérez-Juste, P. Mulvaney and L. M. Liz-Marzán, *Chem. Soc. Rev.*, 2008, **37**, 1783–1791.

10 Y. N. Xia, Y. J. Xiong, B. Lim and S. E. Skrabalak, *Angew. Chem., Int. Ed.*, 2009, **48**, 60–103.

11 N. M. Bedford, H. Ramezani-Dakhel, J. M. Slocik, B. D. Briggs, Y. Ren, A. I. Frenkel, V. Petkov, H. Heinz, R. R. Naik and M. R. Knecht, *ACS Nano*, 2015, **9**, 5082–5092.

12 H. Ramezani-Dakhel, L. Ruan, Y. Huang and H. Heinz, *Adv. Funct. Mater.*, 2015, **25**, 1374–1384.

13 Z. Wang, G. Yang, Z. Zhang, M. Jin and Y. Yin, *ACS Nano*, 2016, **10**, 4559–4564.

14 H. Zhang, M. Jin and Y. Xia, *Angew. Chem., Int. Ed.*, 2012, **51**, 7656–7673.

15 X. Q. Huang, Z. P. Zhao, J. M. Fan, Y. M. Tan and N. F. Zheng, *J. Am. Chem. Soc.*, 2011, **133**, 4718–4721.

16 M. T. M. Koper, *Nanoscale*, 2011, **3**, 2054–2073.

17 B. A. Lu, J. H. Du, T. Sheng, N. Tian, J. Xiao, L. Liu, B. B. Xu, Z. Y. Zhou and S. G. Sun, *Nanoscale*, 2016, **8**, 11559–11564.

18 N. Tian, Z.-Y. Zhou, S.-G. Sun, Y. Ding and Z. L. Wang, *Science*, 2007, **316**, 732–735.

19 H. Jing, Q. Zhang, N. Large, C. Yu, D. A. Blom, P. Nordlander and H. Wang, *Nano Lett.*, 2014, **14**, 3674–3682.

20 M. Chen, B. Wu, J. Yang and N. Zheng, *Adv. Mater.*, 2012, **24**, 862–879.

21 B. Y. Xia, H. B. Wu, X. Wang and X. W. Lou, *Angew. Chem., Int. Ed.*, 2013, **52**, 12337–12340.

22 G. Chen, Y. Tan, B. Wu, G. Fu and N. Zheng, *Chem. Commun.*, 2012, **48**, 2758–2760.

23 X. Xia, J. Zeng, B. McDearmon, Y. Zheng, Q. Li and Y. Xia, *Angew. Chem., Int. Ed.*, 2011, **50**, 12542–12546.

24 H. Zhang, W. Li, M. Jin, J. Zeng, T. Yu, D. Yang and Y. Xia, *Nano Lett.*, 2011, **11**, 898–903.

25 M. J. Mulvihill, X. Y. Ling, J. Henzie and P. Yang, *J. Am. Chem. Soc.*, 2010, **132**, 268–274.

26 O. M. Magnussen, *Chem. Rev.*, 2002, **102**, 679–725.

27 S. E. Lohse, N. D. Burrows, L. Scarabelli, L. M. Liz-Marzán and C. J. Murphy, *Chem. Mater.*, 2013, **26**, 34–43.

28 S. Gómez-Grana, B. Goris, T. Altantzis, C. Fernández-López, E. Carbó-Argibay, A. Guerrero-Martínez, N. Almora-Barrios, N. López, I. Pastoriza-Santos, J. Pérez-Juste, S. Bals, G. Van Tendeloo and L. M. Liz-Marzán, *J. Phys. Chem. Lett.*, 2013, **4**, 2209–2216.

29 M. Liu, Y. Zheng, L. Zhang, L. Guo and Y. Xia, *J. Am. Chem. Soc.*, 2013, **135**, 11752–11755.

30 G. Wulff, *Z. Krystallogr. Mineral.*, 1901, **34**, 449–530.

31 R. Tran, Z. Xu, B. Radhakrishnan, D. Winston, W. Sun, K. A. Persson and S. P. Ong, *Sci. Data*, 2016, **3**, 160080.

32 G. D. Barmparis, Z. Łodziana, N. López and I. N. Remediakis, *Beilstein J. Nanotechnol.*, 2015, **6**, 361–368.

33 K. Honkala, A. Hellman, I. N. Remediakis, A. Logadottir, A. Carlsson, S. Dahl, C. H. Christensen and J. K. Nørskov, *Science*, 2005, **307**, 555–558.

34 K. Reuter and M. Scheffler, *Phys. Rev. B: Condens. Matter*, 2002, **65**, 035406.

35 N. Almora-Barrios, G. Novell-Leruth, P. Whiting, L. M. Liz-Marzán and N. López, *Nano Lett.*, 2014, **14**, 871–875.

36 G. Kresse and J. Furthmüller, *Phys. Rev. B: Condens. Matter*, 1996, **54**, 11169–11186.

37 G. Kresse and J. Furthmüller, *Comput. Mater. Sci.*, 1996, **6**, 15–50.

38 J. P. Perdew, K. Burke and M. Ernzerhof, *Phys. Rev. Lett.*, 1996, **77**, 3865–3868.

39 G. Kresse and D. Joubert, *Phys. Rev. B: Condens. Matter*, 1999, **59**, 1758–1775.

40 P. E. Blochl, *Phys. Rev. B: Condens. Matter*, 1994, **50**, 17953–17979.

41 S. Grimme, *J. Comput. Chem.*, 2006, **27**, 1787–1799.

42 N. Almora-Barrios, G. Carchini, P. Błoński and N. López, *J. Chem. Theory Comput.*, 2014, **10**, 5002–5009.

43 J. Neugebauer and M. Scheffler, *Phys. Rev. B: Condens. Matter*, 1992, **46**, 16067–16080.

44 M. Garcia-Ratés and N. López, *J. Chem. Theory Comput.*, 2016, **12**, 1331–1341.

45 M. Álvarez-Moreno, C. de Graaf, N. López, F. Maseras, J. M. Poblet and C. Bo, *J. Chem. Inf. Model.*, 2015, **55**, 95–103, https://iochem-bd.bsc.es/browse/handle/100/9.

46 N. E. Singh-Miller and N. Marzari, *Phys. Rev. B: Condens. Matter*, 2009, **80**, 235407.

47 I. Chorkendorff and J. W. Niemantsverdriet, *Concepts of Modern Catalysis and Kinetics*, Wiley-VCH Verlag GmbH & Co. KGaA, Weinheim, 2005.

48 H. Heinz and H. Ramezani-Dakhel, *Chem. Soc. Rev.*, 2016, **45**, 412–448.

Bibliography

[1] Sherif, S. A.; Goswami, D. Y.; Stefanakos, E. L.; Steinfeld, A. *Handbook of hydrogen energy*; CRC Press, 2014.

[2] Basile, A.; Iulianelli, A. *Advances in hydrogen production, storage and distribution*; Elsevier, 2014.

[3] Dincer, I.; Zamfirescu, C. *Sustainable hydrogen production*; Elsevier, 2016.

[4] Besson, M.; Gallezot, P.; Pinel, C. Conversion of biomass into chemicals over metal catalysts. *Chem. Rev.* **2013**, *114*, 1827–1870.

[5] Alonso, D. M.; Wettstein, S. G.; Dumesic, J. A. Bimetallic catalysts for upgrading of biomass to fuels and chemicals. *Chem. Soc. Rev.* **2012**, *41*, 8075–8098.

[6] Werpy, T.; Petersen, G.; Aden, A.; Bozell, J.; Holladay, J.; White, J.; Manheim, A.; Eliot, D.; Lasure, L.; Jones, S. *Top value added chemicals from biomass. Volume 1-Results of screening for potential candidates from sugars and synthesis gas*; 2004.

[7] Bozell, J. J.; Petersen, G. R. Technology development for the production of biobased products from biorefinery carbohydrates–the US Department of Energy's "Top 10" revisited. *Green Chem.* **2010**, *12*, 539–554.

[8] Behling, R.; Valange, S.; Chatel, G. Heterogeneous catalytic oxidation for lignin valorization into valuable chemicals: what results? What limitations? What trends? *Green Chem.* **2016**, *18*, 1839–1854.

[9] Rinaldi, R.; Jastrzebski, R.; Clough, M. T.; Ralph, J.; Kennema, M.; Bruijnincx, P. C.; Weckhuysen, B. M. Paving the way for lignin valorisa-

tion: recent advances in bioengineering, biorefining and catalysis. *Angew. Chem. Int. Ed.* **2016**, *55*, 8164–8215.

[10] Chorkendorff, I.; Niemantsverdriet, J. W. *Concepts of modern catalysis and kinetics*; John Wiley & Sons, 2006.

[11] Zhang, X.; Wilson, K.; Lee, A. F. Heterogeneously Catalyzed Hydrothermal Processing of C5–C6 Sugars. *Chem. Rev.* **2016**, *116*, 12328–12368.

[12] Deutschmann, O.; Knözinger, H.; Kochloefl, K.; Turek, T. Heterogeneous catalysis and solid catalysts. *Ullmann's Encyclopedia of Industrial Chemistry* **2011**,

[13] Sabatier, P.; Senderens, J. B. New methane synthesis. *C.R.Acad.Sci.Paris* **1902**, *134*.

[14] Bravo-Suárez, J. J.; Chaudhari, R. V.; Subramaniam, B. *Novel Materials for Catalysis and Fuels Processing*; ACS Publications, 2013; pp 3–68.

[15] Atkins, P.; Paula, J. d. *Atkins's physical chemistry*; 2010.

[16] Eyring, H. The Activated Complex in Chemical Reactions. *J. Chem. Phys.* **1935**, *3*, 107–115.

[17] Laidler, K. J.; King, M. C. Development of transition-state theory. *J. Phys. Chem.* **1983**, *87*, 2657–2664.

[18] Brönsted, J. Acid and Basic Catalysis. *Chem. Rev.* **1928**, *5*, 231–338.

[19] Bell, R. P. The Theory of Reactions Involving Proton Transfers. **1936**, *154*, 414–429.

[20] Evans, M.; Polanyi, M. Inertia and driving force of chemical reactions. *Trans. Faraday Soc.* **1938**, *34*, 11–24.

[21] Ertl, G. Dynamics of reactions at surfaces. *Advances in catalysis* **2000**, *45*, 1–69.

[22] Kresse, G.; Furthmüller, J. Efficiency of ab-initio total energy calculations for metals and semiconductors using a plane-wave basis set. *Comput. Mater. Sci.* **1996**, *6*, 15–50.

[23] Kresse, G.; Furthmüller, J. Efficient iterative schemes for ab initio total-energy calculations using a plane-wave basis set. *Phys. Rev. B* **1996**, *54*, 11169–11186.

BIBLIOGRAPHY

[24] Lopez, N.; Almora-Barrios, N.; Carchini, G.; Błoński, P.; Bellarosa, L.; Garcia-Muelas, R.; Novell-Leruth, G.; Garcia-Mota, M. State-of-the-art and challenges in theoretical simulations of heterogeneous catalysis at the microscopic level. *Catal. Sci. Tech.* **2012**, *2*, 2405–2417.

[25] Schrödinger, E. An Undulatory Theory of the Mechanics of Atoms and Molecules. *Phys. Rev.* **1926**, *28*, 1049–1070.

[26] Koch, W.; Holthausen, M. C. *A chemist's guide to density functional theory*; John Wiley & Sons, 2015.

[27] Sholl, D.; Steckel, J. A. *Density functional theory: a practical introduction*; John Wiley & Sons, 2011.

[28] McQuarrie, D. A. *Quantum chemistry*; University Science Books, 2008.

[29] Atkins, P. W.; Friedman, R. S. *Molecular quantum mechanics*; Oxford university press, 2011.

[30] Levine, I. N. *Quantum Chemistry*; Pearson Prentice Hall Upper Saddle River, NJ, 2009.

[31] Coppens, P. *X-ray charge densities and chemical bonding*; International Union of Crystallography, 1997.

[32] Bader, R. F. *Atoms in Molecules: A Quantum Theory (International Series of Monographs on Chemistry)*; Clarendon Press, 1994.

[33] Stalke, D. *Electron Density and Chemical Bonding I*; Springer, 2012.

[34] Stalke, D. *Electron Density and Chemical Bonding II*; Springer, 2012.

[35] Hohenberg, P.; Kohn, W. Inhomogeneous electron gas. *Phys. Rev.* **1964**, *136*, B864.

[36] Kohn, W.; Sham, L. J. Self-consistent equations including exchange and correlation effects. *Phys. Rev.* **1965**, *140*, A1133.

[37] Perdew, J. P.; Schmidt, K. Jacob's ladder of density functional approximations for the exchange-correlation energy. *AIP Conference Proceedings* **2001**, *577*, 1–20.

[38] Perdew, J. P.; Ruzsinszky, A.; Tao, J.; Staroverov, V. N.; Scuseria, G. E.; Csonka, G. I. Prescription for the design and selection of density functional approximations: More constraint satisfaction with fewer fits. *J. Chem. Phys.* **2005**, *123*, 062201.

[39] Perdew, J. P.; Wang, Y. Accurate and simple analytic representation of the electron-gas correlation energy. *Phys. Rev. B* **1992**, *45*, 13244–13249.

[40] Perdew, J. P.; Burke, K.; Ernzerhof, M. Generalized gradient approximation made simple. *Phys. Rev. Lett.* **1996**, *77*, 3865–3868.

[41] Hellmann, H. A New Approximation Method in the Problem of Many Electrons. *J. Chem. Phys.* **1935**, *3*, 61–61.

[42] Schwerdtfeger, P. The pseudopotential approximation in electronic structure theory. *ChemPhysChem* **2011**, *12*, 3143–3155.

[43] Slater, J. C. Wave Functions in a Periodic Potential. *Phys. Rev.* **1937**, *51*, 846–851.

[44] Blöchl, P. E. Projector augmented-wave method. *Phys. Rev. B* **1994**, *50*, 17953.

[45] Kresse, G.; Joubert, D. From ultrasoft pseudopotentials to the projector augmented-wave method. *Phys. Rev. B* **1999**, *59*, 1758.

[46] McNaught, A. D.; McNaught, A. D. *Compendium of chemical terminology*; Blackwell Science Oxford, 1997; Vol. 1669.

[47] Grimme, S. Semiempirical GGA-type density functional constructed with a long-range dispersion correction. *J. Comput. Chem.* **2006**, *27*, 1787–1799.

[48] Almora-Barrios, N.; Carchini, G.; Błoński, P.; López, N. Costless derivation of dispersion coefficients for metal surfaces. *J. Chem. Theory Comput.* **2014**, *10*, 5002–5009.

[49] Garcia-Ratés, M.; López, N. Multigrid-Based Methodology for Implicit Solvation Models in Periodic DFT.

[50] Cococcioni, M.; Mauri, F.; Ceder, G.; Marzari, N. Electronic-enthalpy functional for finite systems under pressure. *Phys. Rev. Lett.* **2005**, *94*, 145501.

[51] Scherlis, D. A.; Fattebert, J.-L.; Gygi, F.; Cococcioni, M.; Marzari, N. A unified electrostatic and cavitation model for first-principles molecular dynamics in solution. *J. Chem. Phys.* **2006**, *124*, 074103.

[52] Andreussi, O.; Dabo, I.; Marzari, N. Revised self-consistent continuum

solvation in electronic-structure calculations. *J. Chem. Phys.* **2012**, *136*, 064102.

[53] Blöchl, P. E. Projector augmented-wave method. *Phys. Rev. B* **1994**, *50*, 17953–17979.

[54] Kresse, G.; Joubert, D. From ultrasoft pseudopotentials to the projector augmented-wave method. *Phys. Rev. B* **1999**, *59*, 1758–1775.

[55] Monkhorst, H. J.; Pack, J. D. Special points for Brillouin-zone integrations. *Phys. Rev. B* **1976**, *13*, 5188–5192.

[56] Makov, G.; Payne, M. C. Periodic boundary conditions in ab initio calculations. *Phys. Rev. B* **1995**, *51*, 4014–4022.

[57] Bučko, T.; Hafner, J.; Lebegue, S.; Angyán, J. G. Improved description of the structure of molecular and layered crystals: Ab initio DFT calculations with van der Waals corrections. *J. Phys. Chem. A* **2010**, *114*, 11814–11824.

[58] Lide, D. *CRC Handbook of Chemistry and Physics*, 84th ed.; CRC press LLC: Boca Raton London New York Washington, D.C., 2003–2004; pp 12(19–21).

[59] García-Muelas, R.; López, N. Collective Descriptors for the Adsorption of Sugar Alcohols on Pt and Pd(111). *J. Phys. Chem. C* **2014**, *118*, 17531–17537.

[60] Henkelman, G.; Jónsson, H. Improved tangent estimate in the nudged elastic band method for finding minimum energy paths and saddle points. *J. Chem. Phys.* **2000**, *113*, 9978–9985.

[61] Henkelman, G.; Uberuaga, B. P.; Jónsson, H. A climbing image nudged elastic band method for finding saddle points and minimum energy paths. *J. Chem. Phys.* **2000**, *113*, 9901–9904.

[62] Heyden, A.; Bell, A. T.; Keil, F. J. Efficient methods for finding transition states in chemical reactions: Comparison of improved dimer method and partitioned rational function optimization method. *J. Chem. Phys.* **2005**, *123*, 224101(1–14).

[63] Henkelman, G.; Jónsson, H. A dimer method for finding saddle points on high dimensional potential surfaces using only first derivatives. *J. Chem. Phys.* **1999**, *111*, 7010–7022.

[64] Logadottir, A.; Rod, T. H.; Nørskov, J. K.; Hammer, B.; Dahl, S.; Jacobsen, C. The Brønsted–Evans–Polanyi relation and the volcano plot for ammonia synthesis over transition metal catalysts. *J. Catal.* **2001**, *197*, 229–231.

[65] Nørskov, J. K.; Bligaard, T.; Logadottir, A.; Bahn, S.; Hansen, L. B.; Bollinger, M.; Bengaard, H.; Hammer, B.; Sljivancanin, Z.; Mavrikakis, M. Universality in heterogeneous catalysis. *J. Catal.* **2002**, *209*, 275–278.

[66] Pallassana, V.; Neurock, M. Electronic factors governing ethylene hydrogenation and dehydrogenation activity of pseudomorphic PdML/Re (0001), PdML/Ru(0001), Pd(111), and PdML/Au(111) surfaces. *J. Catal.* **2000**, *191*, 301–317.

[67] Liu, Z.-P.; Hu, P. General trends in the barriers of catalytic reactions on transition metal surfaces. *J. Chem. Phys.* **2001**, *115*, 4977–4980.

[68] Alcalá, R.; Mavrikakis, M.; Dumesic, J. A. DFT studies for cleavage of C-C and C-O bonds in surface species derived from ethanol on Pt(111). *J. Catal.* **2003**, *218*, 178–190.

[69] Abild-Pedersen, F.; Greeley, J.; Studt, F.; Rossmeisl, J.; Munter, T.; Moses, P. G.; Skúlason, E.; Bligaard, T.; Nørskov, J. K. Scaling properties of adsorption energies for hydrogen-containing molecules on transition-metal surfaces. *Phys. Rev. Lett.* **2007**, *99*, 016105.

[70] Wang, S.; Petzold, V.; Tripkovic, V.; Kleis, J.; Howalt, J. G.; Skúlason, E.; Fernández, E.; Hvolbæk, B.; Jones, G.; Toftelund, A.; Falsig H, B. M.; Studt, F.; Abild-Pedersen, F.; Rossmeisl, J.; Nørskov, J.; Bligaard, T. Universal transition state scaling relations for (de) hydrogenation over transition metals. *Phys. Chem. Chem. Phys.* **2011**, *13*, 20760–20765.

[71] Wang, S.; Temel, B.; Shen, J.; Jones, G.; Grabow, L. C.; Studt, F.; Bligaard, T.; Abild-Pedersen, F.; Christensen, C. H.; Nørskov, J. K. Universal Brønsted-Evans-Polanyi relations for C–C, C–O, C–N, N–O, N–N, and O–O dissociation reactions. *Catal. Lett.* **2011**, *141*, 370–373.

[72] Wang, S.; Vorotnikov, V.; Sutton, J. E.; Vlachos, D. G. Brønsted–Evans–Polanyi and transition state scaling relations of furan derivatives on Pd(111) and their relation to those of small molecules. *ACS Catal.* **2014**, *4*, 604–612.

[73] Santen, R. A. v.; Neurock, M.; Shetty, S. G. Reactivity theory of

transition-metal surfaces: a Brønsted-Evans-Polanyi linear activation energy-free-energy analysis. *Chem. Rev.* **2009**, *110*, 2005–2048.

[74] Zaffran, J.; Michel, C.; Auneau, F.; Delbecq, F.; Sautet, P. Linear energy relations as predictive tools for polyalcohol catalytic reactivity. *ACS Catal.* **2014**, *4*, 464–468.

[75] Plessow, P. N.; Abild-Pedersen, F. Examining the Linearity of Transition State Scaling Relations. *J. Phys. Chem. C* **2015**, *119*, 10448–10453.

[76] Chen, Y.; Salciccioli, M.; Vlachos, D. G. An efficient reaction pathway search method applied to the decomposition of glycerol on platinum. *J. Phys. Chem. C* **2011**, *115*, 18707–18720.

[77] Sutton, J. E.; Vlachos, D. G. A theoretical and computational analysis of linear free energy relations for the estimation of activation energies. *ACS Catal.* **2012**, *2*, 1624–1634.

[78] Sutton, J. E.; Vlachos, D. G. Effect of errors in linear scaling relations and Brønsted–Evans–Polanyi relations on activity and selectivity maps. *J. Catal.* **2016**, *338*, 273–283.

[79] Ulissi, Z. W.; Medford, A. J.; Bligaard, T.; Nørskov, J. K. To address surface reaction network complexity using scaling relations machine learning and DFT calculations. *Nat. Commun.* **2017**, *8*, 14621.

[80] Liu, B.; Greeley, J. Decomposition pathways of glycerol via C–H, O–H, and C–C bond scission on Pt(111): a density functional theory study. *J. Phys. Chem. C* **2011**, *115*, 19702–19709.

[81] Liu, B.; Greeley, J. Density functional theory study of selectivity considerations for C–C versus C–O bond scission in glycerol decomposition on Pt(111). *Top. Catal.* **2012**, *55*, 280–289.

[82] Liu, B.; Greeley, J. A density functional theory analysis of trends in glycerol decomposition on close-packed transition metal surfaces. *Phys, Chem, Chem, Phys,* **2013**, *15*, 6475–6485.

[83] García-Muelas, R.; Li, Q.; López, N. Density Functional Theory Comparison of Methanol Decomposition and Reverse Reactions on Metal Surfaces. *ACS Catal.* **2015**, *5*, 1027–1036.

[84] Palo, D. R.; Dagle, R. A.; Holladay, J. D. Methanol steam reforming for hydrogen production. *Chem. Rev.* **2007**, *107*, 3992–4021.

[85] Liu, P.; Yang, Y.; White, M. G. Theoretical perspective of alcohol decomposition and synthesis from CO_2 hydrogenation. *Surf. Sci. Rep.* **2013**, *68*, 233–272.

[86] Jung, E.; Jung, U.; Yang, T.; Peak, D.; Jung, D.; Kim, S. Methanol crossover through PtRu/Nafion composite membrane for a direct methanol fuel cell. *Int. J. Hydrogen Energy* **2007**, *32*, 903–907.

[87] Dinh, H. N.; Ren, X.; Garzon, F. H.; Zelenay, P.; Gottesfeld, S. Electrocatalysis in direct methanol fuel cells: in-situ probing of PtRu anode catalyst surfaces. *J. Electroanal. Chem.* **2000**, *491*, 222–233.

[88] Ralph, T.; Hogarth, M. Catalysis for low temperature fuel cells. *Platin. Met. Rev.* **2002**, *46*, 117–135.

[89] Hogarth, M.; Ralph, T. Catalysis for low temperature fuel cells. *Platin. Met. Rev.* **2002**, *46*, 146–164.

[90] Gallagher, J. T.; Kidd, J. M. Methanol Synthesis. 1966; GB1159035.

[91] others,, et al. The active site of methanol synthesis over $Cu/ZnO/Al_2O_3$ industrial catalysts. *Science* **2012**, *336*, 893–897.

[92] Olah, G. A. Beyond oil and gas: the methanol economy. *Angew. Chem. Int. Ed.* **2005**, *44*, 2636–2639.

[93] Greeley, J.; Mavrikakis, M. Methanol decomposition on Cu(111): a DFT study. *J. Catal.* **2002**, *208*, 291–300.

[94] Kattel, S.; Ramírez, P. J.; Chen, J. G.; Rodriguez, J. A.; Liu, P. Active sites for CO2 hydrogenation to methanol on Cu/ZnO catalysts. *Science* **2017**, *355*, 1296–1299.

[95] Hrbek, J.; DePaola, R. A.; Hoffmann, F. M. The interaction of methanol with Ru(001). *J. Chem. Phys.* **1984**, *81*, 2818–2827.

[96] Quispe, C. A.; Coronado, C. J.; Carvalho Jr, J. A. Glycerol: Production, consumption, prices, characterization and new trends in combustion. *Renew. Sustain. Energy Rev.* **2013**, *27*, 475–493.

[97] Ayoub, M.; Abdullah, A. Z. Critical review on the current scenario and significance of crude glycerol resulting from biodiesel industry towards more sustainable renewable energy industry. *Renew. Sustain. Energy Rev.* **2012**, *16*, 2671–2686.

BIBLIOGRAPHY

[98] Cortright, R.; Davda, R.; Dumesic, J. A. Hydrogen from catalytic reforming of biomass-derived hydrocarbons in liquid water. *Nature* **2002**, *418*, 964–967.

[99] Coll, D.; Delbecq, F.; Aray, Y.; Sautet, P. Stability of intermediates in the glycerol hydrogenolysis on transition metal catalysts from first principles. *Phys. Chem. Chem. Phys.* **2011**, *13*, 1448–1456.

[100] Michel, C.; Auneau, F.; Delbecq, F.; Sautet, P. C–H versus O–H Bond Dissociation for Alcohols on a Rh(111) Surface: A Strong Assistance from Hydrogen Bonded Neighbors. *ACS Catal.* **2011**, *1*, 1430–1440.

[101] Cortright, R. D.; Davda, R. R.; Dumesic, J. A. Hydrogen from catalytic reforming of biomass-derived hydrocarbons in liquid water. *Nature* **2002**, *418*, 964–967.

[102] Huber, G. W.; Shabaker, J.; Dumesic, J. Raney Ni-Sn catalyst for H2 production from biomass-derived hydrocarbons. *Science* **2003**, *300*, 2075–2077.

[103] Huber, G. W.; Cortright, R. D.; Dumesic, J. A. Renewable alkanes by aqueous-phase reforming of biomass-derived oxygenates. *Angew. Chem. Int. Ed.* **2004**, *43*, 1549–1551.

[104] Rackemann, D. W.; Doherty, W. O. The conversion of lignocellulosics to levulinic acid. *Biofuels, Bioprod. Bioref.* **2011**, *5*, 198–214.

[105] Tuck, C. O.; Pérez, E.; Horváth, I. T.; Sheldon, R. A.; Poliakoff, M. Valorization of biomass: deriving more value from waste. *Science* **2012**, *337*, 695–699.

[106] van Putten, R.-J.; van der Waal, J. C.; De Jong, E.; Rasrendra, C. B.; Heeres, H. J.; de Vries, J. G. Hydroxymethylfurfural, a versatile platform chemical made from renewable resources. *Chem. Rev.* **2013**, *113*, 1499–1597.

[107] Climent, M. J.; Corma, A.; Iborra, S. Conversion of biomass platform molecules into fuel additives and liquid hydrocarbon fuels. *Green Chem.* **2014**, *16*, 516–547.

[108] Gallezot, P. Conversion of biomass to selected chemical products. *Chem. Soc. Rev.* **2012**, *41*, 1538–1558.

[109] Fegyverneki, D.; Orha, L.; Láng, G.; Horváth, I. T. Gamma-valerolactone-based solvents. *Tetrahedron* **2010**, *66*, 1078–1081.

[110] Wettstein, S. G.; Alonso, D. M.; Chong, Y.; Dumesic, J. A. Production of levulinic acid and gamma-valerolactone (GVL) from cellulose using GVL as a solvent in biphasic systems. *Energy Environ. Sci.* **2012**, *5*, 8199–8203.

[111] Farrán, A.; Cai, C.; Sandoval, M.; Xu, Y.; Liu, J.; Hernáiz, M. J.; Linhardt, R. J. Green solvents in carbohydrate chemistry: From raw materials to fine chemicals. *Chem. Rev.* **2015**, *115*, 6811–6853.

[112] Alonso, D. M.; Wettstein, S. G.; Dumesic, J. A. Gamma-valerolactone, a sustainable platform molecule derived from lignocellulosic biomass. *Green Chem.* **2013**, *15*, 584–595.

[113] Yan, K.; Yang, Y.; Chai, J.; Lu, Y. Catalytic reactions of gamma-valerolactone: a platform to fuels and value-added chemicals. *Appl. Catal., B* **2015**, *179*, 292–304.

[114] Michel, C.; Gallezot, P. Why Is Ruthenium an Efficient Catalyst for the Aqueous-Phase Hydrogenation of Biosourced Carbonyl Compounds? *ACS Catal.* **2015**, *5*, 4130–4132.

[115] Tan, J.; Cui, J.; Deng, T.; Cui, X.; Ding, G.; Zhu, Y.; Li, Y. Water-Promoted Hydrogenation of Levulinic Acid to γ-Valerolactone on Supported Ruthenium Catalyst. *ChemCatChem* **2015**, *7*, 508–512.

[116] Corma, A.; Iborra, S.; Velty, A. Chemical routes for the transformation of biomass into chemicals. *Chem. Rev.* **2007**, *107*, 2411–2502.

[117] Wright, W. R.; Palkovits, R. Development of heterogeneous catalysts for the conversion of levulinic acid to γ-valerolactone. *ChemSusChem* **2012**, *5*, 1657–1667.

[118] Manzer, L. E. Catalytic synthesis of α-methylene-γ-valerolactone: a biomass-derived acrylic monomer. *Appl. Catal., A* **2004**, *272*, 249–256.

[119] Bourne, R. A.; Stevens, J. G.; Ke, J.; Poliakoff, M. Maximising opportunities in supercritical chemistry: the continuous conversion of levulinic acid to γ-valerolactone in CO_2. *Chem. Commun.* **2007**, 4632–4634.

[120] Upare, P. P.; Lee, J.-M.; Hwang, D. W.; Halligudi, S. B.; Hwang, Y. K.; Chang, J.-S. Selective hydrogenation of levulinic acid to γ-valerolactone

over carbon-supported noble metal catalysts. *J. Ind. Eng. Chem.* **2011**, *17*, 287–292.

[121] Abdelrahman, O. A.; Heyden, A.; Bond, J. Q. Analysis of kinetics and reaction pathways in the aqueous-phase hydrogenation of levulinic acid to form γ-valerolactone over Ru/C. *ACS Catal.* **2014**, *4*, 1171–1181.

[122] Xiao, C.; Goh, T.-W.; Qi, Z.; Goes, S.; Brashler, K.; Perez, C.; Huang, W. Conversion of levulinic acid to γ-valerolactone over few-layer graphene-supported ruthenium catalysts. *ACS Catal.* **2015**, *6*, 593–599.

[123] Braden, D. J.; Henao, C. A.; Heltzel, J.; Maravelias, C. C.; Dumesic, J. A. Production of liquid hydrocarbon fuels by catalytic conversion of biomass-derived levulinic acid. *Green Chem.* **2011**, *13*, 1755–1765.

[124] Luo, W.; Sankar, M.; Beale, A. M.; He, Q.; Kiely, C. J.; Bruijnincx, P. C. A.; Weckhuysen, B. M. High performing and stable supported nano-alloys for the catalytic hydrogenation of levulinic acid to γ-valerolactone. *Nat. Commun.* **2015**, *6*, 6540.

[125] Luo, W.; Deka, U.; Beale, A. M.; van Eck, E. R.; Bruijnincx, P. C. A.; Weckhuysen, B. M. Ruthenium-catalyzed hydrogenation of levulinic acid: Influence of the support and solvent on catalyst selectivity and stability. *J. Catal.* **2013**, *301*, 175–186.

[126] Deng, L.; Zhao, Y.; Li, J.; Fu, Y.; Liao, B.; Guo, Q.-X. Conversion of Levulinic Acid and Formic Acid into γ-Valerolactone over Heterogeneous Catalysts. *ChemSusChem* **2010**, *3*, 1172–1175.

[127] Moreno-Marrodan, C.; Barbaro, P. Energy efficient continuous production of γ-valerolactone by bifunctional metal/acid catalysis in one pot. *Green Chem.* **2014**, *16*, 3434–3438.

[128] Kumar, V. V.; Naresh, G.; Sudhakar, M.; Anjaneyulu, C.; Bhargava, S. K.; Tardio, J.; Reddy, V. K.; Padmasri, A. H.; Venugopal, A. An investigation on the influence of support type for Ni catalysed vapour phase hydrogenation of aqueous levulinic acid to γ-valerolactone. *RSC Adv.* **2016**, *6*, 9872–9879.

[129] Galletti, A. M. R.; Antonetti, C.; De Luise, V.; Martinelli, M. A sustainable process for the production of γ-valerolactone by hydrogenation of biomass-derived levulinic acid. *Green Chem.* **2012**, *14*, 688–694.

[130] Zhang, X.; Murria, P.; Jiang, Y.; Xiao, W.; Kenttämaa, H. I.; Abu-Omar, M. M.; Mosier, N. S. Maleic acid and aluminum chloride catalyzed conversion of glucose to 5-(hydroxymethyl) furfural and levulinic acid in aqueous media. *Green Chem.* **2016**, *18*, 5219–5229.

[131] Oosterom, G. E.; Reek, J. N.; Kamer, P. C.; van Leeuwen, P. W. Transition metal catalysis using functionalized dendrimers. *Angew. Chem. Intl. Ed.* **2001**, *40*, 1828–1849.

[132] Pârvulescu, V. I.; Hardacre, C. Catalysis in ionic liquids. *Chem. Rev.* **2007**, *107*, 2615–2665.

[133] Kaushik, A.; Kumar, R.; Arya, S. K.; Nair, M.; Malhotra, B.; Bhansali, S. Organic–inorganic hybrid nanocomposite-based gas sensors for environmental monitoring. *Chem. Rev.* **2015**, *115*, 4571–4606.

[134] Boles, M. A.; Ling, D.; Hyeon, T.; Talapin, D. V. The surface science of nanocrystals. *Nature Mat.* **2016**, *15*, 141.

[135] Witte, P. T.; Berben, P. H.; Boland, S.; Boymans, E. H.; Vogt, D.; Geus, J. W.; Donkervoort, J. G. BASF NanoSelect^{TM} technology: innovative supported Pd-and Pt-based catalysts for selective hydrogenation reactions. *Top. Catal.* **2012**, *55*, 505–511.

[136] Witte, P. T.; Boland, S.; Kirby, F.; van Maanen, R.; Bleeker, B. F.; de Winter, D.; Post, J. A.; Geus, J. W.; Berben, P. H. NanoSelect Pd Catalysts: What Causes the High Selectivity of These Supported Colloidal Catalysts in Alkyne Semi-Hydrogenation? *ChemCatChem* **2013**, *5*, 582–587.

[137] Boymans, E. H.; Witte, P.; Vogt, D. A study on the selective hydrogenation of nitroaromatics to N-arylhydroxylamines using a supported Pt nanoparticle catalyst. *Catal. Sci. Tech.* **2015**, *5*, 176–183.

[138] Vilé, G.; Almora-Barrios, N.; Mitchell, S.; López, N.; Pérez-Ramírez, J. From the Lindlar Catalyst to Supported Ligand-Modified Palladium Nanoparticles: Selectivity Patterns and Accessibility Constraints in the Continuous-Flow Three-Phase Hydrogenation of Acetylenic Compounds. *Chem. Eur. J.* **2014**, *20*, 5926–5937.

[139] Vilé, G.; Almora-Barrios, N.; López, N.; Pérez-Ramírez, J. Structure and Reactivity of Supported Hybrid Platinum Nanoparticles for the Flow Hy-

drogenation of Functionalized Nitroaromatics. *ACS Catal.* **2015**, *5*, 3767–3778.

[140] Albani, D.; Vilé, G.; Mitchell, S.; Witte, P. T.; Almora-Barrios, N.; Verel, R.; López, N.; Pérez-Ramírez, J. Ligand ordering determines the catalytic response of hybrid palladium nanoparticles in hydrogenation. *Catal. Sci. Tech.* **2016**, *6*, 1621–1631.

[141] Albani, D.; Li, Q.; Vilé, G.; Mitchell, S.; Almora-Barrios, N.; Witte, P. T.; López, N.; Pérez-Ramírez, J. Interfacial acidity in ligand-modified ruthenium nanoparticles boosts the hydrogenation of levulinic acid to gamma-valerolactone. *Green Chem.* **2017**, *19*, 2361–2370.

[142] Vollhardt, K. P. C.; Schore, N. E. *Organic chemistry: structure and function*; Macmillan, 2003.

[143] Lari, G. M.; Gröninger, O. G.; Li, Q.; Mondelli, C.; López, N.; Pérez-Ramírez, J. Catalyst and Process Design for the Continuous Manufacture of Rare Sugar Alcohols by Epimerization–Hydrogenation of Aldoses. *ChemSusChem* **2016**, *9*, 3407–3418.

[144] Perlack, R. D.; Wright, L. L.; Turhollow, A. F.; Graham, R. L.; Stokes, B. J.; Erbach, D. C. *Biomass as feedstock for a bioenergy and bioproducts industry: the technical feasibility of a billion-ton annual supply*; 2005.

[145] Calvo-Flores, F. G.; Dobado, J. A. Lignin as renewable raw material. *ChemSusChem* **2010**, *3*, 1227–1235.

[146] Chakar, F. S.; Ragauskas, A. J. Review of current and future softwood kraft lignin process chemistry. *Ind. Crops Prod.* **2004**, *20*, 131–141.

[147] Delidovich, I.; Hausoul, P. J.; Deng, L.; Pfützenreuter, R.; Rose, M.; Palkovits, R. Alternative monomers based on lignocellulose and their use for polymer production. *Chem. Rev.* **2015**, *116*, 1540–1599.

[148] Kai, D.; Tan, M. J.; Chee, P. L.; Chua, Y. K.; Yap, Y. L.; Loh, X. J. Towards lignin-based functional materials in a sustainable world. *Green Chem.* **2016**, *18*, 1175–1200.

[149] Zakzeski, J.; Bruijnincx, P. C.; Jongerius, A. L.; Weckhuysen, B. M. The catalytic valorization of lignin for the production of renewable chemicals. *Chem. Rev.* **2010**, *110*, 3552–3599.

[150] Li, C.; Zhao, X.; Wang, A.; Huber, G. W.; Zhang, T. Catalytic transformation of lignin for the production of chemicals and fuels. *Chem. Rev.* **2015**, *115*, 11559–11624.

[151] Thielemans, W.; Can, E.; Morye, S.; Wool, R. Novel applications of lignin in composite materials. *J. Appl. Polym. Sci.* **2002**, *83*, 323–331.

[152] Song, Q.; Wang, F.; Xu, J. Hydrogenolysis of lignosulfonate into phenols over heterogeneous nickel catalysts. *Chem. Commun.* **2012**, *48*, 7019–7021.

[153] Zhang, J.; Teo, J.; Chen, X.; Asakura, H.; Tanaka, T.; Teramura, K.; Yan, N. A series of NiM (M=Ru, Rh, and Pd) bimetallic catalysts for effective lignin hydrogenolysis in water. *ACS Catal.* **2014**, *4*, 1574–1583.

[154] Lu, X.; Deng, Z.; Guo, C.; Wang, W.; Wei, S.; Ng, S.-P.; Chen, X.; Ding, N.; Guo, W.; Wu, C.-M. L. Methanol Oxidation on Pt3Sn(111) for Direct Methanol Fuel Cells: Methanol Decomposition. *ACS Appl. Mater. Interfaces* **2016**, *8*, 12194–12204.

[155] Hamou, C. A. O.; Réocreux, R.; Sautet, P.; Michel, C.; Giorgi, J. B. Adsorption and Decomposition of a Lignin β-O-4 Linkage Model, 2-Phenoxyethanol, on Pt (111): Combination of Experiments and First-Principles Calculations. *J. Phys. Chem. C* **2017**, *121*, 9889–9900.

[156] Lee, K.; Gu, G. H.; Mullen, C. A.; Boateng, A. A.; Vlachos, D. G. Guaiacol Hydrodeoxygenation Mechanism on Pt(111): Insights from Density Functional Theory and Linear Free Energy Relations. *ChemSusChem* **2015**, *8*, 315–322.

[157] Calvo-Flores, F. G.; Dobado, J. A.; Isac-García, J.; Martí-Martínez, F. J. *Lignin and lignans as renewable raw materials: chemistry, technology and applications*; John Wiley & Sons, 2015.

UNIVERSITAT ROVIRA I VIRGILI
DENSITY FUNCTIONAL THEORY STUDIES OF BIOMASS CONVERSION ON METAL SURFACES:
FROM SMALL TO LARGE MOLECULES
Qiang Li

UNIVERSITAT
ROVIRA i VIRGILI